

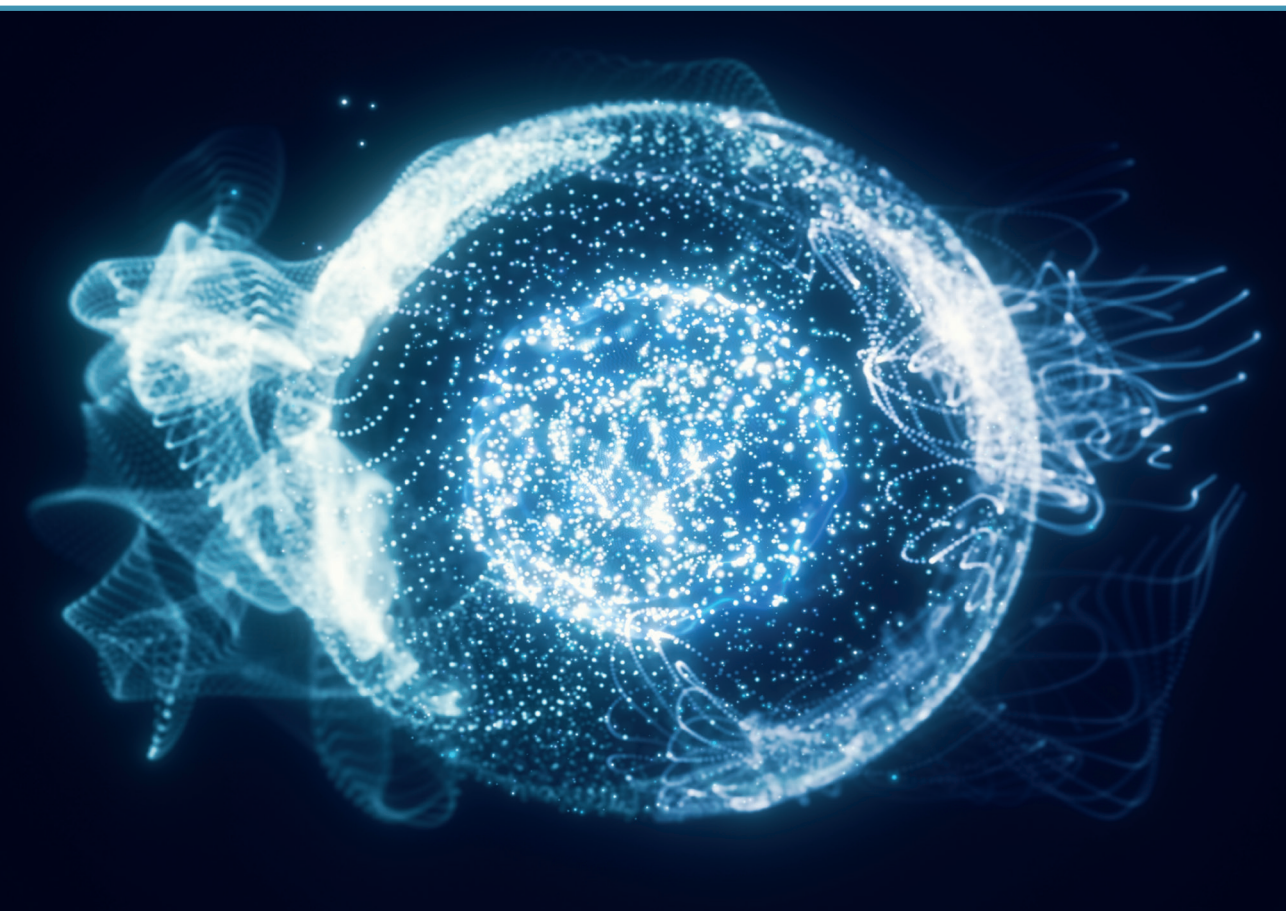


RIGA TECHNICAL  
UNIVERSITY

**Dmitrii Redka**

# **EVALUATION OF DYNAMICS OF NON-SCATTERING STATES IN NANOPHOTONICS**

Doctoral Thesis



RTU Press  
Riga 2024

**RIGA TECHNICAL UNIVERSITY**

Faculty of Computer Science, Information Technology and Energy  
Institute of Photonics, Electronics and Telecommunications

**Dmitrii Redka**

Doctoral Student of the Study Programme “Telecommunications”

**EVALUATION OF DYNAMICS OF NON-SCATTERING  
STATES IN NANOPHOTONICS**

**Doctoral Thesis**

**Scientific supervisor:**

Professor Dr. sc. ing. VJAČESLAVS BOBROVS

RTU Press

Riga 2024

Redka D., Evaluation of dynamics of non-scattering states in nanophotonics. Doctoral Thesis.  
Riga: RTU Press, 2024. 190 pp.

Published in accordance with the decision of the Promotion Council  
“P- 08” of 24. May 2024,  
Minutes No. 32.

This work has been supported by the European Social Fund within Project No. 8.2.2.0/20/I/008, “Strengthening of PhD students and academic personnel of Riga Technical University and BA School of Business and Finance in the strategic fields of specialization” of the Specific Objective 8.2.2 “To Strengthen Academic Staff of Higher Education Institutions in Strategic Specialization Areas” of the Operational Programme “Growth and Employment”.

The research was supported by Doctoral Grant programme of Riga Technical University.

**NATIONAL  
DEVELOPMENT  
PLAN 2020**



**EUROPEAN UNION**  
European Social  
Fund

---

INVESTING IN YOUR FUTURE

# **DOCTORAL THESIS PROPOSED TO RIGA TECHNICAL UNIVERSITY FOR THE PROMOTION TO THE SCIENTIFIC DEGREE OF DOCTOR OF SCIENCE**

To be granted the scientific degree of Doctor of Science (Ph. D.), the present Doctoral Thesis has been submitted for the defense at the open meeting of RTU Promotion Council on 30 August 2024 at the Faculty of Computer Science, Information Technology and Energy of Riga Technical University (RTU), 12 Azenes Str., Room 201.

## **OFFICIAL REVIEWERS**

Researcher, Ph.D. Inga Brice  
University of Latvia, Latvia

Professor, Ph.D, Lei Gao  
Soochow University, China

Professor Dr. sc. ing. Jurgis Poriņš  
Riga Technical University

## **DECLARATION OF ACADEMIC INTEGRITY**

I hereby declare that the Doctoral Thesis submitted for the review to Riga Technical University for the promotion to the scientific degree of Doctor of Science (Ph. D.) is my own. I confirm that this Doctoral Thesis had not been submitted to any other university for the promotion to a scientific degree.

Dmitrii Redka ..... (signature)

Date: .....

The Doctoral Thesis has been prepared as a thematically united collection of scientific publications. It comprises 11 scientific articles and publications in conference proceeding from the 39 author's existing works indexed in SCOPUS, WoS, and IEEE databases. Publications are written in English and are published in SCOPUS, WoS, IEEE databases, their total volume/number of pages is 105 pages.

## LIST OF ABBREVIATIONS

- ADN** – All-Dielectric Nanophotonics
- BICs** – Bound States in the Continuum
- CW** – Continuous Wave
- EDA** – Electric Dipole Anapole
- HA** – Hybrid Anapoles
- HM** – Hyperbolic Modes
- HMM** – Hyperbolic Metamaterial
- LDOS** – Local Density of Optical States
- LTIE** – Low-Temperature Ion Exchange
- MOCT** – Magnetic Octupole
- MSAD** – Mean-Squared Angular Displacements
- QNM** – Quasi-Normal Modes
- SIT** – Self-induced Transparency
- SAM** – Spin Angular Momentum
- SMRFBARs** – Solid Mounted Film Bulk Acoustic Resonators
- SPP** – Surface Plasmon-Polariton
- WGM** – Whispering Gallery Mode

## CONTENTS

CHAPTER 1: GENERAL OVERVIEW OF THE THESIS .....	6
1.1 Introduction.....	6
1.2 The aim and theses of the dissertation .....	8
1.3 The key tasks of the Doctoral Thesis .....	9
1.4 Research methods .....	9
1.5 Scientific novelty and main results .....	10
1.6 The practical value of the doctoral Thesis .....	11
1.7 Structure of the Thesis .....	12
1.8 Publications and approbation of the Thesis .....	12
CHAPTER 2: INVESTIGATING AND MODELING NEW OPTICAL EFFECTS IN NANOSTRUCTURED ENVIRONMENTS .....	14
2.1 Observation and multipole analysis of hybrid anapoles .....	14
2.2 Nanoparticle dynamics in the optical nanovortex and its applications for lab-on-a-chip platforms .....	22
2.3 Controlling ultrashort pulse propagation in disordered layered media.....	30
2.4 Analysis of the diffusion-inspired emission dynamics in nanostructured environments.....	36
2.5 Modeling optical binding effect in hyperbolic metamaterials .....	40
2.6 Modeling superscattering effect emerging from the physics of bound states in the continuum .....	43
2.7 Optical properties of magnetic octupole in silicon quadrumers .....	48
3. REAL-WORLD APPLICATIONS AND EXPERIMENTAL RESULTS.....	53
3.1 Macroporous phononic crystal based structures for FBAR applications.....	53
3.2 Modeling and characterization of microspheres with silver molecular clusters for sensor applications .....	59
CONCLUSIONS.....	64
BIBLIOGRAPHY .....	66
SUPPLEMENTS.....	75

# Chapter 1: General overview of the Thesis

## 1.1 Introduction

In the last decade, the interest in the optical properties of structures of high index semiconductor nanoparticles with low losses (for example, Si, TiO<sub>2</sub>) increased incrementally [1]. Their response in a continuous irradiation mode was studied in detail, and many new optical effects were obtained, arising primarily due to the ability to excite both electrical and magnetic multipole moments in such particles and almost complete absence of absorption [2], [3]. Based on the detected phenomena, several ultra-thin optical systems (about a few tens of nanometers thick) have been developed [4], [5], [6]. These systems have functionality that is unattainable for the conventional ones. Despite the large number of groups in the world carrying out these researches, the field still is far from exhaustion being regularly replenished with new discoveries.

It should be noted that, while the interaction of femtosecond laser pulses with matter is one of the most advanced problems of modern coherent and nonlinear optics, the response of such semiconductor (in the literature the name "dielectric" due to low absorption is also adopted) nanoparticles to ultra-short laser pulses has not been enough studied yet. Bearing in mind that, the characteristic transient time-scale for many resonance phenomena in nanophotonics is comparable with the duration of the femtosecond incident pulse, it creates the ground for the emergence of fundamentally new non-stationary effects. Given the rich mode composition of the fields of dielectric nanostructures, due, as already noted, to the presence of eigenmodes of both types (electric and magnetic), having different resonant frequencies and quality factors, it can be argued that the interaction of ultra-short pulses with them will lead to the emergence of qualitatively new phenomena, which do not exist at stationary scattering.

It seems most interesting to consider the temporal dynamics of states that in the stationary mode are non-scattering (dark modes) and, accordingly, the metasurfaces of such particles are almost completely transparent. In this regard, nanoparticles and metasurfaces in the anapole and hybrid-anapole states (the recently discovered state protected in a stationary regime from both the environment and the substrate, the femtosecond response of which, in turn, strongly depends on the environment and substrate [7]) will be investigated theoretically and experimentally. These states, similar in stationary mode, have completely different mode compositions and will allow realizing different time dynamics and effects. The combination of the completely different properties in continuous and pulse regimes will provide an opportunity to subsequently develop new optical elements with dual functionality (for example, new ultra-thin repetition rate multipliers, light filters, modulators, polarizers, etc.), which presently do not exist.

The planned Thesis lies in a new and extremely rapidly developing field of nanophotonics [8–10]. For example, according to the Scopus database, more than 1,500 articles are published annually in this area. The applications of dielectric nanophotonics are very diverse, for example, waveguides [11], [12], modulators [13], directional radiation sources and nanoantennas [14],

detectors [15], masking and invisibility devices [16], phase metasurfaces [17], [18], etc. The development of dielectric nanophotonics has already made it possible to create various metasurfaces, materials, and meta-devices that realize the control of optical beams with almost no loss [19].

However, there is now a need for new, ultra-thin photonic elements capable of effectively controlling ultrashort laser pulses, which the aforementioned nanophotonic devices, with few exceptions, do not allow [20].

The PhD Thesis is complex and includes a full cycle of work, starting with a theoretical (analytical and numerical) study of the tasks, carried out in close cooperation with the experimental testing, which will make it possible to verify the correctness of the theory and, if necessary, make adjustments to it, and ending with the testing of prototypes that most fully demonstrate new phenomena, this project is devoted to. Specifically, the Thesis is investigating both theoretically and experimentally new effects due to the action of ultrashort laser pulses on high-index semiconductor nanoparticles (e.g. Si, Ge) with low absorption in the visible range. Currently, this area remains poorly explored. The study of transient dynamics in interaction with the pulses of nanoparticles in states that are non-scattering relative to continuous radiation, characterized by non-trivial mode structure in the near field is of a special interest. In particular, the project will focus on the study of the temporal dynamics of the anapole and hybrid-anapole states, as well as the interaction of metasurfaces of such nanoparticles with femtosecond pulses. Note that it is, for the first time, found that at the steady-state the mentioned new hybrid anapole may correspond to the realization at the same frequency of the anapole states simultaneously for all contributing multipoles. Therefore, the irradiated particles occur in a completely non-scattering state (the usual anapole state makes it possible to extinguish only the radiation from a single, usually electric-dipolar, mode).

Remarkably, a hybrid anapole state is accompanied by a strong concentration of the electromagnetic field in the near field zone and the excitation of a large set of the resonant and non-resonant eigenmodes with different Q-factors. At the action of a short (femtosecond) laser pulse, it may result in a strong and non-trivial modulation of its envelope. In the case of the irradiation of an array of such nanoparticles and/or the corresponding metasurfaces, the modulation will depend also on the metasurfaces symmetry as well as on the geometrical and optical properties of the substrate. Note that in the CW irradiation the optical response in the hybrid-anapole state does not depend on the environment and the substrate. Because of that, the metasurfaces made of such nanoparticles, while remaining completely transparent to a CW (though controlling its phase!), should strongly modulate femtosecond pulses. These properties will be used in the project to realize various dual-performance optical systems and devices, whose response to the action of femtosecond and long laser pulses will be qualitatively different.

The focus is on the study of new optical effects in the challenging subfield of ultrafast subwavelength optics. However, the specific subfield, namely transient optics of the non-scattering regimes, practically has not been developed yet and represents a vast field for activity.



The Thesis is aimed at fundamental research in a new area and the implementation of fundamental models of new devices based on the results obtained. Within the Thesis framework, models have been developed and prototypes of new ultra-thin planar photonic elements such as ultra-thin repetition rate multipliers, light filters, beam modulators, etc., have been implemented. These elements are designed for femtosecond optics and have dual-use applications for both short pulses and continuous irradiation.

## **1.2 The aim and theses of the dissertation**

Summarizing the above-mentioned facts about the directions of development of semiconductor nanostructures and their applications in photonic devices and optical communication systems, the following aim of the Doctoral Thesis is proposed:

Study and explore new optical effects arising from the interaction of semiconductor nanoparticles with metasurfaces when exposed to femtosecond laser pulses. Develop new models of nanostructured elements and evaluate their potential applications in modern telecommunication systems and photonics.

### **To achieve the aim set, the following theses were put forward:**

1. The current theory of hybrid anapole conditions demonstrates that effective spatiotemporal control of transients mediated by the underlying substrate can be achieved, while maintaining scattering at negligible levels in the stationary regime.

2. High-k volumetric modes can provide additional channels for the particles' interaction with substrates, thereby significantly enhancing the capabilities of optomechanical manipulation schemes. For semi-infinite (or rather thick) metamaterial slabs, the hyperbolic modes, even though dominant in scattering, do not contribute to optical binding due to the almost absent feedback. Hyperbolic modes excited by one particle do not interact with the second one. In contrast, thin metamaterial slabs provide multiple reflections from boundaries, forming a set of strongly localized hot spots with significant intensity gradients that govern nanoparticles' motion at the nanoscale.

3. The dynamics of time-dependent Purcell effect in a solution of phosphorescent molecules interfacing resonant nanoantenna can be utilized for a contactless all-optical temperature and diffusion measurements. Dynamics of the long life-time phosphorescent molecules decay is shown to be strongly dependent on the Brownian motion next to a resonator. This special interaction is described with temperature and diffusion coefficient of the surrounding liquid. Subsequently, far-field radiation emitted from diffusing molecules is analyzed via the inverse Laplace transform and exploited to recover local properties of a fluid environment.

4. Resonant magnetic octupole (MOCT) response can be obtained by dividing a solid rectangular silicon block to a quadrumer structure with the introduction of narrow gaps between four nanocubes. The spectral position of the MOCT resonance is controlled and tuned by varying the distance between the nanocubes.

5. Bound states in the continuum (BICs) enable unique features in tailoring light-matter interaction on nanoscale. These radiationless localized states drive theoretically infinite quality factors and lifetimes for modern nanophotonics, making room for a variety of emerging applications.

### **1.3 The key tasks of the Doctoral Thesis**

To achieve the set goal of the dissertation and to prove the proposed theses, it is necessary to perform the following key tasks:

1. Theoretically predict and experimentally confirm the existence of hybrid anapoles, previously unnoticed non-scattering regimes requiring the simultaneous destructive interference of electric and magnetic cartesian multipoles with their toroidal counterparts. Establish a more in-depth view of the hybrid anapole by comparing it to its simpler counterpart, the electric dipole anapole and validate an alternative description of conventional anapole states based on the Fano response's separation into a resonant and a non-resonant contribution.

2. Perform theoretical study of the dynamic time-dependent Purcell effect in a solution of phosphorescent molecules interfacing resonant nanoantenna.

3. Study the propagation of ultrashort pulses in the resonant multilayered medium with initial population difference randomly varying along the propagation direction. Consider three potential disorder models and reveal their potential applications for flexible control over the optical response of the medium.

4. Analyze conditions for maximal conversion of spin angular momentum of the incident light to orbital angular momentum of the scattered light via the specially designed transversely scattering silicon nanocube.

### **1.4 Research methods**

To perform the tasks outlined in the Doctoral Thesis and to analyze the problems, mathematical calculations, numerical simulations, and experimental measurements have been used. Numerical simulations were implemented in Matlab, Origin, Comsol Multiphysics, CST MICROWAVE STUDIO, Ansoft Academic Research HF.

Scientific experiments described in the Doctoral Thesis and their results were carried out at the Nanophotonics Research Laboratory (NANO-Photon Lab.) at Institute of Photonics, Electronics and Electronic Communications (IPEEC) of Riga Technical University (RTU), St. Petersburg Electrotechnical University (ETU "LET"), and at the Department of Applied Physics of Royal Swedish Technical University (KTH) in close collaboration with the Swedish research institute RISE Acreo in Sweden and using video calls for online experiment measurements during the COVID-19 pandemic (digital laboratory work called "Zoom-lab") in close collaboration with the Institute of Applied Physics of the Federal Research Center of the Russian

Academy of Sciences (IAP-RAS) in Russia and Information Technologies, Mechanics and Optics University (ITMO) in Russia.

## 1.5 Scientific novelty and main results

Novel achievements of the Doctoral Thesis are as follows:

1. We have theoretically predicted and experimentally confirmed the existence of hybrid anapoles, previously unnoticed non-scattering regimes requiring the simultaneous destructive interference of electric and magnetic cartesian multipoles with their toroidal counterparts. In the transient regime, obtained results have allowed us to design at will the breakdown of the hybrid anapole conditions to obtain ultrafast modulation of the scattered power. Therefore, combining our findings with up-to-date modulation techniques holds great promise for future applications in the emerging field of ultrafast dynamic nanophotonics.

2. For the first time, higher-order (quadrupolar) toroidal moments are shown to contribute to essential features of the scattering response of an isolated high-index nanoparticle. We validated our results by fabricating a series of individual silicon nanocylinders supporting the HA and confirmed its existence experimentally through dark-field spectroscopy measurements.

3. We investigated the propagation of ultrashort pulses in a resonant multilayered medium with randomly varying initial population differences along the propagation direction. The focus was on an active system with a disordered loss-gain distribution and a uniform background. As a result, three potential disorder models were considered, revealing two transitions and three distinct regimes as the disorder increased. The transitions were from the self-induced transparency (SIT) regime to the localization regime and then to the amplification regime. The amplification regime only appeared when negative population differences were possible and the disorder was sufficiently large. These effects provide opportunities for flexible control over the optical response of the medium, enabling adjustments in the reflection-to-transmission ratio and pulse propagation speed through the disorder parameter.

4. We have developed a novel concept for contactless temperature and diffusion measurements utilizing the Purcell effect in phosphorescent molecules near a nanoantenna. By analyzing the emitted radiation, we can extract local properties of the surrounding liquid, enabling efficient and high-resolution measurements across a wide temperature range. This method has potential applications in lab-on-a-chip systems and microfluidics.

5. We have demonstrated novel superscattering regimes by utilizing subwavelength, nonspherical resonators and exploiting the strong coupling of two resonances. Our findings show superscattering originating from an electric super dipole moment, surpassing the currently established limit by almost two times. By disrupting the quasi-BIC condition in resonators without spherical symmetry through parameter adjustments, power exchange between scattering channels enables the manipulation of Q-factors and multipolar contents while maintaining a high scattering cross-section. Our super multipole resonances exhibit enhanced resistance to Ohmic

losses compared to conventional counterparts. These findings have implications in biosensing, energy harvesting, on-chip circuitry and optical manipulation.

## 1.6 The practical value of the doctoral Thesis

1. A new cost-effective material suitable for use in label-free sensors with active WGM resonators has been obtained. The experiment showed that glass samples subjected to Low-Temperature Ion Exchange (LTIE) showed distinct absorption characteristics, particularly the absence of characteristic absorption peaks, which was attributed to the formation of Ag<sub>2</sub>...<sub>5</sub> molecular clusters of silver. Luminescence measurements demonstrated a broad emission band in the visible spectrum, especially in the 500–900 nm range, confirming the formation of silver microcrystals during the LTIE process. According to the simulation results, the difference between the resonant wavelengths for media with different refractive indexes was 0.26 nm. This allows the material to be used for microsphere sensors without direct physical connection. The results obtained show the potential of soda silicate glass with molecular silver clusters as a material for WGM sensors.

2. Resonant MOCT excitation has been confirmed to induce controlled magnetic hotspots and resonant absorption in a nanostructure. We analyzed the multipole contributions to the scattering cross section and identified the excitation of the magnetic octupole due to the coupling effects in this structure, in contrast to the single cube. We demonstrated how to control the resonant excitation of MOCT and its spectral position. In addition, we revealed its potential application for creating magnetic hotspots and absorbing electromagnetic energy in the nanostructure. The utilization of quadrumers as building blocks for metasurfaces holds the promise of achieving even greater magnetic field enhancement, thanks to the potential excitation of trapped modes. Moreover, after being scaled to the microwave region, the considered structure could be very promising for magnetic resonance imaging applications. A strong concentration of magnetic fields is necessary to enhance the contrast and quality of the images. Additionally, the resonant magnetic octupole response can be extensively utilized for spectroscopy, sensing, detecting small quantum objects, and various other potential applications.

3. We have demonstrated the results of theoretical research work focused on studying technologically competitive solutions of phononic structures' performance for the purposes of FBAR devices. We proposed considering the established technological platform for fabricating macroporous structures as an approach that enables the realization of phononic-based acoustic reflectors for FBAR SMR devices and studying appropriate periodic structure solutions using numerical methods. We have shown that the use of macroporous periodic arrangements can facilitate the efficient operation of SMRFBARs across broad frequency ranges without the need to employ a membrane for isolating the piezoelectric film. Computational results for square, triangular, and honeycomb arrangements, demonstrating the achievable bandgap responses have been presented. It was found that the honeycomb arrangement is the most advantageous in terms

of bandgap performance, which should allow the FBAR structures to operate within a broad frequency range. The completed work represents an initial step towards the fabrication of photonic crystal-based FBAR devices, which is the focus of current research.

**The results obtained in the dissertation were used:**

1. Novel non-Hermitian singularities in all-dielectric nanostructures (NEO-NATE) (01.01.2023 - 31.12.2025)
2. Strengthening of PhD students and academic personnel of Riga Technical University and BA School of Business and Finance in the strategic fields of specialization (01.08.2021 - 30.11.2023)
3. Deutsche Forschungsgemeinschaft (DFG, German Research Foundation) within the Cluster of Excellence PhoenixD (EXC 2122, Project ID 390833453).

## **1.7 Structure of the Thesis**

The dissertation is prepared as a thematically unified set of publications on the development and evaluation of quantum effects in nanostructures that can be used in future more efficient hybrid optical communication systems and their elements.

Chapter 1 describes the topicality of the research, evaluates the aim and theses, describes the main tasks, research methodology, the structure of the work and the main results.

Chapter 2 describes the results of theoretical and numerical studies, as well as modeling new optical effects in nanostructured environments. The main stages are:

1. Multipole analysis of hybrid anapoles (contribution from PAPER 1).
2. Study of nanoparticle dynamics (contribution from PAPERS 2 and 9).
3. Study of ultrashort pulse propagation in nanostructured environments (contribution from PAPER 8).
4. Modeling optical effects in nanostructured environments (contribution from PAPERS 3, 4, 6, 9, 10).

Chapter 3 focuses on experimental research on optical sensors and the study of new nanomaterials (contribution from PAPERS 7 and 11).

In Conclusions, both theoretical and experimental results are discussed, and answers to the established questions are given.

## **1.8 Publications and approbation of the Thesis**

The results of the Doctoral Thesis are presented in 11 scientific articles and in publications in conference proceedings indexed in SCOPUS, WoS, and IEEE databases. The author has altogether 39 publications:

PAPER 1. Canós Valero A., Gurvitz E.A., Benimetskiy F.A., Pidgayko D.A., Samusev A., Evlyukhin A.B., Bobrovs V., Redka D., Tribelsky M.I., Rahmani M., Kamali K.Z., Pavlov A.A.,

Miroshnichenko A.E., Shalin A.S., “Theory, Observation, and Ultrafast Response of the Hybrid Anapole Regime in Light Scattering”, (2021) *Laser and Photonics Reviews*, 15 (10), art. no. 2100114, DOI: 10.1002/lpor.202100114

PAPER 2. Canós Valero A., Kislov D., Gurvitz E.A., Shamkhi H.K., Pavlov A.A., Redka D., Yankin S., Zemánek P., Shalin A.S., “Nanovortex-Driven All-Dielectric Optical Diffusion Boosting and Sorting Concept for Lab-on-a-Chip Platforms”, (2020) *Advanced Science*, 7 (11), art. no. 1903049, DOI: 10.1002/advs.201903049

PAPER 3. Novitsky D.V., Shalin A.S., Redka D., Bobrovs V., Novitsky A.V., “Quasibound states in the continuum induced by PT symmetry breaking”, (2021) *Physical Review B*, 104 (8), art. no. 085126, DOI: 10.1103/PhysRevB.104.085126

PAPER 4. Terekhov P.D., Evlyukhin A.B., Redka D., Volkov V.S., Shalin A.S., Karabchevsky A., “Magnetic Octupole Response of Dielectric Quadrumers”, (2020) *Laser and Photonics Reviews*, 14 (4), art. no. 1900331, DOI: 10.1002/lpor.201900331

PAPER 5. Novitsky D.V., Lyakhov D., Michels D., Redka D., Pavlov A.A., Shalin A.S., “Controlling wave fronts with tunable disordered non-Hermitian multilayers”, (2021) *Scientific Reports*, 11 (1), art. no. 4790, DOI: 10.1038/s41598-021-84271-0

PAPER 6. Kostina N.A., Kislov D.A., Ivinskaya A.N., Proskurin A., Redka D.N., Novitsky A., Ginzburg P., Shalin A.S., “Nanoscale Tunable Optical Binding Mediated by Hyperbolic Metamaterials”, (2020) *ACS Photonics*, 7 (2), pp. 425 - 433, DOI: 10.1021/acsp Photonics.9b01378

PAPER 7. Oseev A., Mukhin N.V., Lucklum R., Zubtsov M., Schmidt M.-P., Redka D., Kozyrev A., Hirsch S., “Towards macroporous phononic crystal based structures for FBAR applications. Theoretical investigation of technologically competitive solutions”, (2018) *Microsystem Technologies*, 24 (5), pp. 2389 - 2399, DOI: 10.1007/s00542-017-3616-1

PAPER 8. Novitsky D.V., Redka D., Shalin A.S., “Different Regimes of Ultrashort Pulse Propagation in Disordered Layered Media with Resonant Loss and Gain”, (2019) *Annalen der Physik*, 531 (9), art. no. 1900080, DOI: 10.1002/andp.201900080,

PAPER 9. Kislov D., Novitsky D., Kadochkin A., Redka D., Shalin A.S., Ginzburg P. “Diffusion-inspired time-varying phosphorescent decay in a nanostructured environment”, (2020) *Physical Review B*, 101 (3), art. no. 035420, DOI: 10.1103/PhysRevB.101.035420

PAPER 10. Canós Valero A., Shamkhi H.K., Kupriianov A.S., Weiss T., Pavlov A.A., Redka D., Bobrovs V., Kivshar Y., Shalin A.S., “Superscattering emerging from the physics of bound states in the continuum”, (2023) *Nature Communications*, 14 (1), art. no. 4689, DOI: 10.1038/s41467-023-40382-y

PAPER 11. Mikharev, E.; Lunev, A.; Sidorov, A.; Redka, D. “Modeling and Characterization of Microspheres with Silver Molecular Clusters for Sensor Applications”. (2023) *Eng. Proc.*, 58,95. DOI: 10.3390/ ecsa-10-16196

## Chapter 2: Investigating and modeling new optical effects in nanostructured environments

### 2.1 Observation and multipole analysis of hybrid anapoles

All-dielectric nanophotonics (ADN), a key area in nano-optics research [21], [22], offers a solution to the ohmic losses found in plasmonic structures by utilizing low-loss semiconductor or dielectric materials such as Si, TiO<sub>2</sub>, Ge, and GaAs [23], [24]. These materials enable the manipulation of light's electrical and magnetic components at the nanoscale, resulting in applications in low-loss waveguides [25], [26], directional sources [27], [28], harmonic generation [29], light harvesting, and anti-reflective coatings [30]–[32]. Advances also include all-dielectric metasurfaces [33]–[36], beam deflectors [37], and subwavelength fluid mixing [19]. Critical to controlling light at the nanoscale is accurately describing electromagnetic scattering. This is achieved through electromagnetic multipole expansion methods [38]–[42] and the charge-current Cartesian decomposition [38 - 40], which enables the identification of the toroidal moment family within optical properties [43]–[46].

The transient behavior of electric dipole anapole (EDA) remains largely unexplored, despite its potential for novel applications in ultrafast dynamic resonant phenomena. Most studies have focused solely on the stationary response and the electric dipole term [47]–[50]. However, the existence of magnetic anapoles could lead to enhanced radiation suppression and unprecedented electromagnetic energy confinement, opening new possibilities for light-matter interactions, as well as the creation of so-called Hybrid Anapoles (HA). Recent theoretical advancements [40]–[46], [51], [52] have enabled the investigation of higher-order electric and magnetic anapoles in scatterers with arbitrary shapes, paving the way for further exploration in the field.

This chapter focuses on the design of hybrid anapole configurations and experimentally demonstrates their existence. We demonstrate the emergence of anapoles, which result from multipoles of alternating electric and magnetic nature, interconnected in scatterers with disrupted spherical symmetry. Additionally, we show that the counterintuitive opportunity to satisfy four anapole conditions by varying only two parameters is strongly related to the violation of the scatterer's spherical symmetry. Finally, based on the developed theoretical description, we design and demonstrate a dual-functional metasurface consisting of an array of HA particles. This metasurface combines full transparency in the stationary regime with a highly tunable spatiotemporal response in the transient regime.

The analysis of a nanoparticle's optical response is typically carried out by decomposing the scattering cross-section into a sum of multipoles. These multipoles represent independent scattering channels of the object. Thus, considering the irreducible Cartesian multipole expansion, electric or magnetic anapole of order  $n$  in a subwavelength scatterer is given by the following condition:

$$P^{(e,m)}_{i_1 \dots i_n} + i \frac{k_d}{v_d} T^{(e,m)}_{i_1 \dots i_n} = 0 \quad (2.1)$$

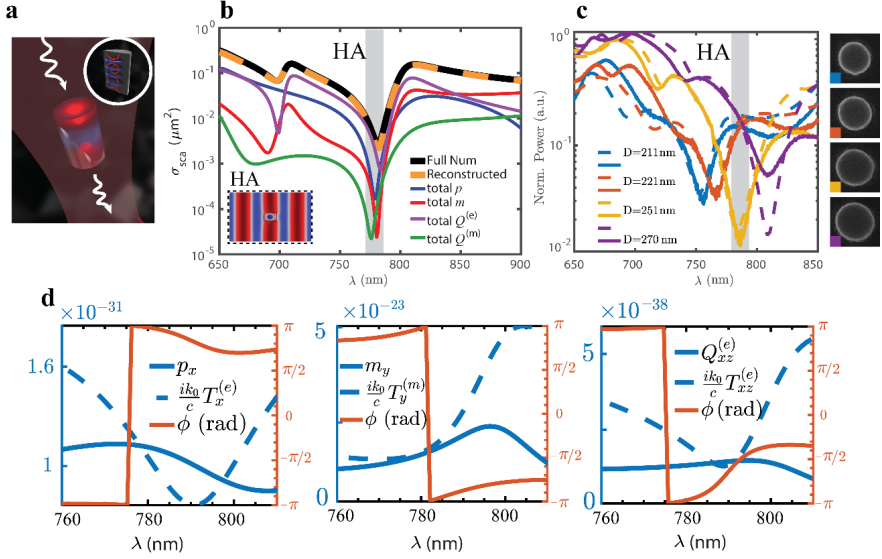
Here we have denoted the  $n_{th}$  order electric or magnetic moments with  $P^{(e)}$  and  $P^{(m)}$ , and the corresponding electric and magnetic toroidal moments with  $T^{(e)}$  and  $T^{(m)}$ , respectively. The number of subscripts indicates each Cartesian tensor's order, i.e., one subscript corresponds to a dipole, two corresponds to a quadrupole, etc.  $k_d$  is the wavenumber and  $v_d$  is the speed of light in the medium. The HA phenomenon occurs when multiple multipole moments satisfy Equation 1 at a specific wavelength, leading to the simultaneous suppression of scattering from two or more channels. However, light, in general, can be radiated through other non-zero multipole moments, which can disrupt the overall effect. Thus, only the cancellation of all the leading multipoles can enable a true HA regime.

Let us consider a cylindrical silicon (a-Si) nanoparticle in the air. A normally incident plane wave excites nontrivial modal contributions in a silicon nanocylinder. The interference with the background field leads to a four-fold hybrid anapole, resulting in the nanoantenna being virtually invisible in the far-field while maintaining a localized near-field. The inset depicts the current distributions of the two resonant eigenmodes caused by standing waves between the top and bottom walls (red) and the lateral walls (blue) in the vertical plane (Fig. 2.1a). In the legend caption (Fig. 2.1b), the term "total" implies that both the basic and toroidal contributions of a given multipole are plotted. The inset corresponds to the x-component of the electric field. The cylinder's geometrical parameters are height  $H = 367$  nm and diameter  $D = 252$  nm. Point HA ( $\lambda = 782$  nm) corresponds to the minima of the absorption spectrum of the substance.

The design methodology is based on the following: We note that the spectral positions of the full (basic together with toroidal contributions), electric dipole, and magnetic quadrupole anapoles are mainly dependent on the cylinder's radius. In contrast, the wavelengths of the full magnetic dipole and electric quadrupole anapoles change as functions of both the cylinder height and radius. Thus, carefully tuning these two geometrical degrees of freedom makes it possible to place the anapoles of all the leading terms ultimately close to each other (Fig. 2.1b), providing a strong scattering minimum (Fig. 2.1b).

Direct scattering spectroscopy measurements on standalone nanocylinders have been carried out in order to confirm the existence of hybrid anapole modes. The measured scattering spectra exhibit a pronounced dip (Fig. 2.1c) that shifts with the nanocylinder diameter, in agreement with theoretical predictions. The most pronounced hybrid anapole mode occurs at a diameter of 251 nm, leading to a significant reduction in scattering efficiency.





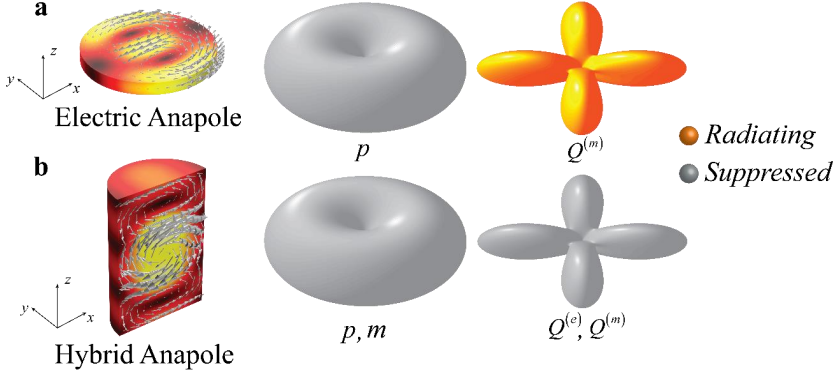
2.1. fig. Analysis of Hybrid Anapoles.

(a) Artistic representation of the novel effect. (b) Multipole reconstruction of the numerically obtained scattering cross section for the cylindrical amorphous silicon nanoparticle. (c) The colored regions indicate the left plot: measured (solid lines) and simulated (dashed lines) scattering spectra of single isolated nanocylinders with different diameters  $D$ . The spectral positions of the hybrid anapoles. Right plot: SEM micrographs of the corresponding nanocylinder samples. The colored edges in each micrograph are associated with the measurements' legend entries. (d) Amplitudes and phase differences between the multipoles and their toroidal counterparts. Panels from left to right, respectively: the basic electric and electric toroidal dipoles, the basic magnetic and magnetic toroidal dipoles, and the basic electric and electric toroidal quadrupoles. Amplitudes correspond to the left ordinate-axis, and phase differences are read from the right ordinate-axis.

Both HAs and EDAs suppress far-field radiation and enhance near-fields. However, HAs offer advantages over EDAs for nanophotonic applications. Fig. 2.2 shows that EDAs exhibit poloidal-like field distributions and significant contributions from the magnetic quadrupole to radiation. This is a fundamental limitation of EDAs, as resonator modes with inversion symmetry will always radiate as combinations of multipoles with even or odd parity [53 -54]. HAs, on the other hand, do not suffer from this limitation and can be designed to have purely electric dipole radiation, making them ideal for nanophotonic applications.

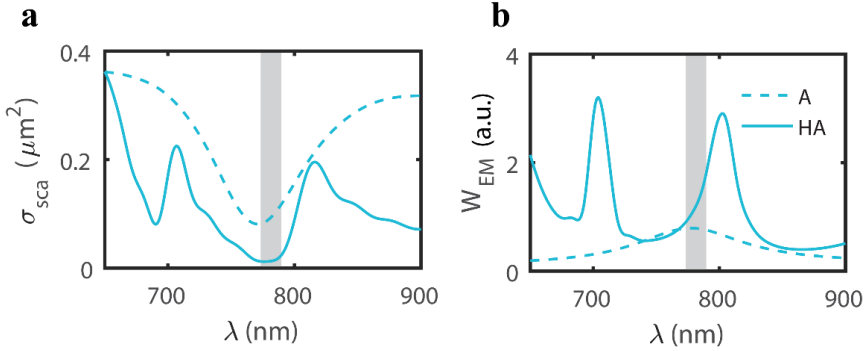
The complex multipole moments of the HA result in a unique internal field distribution, unlike the EDA (Fig. 2.2b). This leads to a suppression of electric and magnetic dipoles and quadrupoles, significantly reducing scattering while maintaining high Local Density of Optical States (LDOS), as demonstrated by the calculations of the total electromagnetic energy stored within the two structures (Fig. 2.3b). The stored energy in the HA is significantly higher than in

the EDA, indicating enhanced light-matter interactions and nonlinear effects. Additionally, the HA modes exhibit larger quality factors.



2.2. fig. Near and far-field characteristics of electric and hybrid anapoles.

(a) From left to right: the normalized intensity of the internal electric field in the electric anapole nanodisk, and corresponding vector field (gray arrows). Angular pattern of the multipoles radiated and suppressed by the EDA. The two designs are obtained by fixing the refractive index  $n = 3.87$ . The considered EDA is obtained at  $kR = 1.795$ ,  $R/H = 5$ , similar to [49 - 72]. (b) Same as in (a), for the HA, with  $kR = 1$ ,  $R/H = 1/3$ .



2.3. fig. Calculations of the total electromagnetic energy.

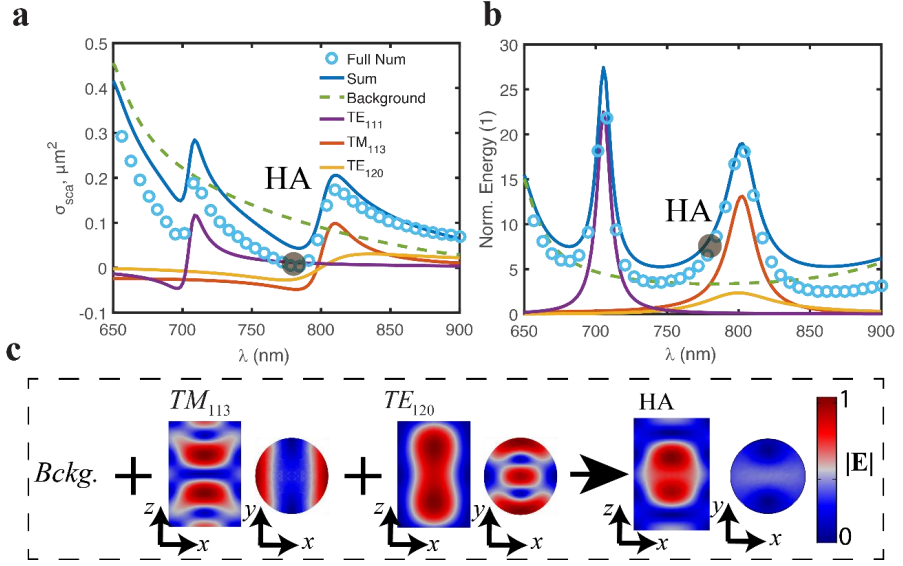
Radiated power (a), and stored electromagnetic energy (b), at the electric anapole (indicated by A) and the hybrid anapole (denoted with HA). The geometrical parameters are the same as in Fig. 2.2. The gray band in the plots indicates the spectral position corresponding to the destructive interference between the electric dipole and the electric toroidal dipole giving rise to the EDA. Despite having a volume around ten times larger than EDAs, the hybrid anapole's radiation suppression is an order of magnitude more efficient and can be considered broadband. Contrarily, the total stored electromagnetic energy is enhanced by more than an order of magnitude. In (b), the electromagnetic energy has been normalized on  $10^{-30} J$  to facilitate the interpretation.

While Cartesian multipoles are suitable for describing far-fields, the process of QNM expansion [73] for near-fields and internal currents allows us to further uncover the physics

behind the HA. QNMs provide a suitable basis for the induced polarization currents, which can then be expanded according to:

$$J(\omega, r) = \sum_{\mu} \alpha_{\mu}(\omega) \hat{J}(\omega, r) - i\omega\delta\epsilon E_{inc}(\omega, r) \quad (2.2)$$

Here  $\hat{J}_{\mu}(r) = -i\omega\delta\epsilon\hat{E}_{\mu}(r)$ ,  $\alpha_{\mu}(\omega)$  and  $\delta\epsilon$  are, respectively, the induced modal scattering current distribution as a function of the internal mode field, the excitation coefficient of the mode  $\mu$  describing its contribution to the total current at a given frequency, and the permittivity contrast with the host environment.



2.4. fig. Application of the QNM expansion method.

(a) Alternative scattering cross section decomposition. Colored lines are the individual contributions of the physical QNMs. (b) Spectra of the volume-averaged electromagnetic field energy inside the cylinder and the excited modes. The electromagnetic energy density has been normalized with respect to the incident electromagnetic energy density in the vacuum. (c) Normalized internal electric field distributions of the two most relevant modal contributions near point A, from left to right, associated with Fabry-Perot ( $TM_{113}$ ) and Mie-like ( $TE_{120}$ ) standing wave patterns ( $TE_{111}$  is very weak near the hybrid anapole), respectively. All the electric fields have been normalized with their respective maxima, to enhance their visualization.

It is important to emphasize the unusual feature of the hybrid anapole: the two resonant QNMs dominating the spectra are simultaneously negatively suppressed by interference with the background. A completely different picture emerges within the resonator. Fig. 2.4b illustrates the modal decomposition of the internal energy stored in the cylinder near point HA. This is one of the main results of the section. Contrary to the multipole expansion, the QNM decomposition enables us to clearly distinguish the contributions of the eigenmodes to the internal fields. Firstly,

we observe a significant enhancement of the electromagnetic energy (approximately nine times) compared to the incident plane wave. Secondly, it is clearly seen that the stored energy at the hybrid anapole is mainly driven by the TM<sub>113</sub> mode due to its higher quality factor and the proximity of its resonant wavelength to the hybrid anapole wavelength, and to a lesser extent by the TE<sub>120</sub> and the sum of the background contributions. Overall, the QNM analysis presented in Fig. 2.4 demonstrates that both the invisibility effect (outside the cylinder) and the internal energy enhancement at the HA are facilitated by the concurrent resonant response of the TM<sub>113</sub> and the TE<sub>120</sub> modes. On the other hand, the background modes, while they may not directly define the spectral features of the figures of merit, also play a crucial role. Their interference with the resonant modes leads to the invisibility effect. This interpretation is consistent with early investigations [74] regarding the formation of Fano lineshapes in the scattering cross section of spherical resonators.

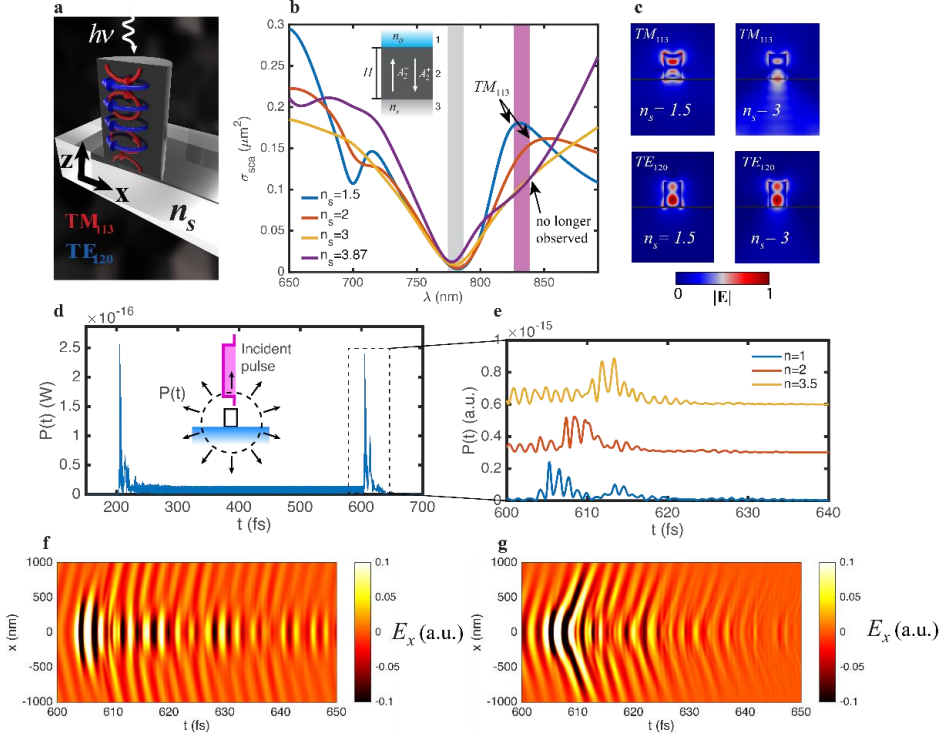
The QNM theoretical framework is highly suitable for quantitative investigations of nanoresonator dynamics under ultrashort pulses. Understanding both the spatial and temporal structure of the scattered field can enhance our comprehension of its interaction with matter under ultrashort pulses. To investigate the system's time dynamics, a series of numerical experiments have been conducted (Fig. 2.5d-g). In the simulations illustrated in Fig. 2.5d-g, the hybrid anapole nanoparticle is excited by a plane wave square pulse with a duration of 400 fs, which is long enough to observe both stationary and transient regimes. The scattered power is then plotted in Fig. 2.5d, and a more detailed view of the transient after the pulse is shown in Fig. 2.5e for various refractive index contrasts with the substrate. HA behaves very differently in the stationary and transient regimes. While it remains non-radiative in the stationary regime for any dielectric substrate, in the transient regime, it emits energy spikes that can be controlled by the underlying substrate. The same behavior is also evident in the spatiotemporal maps of the Ex field shown in Fig. 2.5f-g, where one can fully understand the system's oscillatory patterns. Interestingly, contrary to the conventional Fano resonance [75], we observe the formation of several beats at the trailing edge of the pulse.

The potential that transient modulation offers can be fully exploited in practice by fabricating metasurfaces inheriting (and enhancing), the single-particle mechanism described previously. In particular, the HA can be harnessed to design fully transmissive, all-dielectric metasurfaces without relying on the well-known Huygens condition, and simultaneously realize controllable ultrafast switching by harnessing transients (Fig. 2.5a-d). Contrary to the latter, the light traverses the structure without significant phase variation, thus rendering the metasurface invisible (see shadowed selection in Fig. 2.7b). It can be demonstrated by writing the transmission coefficient as a sum of the relevant multipole contributions of the meta-atoms:

$$t = I + t_p + t_m + t_{Q(m)} + t_{Q(e)} \quad (2.3)$$

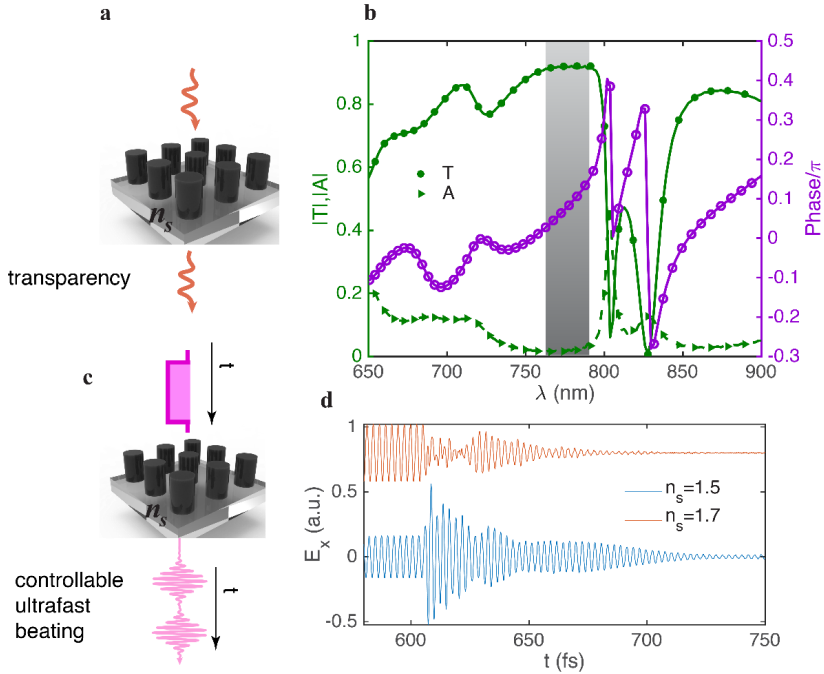
Where each term in the previous sum is proportional to the corresponding total multipole moment (basic and toroidal contributions). When multipolar contributions are zero, we are left

with  $t = 1$  and the incident wave leaves the system unperturbed (Fig. 2.6a). This condition is closely met at  $\lambda = 782 \text{ nm}$ , as indicated in Fig. 2.6b. The results demonstrate (Fig. 2.6d) that transient oscillations of the metasurface are highly sensitive to changes in the substrate index, opening a pathway towards tunable ultrafast beating.



2.5. fig. Stationary and transient response of the hybrid anapole with different index contrasts with the substrate.

(a) Scheme depicting the setup and the excited eigenmodes. (b) Comparison between the numerically obtained scattering cross sections for the nanocylinder deposited on substrates with increasing refractive index. Inset of (b): One-dimensional Fabry Perot model of the  $TM_{113}$  mode. (c)  $xz$  field distributions of the QNMs  $TE_{120}$  and  $TM_{113}$  when the cylinder is deposited over substrates with a different refractive index. (d-f): Temporal response of the hybrid anapole under a plane wave square pulse injected at  $200 \text{ fs}$  with a duration of  $400 \text{ fs}$ ; (d) Scattered power as a function of time; (e) Different beating patterns of the decaying eigenmodes after the plane wave excitation as a function of  $n_s$ ; (f-g) Spatiotemporal maps of the x-component of the scattered electric field measured along the x axis for  $n_s = 1$  (f) and  $n_s = 2$  (g), measured from the beginning of the modal decay. The color bars are saturated for better visualization.



2.6. fig. Design of a subwavelength hybrid anapole-based metasurface, featuring dual functionality in the stationary and ultrafast regimes.

The period is set to 530 nm. (a) artistic representation of the proposed metasurface operating at the hybrid anapole in the stationary regime. (b) Transmission, absorption, and phase of the transmitted wave with respect to the incident one. The out-of-phase basic and toroidal moments induce a transparency band with minimal phase perturbation (shaded region). The calculations have been performed in the presence of a substrate with  $n_s = 1.5$ . (c) Artistic representation illustrating the metasurface response in the sub-ps regime, when excited by a plane wave pulse. (d)  $E_x$  component of the scattered field from the metasurface as a function of time at the end of the plane wave pulse.

As a result of this comprehensive research on Hybrid Anapoles, we have confirmed their existence in the stationary regime where destructive interference between electric and magnetic multipoles creates non-scattering zones. We have experimentally confirmed quadrupole anapoles and magnetic anapoles in subwavelength nanoparticles, which offer potential for enhanced nonlinearities without scattering. Additionally, we have developed a physical model to understand the underlying eigenmodes that influence resonator response. By intentionally breaking the hybrid anapole conditions in the transient regime, we can achieve ultrafast modulation of scattered power while minimizing scattering in the stationary regime. Finally, we propose a non-Huygens metasurface that enables substrate-independent transparency and

substrate-dependent signal modulation, greatly expanding the available degrees of freedom for dynamic tuning. This metasurface shows promise for applications in ultrafast dynamic nanophotonics, including temporal and spectral shaping of femtosecond laser pulses.

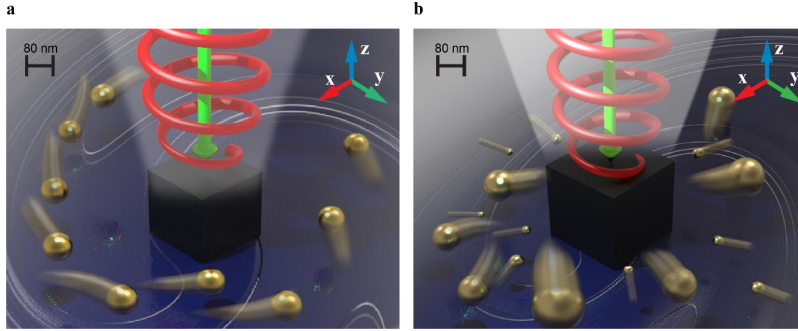
## 2.2 Nanoparticle dynamics in the optical nanovortex and its applications for lab-on-a-chip platforms

Nanophotonic approaches can enhance capabilities in microchambers and microreactors which is essential for control over fluid flows at small scales in the field of microfluidics. This chapter will focus on the concept involving enhanced optically-driven diffusion and nanoparticle sorting utilizing high-index dielectric nanoantennas. Spin-orbit angular momentum transfer and radiation pressure create subwavelength optical nanovortices, enabling moving-part-free nanomixing and precise sorting of gold nanoparticles. This versatile platform enables miniaturized, optically driven microfluidic chips for chemical analysis, emulsion preparation, and light-controlled navigation of nanoparticles, viruses, or biomolecules.

The spiral motion of nano objects in an optical nanovortex driven by an out-of-plane light source requires efficient transformation of spin angular momentum (SAM) of light to in-plane orbital angular momentum (OAM) of the highly confined near fields of the nanocube. This momentum should then be transferred to the surrounding nanoparticles. Therefore, as a primary requirement, there should be sufficient in-plane scattering from the nanocube. This urgent functionality could be enabled, in particular, by the recently observed Transverse Kerker Effect [76], which allows for lateral scattering only. On the other hand, azimuthal forces arising from helicity inhomogeneities in the scattered near field (curl spin forces [77]) may also facilitate rotational motion. Hereinafter, we optimize both effects, considering that we do not necessarily need to completely eliminate forward and backward scattering. Thus, we can adjust the parameters to achieve an improved optical subwavelength vortex.

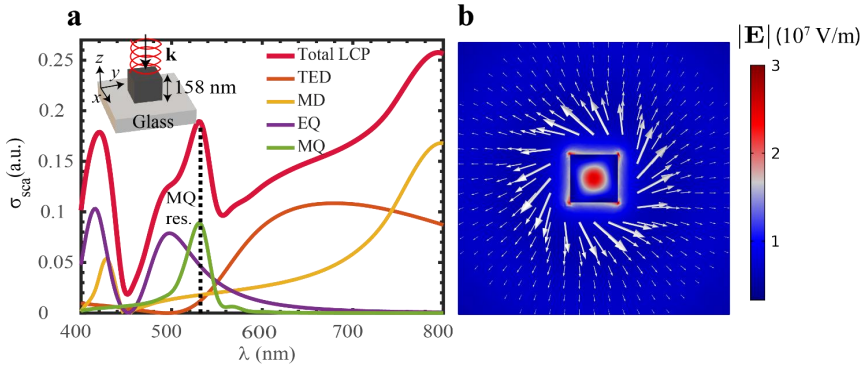
Fig. 2.7 presents a proposed nanomixing scheme: a silicon nanocube with refractive index  $n = 4$  submerged in a water solution is illuminated by a circularly polarized laser beam from the top. The scattered field carries a non-zero tangential component of the Poynting vector in the  $xy$  plane, which induces non-zero orbital angular momentum in the negative  $z$ -direction. The same effect causes the spiral motion of gold nanoparticles around the nanocube. Viscous friction between the moving nanoparticles and the fluid gives rise to convective fluid motion, enhancing fluid mixing. Nanoparticles of different sizes, with opposite signs of the real part of polarizability, are radially displaced in opposite directions – the smaller ones move towards the nanocube, while the larger ones move away from it (Fig. 2.7b). Since the nanostructure has negligible losses, the total angular momentum of the incident and scattered light is conserved. This conservation law for the total angular momentum implies that part of the incident SAM is

transferred to both SAM and OAM of the scattered field leading to spin-orbit coupling phenomena.



2.7. fig. An artistic view of the proposed active nanomixing scheme (left) and radial separation of nanoparticles (right).

In order to gain better physical insight, let us consider the multipole decomposition for the scattering cross-section of the nanocube deposited over a glass substrate (Fig. 2.8a) and illuminated with LCP light in a water host environment (refractive index  $n_m = 1.335$ ). A careful analysis reveals the most pronounced vortex-like energy flux arises at the magnetic quadrupole (MQ) resonance (Fig. 2.8a-b). The total scattered power with incident LCP illumination (Total LCP) is fully reconstructed as the sum of contributions of individual multipoles, respectively, the total electric dipole (TED), magnetic dipole (MD), electric quadrupole (EQ), and the magnetic quadrupole (MQ).



2.8. fig. Multipole decomposition for the scattering cross-section of the nanocube

(a): The geometry is illustrated in the top inset and the ambient medium is water. The dashed black line indicates the position of the resonant MQ mode (green laser, 532 nm). (b) Color plot denotes the norm of the total electric field at 532 nm wavelength in the transverse x-y plane at  $z = 70$  nm. The arrows indicate direction and their lengths illustrate the relative size of the transverse part of the scattered Poynting vector.



Moreover, by varying the size of the nanocube, we can modify the multipolar response of the resonator to align the MQ resonance with the vacuum wavelength of 532 nm (399 nm in water), which corresponds to the most suitable green laser source. Hereinafter, we will proceed with these values; however, it should be noted that an even more enhanced MQ response can be obtained in a free space environment. The magnetic quadrupole (MQ) mode offers a high signal-to-noise ratio compared to other prominent multipoles. The magnetic dipole is nearly one order of magnitude smaller, and the electric quadrupole is not in resonance. The electric dipole radiation is also significantly suppressed by an anapole state near the MQ resonant frequency. Thus, well-pronounced magnetic quadrupole (MQ) fields can be obtained by driving the vorticity of the Poynting vector (Fig. 2.8b).

In order to illustrate the potential applicability of the effect being considered as a mixing method for microfluidic reactors, let us consider a scenario where the water surrounding the nanocube contains a dilute solution of chemically inert and biologically compatible nanoparticles. The dynamics of the latter will be affected by the optical forces arising from the interaction with the cube's scattered field, along with the Brownian and viscous drag forces induced in the fluid. The most obvious and convenient candidates to act as mixing mediators are gold (Au) nanoparticles. They do not interact with the chemical and/or biological compounds dissolved in the solutions and are widely used in a variety of microfluidics applications [78, 79].

In order to enhance the mechanical orbital torque transferred to the Au nanoparticles and prevent them from adhering to the walls of the nanocube due to attractive gradient forces, the ratio  $\langle F_{SC} \rangle / \langle F_0 \rangle$  should be maximized. In this case, scattering forces govern the nanoparticle dynamics, causing them to undergo spiral paths around the nanocube. This action acts as stirrers, enhancing convective fluid motion and thus improving the diffusive mixing of any admixtures present in the water solution.

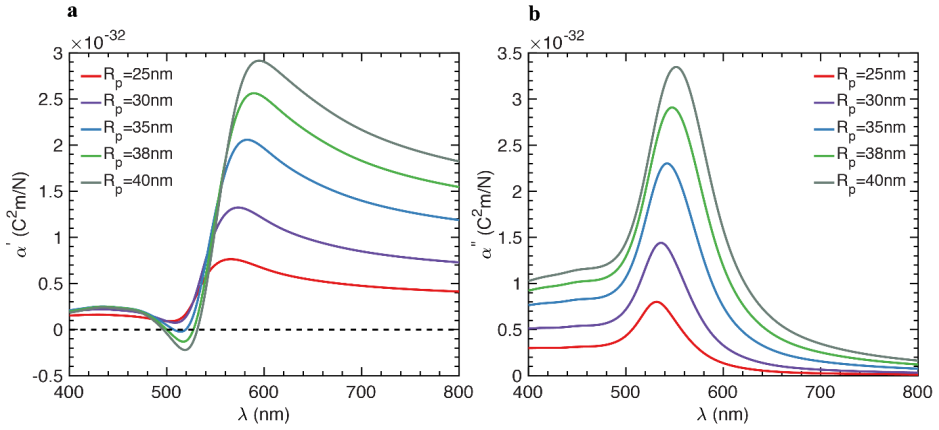
The scattering force can be the dominant force acting on the nanoparticle only if the real part of the nanoparticle's polarizability is significantly smaller than the imaginary part. For simplicity, we assume a spherical shape so that the dipole polarizability can be evaluated analytically using the exact Mie theory [80-82]:

$$\alpha(k_d, R_p) = i \frac{6\pi\epsilon_0 n_m^2}{k_d^3} a_1(m, k_d, R_p) \quad (2.4)$$

where  $k_d$  is the wavenumber in water,  $a_1$  denotes the first electric Mie coefficient, which depends on the refractive index contrast between the particle and the medium as  $m = \sqrt{\epsilon_{Au}(\omega)}/n_m$  and the dimensionless parameter  $k_d R_p$ , where  $R_p$  is the nanoparticle radius.

Fig. 2.9 displays the real and imaginary parts of the polarizability for gold particles of various sizes dispersed in water. To determine the trajectories of Au nanoparticles in water, we assume that the system has achieved stationary equilibrium in the z-direction. This is because the z component of the incident radiation pressure is compensated for in the presence of the glass substrate. Therefore, the trajectories can be treated as two-dimensional, localized only in the

transverse x-y plane. We consider that Au nanoparticles of 40 nm radius are uniformly distributed around the Si nanocube. Their trajectories during a simulation time of 0.1 ms are shown in Fig. 2.10, where illumination wavelength in vacuum was 532 nm (in water 399 nm). If the nanocube is not illuminated, Brownian motion induces random displacements of the nanoparticles regardless of their position in the simulation domain. Conversely, when the system is illuminated with circularly polarized light with intensities around 50 – 80  $mW/\mu m^2$  (corresponding to typical values used in conventional optical trapping schemes [83]), mechanical orbital torque is transferred to the Au nanoparticles, propelling them along spiral trajectories (Fig. 2.10b).



2.9. fig. Real and imaginary parts of the dipole polarizability are calculated for Au nanoparticles of different sizes (dispersed in water).

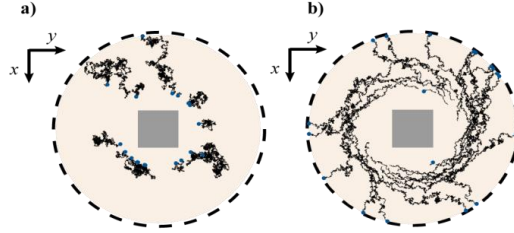
The excitation wavelengths correspond to those in free space. For nanospheres with radius  $R_p \geq 35$  nm, the real part can be equal to zero while the imaginary part is enhanced.

In order to characterize the trajectories of the nanoparticles inside the vortex and the enhancement of their diffusional motion, we calculated their Mean-Squared Angular Displacements (MSAD,  $\langle \Delta\phi^2 \rangle$  in Fig. 2.11a), with respect to the center of the nanocube. Due to the persistent orbital torque inside the vortex, the nanoparticles are actively rotating, as shown by the remarkable increase in the azimuthal angle as a function of time. The MSAD curves can be fitted with the following equation:

$$\langle \phi(t)^2 \rangle = D_R^{eff} t + \omega_{avg}^2 t^2 \quad (2.5)$$

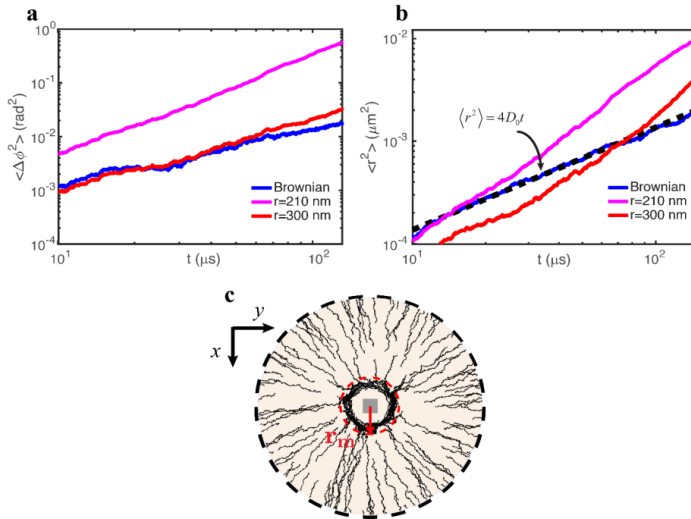
where  $D_R^{eff}$  is an effective rotational diffusion coefficient and  $\omega_{avg}$  is the average angular speed. This analysis leads, as expected, to  $\omega_{avg} = 0$  for the case of passive (Brownian) diffusion,

and  $\omega_{avg} = 0.37deg$  and  $\omega_{avg} = 0.08deg$  for particles placed, respectively, at 210 nm and 300 nm from the center of the nanocube.



2.10. fig. Trajectories of Au nanoparticles of 40 nm radius during 1ms of simulations.

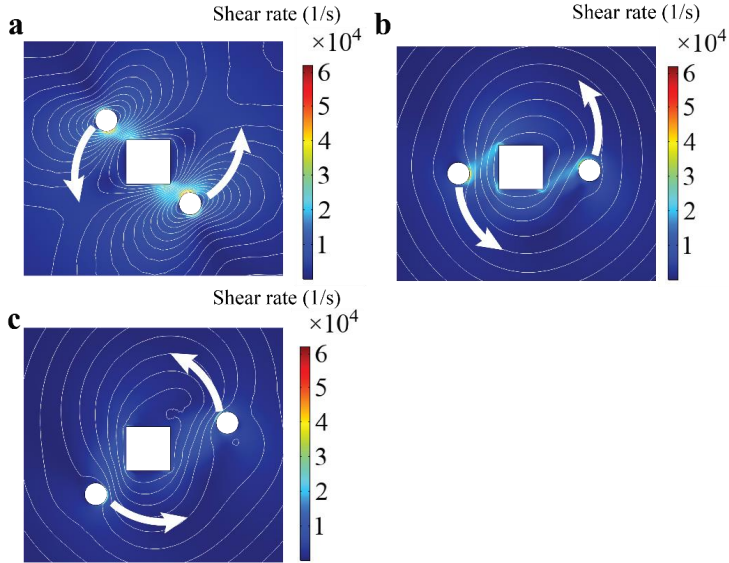
(a) – No incident illumination, only Brownian motion and drag forces act on the particles; (b) – The nanocube is illuminated with a circularly polarized light, and the optical force contributes significantly. The Au nanoparticles spirally move around the cube. The figures are scaled to the length of the cube side equal to 158 nm.



2.11. fig Log-log plots of MSAD and MSD characterizing the diffusional motion of Au nanoparticles under the influence of the optical near fields

(a): Calculated MSAD averaged over 100 Au nanoparticles of 40 nm radius, when the cube is not illuminated (blue), and under LCP illumination at a distance from the center of the nanocube much lower than  $r_m$  (shown in (c)) - violet and at  $r_m$  - red. (b): Averaged MSD in the same conditions as in (a). Dashed line corresponds to the fit with Einstein's relation. (c) Trajectories of 40 nm radius Au nanoparticles inside and outside the nanovortex region delimited by  $r_m$ . The red dashed circle delimits the effective radius  $r_m$ , which determines the range of action of the tangential optical forces. The optical nanomixing effect is achievable at the positions lying inside  $r_m$ .

The radius  $r_m$  reaches about half of the incident wavelength in water. Therefore, the mechanical effect of optical vortices on a nanoparticle occurs in the subwavelength region. Such a reduced scale cannot be achieved using any focused far-field beams, such as radial and Bessel beams [84-86]. Up to our knowledge, this is the first proposal to provide optical nanovortices created in a simple, realizable setup, avoiding the need for lossy plasmonic nanoantennas [87-88], short-wavelength guided modes [89], or complex chiral structures [90]. Such optical nanovortices represent a promising component for on-chip orbital angular momentum (OAM) exchange, driving light-matter interactions such as controlled light emission from quantum dots [90], super-resolution [91-92], and manipulation of nanoobjects [84].



2.12. fig. Formation of a fluid nanovortex due to the movement of two Au nanoparticles (white circles moving anticlockwise) driven by an optical nanovortex formed around the nanocube (white square).

Background color map denotes the distribution of stress in the fluid in 1/s and white contours show the fluid velocity field streamlines of the initially static fluid at different times since the nanoparticles became optically driven. (a)  $t=0.01 \mu\text{s}$ , (b)  $t=150 \mu\text{s}$  and (c)  $t=260 \mu\text{s}$ .

To study the liquid flow in detail driven by the proposed nanomixing design, we employ direct time-domain simulation in COMSOL Multiphysics©. We consider simplified forms of the Navier-Stokes and mass balance equations, assuming laminar, incompressible flow of the fluid. Furthermore, we apply open boundary conditions at the edges and simulate a large fluid domain around the nanocube. Typically, lab-on-a-chip microchambers are on the scale of tens of micrometers. Fig. 2.12 shows the calculated stresses and velocity fields in the fluid during 200

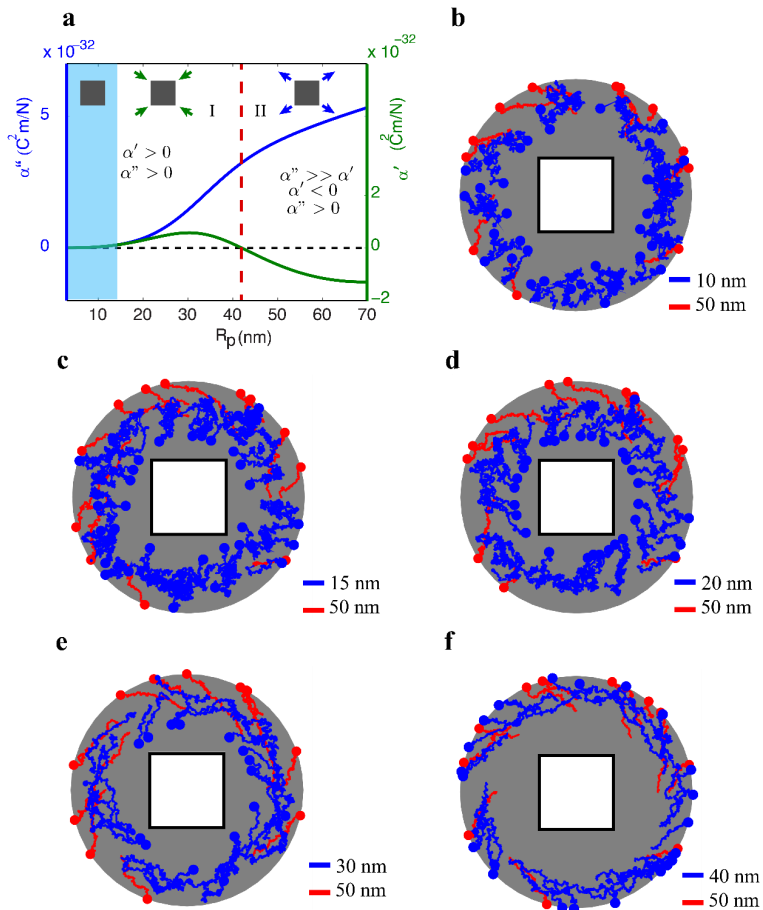
$\mu\text{s}$  propagation with a  $800 \times 800 \text{ nm}$  domain size. Open fluid boundary conditions were imposed at a distance of  $1.5 \mu\text{m}$  from the center of the nanocube. For the sake of clarity, thermal motion is not considered in the simulation. The particles start with zero initial speed and gradually accelerate under the influence of radiation pressure and spin forces arising from their interaction with the optical nanovortex. Consequently, the fluid environment is also displaced, as shown in Fig. 2.12a. At longer times, a single-vortex-like velocity distribution is established. The velocity streamlines are more inhomogeneous at shorter times when the nanoparticles begin to move. At  $150 \mu\text{s}$  only minor fluid distortions take place very close to the nanoparticles and the nanocube. Therefore, a possible way to further enhance the fluid nanomixing would be to implement periodic switching between left- and right-hand circularly polarized incident light. This approach would reverse the direction of particle motion, thereby maintaining a high level of inhomogeneity in the fluid stress field.

These effects enable us to demonstrate a novel, dynamic, contactless size sorting method for gold nanoparticles in liquid solutions, addressing one of the most challenging goals of conventional microfluidics with the assistance of dielectric nanophotonics. At a given incident wavelength, we can categorize the behavior of the Au nanoparticles into regions I and II (Fig. 2.13a). Smaller nanoparticles from region I with a positive  $\alpha'$  are attracted by the radial gradient force towards the nanocube, while larger nanoparticles from region II should be repelled outwards. However, in region I, there is a competition between Brownian, gradient, and scattering forces. Brownian forces introduce unbiased random displacement, while the other two forces drag the nanoparticles in opposite radial directions. A careful analysis considering the contributions of each force is required to determine the viability of the sorting method. Fig. 2.13b-f illustrates the proposed approach for nanoparticle separation by comparing the results of the numerical simulations for two sets of Au nanoparticles. The trajectories colored in blue correspond to nanoparticles with increasing sizes ranging from  $10 \text{ nm}$  to  $40 \text{ nm}$  radii, while the red trajectories represent the paths followed by nanoparticles of  $50 \text{ nm}$  radius. The smaller blue particles are located inside region I, while the larger red ones are in region II.

Nanoparticles smaller than  $15 \text{ nm}$  have very low polarizabilities, resulting in negligible optical forces compared to Brownian forces (Fig. 2.13b). Numerical simulations, however, demonstrate that nanoparticles with radii ranging from  $15$  to  $30 \text{ nm}$  are attracted towards the nanocube, following inward curved paths, and are primarily influenced by gradient forces. The most intense inward forces in region I are experienced by nanoparticles with a size of  $30 \text{ nm}$  (Fig. 2.13e), coinciding with the peak of  $\alpha'$  in Fig. 2.13a (green line). Contrarily, nanoparticles with radii close to  $40 \text{ nm}$  (i.e., in the vicinity or inside region II) spiral away from the dielectric nanocube due to scattering forces. Larger particles are also repelled by the joint scattering and gradient forces because the latter changes sign.

This demonstrates that our novel platform can operate as a sorting device for gold nanoparticles by exploiting their inward or outward motion towards the nanocube based on their dimensions. A precise, in-situ size control of gold nanoparticles is a crucial step in many

applications, such as determining biological cell uptake rates [93], [94], toxicity [95], and Raman signal intensity [96].



2.13. fig. Illustration of optical sorting.

(a) Real ( $\alpha'$ ), and imaginary ( $\alpha''$ ) parts of the dipole polarizability as a function of the particle radius for an incident free space wavelength of 532 nm. Insets depict schematically the radial direction of the optical forces exerted on Au nanoparticles inside the different regions. (b-f) The blue curves show the calculated trajectories followed by particles with sizes from region I: 10 nm (b), 15 nm (c), 20 nm (d), 30 nm (e) and 40 nm (f), respectively. For comparison, in all the plots (b-f) the red curves correspond to the statistically different trajectories followed by nanoparticles with 50 nm radii corresponding to region II.

## 2.3 Controlling ultrashort pulse propagation in disordered layered media

Optical nanostructures with loss and gain components are gaining attention as versatile materials for nanophotonic applications. Active metamaterials, which can be controlled by adjusting nonlinear interactions, offer tunable optical signatures for sensing and signal processing at micro- and nanoscales. This chapter proposes a method to control ultrashort pulses by manipulating population difference disorder in a random active metamaterial. This simple approach enables three interaction regimes: self-induced transparency, localization, and light amplification, each with distinct pulse speeds. The proposed disordered medium presents opportunities for unique active components in various optical applications.

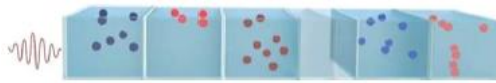
In this chapter, we study a one-dimensional layered structure with resonant loss and gain. We modify the typical loss-gain setting by introducing another variable into the system – disorder. Recently, it has been discovered that disordered metamaterials are of great interest not only because of Anderson localization [97, 98], but also for observing topological state transitions [99], enhancing transmission [100], and shaping wavefronts [101]. Another feature we consider is the emphasis on the dynamics of short pulse propagation. Therefore, our results belong not only to the fields of active and disordered photonics but also continue the long chain of investigations dedicated to the coherent pulse propagation in resonant media [102]. In particular, our analysis is naturally connected to the studies of self-induced transparency (SIT) [103], [104] and related coherent effects such as the formation of population density gratings [105], [106] and collisions between solitonic pulses [107]–[109]. In this case, we are interested in systems with disorder in the parameters of the resonant part, while the background remains uniform.

In contrast to the passive systems [110], [111], here we assume that the density of active particles is uniform and study another class of disordered resonant media with randomly varying initial population differences. Such a medium can be viewed as an active disordered metamaterial, representing a set of layers with varying levels of loss and/or gain. The ordered case represents a uniform resonantly absorbing medium, while the introduction of disorder leads to the formation of excited layers: the greater the disorder, the more extensive the excitation. Since it is not obvious how such systems respond to external pulsed excitation, we analyze several specific models of disorder and demonstrate three different regimes of pulse interaction with the system: the superconductor-insulator transition (SIT) regime, the localization regime, and the amplification regime. The first one is observed at a low disorder and is characterized by almost unperturbed slow soliton propagation. The localization regime that occurs at an intermediate disorder level implies low output and strong absorption of radiation within the structure. At a significant disorder, the signal quickly emerges at the rear end of the structure, and the combined energy of the transmitted and reflected light is amplified. One can switch between these regimes by changing disorder parameters, for example, through a change in pumping. This allows us to obtain dramatically different responses (transmission and reflection) at various levels of disorder, which can serve as a foundation for adjustable optical devices.

The system considered in this chapter consists of a background dielectric doped with active (two-level) atoms (Fig. 2.14). Light propagation in this medium can be described in the semiclassical approximation by the well-known Maxwell–Bloch equations. The model of disorder considered here implies that the initial population difference in the  $j^{\text{th}}$  layer of the medium corresponding to the distance  $(j - 1)\delta L < z \leq j\delta L$  is given by:

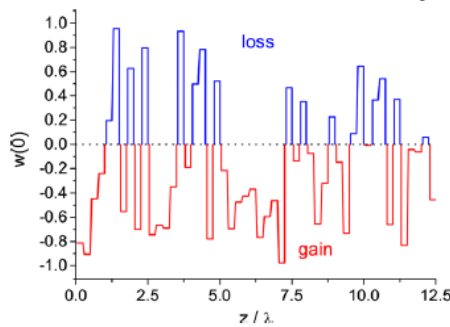
$$w^{(j)}_0 = 1 - 2\xi_j r \quad (2.6)$$

where  $\xi_j$  is the random number uniformly distributed in the range  $[0; 1]$  and  $r$  is the parameter of the disorder strength. When  $r = 0$ , we have the trivial case of purely absorbing (lossy) medium (all  $w^{(j)}_0 = 1$ ). On the contrary,  $r = 1$ , corresponds to the maximal disorder, when loss and gain have equal probability to appear. In other words, the system can be considered as a multilayer (total thickness  $L$ ) consisting of slabs (thickness  $\delta L$ ) with different initial population differences, that is, different parts of the medium are under different pumping. For  $r > 0.5$ , the gain layers with  $w^{(j)}_0 < 0$  becomes possible. Thus, the parameter  $r$  not only governs deviation from the ordered case of pure loss, but also takes on the role of pumping strength resulting in appearance of gain. An example of distribution governed by Equation (5) is depicted in Fig. 2.15 for the period of random density variations  $\delta L = \lambda/4$  and maximal disorder  $r = 1$ .



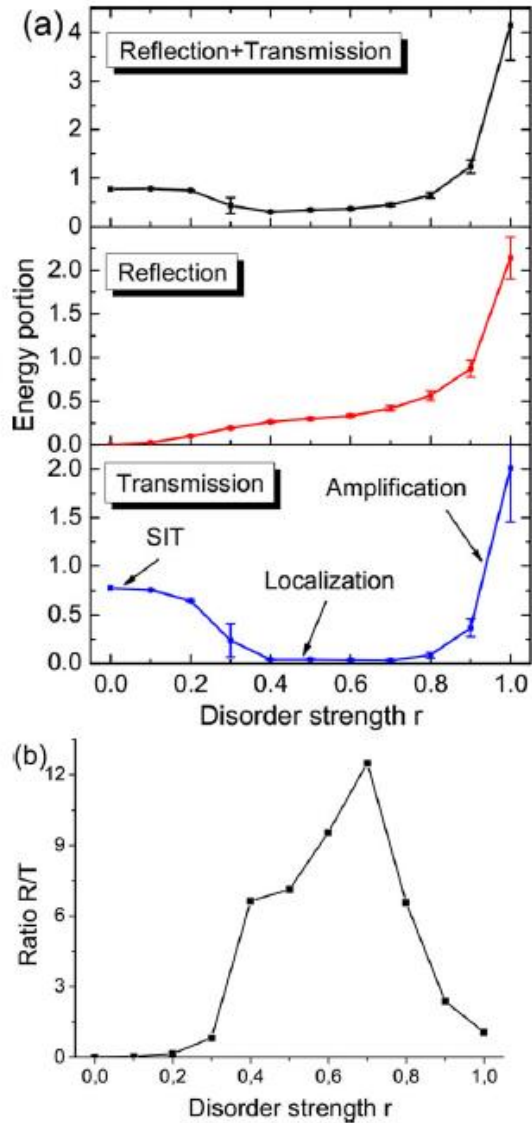
2.14. fig. Schematic depiction of the system under consideration.

Different shades of blue and red denote different levels of loss and gain, respectively.



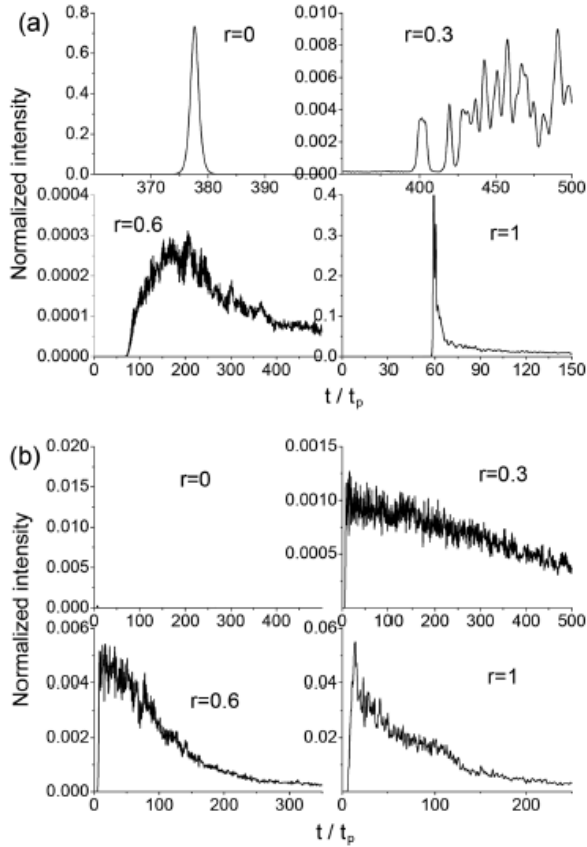
2.15. fig. Examples of initial population difference  $w_0$  distributed along the medium for the model of disorder.





2.16. fig. Calculation of transmission and reflection for different levels of disorder.

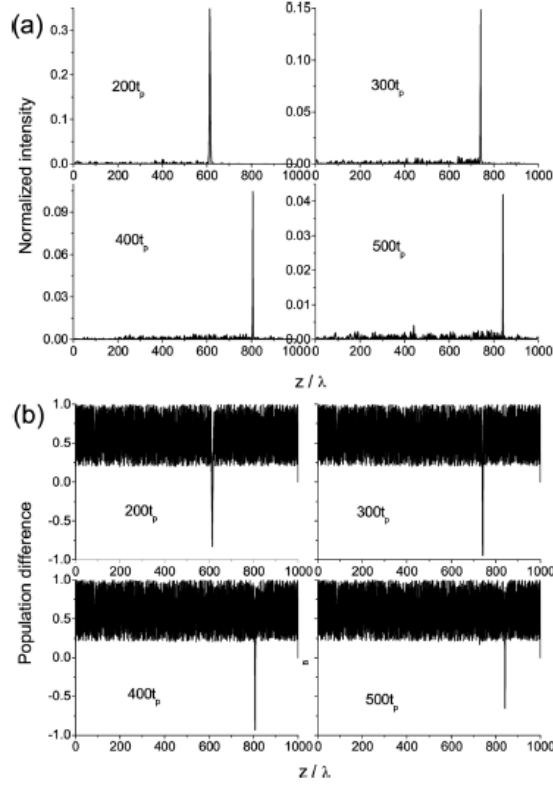
a) Average output energy of transmitted (bottom) and reflected (middle) light as well as their sum (top). Energy averaged over 100 realizations was calculated for the time interval  $500tp$  and was normalized on the input energy. The layer thickness is  $\delta L = \lambda/4$ . The error bars show the unbiased standard deviations for the corresponding average values. b) The ratio of average values of reflection and transmission as a function of  $r$ .



2.17. fig. Profiles of a) transmitted and b) reflected intensity for different values of the disorder parameter  $r$ .

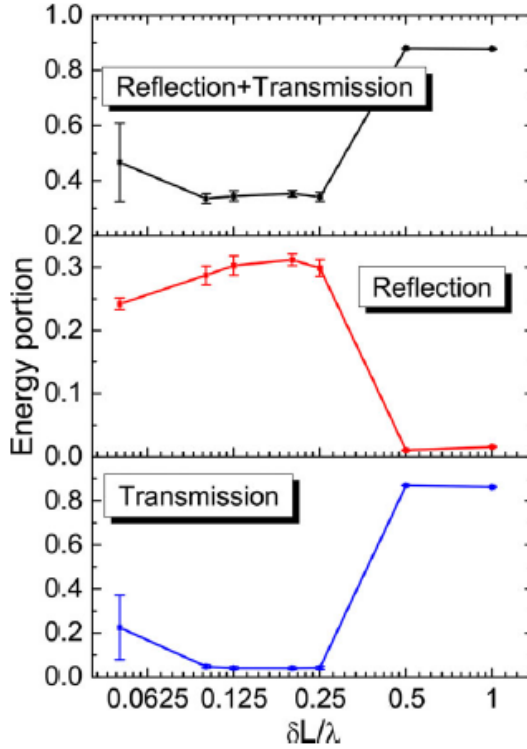
Profiles are averaged over 100 realizations, the layer thickness is  $\delta L = \lambda/4$ .

Fig. 2.16a shows the mean values of transmission and reflection for different levels of disorder calculated within the modeled framework. At low disorder ( $r \leq 0.2$ ), we have the SIT regime with high transmission, and the resulting pulse corresponds to a SIT soliton. As a result, a solitonic pulse of a specific form can be observed propagating through the medium with low attenuation. This is exactly what we see in Fig. 2.17a. For  $r > 0.2$  transition to localization occurs with a gradual decrease in transmission and an increase in reflection and absorption. In this scenario, trapping occurs closer to the entrance as disorder increases. This results in the slowing down of SIT pulses and the observation of an almost standing population inversion, as depicted in Fig. 2.18 for a realization with  $r = 0.4$ .



2.18. fig. The distributions of a) light intensity and b) population difference at different moments of time for a realization of disorder with  $r = 0.4$ .

Varying the degree of disorder allows us to control the reflection-to-transmission ratio. Calculation of the average transmission and reflection for different values of  $\delta L$  at  $r = 0.5$  is shown in Fig. 2.19. We observe that the optimal range for localization is between  $0.1\lambda \leq \delta L \leq 0.25\lambda$  (which corresponds to the findings in [112]). According to our model of disorder, it can be introduced into the system within a side-pumping scheme by periodically placing absorbing strips of random thickness on the structure. Different strips will block various sections of the pump, causing different parts of the medium to be excited in a random manner. The disorder parameter  $r$ , which governs the strength (or degree) of disorder, indicates the magnitude of population difference variations. It can be tuned simply by changing the pump intensity. Therefore, with the same distribution of random numbers, stronger pumping leads to larger amplitudes of population difference variations. Within this conceptual framework, one can generate distributions of loss and gain with varying levels of disorder as needed.



2.19. fig. Average output energy of transmitted (bottom) and reflected (middle) light as well as their sum (top) as a function of the layer thickness  $\delta L$ .

The disorder parameter is  $r = 0.5$ . Energy averaged over 25 realizations was calculated for the time interval  $500tp$  and was normalized on the input energy.

We investigated the propagation of ultrashort pulses in a resonant multilayered medium with randomly varying initial population differences along the propagation direction. The focus was on an active system with a disordered loss-gain distribution and a uniform background. As a result, three potential disorder models were considered, revealing two transitions and three distinct regimes as the disorder increased. The transitions were from the self-induced transparency (SIT) regime to the localization regime and then to the amplification regime. The amplification regime only appeared when negative population differences were possible and the disorder was sufficiently large. These effects offer opportunities for flexible control over the optical response of the medium, allowing for adjustments in the reflection-to-transmission ratio and pulse propagation speed through the disorder parameter.

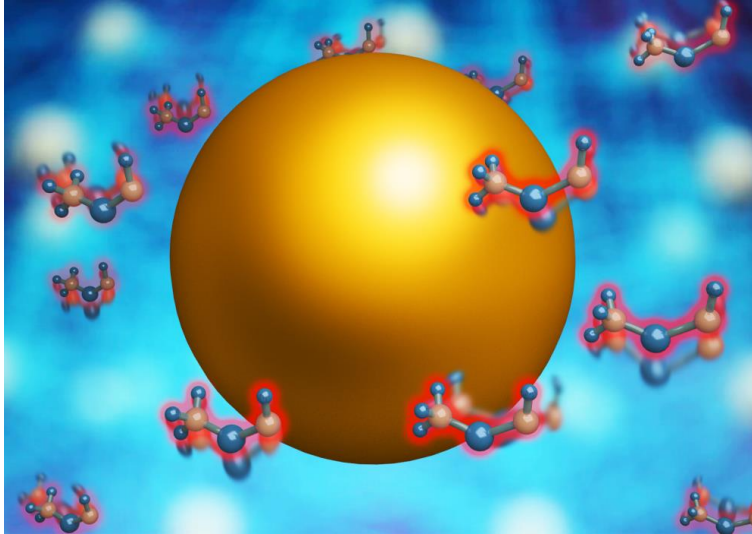
## 2.4 Analysis of the diffusion-inspired emission dynamics in nanostructured environments

In the study of light-matter interaction, the structured environment controls the dynamics by modifying the local density of electromagnetic states. While fast fluorescent processes may overlook mechanical changes, slow-decaying phosphorescent complexes can detect micro- and millisecond-scale motion through near-field interactions. By examining the interplay between time-varying Purcell enhancement and molecular motion, we analyze collective decay phenomena using a modified diffusion equation. Mapping fluid properties onto phosphorescent lifetime distribution enables contactless all-optical thermometry and diffusion measurements. This photonic platform has potential applications in nanofluidic processes and lab-on-a-chip devices, offering insights that are challenging to acquire with other optical methods.

The common approach to solving problems related to light-emission processes is based on time-dependent perturbation theory in the case of weak coupling regimes, or on the complete solution of dynamic equations in more advanced strong coupling scenarios. In both cases, however, the strength of the fundamental interaction parameter is time-independent. This approach is well-justified in cavity quantum electrodynamics, where the environment is static and does not change during the interaction. In colloidal applications, where a solution of particles can undergo either ordered or random motion, dynamical changes of the environment can also be neglected under certain commonly encountered approximations. For example, fast virtual level-assisted nonlinear processes and even dipole-allowed nanosecond-scale fluorescent decays are orders of magnitude faster than slow microsecond-scale changes in the fluidic environment.

In terms of fundamental light-matter interaction processes, phosphorescent timescales can be comparable to conformational changes within the colloidal environment. For example, a spherical molecule in water at room temperature has an average displacement of several hundred nanometers during a time period of 100 microseconds. This nanoscale displacement between an emitter and nanoantenna is sufficient to significantly alter the decay rate, as will be demonstrated subsequently. It is worth noting that conformational changes are still significantly slower than the optical carrier frequency, allowing for the application of a time-scale separation approach in theoretical treatment. This approach has been recently applied for velocimetry mapping with phosphorescent emitters [113] and for the analysis of rotational micro-Doppler effects [114], [115].

Here, we present a theoretical framework for analyzing diffusion processes of slow-decaying phosphorescent compounds in a solution of resonant optical antennas (see Fig. 2.20). An assembly of emitters, dissolved in a liquid mixed with metal nanoparticles, is pumped with external illumination. Slow-decaying dyes diffuse in the vicinity of resonating nanoparticles, which change their emission on a timescale comparable to the spontaneous decay. As a result of this interaction, the information on fluid dynamics is imprinted in the photon statistics.

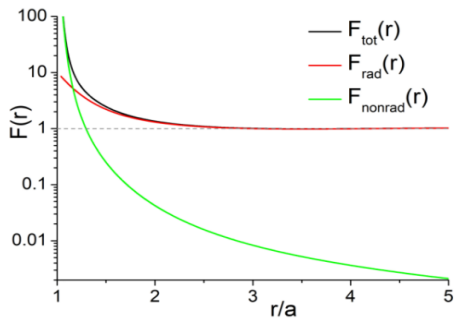


2.20. fig. The schematics of the system – diffusion of slow-decaying phosphorescent dyes next to a resonating nanoantenna.

Radiative and nonradiative enhancements should be distinguished because they influence the interaction between light and matter in different ways. Total radiative lifetime governs the decay dynamics, while the radiative contribution is responsible for the number of photons detected at the far field. The difference between radiative and total rates is the result of losses within the particle [116]. While in the majority of optoelectronic applications, only the radiative enhancement is a factor for maximization, our diffusion model requires knowledge of the total decay rate. The information about local properties of the fluid, however, can be analyzed by collecting emitted photons. Radiative and total enhancements are plotted as a function of the distance from the gold nanoparticle (Fig. 2.21). The following typical parameters have been used: the radius of the spherical particle is 50 nm, and the optical properties of gold were taken from [117]. The central wavelength of phosphorescent emission is 690 nm. It can be seen that nonradiative channels dominate the decay dynamics in the close proximity of the particle, while at distances larger than 100 nm, the influence of the particle diminishes, and Purcell enhancement approaches unity (no enhancement). Qualitatively, this means that fluorophores located far away will contribute to the background radiation and will decay at a rate of 0. The most relevant region for observing the diffusion dynamics via photon counting is situated at distances of 20-100 nm from the nanoparticle surface.

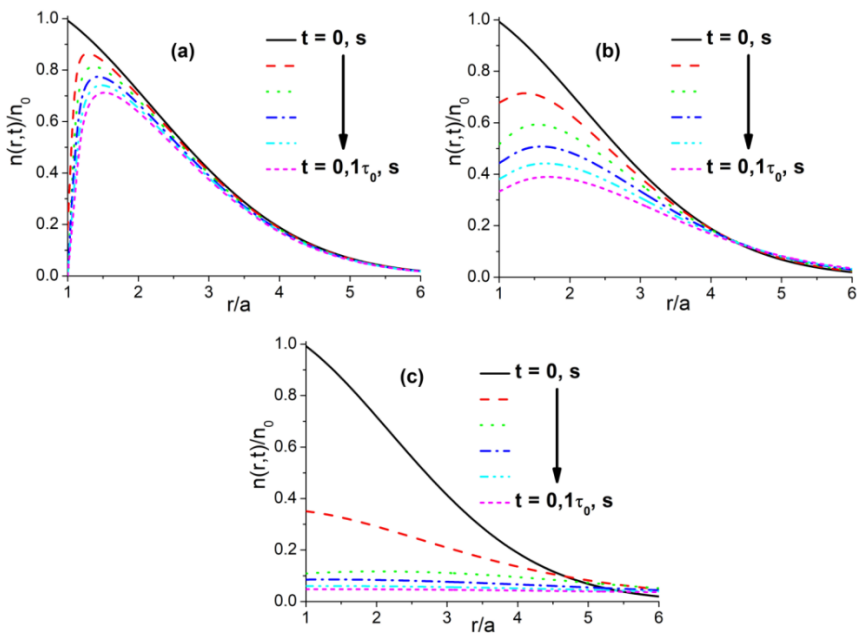
Having the values of the diffusion coefficient and the position-dependent Purcell factor, the entire model can be solved. Fig. 2.22 shows the density of the excited molecules as a function of

the distance from the particle at different time points. Color lines correspond to different times elapsed from the instance of the pulsed pump excitation.



2.21. fig Purcell enhancement next to a gold (50-nm-radius) nanoparticle.

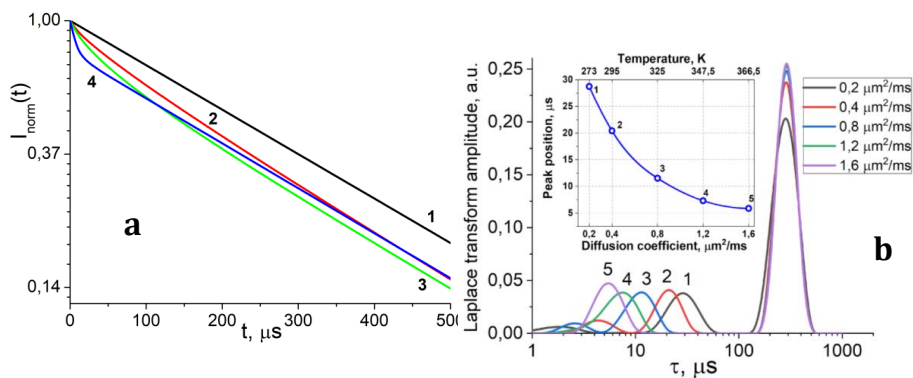
Orientation-averaged total, radiative, and nonradiative enhancements (black, red, and green lines, respectively) as a function of the normalized distance (to the particle's radius) between the dipole and particle's surface.



2.22. fig Radial distribution of excited dye molecules in a vicinity of the particle at different times for different diffusion coefficient values: a) 0, b) 0.2, c) 1.6.

It can be seen from Fig. 2.22 that when the diffusion coefficient is very small, the population of excited dyes drops rapidly near the particle, and there is no Brownian inflow towards it. On the other hand, when diffusion is efficient, slow-decaying molecules (unaffected by Purcell enhancement) flow in and begin to sense the presence of the antenna. As a result, they decay faster. This dynamic behavior is clearly observed by comparing panels a, b, and c. The decay kinetics directly affect the lifetime distribution, which can be measured in the far-field.

Fig. 2.23a demonstrates the time-dependent intensity decay for various values of the diffusion constant. It is clearly seen that in the selected range of parameters, the intensity decreases more rapidly with an increase in diffusivity. When the molecules are randomly moving around the antenna, they have a higher probability of being found in its vicinity, leading to a larger Purcell enhancement. This result is illustrated in Fig. 2.23b, where the non-exponential response of the system is clearly visible. The rightmost peak corresponds to the free-space relaxation time of the molecules. The secondary peak on the left is associated with the Purcell effect and contains information about the diffusion characteristics. Indeed, the increase in the diffusion coefficient leads to a further shift of this secondary peak towards shorter lifetimes. This shift occurs because there is an increasing probability for molecules to approach the metal nanoparticle. The position of this peak as a function of the diffusion coefficient, and consequently, temperature is shown in the inset. Therefore, it becomes possible to measure temperature and diffusion coefficient in a liquid using the proposed photonic contactless design. The pronounced dependence of the optical signature of phosphorescent molecules on their surroundings can be extremely useful in various applications such as microfluidics and microchamber-based chemistry, remote all-optical temperature control, microbiology, and biomedicine.



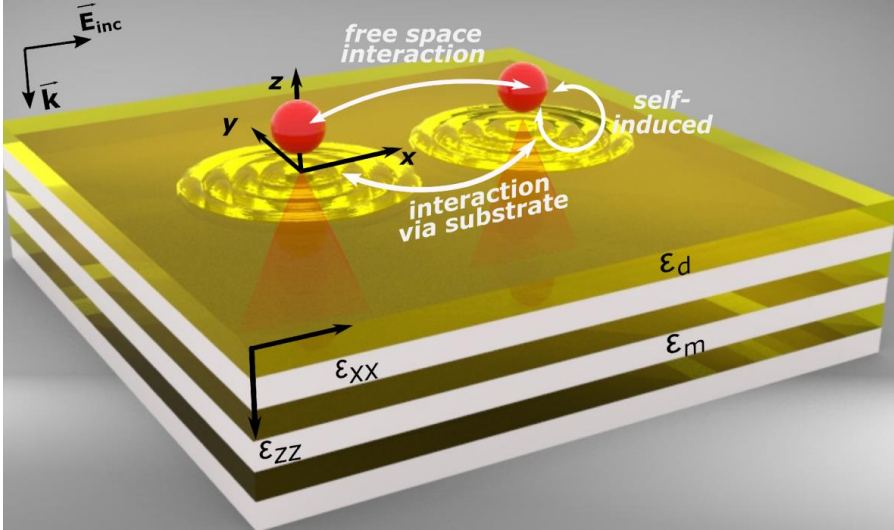
2.23. fig. (a) Normalized intensity (log-scale) decay of the dye molecules in a vicinity of the particle for different diffusion coefficient values (b) Lifetime distribution analysis of the collected luminescence signal.

*Color lines correspond to different diffusion coefficients and, hence, temperatures.*



## 2.5 Modeling optical binding effect in hyperbolic metamaterials

In this chapter we discuss the capabilities of hyperbolic metamaterial (HMM) substrates for optical binding applications. A typical scenario is depicted in Fig. 2.24, where a pair of small particles are linked together by an optical field, mediated by a structured surface. In contrast to free space binding scenarios, a layered metal-dielectric substrate opens additional interaction channels mediated by surface and volumetric modes. As will be demonstrated, the interaction between the surface geometry and the modes within the bulk will enable the achievement of optical binding with deeply subwavelength separation distances. This can be efficiently adjusted by leveraging the strong chromatic dispersion of the metamaterial. Particles' locations in Cartesian coordinates are  $(0, 0, a)$  and  $(x, y, a)$ , where  $a = \lambda_0/30$  is the radius of the particles and  $\lambda_0$  is the incident light wavelength.



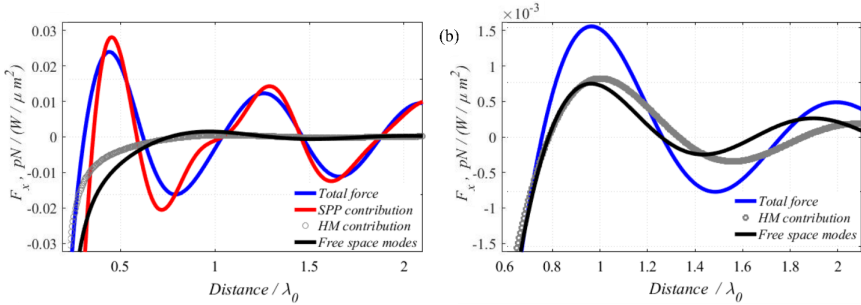
2.24. fig. General concept of optical binding above a metamaterial slab.

Highly confined optical modes within the layered hyperbolic metamaterial (HMM) create additional interaction channels, enabling the formation of dimers and chains with separation distances smaller than the diffraction limit.

To analyze the influence of a semi-infinite anisotropic multilayered metamaterial on optical binding, let us consider a pair of nanoparticles with the same parameters, one of which is fixed at the origin of the coordinates. The period of optical binding can now be defined as the distance between two nearest stable equilibrium positions, and the stiffness is the ratio of the restoring force to the particle's displacement:

$$k = -\Delta F_x / \Delta x \quad (2.7)$$

Fig. 2.25 shows the resulting optical forces corresponding to the dominant contributions of SPPs and hyperbolic modes. In the first case, optical forces are primarily influenced by the strong impact of surface plasmon-polaritons, with these surface waves fully driving the forces, while the contribution of other modes is inadequate. In the latter case, where hyperbolic modes have the predominant influence, optical binding has almost nothing special compared to the free-space scenario. Here, HMs contribution increases the force by almost twice (which is still two orders of magnitude less than that of SPPs) and slightly shifts equilibrium positions, almost not affecting  $L_{bind}$ . Thus, hyperbolic modes excited by the first particle propagate symmetrically in the volume without interacting with the second particle, and vice versa. However, the still existing nonzero contribution of HMs can be explained through the aforementioned cross-terms. In this scenario, modes excited by one particle are scattered by another, resulting in additional HMs with broken symmetry. These, in turn, contribute to the optical force shift [118].

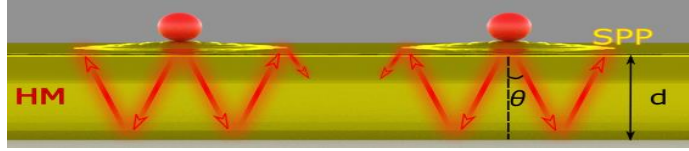


2.25. fig. Dependence of the optical binding force on the distance between the particles.

(a) SPPs, (b) hyperbolic modes. The blue line corresponds to the total optical binding force near anisotropic substrate, the red line is for the surface plasmon-polariton modes contribution only, gray circles depict contribution of hyperbolic modes, and the black lines show optical binding via propagating in the upper half-space modes only.

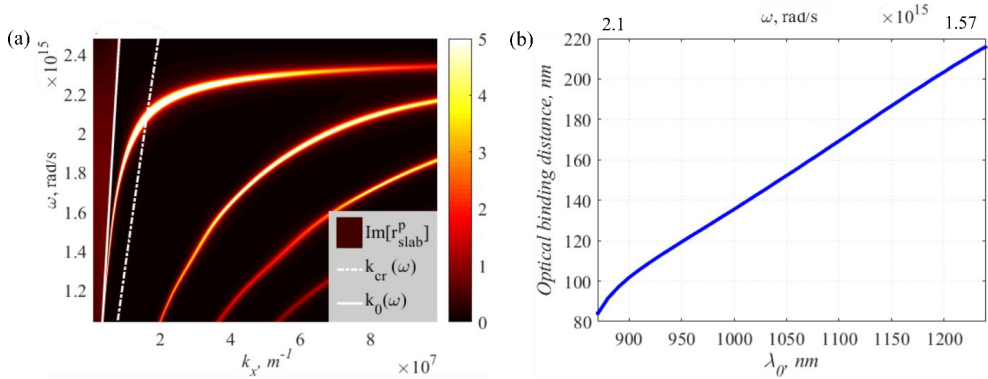
Therefore, it demonstrates that hyperbolic modes, even though dominant in the interaction with the semi-infinite metamaterial, do not provide a sufficient contribution to binding in this case. The main reason for the weak influence of HMs on binding is the absence of feedback from the bulk modes, which propagate away from the particles to infinity. However, strong optical binding can be achieved by using an anisotropic finite thickness slab because of the reflections of hyperbolic modes from the boundaries. The structure under consideration appears in Fig. 2.26.

In contrast to conventional waveguides, the transversal component  $k_x$  in hyperbolic slabs can achieve rather high values. This, combined with the highly confined shape of the modes, could allow for very small distances between the hotspots driven by multiple reflections. This, in turn, paves the way for strongly subwavelength binding of nanoparticles and also provides tunability through changing material parameters, slab thickness, excitation wavelength, etc.



2.26. fig. The scheme of optical binding near anisotropic hyperbolic metamaterial (HMM) slab.

Reflections from the boundaries of the slab form high intensity regions and result in optical binding with separation distances  $L_{bind}$  below the diffraction limit.



2.27. fig. Chromatic tuning for the multilayered structure of silver and Ta2O5 [119], [120] layers with the slab thickness 115 nm and filling factor of 0.133.

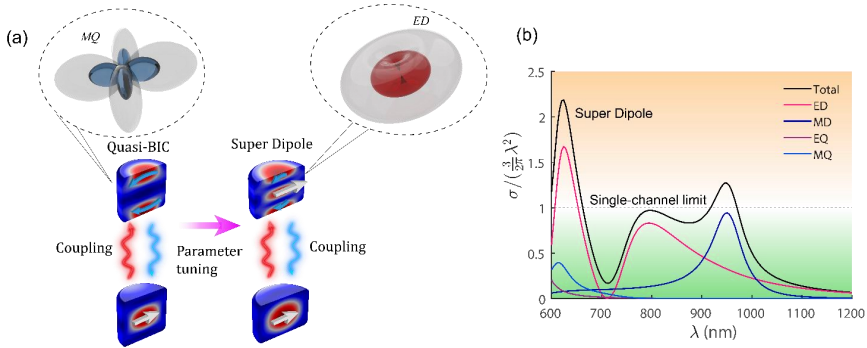
(a) - imaginary part of the reflection coefficient (dispersion diagram). (b) - optical binding period over the frequency.

Additionally, we can consider another important degree of freedom – chromatic tuning of the metamaterial-assisted optical binding. Fig. 2.27a shows the dependence of the reflection coefficient on the incident wave frequency for a slab thickness of 115 nm. It can be seen that the number of HM peaks controlled by the reflections (similar to Fabry-Perot resonances for hyperbolic modes) and contributing to optical binding increases with lower frequency. Therefore, the dependence of optical force becomes more complex. The distance between the bound particles (Fig. 2.27b) now varies with frequency, highlighting the significant role of material dispersion in this context. The binding period is proportional to the ratio of the thickness of the slab and the incident wavelength. In this case, the permittivities are monotonically dependent on the frequency, thus the optical binding distance's dependence is more or less monotonous. However, in other wavelength regions, additional heavy metals (HMs) and non-monotonic dispersion of optical constants could displace the stable equilibrium positions and alter the relationship depicted in Fig. 2.27b. This additional degree of freedom opens up a realm of opportunities for tuning optical binding in a "non-invasive" manner and fabricating novel designs and architectures of nanostructures on metamaterial substrates by adjusting optically induced forces with hyperbolic modes.

## 2.6 Modeling superscattering effect emerging from the physics of bound states in the continuum

In this chapter, we study the Mie-like scattering from an open subwavelength resonator made of a high-index dielectric material when its parameters are tuned to the regime of interfering resonances. We have discovered a novel mechanism of superscattering, closely linked to the strong coupling of resonant modes [121] and described by the physics of bound states in the continuum (BICs). We demonstrate that the enhanced scattering occurs due to constructive interference described by the Friedrich-Wintgen mechanism of interfering resonances [122], which allows the scattering cross section of a multipole resonance to exceed the currently established limit. Here, we develop a comprehensive non-Hermitian model to describe the interference of resonances of quasi-normal modes.

Fig. 2.28a illustrates a proposed concept of the superscattering effect inspired by BIC in an isolated resonator. Strong coupling of two modes reshapes both their near fields and scattering patterns as a function of a tuning parameter. The interfering resonances lead to a quasi-BIC state (destructive interference) and induce power redistribution between multipolar scattering channels, resulting in super-dipole radiation (constructive interference). Mode coupling induces power redistribution within two radiation channels, enabling the overcoming of the single-channel scattering limit. This process allows for the control of not only the Q-factor but also the enhancement of the power scattered by a multipole (e.g., the electric dipole) beyond the limit, as demonstrated in Fig. 2.28b.

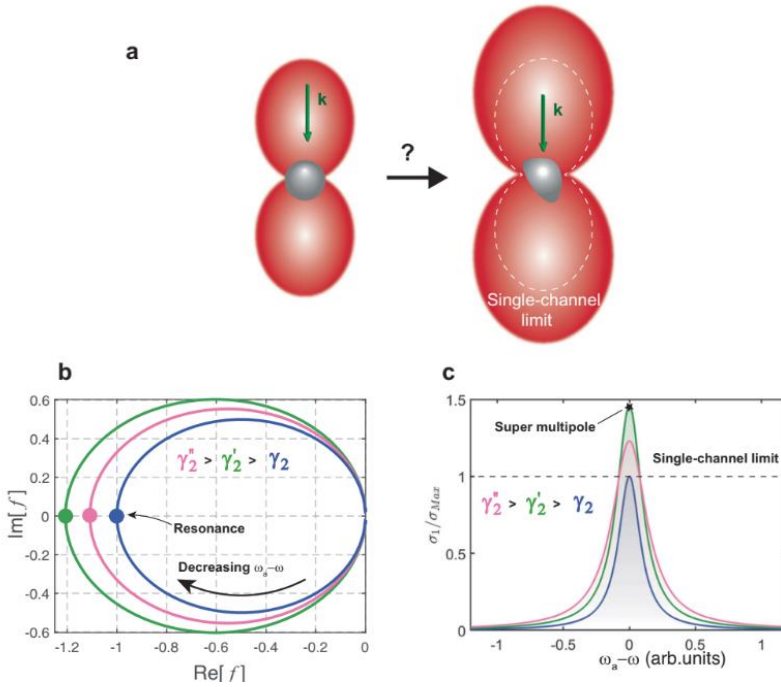


2.28. fig. (a) Concept of BIC-inspired superscattering in an isolated resonator.

(b) Super dipole resonance arising in the scattering cross-section of a dielectric cylinder with refractive index  $n = 3.8$ , radius 130 nm, and height 180 nm. The scattering cross-section of the electric dipole channel significantly exceeds the single-channel limit. This is in contrast with conventional superscattering, where several multipole resonances need to be overlapped.

To design a superscatterer, the resonant frequencies of several Quasinormal Modes (QNMs) associated with different multipolar channels must be brought together through a specific design

of the particle geometry. This design aims to ensure that the total scattering cross-section, which is the sum of their contributions, surpasses the limit. Moreover, depending on the symmetry of the object, the scattering cross-section of one multipole can receive contributions from other multipoles. This suggests that the strength of a multipole could, in theory, be boosted beyond the conventionally accepted limit, as depicted in Fig. 2.29a. In stark contrast to conventional superscattering, the ability to enhance the cross-section of a single multipole allows us not only to increase overall scattering but also to manipulate the radiation pattern. For example, this provides an opportunity to make it larger without significantly altering its shape, as illustrated in Fig. 2.29a.



2.29. fig. Boosting scattering of a multipolar resonance.

(a) Illustration of symmetry breaking. On the left-hand side, a spherical scatterer is illuminated by a plane wave with momentum  $k$ . On the right-hand side, a nonspherical scatterer displays a significantly enhanced scattering pattern. (b, c) General model of a single QNM [a] compatible with two scattering channels  $\tau = 1, 2$ .

This is verified through derivation of an ad-hoc expression for the scattering cross section of channel 1:

$$\sigma_1/\sigma_{Max} = \frac{1}{4} |1 - R_{11} - R_{12}|^2 \equiv |f(\omega)|^2 \quad (2.8)$$

where complex function  $f(\omega)$  determines the ultimate limit for scattering in this case. The radiation rate of the system is the sum of radiation rates to the two channels:  $\gamma_a = \gamma_1 + \gamma_2$ . According to temporal coupled mode theory [121, 122] (TCMT), we also get:

$$f(\omega) = i \frac{\sqrt{\gamma_1 \gamma_2} + \gamma_1}{\omega_a - \omega - i(\gamma_1 + \gamma_2)} \quad (2.9)$$

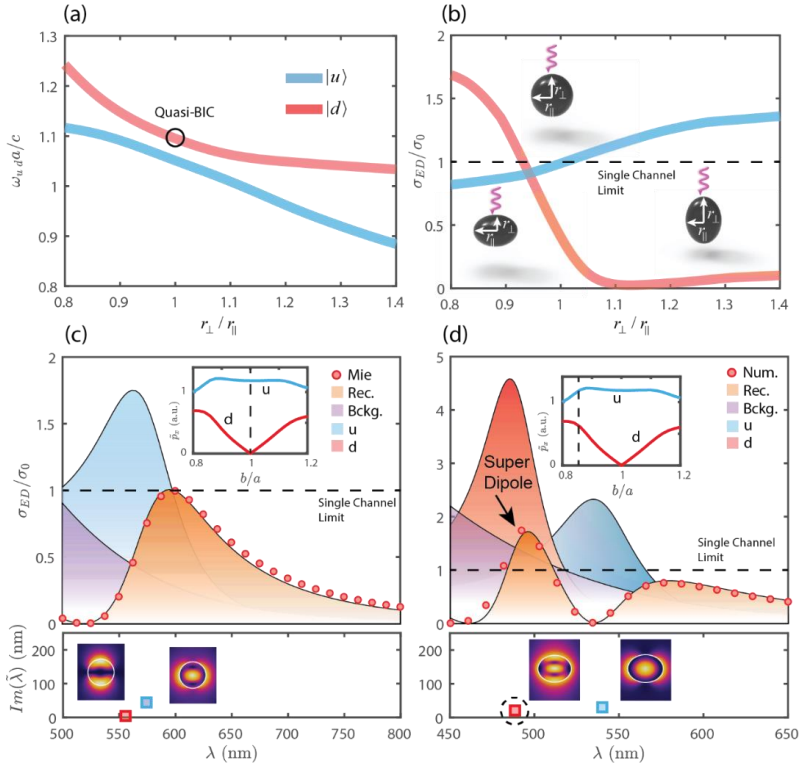
We can observe the behavior of such system by fixing  $\gamma_1 = 1$  (in normalized units) and plotting  $f(\omega)$  as a function of detuning from resonance  $\omega_a - \omega$ , for different values of  $\gamma_2$  (Fig. 2.29b). Strikingly, apart from the conventional maxima cases, we observe a critical  $\gamma_2$  for which  $|f(\omega)|$  reaches a maximum exceeding 1 (green curve). Additionally, for radiation rates larger than the critical (pink curve) we observe a progressive degradation of the enhancement, confirming that there indeed exists an optimal, small  $\gamma_2$  where the cross section is maximized beyond the limit. To provide more insight, the scattering cross section (channel 1) for different cases is displayed in Fig. 2.29c. It is evident that the green spectrum exceeds the limit by nearly 1.5 times. It should be noted that this is the case despite a clear broadening of the resonance caused by the additional losses. Thus, radiation losses can actually enhance the channel cross-section instead of degrading it. The novel regime is referred to as a ‘super-multipole’, contrasting with conventional superscattering, where several QNMs need to overlap in the spectrum.

To illustrate super-multipoles emerging from quasi-BICs, we extend our TCMT model to the case of a structure supporting two QNMs, each compatible with a single scattering channel. In order to model a subwavelength nanoresonator, let us consider a silicon nanosphere in air illuminated by a normally incident, linearly polarized plane wave, with a radius of 100 nm. In the visible range, there are two Quasi-normal modes (QNMs) that correspond to the electric dipole (ED) and magnetic quadrupole (MQ) channels, respectively. The electric field distributions are depicted in the lower panel of Fig. 2.30c. Note that the selected scatterer is significantly subwavelength, with a radius at least 5 times smaller than the incident wavelength.

In order to couple both QNMs, it is necessary to break the spherical symmetry in some fashion. A simple way to do so is by reducing the rotational symmetry in the plane parallel to the direction of propagation, (see schematic insets in Fig. 2.30b). In this case, multipolar modes with the same parity (as in the case for the chosen QNMs), can couple [125]. We gain insight into the mechanism by evaluating the influence of each QNM to the ED scattering cross section (Fig. 2.30c-d). We consider three contributions: the resonant QNMs and a non-resonant background composed of modes outside the spectral range of interest. ED cross section is described as:

$$\sigma_{ED} = \left| \sum_m p_m \right|^2 / I_0 \quad (2.10)$$

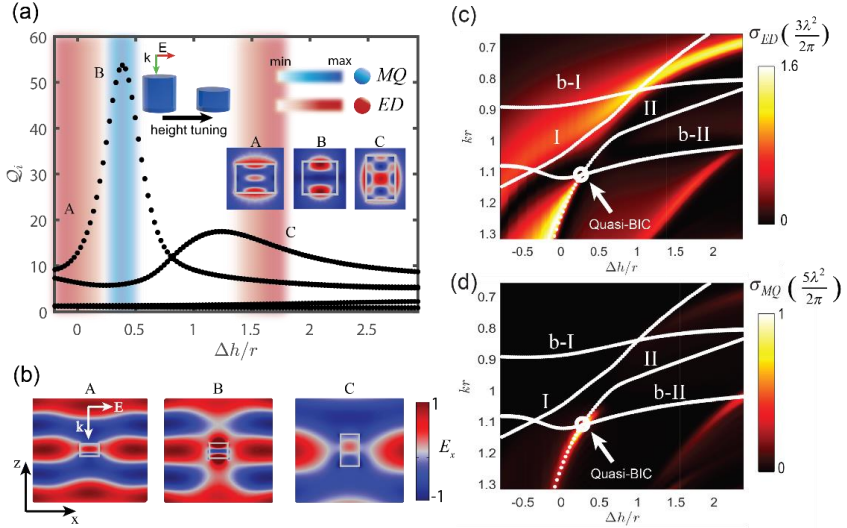
where  $p_m$  is the ED moment of the  $m$ -th QNM, and  $I_0$  is the intensity of the incident plane wave. The reconstruction is in excellent agreement with the exact analytical results of Mie theory for the sphere (Fig. 2.30c), and full-wave numerical simulations for the ellipsoid (Fig. 2.30d). It is important to note that the ‘direct’ cross section of each QNM, by itself, is not bound by any limit.



2.30. fig. Evolution of the resonant frequencies.

(a) Evolution of the resonant frequencies of the ED and MQ modes of a silicon nanosphere (100 nm radius), when breaking the rotational symmetry along one of its axes. (b) Scattering cross-section of the ED channel at the two resonance maxima as a function of ellipticity, under normally incident, linearly polarized plane wave illumination, with momentum oriented along the axis with broken rotational symmetry. (c, d) Contributions of the QNMs to the scattering cross-section of the ED channel in a sphere and a perturbed spheroid.

This example illustrates the formation of a super dipole resulting from a symmetry-breaking perturbation. However, spheroids are generally not easy to fabricate at the nanoscale. Instead, we can also achieve this regime similarly in a silicon nanorod under normally incident illumination (Fig. 2.31a), as the latter also possesses cylindrical symmetry. To do so, we perturb the height of the resonator by an amount of  $\Delta h$ , starting from a height of  $h_0 = 180$  nm, for which two modes radiating as ED and MQ are spectrally close. In the spheroid, we observe a system of two coupled resonant Quasi-normal modes (QNMs) with relatively high Q-factors



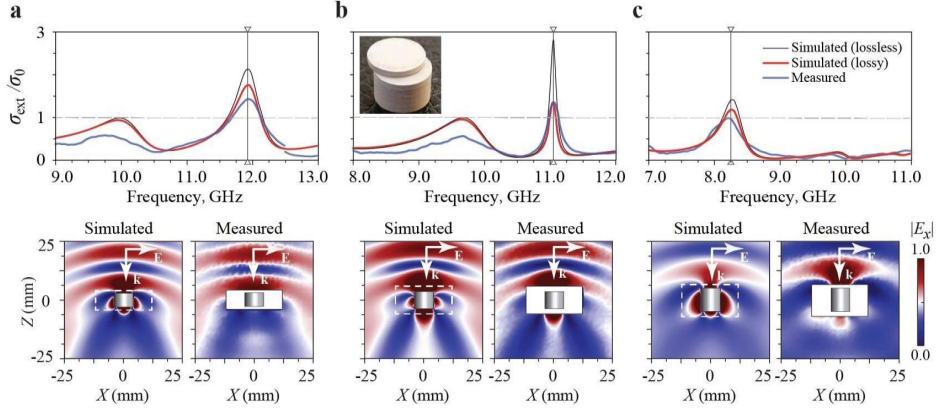
2.31. fig. Design of a super dipole mode in a Si nanorod.

(a) Quality factors and multipolar radiation of the QNMs as a function of a perturbation of the cylinder height  $\Delta h$ , normalized by the radius  $r = 130 \text{ nm}$ . (b)  $E_x$  component of the total field at the superscattering points A-C indicated in (a), under  $x$ -polarized plane wave illumination (in arbitrary units). (c)-(d) 2D maps of the ED and MQ scattering cross sections as a function of  $kr$  and  $\Delta h/r$ . White dotted lines indicate the paths followed by the eigenfrequencies I, II correspond to the resonant QNMs, and b-I, b-II are the background ones. In agreement with theory, departing from the quasi-BIC condition results in hybridization and the possibility to enhance scattering of a single mode beyond the limit.

Next, we conducted a proof-of-concept experiment by measuring the extinction cross-section and scattering patterns of disk-shaped resonators in the microwave range. We replicated the geometrical parameters of the rod by utilizing a set of ceramic resonators with fixed 4.0 mm radii, and permittivity  $\epsilon = 22$  with a loss tangent of 0.001. As shown in the inset of Fig. 2.32b, three samples are assembled from multiple disks to achieve the desired aspect ratios for the resonators. The measurement results of both the total extinction cross-section and electric near-field patterns are presented in Fig. 2.32. The spectra are normalized based on the ED single-channel limit. The experimental measurements are in reasonable agreement with the numerical simulations, although the resonances appear suppressed due to material losses in the ceramic. Since the resonances redshift with increasing size, the observations were performed over a wide frequency range. In the highlighted frequencies of Fig. 2.32a and Fig. 2.32c, we observe wide resonances with large extinction values, characteristic of the proposed super dipole modes. Indeed, the plane wave is strongly distorted in the near field. Furthermore, numerical calculations



confirm that the ED exceeds its limit, even when considering losses. The quasi-BIC appears at the expected value of  $\Delta h/r = 0.48$ , manifesting itself as a sharp peak in the spectra (Fig. 2.32b). The results provide experimental evidence of controlling both the Q-factor and scattered power between two resonances to achieve the superscattering regime with just a single mode.



2.32. fig. Simulated and measured total extinction cross-sections and scattered electric near-field patterns.

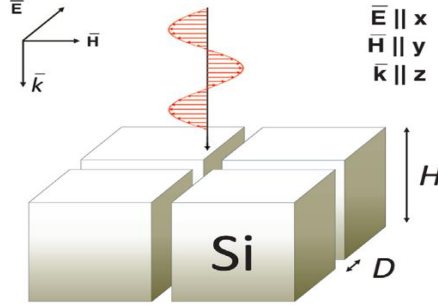
All the cross sections are normalized by the single channel limit for the ED. Insets show an example of the experimental resonator and the electric field norms in the  $x$ - $z$  plane of the resonances indicated by vertical lines in the top plots. The white regions in the near-field patterns correspond to the physically inaccessible zones for the measurements. The aspect ratios of the disks are: (a)  $\Delta h/r = 0.25$ , (b)  $\Delta h/r = 0.475$ , and (c)  $\Delta h/r = 1.25$ .

We have demonstrated novel superscattering regimes by utilizing subwavelength, nonspherical resonators and exploiting the strong coupling of two resonances. Our findings show superscattering originating from an electric super dipole moment, surpassing the currently established limit by almost two times. By disrupting the quasi-BIC condition in resonators without spherical symmetry through parameter adjustments, power exchange between scattering channels enables the manipulation of Q-factors and multipolar contents while maintaining a high scattering cross-section. Our super multipole resonances exhibit enhanced resistance to Ohmic losses compared to conventional counterparts. These findings have implications in biosensing [126], [127], energy harvesting [128]–[130], on-chip circuitry [131] and optical manipulation [132]–[133].

## 2.7 Optical properties of magnetic octupole in silicon quadrumers

The development of new approaches to tuning the resonant magnetic response of simple all-dielectric nanostructures is crucial in modern nanophotonics. In this chapter, we demonstrate that a resonant magnetic octupole (MOCT) response can be achieved by dividing a solid rectangular

silicon block into a quadrumer structure with the introduction of narrow gaps between four nanocubes. We learn how to use controllable resonant MOCT excitation to tailor magnetic hotspots and resonant energy absorption.

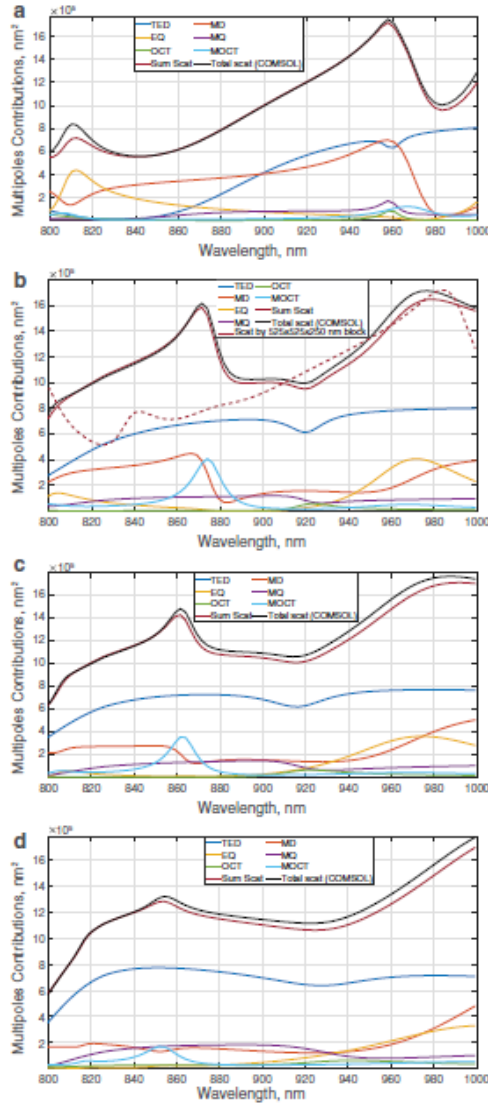


2.33. fig. The artistic representation of the quadrumer of silicon cubes.

The systems under consideration include a silicon block measuring  $500 \times 500 \times 250$  nm, representing the zero distance between silicon cubes in Fig. 2.33, and silicon quadrumers composed of four Si cubes ( $250 \times 250 \times 250$  nm) with distances between them of  $D = 25, 50,$  and  $100$  nm. These structures are illuminated with a linearly polarized monochromatic plane wave with time dependence as shown in Fig. 2.33. Material data for silicon has been taken from the reference [134]. To investigate spectral resonances in scattering cross sections, we apply the multipole decomposition technique, which demonstrates good performance in all cases considered (Fig. 2.34). The nearly perfect agreement between the sum of the multipole contributions and the directly calculated scattered cross section demonstrates that the multipole approach is sufficiently accurate. Fig. 2.34a shows the scattering cross-section spectrum calculated for the solid silicon block. One can observe that both the resonant multipole contributions and the total scattering cross-section in this case significantly differ from the spectra in Fig. 2.34b-d due to the introduction of inhomogeneity to the system. In this way, the conversion of the solid block into the quadrumer structure results in a significant reconfiguration of electric and magnetic fields within the system, leading to a higher-order multipole excitation. Surprisingly, the presence of narrow air gaps in the quadrumer leads to the excitation of the MOCT moment in the spectral range under consideration. Note that this is not related to the increase in the total structure size, as our calculations for solid blocks with an edge of  $525$  nm do not show MOCT resonances in the considered spectral range. To visualize this, we display the total scattering cross-section of a  $525 \times 525 \times 250$  nm silicon block (dashed line in Fig. 2.34b) to compare it with the corresponding quadrumer case. It can be seen that there is no resonant response between  $\lambda = 850$  nm and  $\lambda = 900$  nm; a small resonant peak at  $\lambda = 840$  nm corresponds to EQ. Let us consider in detail the resonant excitation of the magnetic octupole moment at the wavelengths of  $850$ – $900$  nm. Cutting the solid block weakens the MOCT resonance by increasing the distance between the cubes. The resonant MOCT peak occurs at  $\lambda =$

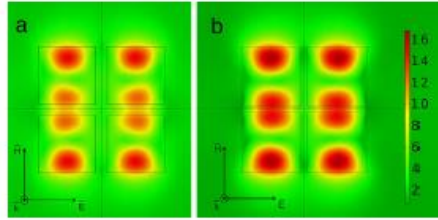
874 nm in Fig. 2.34b, at  $\lambda = 863$  nm in Fig. 2.34c, and at  $\lambda = 852$  nm in Fig. 2.34d. While attenuating, the resonant peak also experiences a blue shift. Fig. 2.35 shows the distribution of the normalized magnetic field at the MOCT resonance, relative to the magnetic field amplitude of the incident wave. It is important for practical applications to be able to create the so-called magnetic hotspots in free space. Due to structuring, the total magnetic field in the gaps can be enhanced (compared to the incident one) by up to approximately 10 times for  $D = 50$  nm (Fig. 2.33a) and around 14 times for  $D = 25$  nm (Fig. 2.33b).

It is possible to exploit this effect to design magnetic switchers at the nanoscale. It is important to go in detail with the physics of the considered process. Fig. 2.35a, c show the absolute value of the x component of the electric field ( $E_x$ ) in the solid block and in the quadramer, respectively. Following Maxwell's equations, in the oligomer structure the electric field enhancement appears in the slits along the polarization of the incident wave due to the discontinuity of the normal component. In addition, Fig. 2.35b, d show the absolute value of the y-component of the magnetic field ( $H_y$ ) and the crucial redistribution of the magnetic field because of the structuring. This leads to six different field concentration zones in the quadramer structure constructing a magnetic octupole nearfield pattern. The magnetic field does not undergo a discontinuity in the gaps along  $H_y$  ( $\mu = 1$  in the both media) that is why the magnetic hot-spots take place between the cubes too. In addition to the magnetic field enhancement, MOCT resonance can provide a strong electromagnetic absorption in the quadramer. Fig. 2.35a shows the comparison of absorbed power for  $\lambda$  between 850 and 900 nm for the solid silicon block and the quadramer with the distance  $D = 25$  nm between the cubes. Fig. 2.35b proves that the discovered energy absorption peak spectrally corresponds to the MOCT resonance. It is worth noting that in this spectral range natural light absorption by silicon is small. Therefore, air gaps in the quadramer structure cause strong absorption in silicon, despite its very small  $\text{Im}(n) \approx 0.08$ . Fig. 2.35c compares the electric field inside the silicon block and quadramer structure. Clearly, resonant magnetic octupole response leads to a strong electric field concentration and, therefore, to the resonant absorption in the silicon quadramer. The spectral position of the MOCT resonance and, hence, the position of the absorption peak can be changed by varying the distance between the cubes. Such tunable absorption can be widely used to control the energy concentration by dielectric structures and to design modern optical devices.



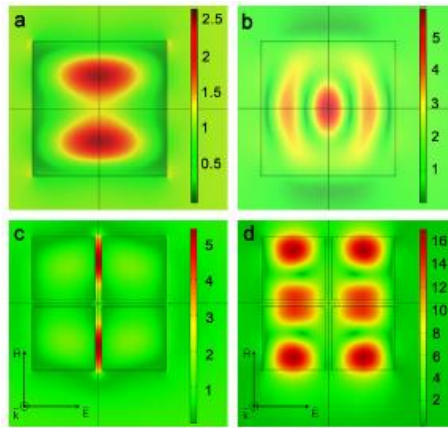
2.33. fig. Scattering cross-section spectra and corresponding multipoles' contributions.

a) Calculations for the single silicon block of height  $H = 250$  nm and base edge 500 nm; b–d) the quadrumer of silicon cubes. The distance between cubes in the quadrumer is b)  $D = 25$  nm c)  $D = 50$  nm d)  $D = 100$  nm. 'Sum Scat' states for the scattering cross section as the sum of the multipole contributions; 'Total scat (COMSOL)' states for the total scattering cross sections calculated directly in COMSOL.

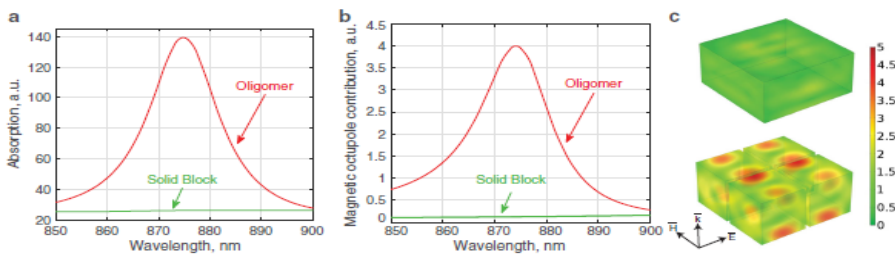


2.34. fig Distribution of the normalized magnetic field in (xy) - plane ( $z = 0$ ) of the silicon quadramer.

with a)  $D = 50$  nm,  $\lambda = 863$  nm, b)  $D = 25$  nm,  $\lambda = 874$  nm. Color bar is the same for both pictures.



2.35. fig. The absolute value of a,c)  $E_x$  and b,d)  $H_y$  in a,b) the solid silicon block and c,d) the silicon quadramer with  $D = 25$  nm at  $\lambda = 874$  nm.



2.36. fig. Spectra for the MOCT.

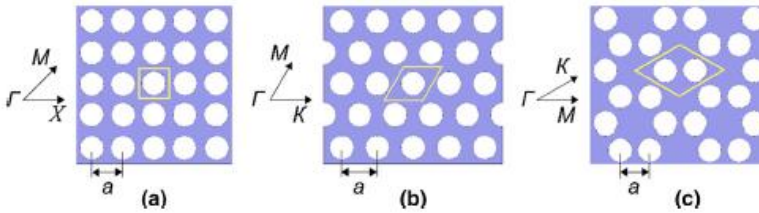
a) absorption power and b) MOCT contribution to the scattering cross section calculated for a single silicon block of height  $H = 250$  nm and base edge 500 nm (green lines) and the quadramer of silicon cubes with the distance between cubes  $D = 25$  nm (red lines). The absorption peak in the structure clearly corresponds to the resonant excitation of the MOCT moment. c) Normalized electric field inside the solid block (top) and quadramer (bottom) at  $\lambda = 874$  nm. One can see that resonant MOCT response provides strong electric field concentration leading to the resonant absorption in the silicon quadramer.

### 3. Real-world applications and experimental results

#### 3.1 Macroporous phononic crystal-based structures for FBAR applications

In this chapter we investigate the most optimal solutions of the periodic structure design considering the technological aspects of the structure fabrication. The study was performed with the help of finite element method using COMSOL Multiphysics FEM software. The prime requirement is that the periodic structure should exhibit an existence of bandgaps at several frequency regions of the switchable FBAR. The current work is focused on the consideration of periodic structure designs that are technologically achievable for sub-micrometer dimensions using standard microfabrication approaches. With regard to that, the application of macroporous structures is proposed. Macroporous silicon-based structure can be fabricated utilizing standard masked electrochemical etching with the structure design that is predetermined by the photolithography.

In the current work we found optimal solutions for pore arrangements of different symmetry that are completed as arrays of air-filled cylindrical inclusions in the silicon host material. 2D square, triangular and honeycomb arrangements of holes were used for this study as shown in Fig. 3.1



3.1. fig. Material and propagation directions for 2D phononic crystals.

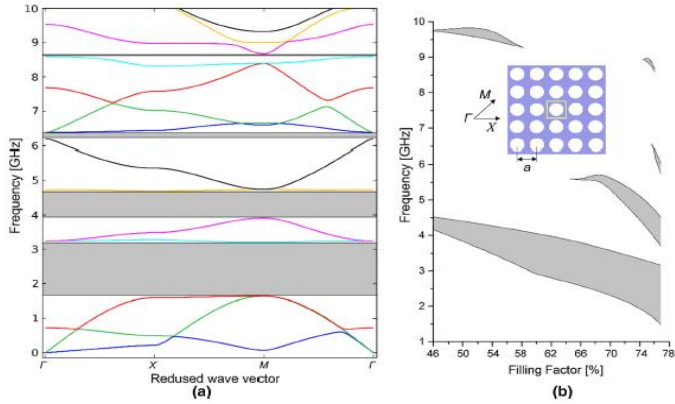
The silicon-based porous artificial periodic structures were modeled as arrays of air-filled cylinders for three different symmetry cases. This arrangement is obtained by translating the unit cells for each case as shown in Fig. 3.1. The cylinders are assumed to be parallel to the z-axis; thus, in this study, we only consider the elastic waves that propagate in the x-y plane. For square 2D structures, the irreducible Brillouin zone spans from C to X to M and back to C. The results of the band diagram computation for the infinite periodic arrangement with a lattice constant of  $0.94 \mu\text{m}$ , square symmetry, and a hole filling factor of 76% are demonstrated in Fig. 3.2a. The filling factor is defined as the percentage ratio of the area of the holes per unit cell square. The dependence of absolute bandgap boundaries on the filling factor is demonstrated in Fig. 3.2b.

Demonstrated in Fig. 3.2b, computational results show variations in bandgaps depending on the filling factor. The results indicate that increasing the diameter of the holes for the same lattice

constant leads to a broadening of the low-frequency bandgap and the emergence of higher-frequency stop bands. At the same time, it can be seen that a relatively narrow high-frequency bandgap, which is found for low filling factors, completely vanishes with an increase in the diameter of the holes. It should be mentioned that at a relatively high filling factor, the square symmetry arrangement exhibits a broad complete bandgap in the lower frequency range and a narrower bandgap at higher frequencies, which is advantageous for switchable FBAR applications. The displacement distribution and the analysis of frequency dependence of the structural reflection for the shear component of displacement are demonstrated in Fig. 3.3. In comparison to a complete FBAR structure, the simulation model should be extended to include top and bottom electrodes with a piezoelectric film in between. However, in order to simplify the calculations and obtain the results that determine the behavior of the periodic structure separately from the piezoelectric film, the model was reduced to the prescribed shear displacement at the boundary of the presumed FBAR reflector. In contrast to the simplified model, the finite FBAR structure will be expanded by incorporating a piezoelectric layer and electrodes of specific dimensions.

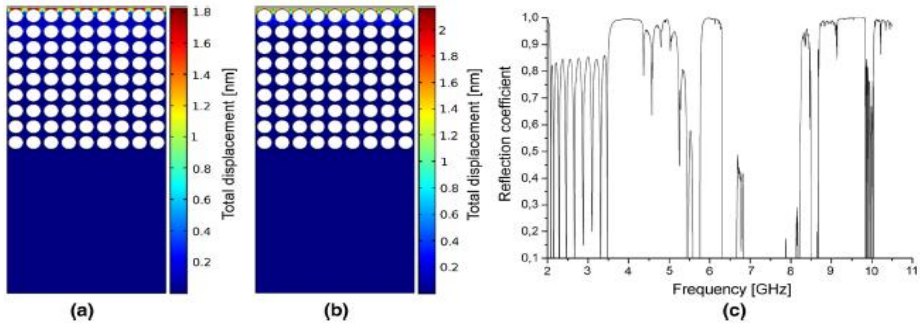
In order to reduce the deterioration of the resonator performance caused by the leakage of acoustic energy, it is advantageous to have a complete bandgap in the reflecting phononic structure near the resonance mode. This helps isolate the top piezoelectric structure modes regardless of their polarization. Even though the unwanted resonance modes should be suppressed by the finite FBAR design, the leakage of acoustic energy is minimized by the efficient complete bandgap reflector. More detailed consideration of the potential effects that may arise in a 3D arrangement should be addressed during the final stages of device development and are the subject of a separate study. The completed analysis of the finite structure reflection for the case of horizontally polarized excitation of the top structure boundary demonstrates an effective isolation of the surface displacement at several relatively narrow frequency ranges. Despite the fact that the complete bandgaps for the structure filling factor of 54% exist only around 4 and 10 GHz, efficient isolation of the shear displacement component is also achievable at a frequency around 6 GHz.

The analysis of triangular symmetry arrangement demonstrates the absence of a complete bandgap at low filling factors and several rather narrow complete bandgaps for higher filling ratios. The band diagram computed for the infinite periodic arrangement with a lattice constant of  $6.3 \mu\text{m}$  and a filling factor of 65% is illustrated in Fig. 3.4a. The structure exhibits several relatively narrow complete bandgaps that do not widen with an increase in the filling factor, as demonstrated in Fig. 3.4b. The reduced wave vector in this case spans in the direction of C–K–M–C, as illustrated in Fig. 3.1b. The computational results of triangular arrangement demonstrate the possibility of achieving several relatively narrow bandgaps at a high filling factor. From a practical standpoint, that arrangement is not optimal because the achievable bandgaps are relatively narrow for applications requiring multiple operation bands and support frequency switching within very limited regions.



3.2. fig Band diagram for the pore silicon infinite square arrangement, filling factor 76%

(a), and the dependence of the width of the absolute bandgaps from the filling factor (b) for fixed value of lattice constant of 0.94  $\mu\text{m}$ .



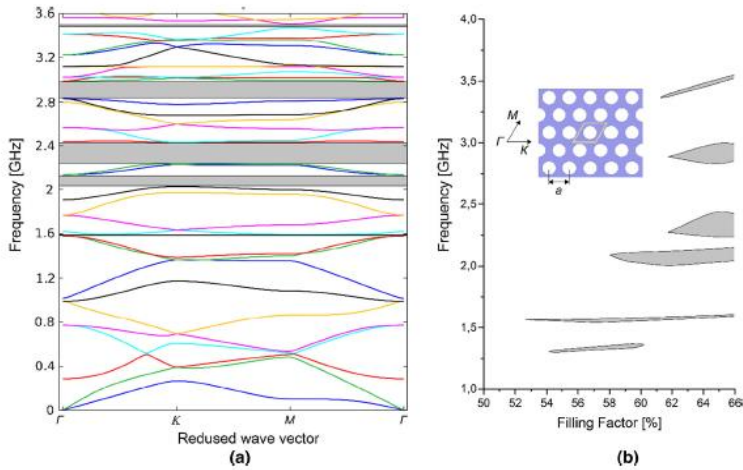
3.3. fig. Simulation results of square arrangement of air-filled cylinders in the silicon matrix (filling factor 54%).

Displacement distribution of the structure excited with a shear displacement applied to the top structure boundary taken at frequencies of 4 GHz (a) and 9.5 GHz (b), and the structure reflection coefficient.

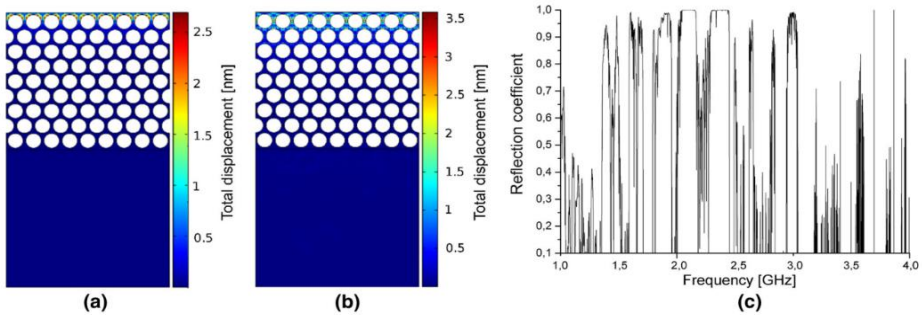
The analysis of the finite structure reflection for the shear-excited top boundary reveals that efficient isolation can only be achieved at narrow frequency ranges that align with the complete bandgap computation results. The structure displacement distribution for the frequencies of high reflection and the computed reflection coefficient for the broad frequency range are illustrated in Fig. 3.5. The honeycomb arrangement was theoretically investigated as an alternative solution for the periodic design arrangement. The results of completed band diagram computations for the filling factor of 58% and a lattice constant of 0.9  $\mu\text{m}$  are illustrated in Fig. 3.6a. As can be seen, the honeycomb structure design supports the appearance of a broad bandgap at lower frequencies and several narrower bandgaps at higher frequencies. In terms of FBAR applications, the designed structure enables the operation of switchable FBARs and the operation of multiple



isolated bands within the frequency range of the wide bandgap. The dependence of the structural response on the filling factor of cylindrical scatterers (for a fixed lattice constant of  $0.9 \mu\text{m}$ ) is demonstrated in Fig. 3.6b. The computational results indicate that for a low filling factor, the lower frequency bandgap becomes narrower, and the higher frequency bandgaps disappear when the filling factor is below 52%. The most promising aspect of the described structural design is its ability to maintain a relatively wide bandgap across a broad range of filling factors. The honeycomb structure design appeared to be the most promising for switchable FBARs.

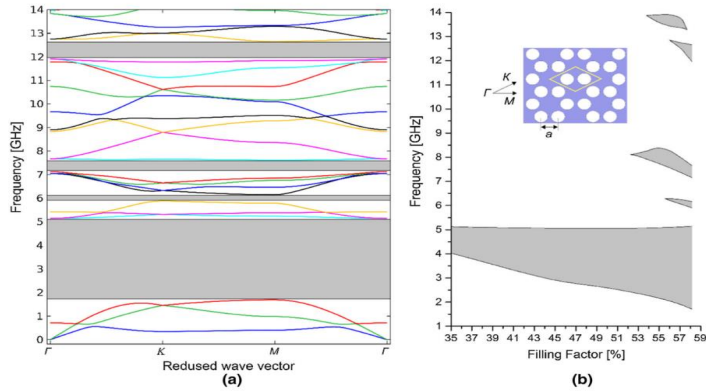


3.4. fig. Band diagram for the pore silicon infinite trigonal arrangement, filling factor 65% (a) and the dependence of the width of the absolute forbidden acoustic bands on the filling factor (b) for fixed lattice constant of  $6.3 \mu\text{m}$ .



3.5 fig. Simulation results of trigonal arrangement of air-filled cylinders in the silicon matrix (filling factor 65%).

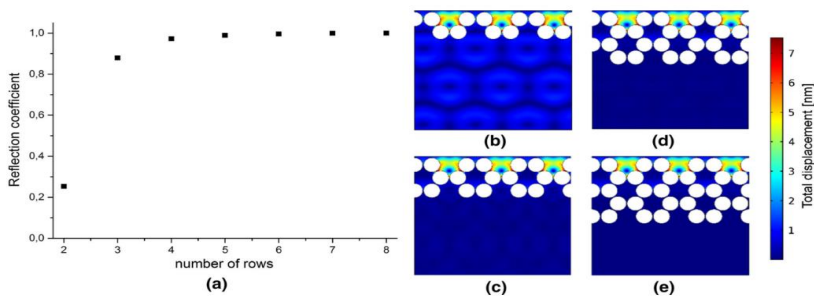
Displacement distribution of the structure excited with a shear displacement applied to the top structure boundary taken at frequency of 2.1 GHz (a) and 3 GHz (b), and the structure reflection coefficient (c).



3.6. fig. Band diagram for the pore silicon infinite graphite arrangement, filling factor 58%

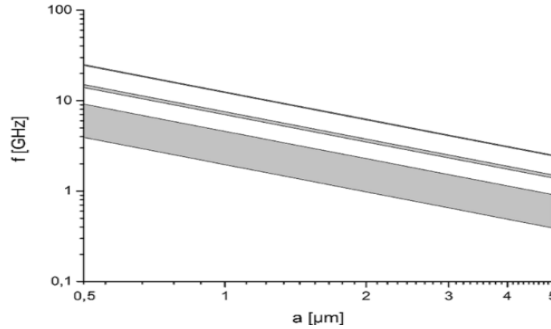
(a) and the dependence of the width of the absolute forbidden acoustic bands on the filling factor (b) for the distance between neighboring scatters  $a = 0.9 \mu\text{m}$ .

The structure dimensions, as demonstrated in the simulations, are on the order of micrometers and submicrometers. In most cases, achieving theoretically optimal structural designs can be quite challenging when it comes to fabricating dimensions at the micrometer and sub-micrometer scales. In order to estimate the performance of the structures within finite dimensions, an analysis of the reflection coefficient depending on the number of structure periods was completed. The analysis was completed for the honeycomb arrangement. Summarized computational results are demonstrated in Fig. 3.7. The reflection coefficient was computed for a frequency of 4 GHz. The results obtained demonstrate that the structure with 8 periods already exhibits reflection behavior comparable to the infinite case. Considering this observation, the minimum number of arrangement periods required for honeycomb symmetry can be reduced to the point where the maximum structure reflection coefficient is already achieved.



3.7. fig Dependence of the structure reflection coefficient on the number of rows of the arrangement

(a) and the simulation results of displacement distribution for number of rows equal 2 (b), 3 (c), 4 (d), 5 (f), taken at frequency of 4 GHz.



3.8. fig. Honeycomb arrangement bandgap variation depending on the structure lattice constant for fixed filling factor of 55%.

The ability to design structures for specific frequency bands involves varying the geometry in relation to the wavelength. Theoretical investigations of variable lattice constants and pore dimensions demonstrate the ability to adjust the structure for the required frequency ranges. The computational results of the honeycomb structure's band gap variation depending on the wavelength structure scaling are summarized in Fig. 3.8. The obtained results show that increasing the structure's wavelength shifts the bandgaps towards lower frequency regions, as expected. In this current contribution, we have presented the results of theoretical research focused on studying technologically competitive solutions of phononic structures for enhancing the performance of FBAR devices. We proposed to consider the established technological platform. In the current contribution, we have demonstrated the results of theoretical research work focused on studying technologically competitive solutions of phononic structures' performance for the purposes of FBAR devices. We propose considering the established technological platform for fabricating macroporous structures as an approach that enables the realization of phononic-based acoustic reflectors for FBAR SMR devices and studying appropriate periodic structure solutions using numerical methods. We have shown that the use of macroporous periodic arrangements can facilitate the efficient operation of SMRFBARs across broad frequency ranges without the need to employ a membrane for isolating the piezoelectric film. The work presented the computational results for square, triangular, and honeycomb arrangements, demonstrating the achievable bandgap responses. It was found that the honeycomb arrangement is the most advantageous in terms of bandgap performance, which should allow the FBAR structures to operate within a broad frequency range. The completed work represents an initial step towards the fabrication of photonic crystal-based FBAR devices, which is the focus of current research.

### 3.2 Modeling and characterization of microspheres with silver molecular clusters for sensor applications

This chapter explores silver-molecular-cluster-containing microspheres for advanced sensors. These microspheres are synthesized through an ion exchange process with silver nitrate and sodium nitrate, creating unique optical properties. A simulation shows an enhanced radiation interaction due to extended fundamental mode propagation. This study investigates luminescence in the visible range (400–600 nm) when excited by long-wavelength UV light (360–410 nm), offering the potential for sensing applications. These microspheres find use in environmental sensing (pollutant detection), biomedicine (drug delivery, bioimaging), and industrial process monitoring.

To create the silicate glass microspheres, we employed glass with the composition detailed in Table 3.1. The production process involved several steps. Initially, we crafted a thin fiber, and subsequently, we formed the microspheres by melting the fiber's end using a propane flame. The microspheres were then subjected to the Low-Temperature Ion Exchange (LTIE) process.

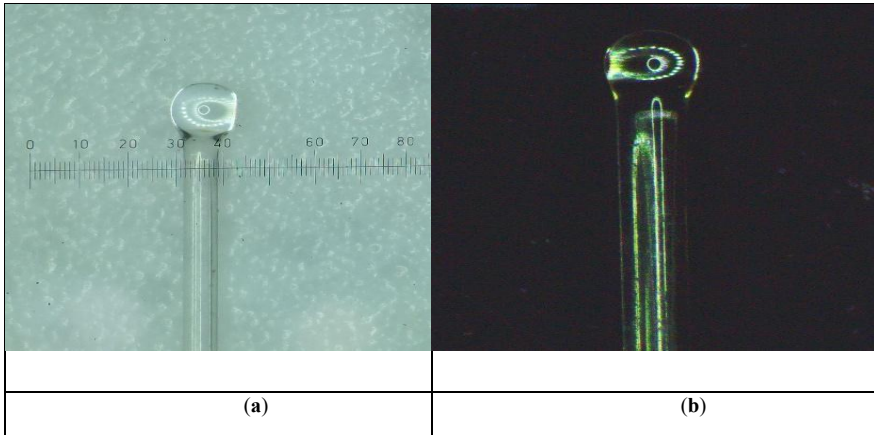
3.1. Table

Composition of glass used for making samples

Chemical Constituents	Glass (% Mass)
SiO <sub>2</sub>	72.2%
Na <sub>2</sub> O	14.3%
K <sub>2</sub> O	1.2%
CaO	6.4%
MgO	4.3%
Al <sub>2</sub> O <sub>3</sub>	1.2%
Fe <sub>2</sub> O <sub>3</sub>	0.03%
SO <sub>3</sub>	0.3%

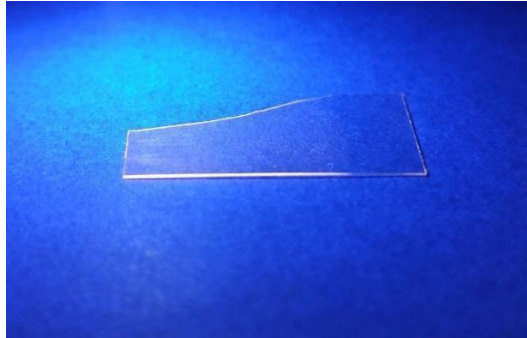
The ion exchange process occurred in a molten salt mixture of silver nitrate (AgNO<sub>3</sub>) and sodium nitrate (NaNO<sub>3</sub>) at a temperature of 330 °C for a duration of 15 min. To monitor the progress of the process, we also included witness glasses with the same composition. The glasses, with a thickness of 0.17 mm, underwent the ion exchange process together with the microspheres in a shared crucible. Following the LTIE process, we meticulously cleansed the samples. This cleansing process involved washing with distilled water and then with isopropyl alcohol to eliminate any residual salts remaining on the surface after the process. Fig. 3.9 displays photographs of the samples we obtained. Notably, the smallest sample achievable through the

described method had a diameter of 200 microns. Fig. 3.10 displays one of the witness samples that was not fully immersed in the crucible. When the sample was illuminated with a 390 nm LED, the luminescence of silver molecular clusters was distinctly visible, and the region where the glass passed was not submerged in the molten salts.



3.9. fig. The obtained microsphere samples.

(a) microsphere with a diameter of 380  $\mu\text{m}$ ; (b) microsphere with a diameter of 200  $\mu\text{m}$ .



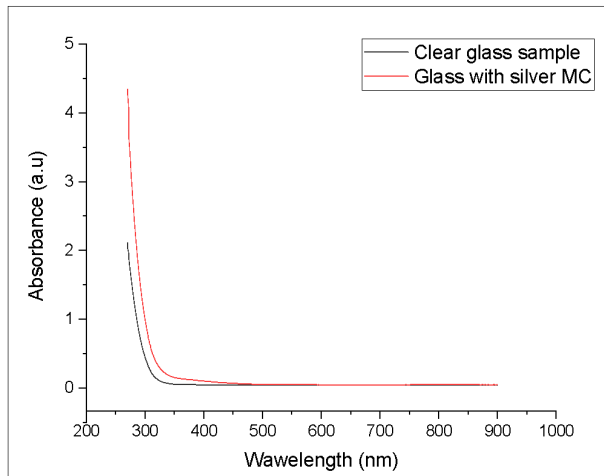
3.10. fig. Witness sample visible luminescence.

Comsol Multiphysics was employed to determine the resonant frequencies and fundamental modes of the resonator. For an effective modeling of the WGM resonator, a two-dimensional axisymmetric approach was adopted. The grid was manually adjusted to facilitate a two-dimensional axisymmetric natural frequency analysis. The investigation of the properties of silicate glass containing silver molecular clusters, synthesized through the LTIE method, encompassed both absorption measurements and luminescence spectra measurements. Absorbance measurements were conducted on the witness samples using a UV-VIS spectrophotometer (PB 2201). Luminescence spectral acquisition measurements were performed

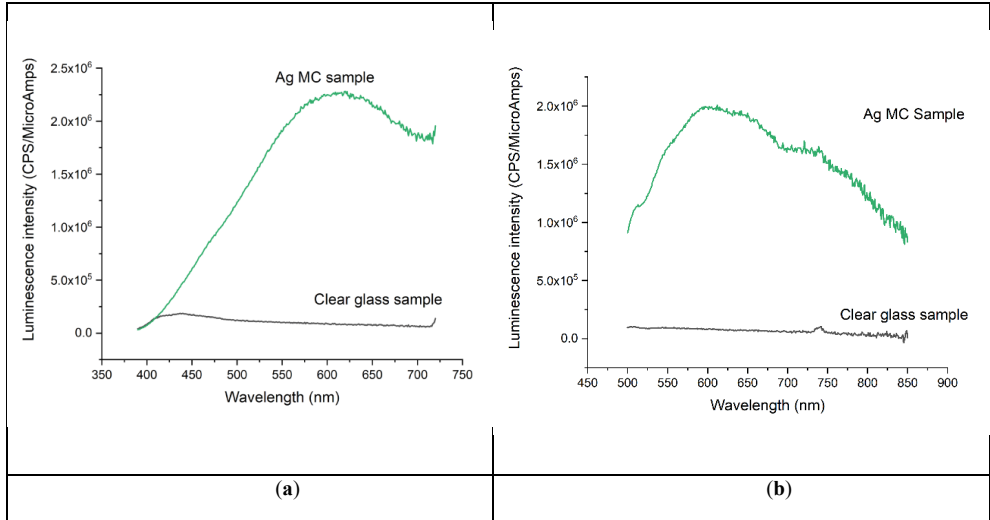
using a Fluorolog®-3 instrument with FluorEssence™ (Manufacturer: HORIBA Jobin Yvon SAS, France). For all luminescence measurements, the integration time was 0.1 s.

An experiment was conducted to measure the absorption of glass samples that underwent Low-Temperature Ion Exchange (LTIE), as well as transparent glass samples that were not subjected to LTIE treatment. The resulting spectrum is depicted in Fig. 3.11. Notably, the absorption spectrum of the samples after the LTIE process lacks characteristic absorption peaks. This absence is attributed to the fact that, under the same process parameters used in the treatment, predominantly silver molecular clusters, such as  $\text{Ag}_2\text{...}_5$ , are formed [139].

Fig. 3.12 presents the results of measuring the luminescence intensity. When excited at wavelengths of 370 nm and 390 nm, the luminescence spectra of all synthesized glasses exhibit a broad luminescence band within the visible spectrum. This broadband luminescence spanning from 500 to 900 nm corresponds to the emission emanating from a small quantity of silver microcrystals formed directly during the LTIE process [140]. To generate molecular clusters (MC), it is imperative to reduce silver ions to their atomic state. This transformation leads to the creation of a certain quantity of silver microcrystals during the LTIE process, consequently giving rise to weak luminescence across the entire visible range.



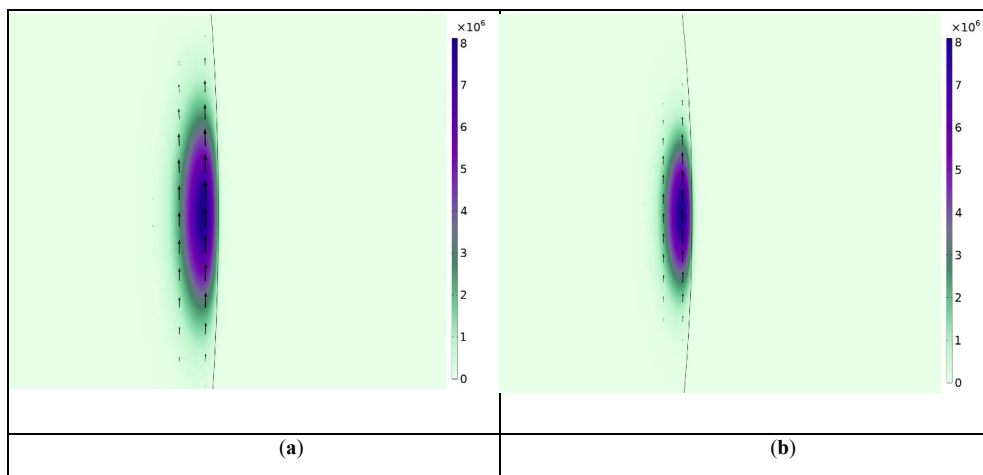
3.11. fig. Measured absorption spectra of glass samples.



3.12. fig. Luminescence intensity.

(a) first sample,  $\lambda_{exc}$  370 nm; (b) second sample,  $\lambda_{exc}$  390 nm.

The simulated microspheres had a radius of 100  $\mu\text{m}$ . During the LTIE process with silver, glass changes its refractive index from 1.585 at the surface to 1.515. The simulated microsphere had a gradient refractive index from the edge to the center. To explore the potential of this material, simulations of microspheres in air and water were conducted. Fig. 3.13 shows the distribution of the electromagnetic field in the cross-section of the microcavity in air (a) and water (b). The resonant wavelength for the fundamental mode of the microresonator near the luminescence peak was determined. For a microsphere in air, the resonant wavelength for the fundamental TE mode with an azimuthal number of 1608 was 600.988 nm. For a microsphere in water, the resonant wavelength for the fundamental TE mode with an azimuthal number of 1608 was 601.294 nm. The difference between the resonant wavelengths was 0.25 nm.



3.13. fig. Fundamental mode localization.

(a) microsphere in air; (b) microsphere in water.

As a result of this study, we have obtained a new material that is suitable for use in label-free sensors with active WGM resonators. This material is very simple to obtain and cost-effective. The experiment showed that glass samples subjected to Low-Temperature Ion Exchange (LTIE) showed distinct absorption characteristics, particularly the absence of characteristic absorption peaks, which was attributed to the formation of Ag<sub>2</sub>...<sub>5</sub> molecular clusters of silver. Luminescence measurements demonstrated a broad emission band in the visible spectrum, particularly in the 500–900 nm range, confirming the formation of silver microcrystals during the LTIE process. According to the simulation results, the difference in resonant wavelengths between media with different refractive indices was 0.26 nm. This allows the material to be used for microsphere sensors without requiring a direct physical connection. The results obtained demonstrate the potential of soda-lime silicate glass with molecular silver clusters as a material for whispering gallery mode (WGM) sensors.



## CONCLUSIONS

This PhD Thesis presents theoretical predictions and practical validations of previously unexplored non-scattering regimes, specifically focusing on hybrid anapoles. These regimes require the simultaneous interference of electric and magnetic multipoles. The obtained results pave the way for the development of substrate-independent metasurfaces with dual functionality, as well as ultrafast modulation approaches. Furthermore, the study of spin-to-orbital angular momentum conversion has opened up new and exciting possibilities for directional fluid navigation on-chip and nanoscale fluid manipulation. Driven fluid flows and size separation within microfluidic systems are enabled by leveraging the optical properties of dielectric nanoantennas along with the dynamics induced by incident light. Additionally, the study of pulse propagation in resonant multilayered media with disorder distributions has revealed transitions and regimes that provide flexible control over the optical response of the medium.

These results have potential applications where controlling the reflection-to-transmission ratio and the propagation of ultrafast pulses in nanomaterials is crucial. Moreover, a novel method for contactless temperature and diffusion measurements is demonstrated by utilizing the Purcell effect in phosphorescent molecules near nanoantennae. This technique holds potential applications in microfluidics and lab-on-a-chip systems. Subwavelength nonspherical resonators are being used to explore superscattering regimes, highlighting increased multipolar resonances with applications ranging from biosensing to energy harvesting, on-chip circuitry, and optical manipulation. An understanding of transverse optical binding around hyperbolic metamaterials provides valuable insights into enhanced optomechanical manipulation techniques driven by high- $k$  volumetric modes. Multiple reflections from boundaries are facilitated by thin metamaterial slabs, leading to highly localized hotspots with significant intensity gradients.

In summary, the combined results of this research contribute to the development of nanophotonics by revealing novel optical phenomena, simplifying the design of creative systems and devices, and providing access to a wide variety of applications in diverse fields. These findings provide a solid foundation for future research and development in ultrafast subwavelength optics and related fields as the discipline progresses.

Key conclusions and remarks of theoretical research:

1. Discovery of hybrid anapoles and their potential for ultrafast modulation techniques.
2. Potential applications of spin-to-orbital angular momentum conversion for nanoscale fluid manipulation.
3. Flexible control over pulse propagation in resonant multilayered media with disorder distributions.
4. Utilization of the Purcell effect for contactless temperature and diffusion measurements in microfluidics.
5. Enhanced multipolar resonances in superscattering regimes for various applications.
6. Insights into transverse optical binding near hyperbolic metamaterials and its

implications for optomechanical manipulation schemes.

Experimental research for this Thesis focused on the study and applications of optical sensing devices. In the third chapter, efforts were directed towards enhancing Film Bulk Acoustic Resonator (FBAR) devices with phononic structures. Theoretical research explored technologically competitive solutions for FBAR devices, demonstrating the efficiency of macroporous periodic arrangements in facilitating a broad frequency range of operation. Computational results favored the honeycomb arrangement for optimal bandgap performance, marking an initial step towards the fabrication of photonic crystal-based FBAR devices. Finally, we introduced a new material for label-free sensors with active Whispering Gallery Mode (WGM) resonators. The material obtained through Low-Temperature Ion Exchange (LTIE) exhibited distinct absorption characteristics and luminescence, demonstrating its potential for WGM sensors without requiring direct physical connection.

## BIBLIOGRAPHY

1. S.M. Kamali, E. Arbabi, A. Arbabi, and A. Faraon "A review of dielectric optical metasurfaces for wavefront control" *Nanophotonics*, vol. 7, no. 6, 2018, pp. 1041-1068, DOI:<https://doi.org/10.1515/nanoph-2017-0129>
2. S. Liu, M.B. Sinclair, S. Saravi, G.A. Keeler, Y. Yang, J. Reno, G.M. Peake, F. Setzpfandt, I. Staude, T. Pertsch, and I. Brener "Resonantly Enhanced Second-Harmonic Generation Using III-V Semiconductor All Dielectric Metasurfaces," *Nano Lett.* 2016 Sep 14;16(9), DOI:<https://doi.org/10.1021/acs.nanolett.6b01816>
3. D.G. Baranov, D.A. Zuev, S.I. Lepeshov, O.V. Kotov, A.E. Krasnok, A.B. Evlyukhin, B.N. Chichkov, "All dielectric nanophotonics: the quest for better materials and fabrication techniques," *Optica* 4, 814-825 (2017), DOI: <https://doi.org/10.1364/OPTICA.4.000814>
4. P.D. Terekhov, K.V. Baryshnikova, Y. Greenberg, Y. H. Fu, A.B. Evlyukhin, A. S. Shalin, A. Karabchevsky, "Enhanced absorption in all-dielectric metasurfaces due to magnetic dipole excitation," *Sci Rep* 9, 3438 (2019), DOI: <https://doi.org/10.1038/s41598-019-40226-0>
5. J. Algorri, D. Zografopoulos, A. Ferraro, B. García-Cámara, R. Vergaz, R. Beccherelli, J. Sánchez-Pena "Anapole Modes in Hollow Nanocuboid Dielectric Metasurfaces for Refractometric Sensing," *Nanomaterials* 2019, 9, 30, DOI: <https://doi.org/10.3390/nano9010030>
6. H. K. Shamkhi, K. V. Baryshnikova, A. Sayanskiy, P. Kapitanova, P. D. Terekhov, P. Belov, A. Karabchevsky, A. B. Evlyukhin, Y. Kivshar, A. S. Shalin, "Transverse Scattering and Generalized Kerker Effects in All Dielectric Mie-Resonant Metaoptics," *Phys. Rev. Lett.* 122, 193905 (2019), DOI: <https://doi.org/10.1103/PhysRevLett.122.193905>
7. A.C. Valero, E.A. Gurvitz, F.A. Benimetskiy, D.A. Pidgayko, A. Samusev, A.B. Evlyukhin, V. Bobrovs, D. Redka, M.I. Tribelsky, M. Rahmani, K.Z. Kamali, A.A. Pavlov, A.E. Miroshnichenko, A.S. Shalin, "Theory, Observation, and Ultrafast Response of the Hybrid Anapole Regime in Light Scattering," *Laser & Photonics Reviews*, Vol. 1, No. 1, pp.1-14. ISSN 1863-8880, DOI: <https://doi.org/10.1002/lpor.202100114>.
8. L. Khriachtchev, (2016). *Silicon Nanophotonics: Basic Principles, Present Status, and Perspectives*, Second Edition, Jenny Stanford Publishing, DOI: <https://doi.org/10.1201/9781315364797>
9. S. Jahani, Z. Jacob, "All-dielectric metamaterials," *Nature Nanotech* 11, 23–36 (2016), DOI:<https://doi.org/10.1038/nnano.2015.304>
10. P. Rufangura, T. Folland, A. Agrawal, J. Caldwell, F. Lacopi "Towards low- loss on-chip nanophotonics with coupled graphene and silicon carbide: a review," *Journal of Physics: Materials* 3 , 2020, DOI:10.1088/2515 7639/ab9d10
11. R.S. Savelev, D.S. Filonov, M.I. Petrov, A.E. Krasnok, P.A. Belov, Y.S. Kivshar, "Resonant transmission of light in chains of high-index dielectric particles," *Physical Review B*, " 2015, 92(15), pp. 1–5, 2015, DOI:<https://doi.org/10.1103/PhysRevB.92.155415>

12. R. Savelev, D. Filonov, P. Kapitanova, A. Krasnok, A. Miroshnichenko, P. Belov, Y.S. Kivshar, "Bending of electromagnetic waves in all-dielectric particle array waveguides," *Applied Physics Letters*. 105., (2014), DOI:<https://doi.org/10.1063/1.4901264>
13. O. Limon, L. Businaro, A. Gerardino, O. Bitton, A. Frydman, Z. Zalevsky, "Fabrication of electro optical nano modulator on silicon chip," *Microelectronic Engineering* 86, 1099-1102, (2009), DOI:<https://doi.org/10.1016/j.mee.2009.01.007>
14. A.E. Krasnok, A.E. Miroshnichenko, P.A. Belov, Y.S. Kivshar, "All-dielectric optical nanoantennas," *Opt. Express* 20, 20599-20604 (2012)
15. J. Henry, J. Livingstone, "Thin-Film Amorphous Silicon Position-Sensitive Detectors," *Advanced Materials* 13, (2001), 1022-1026, DOI: [https://doi.org/10.1002/1521-4095\(200107\)13:12/133.0.CO;2-I](https://doi.org/10.1002/1521-4095(200107)13:12/133.0.CO;2-I)
16. A.M., Miroshnichenko, A.E., Shadrivov, I.V. Shadrivov, Y.S. Kivshar, "All-Dielectric Multilayer Cylindrical Structures for Invisibility Cloaking," *Sci Rep* 5, (2015), DOI:<https://doi.org/10.1038/srep09574>
17. W.T. Chen, A.Y. Zhu, F. Capasso, "Flat optics with dispersion-engineered metasurfaces," *Nat Rev Mater* 5, 604–620, (2020), DOI:<https://doi.org/10.1038/s41578-020-0203-3>
18. D. Lin, P. Fan, E. Hasman, M.L. Brongersma, "Dielectric gradient metasurface optical elements," *Science*, 2014 Jul 18;345(6194):298-302, DOI:10.1126/science.1253213
19. E. Nazemosadat, M. Mazur, S. Kruk, I. Kravchenko, J. Carpenter, J. Schröder, P. Andrekson, M. Karlsson, Y.S. Kivshar, "Dielectric Broadband Metasurfaces for Fiber Mode-Multiplexed Communications," *Advanced Optical Materials*. 7, (2019), DOI: <https://doi.org/10.1002/adom.201801679>
20. J. Yan, J., Liu, X., Ma, C., Huang, Y., Yang, G., "All-dielectric materials and related nanophotonic applications", (2020) *Materials Science and Engineering R: Reports*, 141, art. no. 100563.
21. Kamali, S.M., Arbabi, E., Arbabi, A., Faraon, A., "A review of dielectric optical metasurfaces for wavefront control", (2018) *Nanophotonics*, 7 (6), pp. 1041-1068.
22. M. L. Brongersma, "The road to atomically thin metasurface optics", *Nanophotonics* **10**, 643–654 (2020).
23. D. G. Baranov, D. A. Zuev, S. I. Lepeshov, O. V. Kotov, A. E. Krasnok, A. B. Evlyukhin, and B. N. Chichkov, "All-dielectric nanophotonics: the quest for better materials and fabrication techniques" *Optica* 4, 814-825 (2017).
24. S. Liu, M. B. Sinclair, S. Saravi, G. A. Keeler, Y. Yang, J. Reno, G. M. Peake, F. Setzpfandt, I. Staude, T. Pertsch, and I. Brener, "Resonantly enhanced second-harmonic generation using III-V semiconductor all-dielectric metasurfaces", *Nano Lett.* 16, 5426–5432 (2016).
25. R. S. Savelev, D. S. Filonov, P. V. Kapitanova, A. E. Krasnok, A. E. Miroshnichenko, P. A. Belov, and Y. S. Kivshar, "Bending of electromagnetic waves in all-dielectric particle array waveguides", *Appl. Phys. Lett.* 105, (2014).

26. R. M. Bakker, Y. F. Yu, R. Paniagua-Domínguez, B. Luk'yanchuk, and A. I. Kuznetsov, "Resonant light guiding along a chain of silicon nanoparticles", *Nano Lett.* 17, 3458–3464 (2017).
27. Y. H. Fu, A. I. Kuznetsov, A. E. Miroshnichenko, Y. F. Yu, and B. Luk'yanchuk, "Directional visible light scattering by silicon nanoparticles", *Nat. Commun.* 4, 1527 (2013).
28. K. Chen, Y. Feng, F. Monticone, J. Zhao, B. Zhu, T. Jiang, L. Zhang, Y. Kim, X. Ding, S. Zhang, A. Alù, and C. W. Qiu, "A Reconfigurable Active Huygens' Metalens", *Adv. Mater.* 29, 1–7 (2017).
29. K. Koshelev, S. Kruk, E. Melik-Gaykazyan, J. H. Choi, A. Bogdanov, H. G. Park, and Y. Kivshar, "Subwavelength dielectric resonators for nonlinear nanophotonics", *Science* (80-.). 367, 288–292 (2020).
30. A. S. Shalin, "Microscopic theory of optical properties of composite media with chaotically distributed nanoparticles", *Quantum Electron.* 40, 1004–1011 (2010).
31. P. M. Voroshilov, C. R. Simovski, P. A. Belov, and A. S. Shalin, "Light-trapping and antireflective coatings for amorphous Si-based thin film solar cells", *J. Appl. Phys.* 117, (2015).
32. Y. Cui, D. van Dam, S. A. Mann, N. J. J. van Hoof, P. J. van Veldhoven, E. C. Garnett, E. P. A. M. Bakkers, and J. E. M. Haverkort, "Boosting solar cell photovoltage via nanophotonic engineering", *Nano Lett.* 16, 6467–6471 (2016).
33. P. D. Terekhov, K. V. Baryshnikova, Y. Greenberg, Y. H. Fu, A. B. Evlyukhin, A. S. Shalin, and A. Karabchevsky, "Enhanced absorption in all-dielectric metasurfaces due to magnetic dipole excitation", *Sci. Rep.* 9, 3438 (2019).
34. J. Algorri, D. Zografopoulos, A. Ferraro, B. García-Cámara, R. Vergaz, R. Beccherelli, and J. Sánchez-Pena, "Anapole modes in hollow nanocuboid dielectric metasurfaces for refractometric sensing", *Nanomaterials* 9, 30 (2018).
35. S. Jahani, and Z. Jacob, "All-dielectric metamaterials", *Nat. Nanotechnol.* 11, 23–36 (2016).
36. H. K. Shamkhi, K. V. Baryshnikova, A. Sayanskiy, P. Kapitanova, P. D. Terekhov, P. Belov, A. Karabchevsky, A. B. Evlyukhin, Y. Kivshar, and A. S. Shalin, "Transverse Scattering and Generalized Kerker Effects in All-Dielectric Mie-Resonant Metaoptics", *Phys. Rev. Lett.* 122, 193905 (2019).
37. D. Wang, Q. Fan, J. Wang, Z. Zhang, Y. Liang, and T. Xu, "All-dielectric metasurface beam deflector at the visible frequencies", *Guangdian Gongcheng/Opto-Electronic Eng.* 44, 103–107 (2017).
38. P. Grahn, A. Shevchenko, and M. Kaivola, "Electromagnetic multipole theory for optical nanomaterials", *New J. Phys.* 14, (2012).
39. R. Alaei, C. Rockstuhl, and I. Fernandez-Corbaton, "An electromagnetic multipole expansion beyond the long-wavelength approximation", *Opt. Commun.* 407, 17–21 (2018).
40. A. B. Evlyukhin, T. Fischer, C. Reinhardt, and B. N. Chichkov, "Optical theorem and multipole scattering of light by arbitrarily shaped nanoparticles", *Phys. Rev. B* 94, 1–7 (2016).

41. R. E. Raab, and O. L. Lange, *Multipole Theory in Electromagnetism* (Oxford Science Publications, New York, n.d.).
42. J. D. Jackson, *Classical Electrodynamics*, 3rd ed. (New York, {NY}, 1999).
43. N. Papasimakis, V. A. Fedotov, V. Savinov, T. A. Raybould, and N. I. Zheludev, “Electromagnetic toroidal excitations in matter and free space”, *Nat. Mater.* 15, 263–271 (2016).
44. V. M. Dubovik, and V. V. Tugushev, “Toroid Moments in Electrodynamics and Solid-State Physics”, *Phys. Rep.* 187, 145–202 (1990).
45. A. T. Góngora, and E. Ley-Koo, “Complete electromagnetic multipole expansion including toroidal moments”, *Rev. Mex. Fis. E* 52, 188–197 (2006).
46. V. A. Fedotov, A. V. Rogacheva, V. Savinov, D. P. Tsai, and N. I. Zheludev, “Resonant Transparency and Non-Trivial Non-Radiating Excitations in Toroidal Metamaterials”, *Sci. Rep.* 3, 1–5 (2013).
47. W. Liu, B. Lei, J. Shi, H. Hu, and A. E. Miroshnichenko, “Elusive Pure Anapole Excitation in Homogenous Spherical Nanoparticles with Radial Anisotropy”, *J. Nanomater.* 2015, 382 (2015).
48. W. Liu, J. Zhang, B. Lei, H. Hu, and A. E. Miroshnichenko, “Invisible nanowires with interfering electric and toroidal dipoles”, *Opt. Lett.* 40, 2293 (2015).
49. J. Tian, H. Luo, Y. Yang, F. Ding, Y. Qu, D. Zhao, M. Qiu, and S. I. Bozhevolnyi, “Active control of anapole states by structuring the phase-change alloy  $\text{Ge}_2\text{Sb}_2\text{Te}_5$ ”, *Nat. Commun.* 10, 1–9 (2019).
50. A. K. Ospanova, I. V. Stenishchev, and A. A. Basharin, “Anapole mode sustaining silicon metamaterials in visible spectral range”, *Laser Photon. Rev.* 12, 1800005 (2018).
51. N. A. Nemkov, A. A. Basharin, and V. A. Fedotov, “Electromagnetic sources beyond common multipoles”, *Phys. Rev. A* 98, 1–9 (2018).
52. E. A. Gurvitz, K. S. Ladutenko, P. A. Dergachev, A. B. Evlyukhin, A. E. Miroshnichenko, and A. S. Shalin, “The high-order toroidal moments and anapole states in all-dielectric photonics”, *Laser Photon. Rev.* 13, 1800266 (2019).
53. S. Gladyshev, K. Frizyuk, and A. Bogdanov, “Symmetry analysis and multipole classification of eigenmodes in electromagnetic resonators for engineering their optical properties”, *Phys. Rev. B* 102, 075103 (2020).
54. E. Takou, A. C. Tasolamprou, O. Tsilipakos, and E. N. Economou, “Dynamic anapole in metasurfaces made of sculptured cylinders”, *Phys. Rev. B* 100, 085431 (2019).
55. G. Grinblat, Y. Li, M. P. Nielsen, R. F. Oulton, and S. A. Maier, “Enhanced Third Harmonic Generation in Single Germanium Nanodisks Excited at the Anapole Mode”, *Nano Lett.* 16, 4635–4640 (2016).
56. T. Shibanuma, G. Grinblat, P. Albella, and S. A. Maier, “Efficient Third Harmonic Generation from Metal–Dielectric Hybrid Nanoantennas”, *Nano Lett.* 17, 2647–2651 (2017).
57. S. V. Makarov, M. I. Petrov, U. Zywiets, V. Milichko, D. Zuev, N. Lopanitsyna, A. Kuksin, I. Mukhin, G. Zograf, E. Ubyivovk, D. A. Smirnova, S. Starikov, B. N. Chichkov, and

- Y. S. Kivshar, “Efficient Second-Harmonic Generation in Nanocrystalline Silicon Nanoparticle”, *Nano Lett.* 17, 3047–3053 (2017).
58. A. Kaldun, A. Blättermann, V. Stooß, S. Donsa, H. Wei, R. Pazourek, S. Nagele, C. Ott, C. D. Lin, J. Burgdörfer, and T. Pfeifer, “Observing the ultrafast buildup of a Fano resonance in the time domain”, *Science* 354, 738–741 (2016).
59. S. Lepeshov, and A. Krasnok, “Virtual Optical Pulling Force”, *Optica* 7, 1024-1030 (2020).
60. S. A. Maier, M. P. Nielsen, G. Grinblat, Y. Li, and R. F. Oulton, “Efficient third harmonic generation and nonlinear subwavelength imaging at a higher-order anapole mode in a single germanium nanodisk”, *ACS Nano* 11, 953–960 (2016).
61. Z.-J. Yang, Y.-H. Deng, Y. Yu, and J. He, “Magnetic toroidal dipole response in individual all-dielectric nanodisk clusters”, *Nanoscale* 12, 10639–10646 (2020).
62. B. Luk’yanchuk, R. Paniagua-Dominguez, A. I. Kuznetsov, A. E. Miroshnichenko, and Y. S. Kivshar, “Hybrid anapole modes of high-index dielectric nanoparticles”, *Phys. Rev. A* 95, 1–8 (2017).
63. A. K. Ospanova, A. Basharin, A. E. Miroshnichenko, and B. Luk’yanchuk, “Generalized hybrid anapole modes in all-dielectric ellipsoid particles”, *Opt. Mater. Express* 11, 23-34 (2021).
64. E. A. Gurvitz, K. S. Ladutenko, P. A. Dergachev, A. B. Evlyukhin, A. E. Miroshnichenko, and A. S. Shalin, “The high-order toroidal moments and anapole states in all-dielectric photonics”, *Laser Photonics Rev.* 13, 1800266 (2019).
65. W. Yan, R. Faggiani, and P. Lalanne, “Rigorous modal analysis of plasmonic nanoresonators”, *Phys. Rev. B* 97, 205422 (2018).
66. P. Lalanne, W. Yan, K. Vynck, C. Sauvan, and J. P. Hugonin, “Light interaction with photonic and plasmonic resonances”, *Laser Photonics Rev.* 12, 1–38 (2018).
67. M. I. Tribelsky, and A. E. Miroshnichenko, “Giant in-particle field concentration and Fano resonances at light scattering by high-refractive-index particles”, *Phys. Rev. A* 93, 053837 (2016).
68. O. Ávalos-Ovando, L. V. Besteiro, Z. Wang, and A. O. Govorov, “Temporal plasmonics: Fano and Rabi regimes in the time domain in metal nanostructures”, *ArXiv* 9, 3587–3595 (2020).
69. M. I. Tribelsky, and A. E. Miroshnichenko, “Giant in-particle field concentration and Fano resonances at light scattering by high-refractive-index particles”, *Phys. Rev. A* 93, 053837 (2016).
70. L. Wei, Z. Xi, N. Bhattacharya, and H. P. Urbach, “Excitation of the radiationless anapole mode”, *Optica* 3, 799-802 (2016).
71. J. A. Parker, H. Sugimoto, B. Coe, D. Eggena, M. Fujii, N. F. Scherer, S. K. Gray, and U. Manna, “Excitation of nonradiating anapoles in dielectric nanospheres”, *Phys. Rev. Lett.* (2020).
72. V. A. Zenin, S. M. Novikov, Y. Yang, B. N. Chichkov, S. I. Bozhevolnyi, A. B. Evlyukhin, R. Malureanu, and A. V Lavrinenko, “Direct amplitude-phase near-field observation of higher-order anapole states”, *Nano Lett.* 17, 7152–7159 (2017).

73. P. Lalanne, W. Yan, K. Vynck, C. Sauvan, and J. P. Hugonin, “Light interaction with photonic and plasmonic resonances”, *Laser Photonics Rev.* **12**, 1–38 (2018).
74. M. I. Tribelsky, and A. E. Miroshnichenko, “Giant in-particle field concentration and Fano resonances at light scattering by high-refractive-index particles”, *Phys. Rev. A* **93**, 053837 (2016).
75. O. Ávalos-Ovando, L. V. Besteiro, Z. Wang, and A. O. Govorov, , “Temporal plasmonics: Fano and Rabi regimes in the time domain in metal nanostructures”, *ArXiv* **9**, 3587–3595 (2020).
76. Shamkhi, H. K. et al. Transverse scattering and generalized kerker effects in all-dielectric mie-resonant metaoptics. *Phys. Rev. Lett.* **122**, 1–22 (2019).
77. Albaladejo, S., Marqués, M. I., Laroche, M. & Sáenz, J. J. Scattering forces from the curl of the spin angular momentum of a light field. *Phys. Rev. Lett.* **102**, 1–4 (2009).
78. Papra, A. et al. Microfluidic Networks Made of Poly(dimethylsiloxane), Si, and Au Coated with Polyethylene Glycol for Patterning Proteins onto Surfaces. *Langmuir* **17**, 4090–4095 (2007).
79. Ge, L. et al. Molecularly imprinted polymer grafted porous Au-paper electrode for an microfluidic electro-analytical origami device. *Adv. Funct. Mater.* **23**, 3115–3123 (2013).
80. Evlyukhin, A. B. et al. Demonstration of magnetic dipole resonances of dielectric nanospheres in the visible region. *Nano Lett.* **12**, 3749–3755 (2012).
81. Evlyukhin, A. B., Reinhardt, C., Seidel, A., Luk’Yanchuk, B. S. & Chichkov, B. N. Optical response features of Si-nanoparticle arrays. *Phys. Rev. B - Condens. Matter Mater. Phys.* **82**, 1–12 (2010).
82. Doyle, W. T. Optical properties of a suspension of metal spheres. *Phys. Rev. B* **39**, 9852–9858 (1989).
83. Albaladejo, S., Marqués, M. I. & Sáenz, J. J. Light control of silver nanoparticle’s diffusion. *Opt. Express* **19**, 11471 (2011).
84. Garcés-Chávez, V., Volke-Sepulveda, K., Chávez-Cerda, S., Sibbett, W. & Dholakia, K. Transfer of orbital angular momentum to an optically trapped low-index particle. *Phys. Rev. A - At. Mol. Opt. Phys.* **66**, 8 (2002).
85. Sokolovskii, G. S. et al. Bessel beams from semiconductor light sources. *Prog. Quantum Electron.* **38**, 157–188 (2014).
86. Shamkhi, H. K. et al. Transverse scattering and generalized kerker effects in all-dielectric mie-resonant metaoptics. *Phys. Rev. Lett.* **122**, 1–22 (2019).
87. Donner, J. S., Baffou, G., McCloskey, D. & Quidant, R. Plasmon-assisted optofluidics. *ACS Nano* **5**, 5457–5462 (2011).
88. Huang, C., Chen, X., Oladipo, A. O., Panoiu, N. C. & Ye, F. Generation of Subwavelength Plasmonic Nanovortices via Helically Corrugated Metallic Nanowires. *Sci. Rep.* **5**, 1–10 (2015).
89. David, A., Gjonaj, B. & Bartal, G. Two-dimensional optical nanovortices at visible light. *Phys. Rev. B* **93**, 1–5 (2016).



90. Young, A. B. et al. Polarization Engineering in Photonic Crystal Waveguides for Spin-Photon Entanglers. *Phys. Rev. Lett.* **115**, 1–5 (2015).
91. David, A., Gjonaj, B., Blau, Y., Dolev, S. & Bartal, G. Nanoscale shaping and focusing of visible light in planar metal–oxide–silicon waveguides. *Optica* **2**, 1045 (2015).
92. Willig, K. I. et al. Nanoscale resolution in GFP-based microscopy. *Nat. Methods* **3**, 721–723 (2006).
93. Chithrani, B. D., Ghazani, A. A. & Chan, W. C. W. Determining the size and shape dependence of gold nanoparticle uptake into mammalian cells. *Nano Lett.* **6**, 662–668 (2006).
94. Chithrani, B. D. & Chan, W. C. W. Elucidating the mechanism of cellular uptake and removal of protein-co
95. Pan, Y. et al. Size-dependent cytotoxicity of gold nanoparticles. *Small* **3**, 1941–1949 (2007).
96. Kern, A. M. & Martin, O. J. F. Excitation and reemission of molecules near realistic plasmonic nanostructures. *Nano Lett.* **11**, 482–487 (2011).
97. S. A. Gredeskul, Yu. S. Kivshar, A. A. Asatryan, K. Y. Bliokh, Yu. P. Bliokh, V. D. Freilikher, I. V. Shadrivov, “Anderson localization in metamaterials and other complex media”, *Low Temp. Phys.* 2012, 38, 570-602.
98. H. H. Scheinflux, Y. Lumer, G. Ankonina, A. Z. Genack, G. Bartal, M. Segev, “Observation of Anderson localization in disordered nanophotonic structures”, *Science* 2017, 356, 953-956.
99. C. Liu, W. Gao, B. Yang, S. Zhang, “Disorder-induced topological state transition in photonic metamaterials”, *Phys. Rev. Lett.* 2017, 119, 183901.
100. H. H. Scheinflux, I. Kaminer, A. Z. Genack, M. Segev, “Interplay between evanescence and disorder in deep subwavelength photonic structures”, *Nat. Commun.* 2016, 7, 12927., Y. Liu, S. M. Kamali, A. Arbabi, H. Ruan, A. Faraon, C. Yang, “Wavefront shaping with disorder-engineered metasurfaces”, *Nat. Photon.* 2018, 12, 84-90.
101. L. Allen, J. H. Eberly, *Optical Resonance and Two-Level Atoms*, Wiley, New York 1975.
102. S. L. McCall, E. L. Hahn, “Self-Induced Transparency”, *Phys. Rev.* 1969, 183, 457.
103. I. A. Poluektov, Yu. M. Popov, V. S. Roitberg, “Self-induced transparency effect”, *Sov. Phys. Usp.* 1975, 17, 673.
104. R. M. Arkhipov, M. V. Arkhipov, I. Babushkin, A. Demircan, U. Morgner, N. N. Rosanov, “Ultrafast creation and control of population density gratings via ultraslow polarization waves”, *Opt. Lett.* 2016, 41, 4983.
105. R. M. Arkhipov, A. V. Pakhomov, M. V. Arkhipov, I. Babushkin, A. Demircan, U. Morgner, N. N. Rosanov, “Population density gratings induced by few-cycle optical pulses in a resonant medium”, *Sci. Rep.* 2017, 7, 12467.
106. A. A. Afanas’ev, V. M. Volkov, V. V. Dritz, B. A. Samson, “Interaction of counter-

propagating self-induced transparency solitons”, *J. Mod. Opt.* 1990, 37, 165.

107. M. J. Shaw, B. W. Shore, “Collisions of counterpropagating optical solitons”, *J. Opt. Soc. Am. B* 1991, 8, 1127.

108. D. V. Novitsky, “Femtosecond pulses in a dense two-level medium: Spectral transformations, transient processes, and collisional dynamics”, *Phys. Rev. A* 2011, 84, 013817.

109. D. V. Novitsky, “Disordered resonant media: Self-induced transparency versus light localization”, *Phys. Rev. A* 2018, 97, 013826

110. D. V. Novitsky, A. S. Shalin, “All-Optical Transmission Modulation Due to Inelastic Interactions of Ultrashort Pulses in a Disordered Resonant Medium”, *Ann. Phys.* 2019, 531, 1800405.

111. D. V. Novitsky, “Disordered resonant media: Self-induced transparency versus light localization”, *Phys. Rev. A* 2018, 97, 013826.

112. A. S. Kadochkin, I. I. Shishkin, A. S. Shalin, and P. Ginzburg, “Quantum Sensing of Motion in Colloids via Time-Dependent Purcell Effect”, *Laser Photonics Rev.* 12, 1800042 (2018).

113. V. Kozlov, D. Filonov, Y. Yankelevich, and P. Ginzburg, “Micro-Doppler frequency comb generation by rotating wire scatterers”, *J. Quant. Spectrosc. Radiat. Transf.* 190, 7 (2017).

114. D. Filonov, B. Z. Steinberg, and P. Ginzburg, “Asymmetric micro-Doppler frequency comb generation via magnetoelectric coupling”, *Phys. Rev. B* 95, 235139 (2017).

115. D. V. Guzатов, S. V. Vaschenko, V. V. Stankevich, A. Y. Lunevich, Y. F. Glukhov, and S. V. Gaponenko, “Plasmonic enhancement of molecular fluorescence near silver nanoparticles: theory, modeling, and experiment”, *J. Phys. Chem. C* 116, 10723 (2012).

116. A. N. Poddubny, P. Ginzburg, P. A. Belov, A. V. Zayats, and Y. S. Kivshar, “Tailoring and enhancing spontaneous two-photon emission using resonant plasmonic nanostructures”, *Phys. Rev. A At. Mol. Opt. Phys.* 86, 033826 (2012).

117. Ivinskaya, A.; Kostina, N.; Proskurin, A.; Petrov, M. I.; Bogdanov, A. A.; Sukhov, S.; Krasavin, A. V.; Karabchevsky, A.; Shalin, A. S.; Ginzburg, P. *Optomechanical Manipulation with Hyperbolic Metasurfaces.* *ACS Photonics* 2018, 5 (11), 4371–4377.

118. Johnson, P. B.; Christy, R. W. *Optical Constants of the Noble Metals.* *Phys. Rev. B* 1972, 6 (12), 4370–4379.

119. Rodríguez-de Marcos, L. V.; Larruquert, J. I.; Mendez, J. A.; Aznarez, J. A. *Self-Consistent Optical Constants of SiO<sub>2</sub> and Ta<sub>2</sub>O<sub>5</sub> Films.* *Opt. Mater. Express* 2016, 6 (11), 3622.

120. Rybin, M. V. et al. *High-Q supercavity modes in subwavelength dielectric resonators.* *Phys. Rev. Lett.* 119, 1–5 (2017).

121. Friedrich, H. *Interfering resonances and BIC.* *Phys. Rev. A* 32, 3231–3242 (1985).

122. Ruan, Z. & Fan, S. *Design of subwavelength superscattering nanospheres.* *Appl. Phys. Lett.* 98, 43101 (2011).

123. Hsu, C. W., DeLacy, B. G., Johnson, S. G., Joannopoulos, J. D. & Soljačić, M. Theoretical criteria for scattering dark states in nanostructured particles. *Nano Lett.* 14, 2783–2788 (2014).
124. Gladyshev, S., Frizyuk, K. & Bogdanov, A. Symmetry analysis and multipole classification of eigenmodes in electromagnetic resonators for engineering their optical properties. *Phys. Rev. B* 102, 075103 (2020).
125. Kostina, N. et al. Optical binding via surface plasmon polariton interference. *Phys. Rev. B* 99, 125416 (2017).
126. Barhom, H. et al. Biological Kerker effect boosts light collection efficiency in plants. *Nano Lett* 19, 7062–7071 (2019).
127. Terekhov, P. D. et al. Broadband forward scattering from dielectric cubic nanoantenna in lossless media. *Opt. Express* 27, 10924 (2019).
128. Terekhov, P. D. et al. Enhanced absorption in all-dielectric metasurfaces due to magnetic dipole excitation. *Sci. Rep.* 9, 3438 (2019).
129. Kozlov, V., Filonov, D., Shalin, A. S., Steinberg, B. Z. & Ginzburg, P. Asymmetric backscattering from the hybrid magneto-electric metaparticle. *Appl. Phys. Lett.* 109, 203503 (2016).
130. Guo, R. et al. High-bit rate ultra-compact light routing with mode-selective on-chip nanoantennas. *Sci. Adv.* 3, e1700007 (2017).
131. Wang, S. B. & Chan, C. T. Lateral optical force on chiral particles near a surface. *Nat. Commun.* 5, 1–8 (2014).
132. Kislov, D. A. et al. Multipole engineering of attractive–repulsive and bending optical forces. *Adv. Photonics Res.* 2, 2100082 (2021).
133. E. D. Palik, *Handbook of Optical Constants of Solids: Handbook of Thermo-Optic Coefficients of Optical Materials with Applications*, Elsevier, New York 1997.
134. COST 323, European WIM Test Program 1996-1998 (CET & CMT), Technical report of the Management Committee, draft 2, COST323/WAVE, EC/DGVII, COST Transport, 1996.
135. M. Y. Shahin, *Pavement Management for Airports, Roads, and Parking Lots*, Springer, 2 edition, 2017.
136. “SJSC Latvian State Roads, online traffic intensity at highway A2 76th km, ” January 2020, <https://lvceli.lv/traffic/>.
137. Liu, X.; Luan, H.; Dai, B.; Lan, B. Influence of fiber link impairments to Eb/No estimation in CO-OFDM systems with QPSK mapping. *Optik* 2013, 124, 1977–1981.
138. Sheng, J.; Li, J.; Yu, J. The development of silver nanoclusters in ion-exchanged soda-lime silicate glasses. *Int. J. Hydrog. Energy* **2007**, 32, 2598–2601.
139. Simo, A.; Polte, J.; Pfander, N.; Vainio, U.; Emmerling, F.; Rademann, K. Formation Mechanism of Silver Nanoparticles Stabilized in Glassy Matrices. *J. Am. Chem. Soc.* **2012**, 134, 18824–18833.

## **Supplements**

**1-PAPER:** Theory, observation, and ultrafast response of the hybrid anapole regime in light scattering

Canós Valero A., Gurvitz E.A., Benimetskiy F.A., Pidgayko D.A., Samusev A., Evlyukhin A.B., Bobrovs V., Redka D., Tribelsky M.I., Rahmani M., Kamali K.Z., Pavlov A.A., Miroshnichenko A.E., Shalin A.S., “Theory, Observation, and Ultrafast Response of the Hybrid Anapole Regime in Light Scattering”, (2021) *Laser and Photonics Reviews*, 15 (10), art. no. 2100114, DOI: [10.1002/lpor.202100114](https://doi.org/10.1002/lpor.202100114)

# Theory, Observation, and Ultrafast Response of the Hybrid Anapole Regime in Light Scattering

Adrià Canós Valero,\* Egor A. Gurvitz, Fedor A. Benimetskiy, Dmitry A. Pidgayko, Anton Samusev, Andrey B. Evlyukhin, Vjaceslavs Bobrovs, Dmitrii Redka, Michael I. Tribelsky, Mohsen Rahmani, Khosro Zangeneh Kamali, Alexander A. Pavlov, Andrey E. Miroshnichenko, and Alexander S. Shalin

Modern nanophotonics has witnessed the rise of “electric anapoles” (EDAs), destructive interferences of electric and toroidal electric dipoles, actively exploited to resonantly decrease radiation from nanoresonators. However, the inherent duality in Maxwell equations suggests the intriguing possibility of “magnetic anapoles,” involving a nonradiating composition of a magnetic dipole and a magnetic toroidal dipole. Here, a hybrid anapole (HA) of mixed electric and magnetic character is predicted and observed experimentally via dark field spectroscopy, with all the dominant multipoles being suppressed by the toroidal terms in a nanocylinder. Breaking the spherical symmetry allows to overlap up to four anapoles stemming from different multipoles with just two tuning parameters. This effect is due to a symmetry-allowed connection between the resonator multipolar response and its eigenstates. The authors delve into the physics of such current configurations in the stationary and transient regimes and explore new ultrafast phenomena arising at sub-picosecond timescales, associated with the HA dynamics. The theoretical results allow the design of non-Huygens metasurfaces featuring a dual functionality: perfect transparency in the stationary regime and controllable ultrashort pulse beatings in the transient. Besides offering significant advantages with respect to EDAs, HAs can play an essential role in developing the emerging field of ultrafast resonant phenomena.

## 1. Introduction

Over the past few years, all-dielectric nanophotonics has become one of the cornerstones of modern research in nano-optics.<sup>[1,2]</sup> Unlike plasmonic structures, dielectric ones make it possible to overcome the fundamental limitation of Ohmic losses. Utilizing electric and magnetic Mie-like resonances of nanoparticles, consisting of low-loss high-index semiconductor or dielectric materials, such as Si, TiO<sub>2</sub>, Ge, and GaAs,<sup>[3,4]</sup> enables manipulating both the electric and magnetic components of light at the nanoscale. This emerging field has already led to a wide range of exciting applications, such as low-loss discrete dielectric waveguides,<sup>[5,6]</sup> passive and reconfigurable directional sources,<sup>[7,8]</sup> efficient high harmonic generation mechanisms,<sup>[9]</sup> light-harvesting and antireflective coatings,<sup>[10–12]</sup> all-dielectric metasurfaces with artificially tailored optical response,<sup>[13–16]</sup> dielectric beam deflectors,<sup>[17]</sup> and subwavelength all-optical liquid mixing,<sup>[18]</sup> to mention just a few.

A. Canós Valero, Dr. E. A. Gurvitz, F. A. Benimetskiy, D. A. Pidgayko, Dr. A. Samusev, Dr. A. B. Evlyukhin, Dr. A. S. Shalin  
ITMO University  
Kronverksky prospect 49, St. Petersburg 197101, Russia  
E-mail: adria.canos@optomech.ifmo.ru  
Dr. A. B. Evlyukhin  
Institute of Quantum Optics  
Leibniz Universität Hannover  
Welfengarten Street 1, Hannover 30167, Germany  
Dr. V. Bobrovs, Dr. D. Redka, Dr. A. S. Shalin  
Institute of Telecommunications, Riga  
Technical University  
Azenes street 12, Riga 1048, Latvia

Dr. D. Redka  
Electrotechnical University “LETI” (ETU)  
5 Prof. Popova Street, Saint Petersburg 197376, Russia  
Prof. M. I. Tribelsky  
Faculty of Physics  
M. V. Lomonosov Moscow State University  
Moscow 119991, Russia  
Prof. M. I. Tribelsky  
Moscow Engineering Physics Institute  
National Research Nuclear University  
Moscow 115409, Russia  
Prof. M. I. Tribelsky  
School of Physical Science and Technology and  
Jiangsu Key Laboratory of Thin Film  
Soochow University  
Suzhou 215006, China

 The ORCID identification number(s) for the author(s) of this article can be found under <https://doi.org/10.1002/lpor.202100114>

DOI: 10.1002/lpor.202100114

The ability to adequately describe and predict electromagnetic scattering is of prime importance to manipulate the behavior of light at the nanoscale. For this purpose, different types of electromagnetic multipole expansions were introduced.<sup>[19–23]</sup> The charge-current Cartesian decomposition is widely used for describing optical signatures of nano-objects of arbitrary shape.<sup>[19–21]</sup> One of the most intriguing possibilities delivered by this formalism is the ability to define the so-called toroidal moment family.<sup>[24–27]</sup> While the well-known electric toroidal dipole moment is associated with the poloidal currents flowing along the meridians of a torus,<sup>[25]</sup> higher-order toroidal moments, also known as mean square radii, feature more complex current distributions recently investigated theoretically in refs. [28,29].

The electric toroidal dipole is now widely exploited in nanophotonics and metamaterials, active photonics,<sup>[30]</sup> ultra-sensitive biosensing,<sup>[24]</sup> and applications requiring strong near-field localization.<sup>[31,32]</sup> The fields radiated by toroidal moments share the same angular momentum and far-field properties as their electric or magnetic multipolar counterparts, allowing for the realization of two exciting effects: i) enhanced multipolar responses<sup>[31]</sup> enabled by the constructive interference of the fields, and ii) mutual cancellation of the far-field contributions via the destructive one, so-called “anapole.”<sup>[14]</sup>

In the aforementioned scenario, an anapole corresponded to a scattering minimum from a given multipole channel<sup>[34,35]</sup> leading to a reduction of the overall far-field scattering and confined near-fields.<sup>[34]</sup> This promising feature has motivated widespread investigations in diverse applications of nanoscale light–matter interactions, such as photocatalysis,<sup>[36]</sup> Raman scattering,<sup>[37]</sup> strong exciton coupling,<sup>[38]</sup> and second and third harmonic generation.<sup>[39–42]</sup>

It should be stressed, however, that while there exists a large amount of literature regarding the stationary (frequency domain) response of the electric dipole anapole (EDA), the number of publications devoted to discussions of transient behavior in the time domain is much fewer. On the other hand, emergent studies point out that the transient regimes may exhibit qualitatively

new effects, not observable in the stationary states.<sup>[43]</sup> In this regard, the understanding and control of the transient response of anapoles is yet to be developed and remains an unexplored realm with potential applications in the novel field of ultrafast dynamic resonant phenomena.<sup>[43,44]</sup>

Furthermore, the vast majority of the investigations on EDAs are limited to the electric dipole term only.<sup>[45–48]</sup> Despite the observation of high order EDAs in Ge and Si nanodisks,<sup>[49]</sup> no experimental works have proven the existence of magnetic anapoles. If the magnetic anapoles do exist, their spectral overlap with electric ones should give rise to the enhanced radiation suppression and lead to unprecedentedly concentration and confinement of the electromagnetic energy within the scattering particle. In turn, this effect should provide new exciting degrees of freedom for designing light–matter interactions. Until now, this issue has remained a challenging task since the formation of hybrid anapoles (HAs) requires a careful overlap of electric and magnetic multipoles with their toroidal counterparts. Indeed, magnetic toroidal moments themselves have only been discussed in a very recent work, where a complex cluster of nanodisks was necessary to induce the desired multipole response.<sup>[50]</sup>

Importantly, spherically symmetric structures are unable to exhibit HAs<sup>[51,52]</sup> since the latter always remain hidden by the contributions of other multipole moments with non-negligible scattering. Nevertheless, recent developments in the theory of multipole expansions<sup>[30,29]</sup> have opened the possibility to qualitatively and quantitatively investigate higher-order electric and magnetic anapoles in scatterers with arbitrary shape, beyond the limitations of the quasistatic regime.

Here, for the first time we design and demonstrate experimentally the existence of such exotic current configurations, schematically illustrated in **Figure 1a**. In the stationary regime, making use of our recently developed multipolar formalism,<sup>[53]</sup> we show how anapoles come into being, arising from multipoles of alternate electric and magnetic origin, linked in scatterers with broken spherical symmetry. This feature makes it possible to spectrally overlap up to four anapoles varying just two geometrical parameters of the proposed resonator.

We show that the counterintuitive opportunity to satisfy four anapole conditions varying only two parameters is strongly related to the violation of the scatterer’s spherical symmetry, playing a key role in our study. As a result, the four conditions become non-independent. The latter is clearly shown by treating the problem in terms of open cavity modes, that is, quasi-normal modes<sup>[54,55]</sup> (QNMs, depicted in **Figure 1a**). The expansion of the fields on a basis of QNMs demonstrates that the overlap of four anapoles occurs owing to the superposition of just two fundamental QNMs supported by the structure.

Physically, the overlap gives rise to the excitation of a “super” dark anapole with strongly minimized scattering, accompanied by an extremely effective electromagnetic energy concentration within the scatterer (achieving an order of magnitude enhancement with respect to the EDA), resulting in highly confined near-fields. The performed analysis also provides a complete physical picture of the effect, establishing general theoretical guidelines valid for anapoles of arbitrary order and their combinations, in scatterers of arbitrary shape.

The HA originates from the far-field destructive interference of all the leading electric and magnetic Cartesian multipoles of

---

Dr. M. Rahmani  
Advanced Optics and Photonics Laboratory  
Department of Engineering  
School of Science and Technology  
Nottingham Trent University  
Nottingham NG11 8NS, UK

K. Z. Kamali  
IARC Centre of Excellence for Transformative Meta-Optical Systems  
Research School of Physics  
The Australian National University  
Canberra ACT 2601, Australia

Dr. A. A. Pavlov  
Institute of Nanotechnology of Microelectronics of the Russian Academy of Sciences (INME RAS)  
Nagatinskaya street, house 16A, building 11, Moscow 115487, Russia  
Prof. A. E. Miroshnichenko  
School of Engineering and Information Technology  
UNSW Canberra  
Canberra, ACT 2600, Australia

Dr. A. S. Shalin  
Kotel'nikov Institute of Radio Engineering and Electronics of  
Russian Academy of Sciences (Ulyanovsk branch)  
Goncharova Str.48, Ulyanovsk 432000, Russia

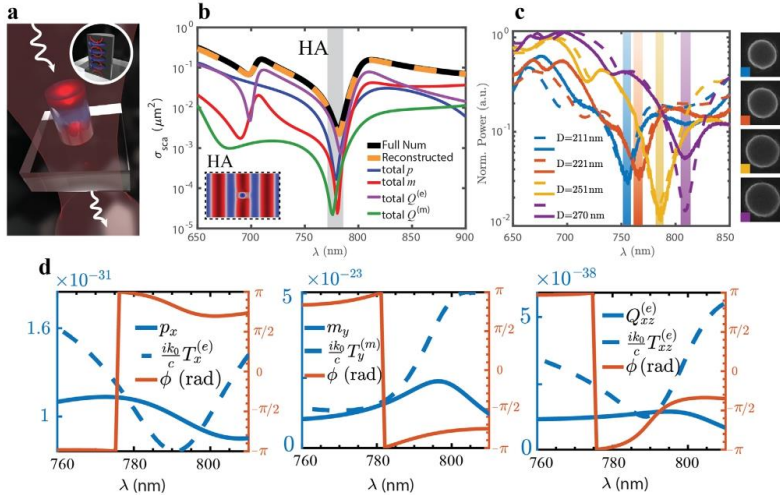


**Figure 1.** a) Artistic representation of the novel effect. A normally incident plane wave excites nontrivial modal contributions in a Si nanocylinder whose interference with the background field leads to a fourfold HA yielding the nanoantenna virtually invisible in the far-field, with localized near-field. Inset depicts the two resonant eigenmodes' current distributions arising due to standing waves between the top and bottom walls (red) and lateral walls (blue) in the vertical plane. b) Multipole reconstruction of the numerically obtained scattering cross section for the cylindrical amorphous silicon nanoparticle. In the legend caption, "total" implies that both basic and toroidal contributions of a given multipole are plotted. The inset corresponds to the x-component of the electric field. The cylinder's geometrical parameters are height  $H = 367$  nm and diameter  $D = 252$  nm. Point HA ( $\lambda = 782$  nm) corresponds to the minima of the HA. c) The colored regions indicate the left plot: measured (solid lines) and simulated (dashed lines) scattering spectra of single isolated nanocylinders with different diameters  $D$ . The spectral positions of the HAs. Right plot: SEM micrographs of the corresponding nanocylinder samples. The colored edges in each micrograph are associated with the measurements' legend entries. d) Amplitudes and phase differences between the multipoles and their toroidal counterparts. Panels from left to right, respectively: the basic electric and electric toroidal dipoles, the basic magnetic and magnetic toroidal dipoles, and the basic electric and electric toroidal quadrupoles. Amplitudes correspond to the left ordinate-axis, and phase differences are read from the right ordinate-axis.

a finite cylindrical scatterer with their associated toroidal moments. For the first time, higher-order (quadrupolar) toroidal moments are shown to contribute to essential features of the scattering response of an isolated high-index nanoparticle. We validate our results by fabricating a series of individual silicon nanocylinders supporting the HA and confirm its existence experimentally via dark-field spectroscopy measurements.

The discussion is further extended to envision future applications of our effect in the novel field of ultrafast resonant phenomena. We predict and theoretically describe the unconventional temporal dynamics of the HA nanoresonator under a pulse with a sharp temporal cutoff. The analysis shows the emission of two ultrashort energy "flashes"<sup>[56]</sup> at the leading and trailing edges of the excitation and the formation of coherent beating oscillations<sup>[57]</sup> in the scattered electric field.

It should be stressed that contrarily to the conventional EDA, the HA preserves its nonradiating nature in the presence of any dielectric substrate. The QNM formalism allows us to unveil the physical mechanism behind such a counterintuitive effect, and

further demonstrate its breakdown in the transient regime. The spatiotemporal maps reveal relevant changes in the beating pattern of the decaying modes, explicitly dependent on the substrate refractive index.

Finally, based on the developed theoretical description, we design and demonstrate a dual-functional metasurface consisting of an array of HA particles combining full transparency in the stationary regime and a highly tunable spatiotemporal response in the transient one.

### 1.1. The Cartesian Multipole Expansion and High-Order Anapole Conditions

The analysis of a nanoparticle's optical response is usually carried out via the decomposition of the scattering cross section as a sum of multipoles, which represent independent scattering channels of the object. Here we utilize the irreducible Cartesian multipole expansion derived in ref. [29] (for completeness, also given in the



Section S1, Supporting Information), which explicitly considers higher-order toroidal moments. The latter interpretation is our starting point toward the physical understanding of higher-order anapoles.

Within this approach, an electric or magnetic anapole of order  $n$  in a subwavelength scatterer is given by the condition:

$$P_{i_1 \dots i_n}^{(e,m)} + i \frac{k_d}{v_d} T_{i_1 \dots i_n}^{(e,m)} = 0 \quad (1)$$

Here we have denoted  $n$ th order electric or magnetic moments with  $P^{(e)}$  and  $P^{(m)}$ , and the corresponding electric and magnetic toroidal moments with  $T^{(e)}$  and  $T^{(m)}$ , respectively. The number of subscripts indicates each Cartesian tensor's order, that is, one subscript corresponds to a dipole, two correspond to a quadrupole, etc.  $k_d$ ,  $\epsilon_d$  are the wavenumber and the dielectric permittivity of the host medium, and  $v_d$  is the speed of light in the medium. In the previous we have chosen to depart from the usual terminology employed for denoting toroidal moments, which refers to the  $T^{(e)}$  as simply "toroidal," to clearly differentiate between toroidal moments contributing to radiation of the "electric" type, and those contributing to radiation of the "magnetic" type. Their physical origin is also different:<sup>[29]</sup> the  $T^{(e)}$  originate from poloidal currents, while the  $T^{(m)}$  arise due to circulating magnetic fields. We also clarify that in order to minimize the number of involved terms,<sup>[22]</sup> the coordinate origin for the multipole expansion has been set to the particle center of mass.

The HA occurs when more than one multipole moment fulfills Equation (1) at a given wavelength, resulting in a simultaneous suppression of scattering of two or more channels. However, as mentioned above, light, in general, can be radiated out through other non-zero multipole moments, destroying the overall effect. Thus, only the cancellation of all the leading multipoles can enable a true HA.

For the sake of clarity, in the rest of the manuscript, we will rely on the widespread notation for low-order multipoles, that is,  $p$ ,  $m$  for electric and magnetic dipoles, and  $Q^{(e)}$ ,  $Q^{(m)}$  for electric and magnetic quadrupoles.

## 2. Results

### 2.1. Observation and Multipole Analysis of HAs

Under conventional plane wave illumination, HA of homogeneous spherical particles are hidden by the contributions of other multipoles.<sup>[51,58]</sup> We will show that this restriction naturally vanishes for nano-objects with additional geometrical degrees of freedom, like finite cylinders or parallelepipeds. We will unveil the fundamental reason behind this unusual behavior throughout this work.

Let us consider a cylindrical silicon nanoparticle embedded in air. Starting now, we will use amorphous silicon (a-Si) in both theoretical and experimental studies (for details refer to the Section S13, Supporting Information). The illumination scheme is presented in the left inset of Figure 1b (normally incident  $x$ -polarized plane wave propagating along  $-z$ -direction).

The design methodology is based on the following: We note that the spectral positions of the full (basic together with toroidal

contributions), electric dipole and magnetic quadrupole anapoles are mainly dependent on the cylinder's radius. In contrast, the wavelengths of the full magnetic dipole and electric quadrupole anapoles change both as functions of the cylinder height and radius. Figure S2, Supporting Information illustrates the spectral behavior of the multipolar anapoles with variations of the geometrical parameters in detail. Thus, carefully tuning these two geometrical degrees of freedom makes it possible to place the anapoles of all the leading terms ultimately close to each other (Figure 1b), providing a strong scattering minimum (Figure 1b,c, point HA).

The total scattering cross section and its multipole decomposition after the numerical optimization are shown in Figure 1b. Good agreement between the sum of the multipole contributions given by Equation (S1), Supporting Information and the result of the full-wave simulations in Comsol Multiphysics is demonstrated, proving that only the first four multipoles are sufficient to fully describe the optical response of the nanocylinder in the visible range. Therefore, the low-scattering regime renders it perfectly dark to the incident radiation (see the inset on Figure 1b).

The different panels in Figure 1d show the amplitudes and phase differences of the three most relevant multipoles with their toroidal moments. The results further confirm that the generalized anapole condition in Equation (1) is well fulfilled for each pair (the amplitudes are equal, and they are  $\pi$  rad out of phase) at the HA wavelength  $\lambda = 782$  nm. Particularly, this implies that we have succeeded in exciting, for the first time, quadrupole anapole moments in the visible range. Here we recognize that owing to the presence of polarization losses of the dielectric, the cancellation of the electric quadrupole is not as pronounced as in a lossless structure (see Section S17, Supporting Information).

To confirm our theoretical predictions on the HA, we have carried out direct scattering spectroscopy measurements for a set of standalone nanocylinders with tailored dimensions in the optical spectral range (Figure 1c). The measured scattering spectra (solid lines, Figure 1c) exhibit a pronounced dip, shifting with the increase of the nanocylinder diameter  $D$ , in excellent agreement with the calculations (dashed lines, Figure 1c). Technical details on the fabrication and the optical measurement setup can be found in the Section S14, Supporting Information. While an increase of the nanocylinder's lateral size leads to an overall redshift of the multipole anapoles, they almost perfectly overlap at  $D = 251$  nm, where the most pronounced HA results in a large drop in scattering efficiency, of almost two orders of magnitude, rendering the nanocylinder virtually invisible. We note that the other dips indicated in the measured spectra also correspond to HAs, although their overlap is not as much pronounced, but still results in a significant scattering reduction.

The near-zero values of the full scattering coefficients do not imply the induced polarization currents in the particle to be also close to zero. This is in agreement with the usual anapole behavior,<sup>[59]</sup> but due to the suppression of several multipoles simultaneously, the HA also displays much better confined internal fields and strongly minimizes the interaction of the cavity with the surroundings (see the following sections).

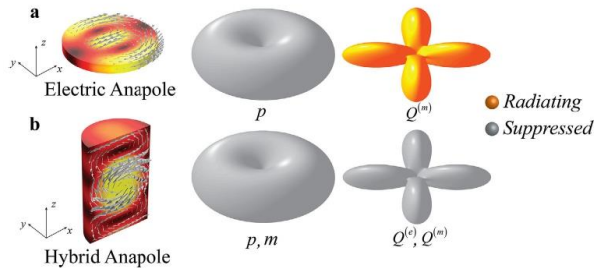


**Figure 2.** Near and far-field characteristics of electric and HAs. a) From left to right: the normalized intensity of the internal electric field in the electric anapole nanodisk, and corresponding vector field (gray arrows). Angular pattern of the multipoles radiated and suppressed by the EDA. The two designs are obtained by fixing the refractive index  $n = 3.87$ . The considered EDA is obtained at  $kR = 1.795$ ,  $R/H = 5$ , similar to refs. [40,63]. b) Same as in (a), for the HA, with  $kR = 1$ ,  $R/H = 1/3$ .

## 2.2. New Perspectives Offered by Individual HA Nanoresonators

Both HAs and EDAs are characterized by suppressing far-field radiation while displaying enhanced near-fields. This naturally poses the question of whether HAs can present any uncommon features and/or fundamental advantages with respect to EDAs for nanophotonics applications. To answer this question in detail, Figure 2 shows the internal field distributions and multipole moments associated with the conventional nanodisks supporting EDAs, commonly employed in nanophotonic designs, in comparison with the HA. The near and far-field characteristics of EDAs are currently well understood in terms of the destructive interference of the electric dipole and electric toroidal dipole excitations within the nanoresonator,<sup>134</sup> whose peculiar signature can be appreciated from the poloidal-like field distributions arising within the nanoparticle (see Figure 2a). However, the multipole decomposition of the scattering spectra reveals that while the electric dipole radiation can be significantly suppressed, EDAs display nonnegligible contributions of the magnetic quadrupole to radiation.<sup>134</sup> This corresponds to a fundamental limitation of the EDA design, since modes of resonators with inversion symmetry in the  $z$ -direction will always radiate as combinations of multipoles possessing even or odd parity,<sup>60,61</sup> and can only be overcome with careful tuning of the incident beam profile.<sup>62</sup>

Conversely, the complex mixture of electric and magnetic multipole moments giving rise to the HA leads to an internal field distribution unlike the EDA (Figure 2b). It hinders a straightforward interpretation of the near-fields in terms of Cartesian multipoles, which already points at a different physical origin. As illustrated in Figure 2b, and shown quantitatively in Figure 1b, the HA allows to simultaneously suppress the electric and magnetic dipoles and quadrupoles under plane wave illumination. Here we must clarify that with the term “suppression” we refer to the appearance of strong local minima in the spectra of each multipole channel. The effect is clearly appreciable when comparing the scattering cross sections of the two structures (Figure 3a); despite that the total volume of the nanoresonator is almost ten times larger than the EDA nanodisk, the scattering intensity for

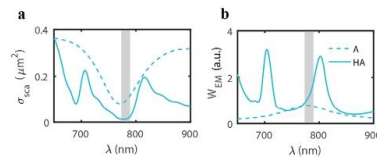


**Figure 3.** a) Radiated power and b) stored electromagnetic energy at the electric anapole (indicated with A) and the HA (denoted with HA). The geometrical parameters are the same as in Figure 2. The grey band in the plots indicates the spectral position corresponding to the destructive interference between the electric dipole and the electric toroidal dipole giving rise to the EDA. Despite having a volume around ten times larger than EDAs, the radiation suppression due to the HA is an order of magnitude more efficient and can be considered broadband. Contrarily, the total stored electromagnetic energy is enhanced by more than an order of magnitude. In (b), the electromagnetic energy has been normalized on  $10^{-30}$  J to facilitate the interpretation.

the HA is found to be more than ten times weaker and can be considered broadband.

Interestingly, this fact does not decrease the local density of optical states, as demonstrated by the calculations of the total electromagnetic energy stored within the two structures (Figure 3b). The energy stored at the HA nanoresonator surpasses that of the EDA by more than an order of magnitude, which promises essential benefits for boosting light-matter interactions and enhance nonlinear effects. The stored energy is also significantly higher than that of the recently observed 2nd order EDAs,<sup>40,63</sup> (a quantitative comparison between EDAs, 2nd order EDAs and HAs is provided in Section S4, Supporting Information). Finally, it can be seen that the modes supporting the HA display significantly larger quality factors than the EDA.

Overall, the numerical studies carried out in this section provide conclusive evidence on the superiority of HAs with respect to EDAs as nonradiating sources capable of enhancing light-matter

interactions at the nanoscale. A more thorough understanding of the effect is thus desirable as a means to properly design future applications.

### 2.3. Intrinsic Modal Content of the HA

While Cartesian multipoles are suitable for the description of far-fields, in this section we employ the natural QNM expansion<sup>[51]</sup> of near-fields and internal currents, which in the following will allow us to unveil the physics behind the HA further. QNMs provide a suitable basis for the induced polarization currents, which can then be expanded according to:

$$J(\omega, r) = \sum_{\mu} \alpha_{\mu}(\omega) J_{\mu}(\omega, r) - i\omega\delta\epsilon E_{\text{inc}}(\omega, r) \quad (2)$$

Here  $J_{\mu}(r) = -i\omega\delta\epsilon E_{\mu}(r)$ ,  $\alpha_{\mu}(\omega)$  and  $\delta\epsilon$  are, respectively, the induced modal scattering current distribution as a function of the internal mode field, the excitation coefficient of the mode  $\mu$  describing its contribution to the total current at a given frequency, and the permittivity contrast with the host environment.

We use a modified version of the freeware MAN developed by the authors of ref. [54]. More details on the approach can be found in the Sections S5, S6, Supporting Information. For simplicity, we consider a dispersionless, lossless nanocylinder with a constant refractive index  $n \approx 3.87$  (corresponding to aSi at 780 nm), so that the excitation coefficients depend solely on the fields of an individual QNM.<sup>[54]</sup> Losses and refractive index dispersion of the original design are negligible in the considered spectral range (see Section S12, Supporting Information). Therefore, this approximation does not significantly change the scattering cross section and average electromagnetic energy density.

The QNM expansion results are displayed in the different panels of Figure 2. The correctness of our calculations in the studied spectral range, particularly near the scattering dip, is well validated in Figure 2a,b by comparing the sum of the individual QNM contributions with the numerically obtained total scattering cross section (a) and average electromagnetic energy density inside the cylinder (b). From here on, we shall label the QNMs with the standardized notation for the modes of isolated cylindrical cavities,<sup>[64]</sup> that is,  $(TE, TM)_{\text{order}}$ , where the sub-indices denote the number of standing wave maxima in the azimuthal ( $u$ ), radial ( $v$ ), and axial ( $\ell$ ) directions.  $TE$  and  $TM$  indicate the predominant nature of the internal field distribution. Specifically,  $TM$  (transverse magnetic) modes have  $H_z \approx 0$ , while  $TE$  (transverse electric) have  $E_z \approx 0$ .

The spectral behavior of each resonant QNM is described by a Fano lineshape,<sup>[65]</sup> (see Section S6, Supporting Information). The other nearby QNMs constitute the background scattering contribution of the particle.

In Figure 4a we note that a total of three QNMs resonate in the visible range. The correct reconstruction of the scattering cross section requires considering background modes, despite their resonances being outside the considered spectral range (green dashed line). Nevertheless, only the  $TM_{113}$  and  $TE_{120}$  modes present a "Fano-like" response at point HA.

The pronounced low scattering regime can be easily grasped as a consequence of modal interference: a clear sign that this is

indeed the case are the resonant negative contributions to scattering presented by both the  $TE_{120}$  and  $TM_{113}$  modes. It implies that, when the incident field impinges in the resonator, energy exchange takes place between the two and the background QNM fields.<sup>[64]</sup> This owes to the fact that the QNMs do not obey the usual conjugate inner product relation of orthogonal modes in Hermitian systems.<sup>[67]</sup> It is important to emphasize the unusual feature of the HA: the two resonant QNMs dominating the spectra are simultaneously negatively suppressed by interference with the background. For comparison, the QNM decomposition of a conventional dipole anapole disk is given in the Section S7, Supporting Information.

A completely different picture arises within the resonator. Figure 4b presents the modal decomposition of the internal energy stored in the cylinder in the vicinity of point HA. This is one of the main results of the section. Contrarily to the multipole expansion, the QNM decomposition allows us to distinguish the eigenmodes contributions to the internal fields clearly. First, we observe a significant enhancement of the electromagnetic energy (around nine times), with respect to the incident plane wave. Second, it is clearly seen that the stored energy at the HA is mainly driven by the  $TM_{113}$  mode due to its higher quality factor and the proximity of its resonant wavelength to the HA wavelength, in a minor measure by the  $TE_{120}$  and the sum of the background contributions. Overall, the QNM analysis given in Figure 4 demonstrates that both the invisibility effect (outside the cylinder) and the internal energy enhancement at the HA are mediated by the simultaneous resonant response of the  $TM_{113}$  and the  $TE_{120}$  modes. On the other hand, the background modes, while they do not apparently define the spectral features of the figures of merit, also play an important role since their interference with the resonant ones gives rise to the invisibility effect. This interpretation is consistent with early investigations regarding the formation of Fano lineshapes in the scattering cross section of spherical resonators.<sup>[58]</sup>

The electric field distributions of the  $TE_{120}$  and  $TM_{113}$  modes are shown in Figure 4c. Following refs. [68,69] we can classify the first as a "Mie" type mode, similar to the ones supported by an infinite cylinder, while the second is of the "Fabry-Perot" (FP) type,<sup>[68]</sup> arising due to the formation of a standing wave pattern between the top and bottom walls of the resonator, that is, having non-zero axial wavenumber ( $\ell \geq 1$ ). Their distinct origin unveils the reason why it is possible to obtain a HA in this particular geometry, contrarily to spherical scatterers. As shown in Section S8, Supporting Information, the real parts of the eigenwavelengths of the modes in the cylinder can be estimated as<sup>[70]</sup>

$$\lambda_{\text{order}} \approx \frac{\pi D}{n_p \sqrt{\left(\frac{z_{\ell v}}{2} \frac{D}{H}\right)^2 + z_{\ell v}^2}} \quad (3)$$

where  $z_{\ell v}$  is the  $v$ th root of the  $\ell$ th Bessel function of the first kind for  $TE$  modes, or its first derivative for  $TM$  modes. For FP modes,  $\ell \neq 0$  and the denominator in Equation (3) displays a strong dependence on the cylinder's aspect ratio  $D/H$ . In contrast, since  $\ell = 0$  for Mie modes, their eigenwavelengths only change with  $D$ . Thus, the eigenwavelengths and the multipolar content of these two mode types are independently tunable, resulting in a flexible control over the resonator's optical response



**Figure 4.** a) Alternative scattering cross section decomposition using the QNM expansion method. The full-wave simulation is nearly the same (without losses), as in Figure 4, but linearly. Colored lines are the individual contributions of the physical QNMs. The contributions of modes having their resonances outside the considered spectral range are added up in the green dashed line. The resonant modes in the considered spectral range are associated with the  $TE_{111}$ ,  $TE_{120}$ , and  $TM_{113}$  modes of an isolated cylinder. The blue line corresponds to the reconstructed scattering cross section, confirming that all the resonant spectral features can be successfully recovered via this method, and demonstrating good agreement near the HA, point HA. b) Spectra of the volume-averaged electromagnetic field energy inside the cylinder and the excited modes (see Section S15, Supporting Information, for a numerical justification of the latter decomposition). Colors and legends are the same as in (a). The electromagnetic energy density has been normalized with respect to the incident electromagnetic energy density in the vacuum  $w_{EM} = \epsilon_0 E_0^2$ . Excellent agreement is obtained with the full-wave simulations. c) Normalized internal electric field distributions of the two most relevant modal contributions near point A, from left to right, associated with Fabry–Perot ( $TM_{113}$ ) and Mie-like ( $TE_{120}$ ) standing wave patterns ( $TE_{111}$  is very weak near the HA), respectively. Their addition via Equation (2), together with the background modes (Bckg.), leads to the reconstruction of the internal fields of the HA, also displayed on the right-hand side of (c). All the electric fields have been normalized with their respective maxima, to enhance their visualization.

and enabling the simultaneous scattering suppression observed in Figures 1a,b, 4a–the HA.

A straightforward comparison between the QNM and multipolar methods allows determining the multipoles radiated by a given QNM (see the Section S9, Supporting Information). Specifically, Figure S5, Supporting Information leads us to conclude that the  $TE_{120}$  mode emits primarily as  $p$ , with a minor  $Q^{(m)}$ . In contrast, the  $TM_{113}$  mode scatters as a combination of  $m$  and  $Q^{(m)}$  (in both cases, referring to both their basic and toroidal counterparts). When scattering from a mode is resonantly suppressed, radiation from the multipoles associated with it is also strongly minimized, and results in the different multipole anapoles observed in the decomposed spectra of Figure 4a. Thus, the close proximity of the destructive interference points of the  $TE_{120}$  and  $TM_{113}$  modes at point HA leads to an overlap of the anapoles of the four dominant multipoles. In this fashion, using the QNM expansion approach, we have shown an alternative and general physical explanation of dark scattering regimes and qualitatively illustrated its link to the particle's multipolar response. This self-

consistent approach will further be effectively applied to understand the physics behind the particle–substrate interaction.

As a final remark, we point out that the quality factors of the  $TE_{120}$  and  $TM_{113}$  modes are, respectively, 12 and 33. A direct comparison with the  $TE_{120}$  supporting a conventional anapole disk (see Section S7, Supporting Information) shows that the mode's quality factor at the HA is more than four times larger, confirming the earlier discussion of Figure 3b. Therefore, we anticipate a much better performance of the HA for second and third harmonic generation processes with respect to conventional EDA disks, since nonlinear scattering cross sections scale linearly with the quality factors of the modes involved.<sup>[71]</sup>

#### 2.4. Hidden Mechanism Inducing the Preservation of the HA for an Arbitrary Dielectric Substrate

We will now illustrate a novel effect in detail, unique to the HA, by which its nonradiating nature can be preserved in the stationary regime when deposited on any dielectric substrate.

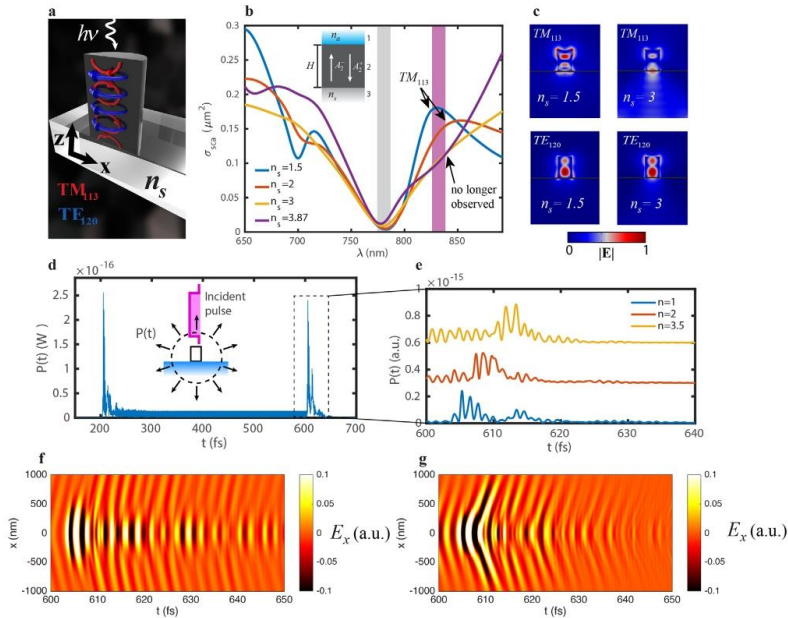


**Figure 5.** Stationary and transient response of the HA with different index contrasts with the substrate. a) Scheme depicting the setup and the excited eigenmodes. b) Comparison between the numerically obtained scattering cross sections for the nanocylinder with the size from Figure 1, deposited on substrates with increasing refractive index. The calculations are performed with the full experimental aSi refractive index given in the Section S13, Supporting Information. Inset of (b): 1D Fabry–Perot model of the  $TM_{113}$  mode. c)  $xz$  field distributions of the QNMs  $TE_{120}$  and  $TM_{113}$  when the cylinder is deposited over substrates with different refractive index. As predicted by our theory, losses from the  $TM_{113}$  mode increase when decreasing the refractive index contrast. Contrarily, the  $TE_{120}$  mode remains confined in the scatterer. Temporal response of the HA under a plane wave square pulse injected at 200 fs with a duration of 400 fs; d) scattered power as a function of time; e) different beating patterns of the decaying eigenmodes after the plane wave excitation as a function of  $n_s$ ; f, g) spatiotemporal maps of the  $x$ -component of the scattered electric field measured along the  $x$  axis for  $n_s = 1$  (f) and  $n_s = 2$  (g), measured from the beginning of the modal decay. The color bars are saturated for better visualization.

The underlying mechanism will be harnessed in the following sections to modulate the transient response of the isolated nanocylinder.

In comparison with any other scattering phenomena including conventional anapoles, the HA is remarkably robust in the presence of a substrate. This particular behavior is illustrated in Figure 5a, where we have plotted the calculated scattering cross sections of the cylinder in free space and deposited over glass ( $n_s = 1.5$ ), hypothetical substrates with  $n_s = 2, 3$  and over amorphous silicon ( $n_s = 3.87$ ). The amplitude and spectral position of the scattering dip are almost undisturbed from the free-space values while the refractive index contrast at the bottom of the particle remains non-zero. However, we observe drastic changes in

the Fano profile's shape, once the contrast is absent (silicon particle over silicon substrate). There is a nontrivial underlying mechanism by which the HA is "protected" against modifications of the substrate refractive index. The physics becomes transparent when examining the distinct nature of the two resonant modes involved in forming the HA (Figure 5c). On the one hand, increasing the substrate refractive index leads to a decrease in the lower wall reflectivity, which is crucial for the standing FP mode  $TM_{113}$  inside the resonator, while approaching  $n_s$  at the particle's refractive index results in a higher energy leak toward the substrate and a substantial decrease in the quality factor  $Q_c$ . Consequently, the resonance flattens and disappears when the lower boundary becomes transparent, as shown in Figure 5b.

The standing wave pattern of the  $TM_{113}$  resembles a 1D FP cavity on a dielectric substrate. The QNMs of this simplified model have the advantage of being analytically solvable,<sup>[55]</sup> thus providing valuable physical insight easy to extrapolate to the problem at hand. As we derive in the Section S11, Supporting Information, the QNMs are formed by two interfering plane waves traveling in opposite directions inside the cavity, when the driving wavelength satisfies the condition

$$r_{21}r_{23}w^2 = 1 \quad (4)$$

where  $w = \exp(ik_z n_s H)$  and  $r_{21}$ ,  $r_{23}$  are the Fresnel reflection coefficients from the cavity–air and the cavity–substrate interfaces, respectively. The quality factor of a QNM with axial index  $\ell$  is calculated as

$$Q_\ell = -\frac{\ell \pi}{\ln(r_{23}r_{21})} \quad (5)$$

Equation (5) serves very well to illustrate the substrate influence on the  $TM_{113}$  mode. When the two reflection coefficients are unity, the energy is completely stored inside the resonator and  $Q_\ell$  is infinite. Similarly, a decrease in the substrate reflection coefficient leads to radiative losses and a decrease in the quality factor, effectively becoming zero when the contrast is absent. Indeed, a lower quality factor leads to less appreciable spectral features, as observed in the simulations (Figure 5b). Another important conclusion can be drawn from the expression of the eigenfrequency  $\nu_\ell$ , given by (see Section S11, Supporting Information):

$$\nu_\ell = \frac{c\ell}{2n_s H} + i\frac{c}{4\pi n_s H} \ln(r_{23}r_{21}) \quad (6)$$

The real part of the resonant wavelength of the QNM is independent of the refractive index at the walls. Thus, modifying  $n_s$  does not shift the spectral position of the resonance (i.e., does not shift the HA wavelength), but simply changes the amplitude and width of the Fano profile.

With proper normalization, and employing the notation of the inset in Figure 5b, the amplitudes of the incoming and outgoing plane waves inside the resonator are  $|A_1^+| = \sqrt{\alpha r_{12}}w$  and  $|A_2^+| = \sqrt{\alpha r_{23}}w$ , with  $\alpha = 1/(4He)$  (see Section S11, Supporting Information for details). Plane waves reflected from the substrate are thus decreased with decreasing index contrast. Consequently, the same occurs with the lower field maxima of the  $TM_{113}$ . While this prediction is observed in the simulations for relatively low contrasts, the behavior at minimal differences is very different (see the case  $n_s = 3$  in Figure 5c). In the latter situation, the standing waves along  $z$  become negligible compared to the initially weaker standing waves in the  $x$ - $y$  plane, and the QNM can only be well described numerically.

Contrarily, it is noteworthy that even comparably small contrast (3–3.87) leads to enough contribution of the  $TE_{120}$  mode to preserve the scattering dip (see Figure 5b). The standing wave pattern of this second mode develops in the lateral walls of the cylinder, and therefore depends much less on variations of the reflectivity of the lower wall, keeping an almost constant quality factor (see Section S10, Supporting information). Most of the QNM energy is then stored in the resonator even in the case of zero ef-

fective contrast with the substrate, as demonstrated in Figure 5c. It results in a larger contribution of the  $TE_{120}$  mode to extinction at small contrasts, and a decrease of radiation from the electric quadrupole and magnetic dipole. The HA is now mainly driven by electric dipole radiation stemming from the  $TE_{120}$  mode (see Figure S6b, Supporting Information). Thus, for large  $n_s$ , the HA degenerates into a conventional EDA, but still retains its non-radiative nature, since the other multipoles become negligible due to the small reflections at the lower wall of the nanocylinder.

## 2.5. Characteristics and Substrate-Mediated Modulations of the Temporal Dynamics of HAs

The QNM theoretical framework is highly suited for quantitative investigations of nanoresonator dynamics under ultrashort pulses.<sup>[54]</sup> While challenging to explore, the effects taking place at the scale of tens of fs are gradually becoming experimentally accessible.<sup>[72,73]</sup> They can result in counterintuitive phenomena challenging to interpret in terms of the multipolar machinery commonly utilized to design the optical response of nanoresonators under continuous wave (CW) illumination.

The study of the temporal dynamics of Fano resonances arising in different photonic systems has been gaining increasing interest recently<sup>[44,57,74]</sup> since the knowledge of both the spatial and temporal structure of the scattered field can enable a more comprehensive understanding of its interaction with matter<sup>[75]</sup> under ultrashort pulses. Among the novel, promising effects, Fano resonances have been shown to display ultrafast energy spikes when illuminated by a pulse with sharp variation.<sup>[75]</sup> Such energy spikes were tentatively associated with the rapid breakdown of the balance between the high and low Q modes whose mutual destructive interference leads to the Fano profile under CW illumination.

While the spikes were predicted in infinite cylindrical scatterers, here we anticipate for the first time their occurrence in a realistic structure in the optical regime. Simultaneously, the coherent interplay between the  $TE_{120}$ ,  $TM_{113}$ , and the background modes induce beating. While this second effect might not seem remarkable at first glance, it opens the possibility to realize ultrafast time modulation of the scattered signal in the transient regime.

To investigate the system's time dynamics, we initially perform a series of numerical experiments (see Figure 5d–g). In the simulations shown in Figure 5d–g, the HA nanoparticle is excited by a plane wave square pulse with duration  $\tau = 400$  fs, (see inset in Figure 5d) sufficiently long to observe both stationary and transient regimes. The scattered power is then plotted in Figure 5d, and a more detailed view of the transient after the pulse is shown in Figure 5e for different refractive index contrasts with the substrate. In all cases, sharp energy spikes occur right after the pulse shut-off. However, the number and shape of the peaks are different for each scenario. Remarkably, regardless of the substrate index, the radiated power in the stationary regime remains negligible due to the mechanism described above. The HA thus behaves very differently in the stationary and transient regimes; while being nonradiative in the stationary regime for any dielectric substrate, in the transient, it emits energy spikes that can be controlled with the underlying substrate.

The latter behavior is also reflected on the recorded spatiotemporal maps of the  $E_x$  field in Figure 5f,g, where the characteristics of the system's beating can be fully grasped. Interestingly, contrary to the conventional Fano resonance,<sup>[57]</sup> we observe the formation of several beatings at the trailing edge of the pulse.

We note that, unlike in ref. [76] for our system, it would be incorrect to trace an analogy with a two-level quantum system to describe the time dynamics, since the optical response of the structure is driven by several eigenmodes (several QNMs). We investigate the system's modal dynamics in detail by calculating the QNM contributions to the scattered field in the time domain via a fast Fourier transform algorithm, following ref. [54]. The scattered field at any point in space can then be written as  $E_{\text{sc}}(r, t) = \sum_{\mu} A_{\mu}(t) \tilde{E}_{\mu}(r)$ , where  $A_{\mu}(t)$  is the contribution of mode labeled with  $\mu$  (see specifics in Section S16, Supporting Information). The calculations demonstrate that, despite the broader content of Fourier harmonics contained in the square pulse, the transient effects at the start and end of the latter are mediated by the same QNMs responsible for the HA in the CW regime (see Figure S11, Supporting Information).

At high contrasts, the  $TM_{1,1}$  mode leaks from the resonator, and a well-defined beating pattern is observed. The beating is even along the  $x$ -axis, reflecting the symmetry of the fields of the dominant modes. At lower contrast, the decreased contribution of the  $TM_{1,1}$  leads to exponential damping, a clear sign of the predominance of a single resonant mode.

To gain insight into the mechanism responsible for the energy spikes, we develop a simple approach to calculate the QNM decomposition of the instantaneous power radiated by the nanoresonator, given by:

$$P(t) = \int_{\partial V^+} \left[ \sum_{\mu} A_{\mu}(t) \tilde{E}_{\mu}(r) \right] \times \left[ \sum_{\mu} A_{\mu}(t) \tilde{H}_{\mu}(r) \right] \cdot dS \quad (7)$$

The integral runs over the resonator's external boundary  $\partial V^+$ . Equation (7) is quite general and can be applied to calculate  $P(t)$  from an arbitrary nanoresonator embedded in an arbitrary non-absorptive, passive environment and illuminated by an arbitrary pulse. The derivation is given in Section S16, Supporting Information. We first reconstruct  $P(t)$  with Equation (7), with a basis of 50 QNMs, obtaining good agreement with FDTD simulations (Figure 6a,b). A mismatch is observed in the amplitude of the two energy spikes, but the calculation successfully reproduces the main features of the transient effects. We attribute the mismatch to a reduced QNM basis and the strong dependence on the finite-element mesh utilized to calculate the modal fields. However, the underlying mechanisms are better understood with a simplified model with three QNMs, corresponding to the resonant  $TE_{1,20}$  and  $TM_{1,1}$ , together with a single background mode. A comparison of this model with the basis with 50 QNMs (including discretized modes of the continuum, so-called PML modes<sup>[55,77]</sup>) is given in Figure S13, Supporting Information.

Interestingly, Equation (7) features interference terms between different QNMs of the form  $\int_{\partial V^+} A_{\mu}(t) A_{\nu}(t) \tilde{E}_{\mu}(r) \times \tilde{H}_{\nu}(r) \cdot dS$ , which play an important role, as shown in Figure 6c (green curve). In the stationary regime, the interference between the  $TM_{1,1}$  and the background mode

results in a negative contribution to the radiated power. On the other hand, the direct terms contribute positively, and the addition of the two results in smaller scattering (destructive interference), in analogy with the classical interpretation with toroidal moments. When the incident pulse is shut-off at 600 fs, the direct terms start decaying exponentially, but the interference terms abruptly become positive. Since the QNMs responsible for the interference terms have very different eigenfrequencies, beating is induced, and as a result, two positive energy peaks appear in the spectra.

We note that the interference terms in vacuum are mainly driven by the interaction of the  $TM_{1,1}$  mode with the background. However, as shown in Figure 5b, the  $TE_{1,20}$  mode increases its overall contribution to scattering when the index contrast with the substrate decreases. A controlled variation of the substrate index can therefore modify the modal content, and consequently modify the number, shape, and amplitude of the energy spikes.

## 2.6. Non-Huygens Transparent Metasurface with Controllable Transients

The potential that transient modulation offers can be fully exploited in practice by fabricating metasurfaces inheriting (and enhancing), the single-particle mechanism described in the previous section.

In particular, the HA can be harnessed to design fully transmissive, all-dielectric metasurfaces without relying on the well-known Huygens condition,<sup>[7,79]</sup> and simultaneously realize controllable ultrafast switching by harnessing transients (see Figure 5a-d). Contrarily to the latter, the light traverses the structure without significant phase variation, thus rendering the metasurface invisible (see shadowed selection in Figure 7b). This is a direct consequence of Equation (1). It can be easily seen by writing the transmission coefficient as a sum of the relevant multipole contributions of the meta-atoms:<sup>[80]</sup>

$$t = 1 + t_p + t_m + t_{Q(m)} + t_{Q(l)} \quad (8)$$

Each term in the previous sum is proportional to the corresponding total multipole moment (basic and toroidal contributions).

When Equation (1) is fulfilled, the multipolar contributions in Equation (8) are zero. Consequently, we are left with  $t \approx 1$  in Equation (8), and the incident wave leaves the system unperturbed (see Figure 7a). This condition is closely fulfilled in a transmission band around the HA wavelength ( $\lambda = 782$  nm as previously), as indicated in Figure 7b. Polarization losses induce absorption, which slightly decreases transmission. The considered period (530 nm) is not unique, that is, once the geometry supporting the HA for an isolated particle is known, a subwavelength metasurface of such particles will mimic the single-particle behavior far away from the first diffraction order.<sup>[81]</sup>

In analogy with the single-particle behavior, the metasurface induces ultrafast beating of the scattered field in the transients at the beginning and the end of a plane wave pulse (see Figure 7c,d). Remarkably, however, the sensitivity to the contrast with the underlying substrate is significantly accentuated, inducing large

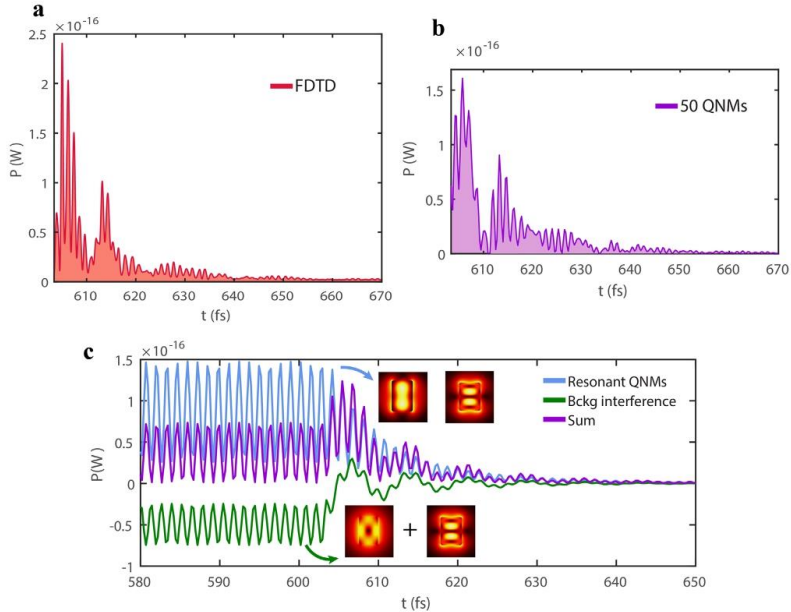


**Figure 6.** Modal decomposition of the radiated power as a function of time. a) FDTD calculations of the radiated power in the transient, for the pulse depicted in Figure 5d (in all the calculations, the cylinder is in the air). b) Reconstruction of the radiated power with 50 QNMs. c) Reduced QNM model with only three QNMs (their normalized electric field norms) also allows reproducing all the essential physics of the system dynamics. The curve captioned “Bckg interference” includes the cross terms between a background mode, identifiable as the well-known magnetic dipole mode,<sup>[78]</sup> and the resonant  $TM_{113}$  mode. The curve captioned “Resonant QNMs” consists of the direct terms of the  $TM_{113}$  and  $TE_{120}$  modes. “Sum” corresponds to the addition of the direct and interference terms. The colored arrows indicate which QNMs have been used to calculate each curve.

changes in the modulated scattered signal with an increase of  $n_s$  of only 0.2.

The sub-ps relaxation times of the metasurface, together with the high sensitivity of the transients to the substrate index opens an exciting pathway toward the spatiotemporal control of ultra-fast dynamic effects. Among the interesting perspectives, ultra-short laser pulses can be effectively modulated in time by tailoring the transient phenomena. The high substrate sensitivity can be exploited to dynamically tune the transient response of the metasurface in different temporal regimes by selecting the appropriate modulation technology.<sup>[82]</sup> The bulk refractive index of the substrate can be tuned, for example, using phase-change materials such as GeTe<sup>[83]</sup> using temperature as a control parameter. More sophisticated, yet much faster refractive index changes could be achieved by tuning optical nonlinearities arising in the substrate as a function of the incident beam intensity (e.g., if

ITO constitutes the underlying substrate<sup>[84]</sup>). Finally, modifying the free electron density in the substrate with electrical gating<sup>[85]</sup> might be a promising approach to achieve the desired tunability in practical applications.

### 3. Discussion

In the stationary regime, we have theoretically predicted and experimentally confirmed the existence of HA, previously unnoticed non-scattering regimes requiring the simultaneous destructive interference of electric and magnetic Cartesian multipoles with their toroidal counterparts. Remarkably, only two design parameters are necessary to spectrally overlap four multipole anapoles. This counterintuitive behavior is explained by a careful analysis of the eigenmodes, which confirms that breaking the spherical symmetry leads to additional conditions linking the



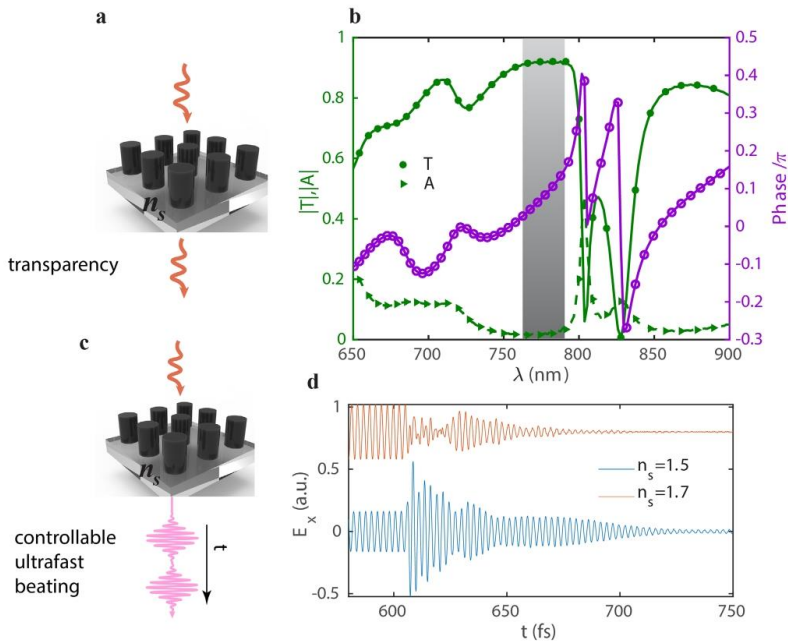


**Figure 7.** Design of a subwavelength HA-based metasurface, featuring dual functionality in the stationary and ultrafast regimes. The period is set to 530 nm. a) artistic representation of the proposed metasurface operating at the HA in the stationary regime. The structure is illuminated by an x-polarized plane wave, passing through the array completely undistorted. b) Transmission, absorption, and phase of the transmitted wave with respect to the incident one. As predicted by Equations (1) and (8), the out-of-phase basic and toroidal moments induce a transparency band with minimal phase perturbation (shaded region). The calculations have been performed in the presence of a substrate with  $n_s = 1.5$ . c) Artistic representation illustrating the metasurface response in the sub-ps regime, when excited by a plane wave pulse. d)  $E_x$  component of the scattered field from the metasurface as a function of time at the end of the plane wave pulse, for  $n_s = 1.5$  and after increasing the substrate index by 0.2. The results demonstrate that transient oscillations of the metasurface are highly sensitive to changes in the substrate index, opening a pathway toward tunable ultrafast beating.

electric and magnetic anapoles to the same QNM. For the first time, quadrupole anapoles and magnetic anapoles have been confirmed experimentally in isolated subwavelength nanoparticles. To broaden our knowledge of anapole electrostatics beyond the electric dipole approximation, we have developed a solid physical picture regarding the fundamental eigenmodes driving the resonator response. Magnetic anapoles and quadrupole anapoles display field confinements several times larger than electric anapoles, promising higher enhancements of nonlinearities in the absence of linear scattering. In Section S18, Supporting Information, we also demonstrate the possibility to obtain the HA regime under illumination by a focused Gaussian beam possessing orbital angular momentum. Theoretically, the HA, unlike a conventional nanoantenna, should not experience

any torque nor net force, an “unmovable” object. This could open interesting opportunities for optical manipulation.

In the transient regime, the developed QNM analysis has allowed us to design at will the breakdown of the HA conditions to obtain ultrafast modulation of the scattered power. The present theory shows that efficient spatiotemporal control of the transients mediated by the underlying substrate can be achieved while maintaining scattering in the stationary regime at the vanishing level. Following the established theoretical guidelines, we propose and verify numerically a non-Huygens, subwavelength metasurface obeying the same principles and therefore featuring a double functionality: i) substrate-independent full transparency in both amplitude and phase mediated by the HA in the stationary regime, and ii) ultrafast, substrate-dependent signal

modulation in the transient regime, mediated by its breakdown. The necessary changes in the substrate refractive index to observe appreciable modifications of the transient response of the metasurface are well in the range of available technologies for dynamic tuning,<sup>[8,31]</sup> drastically expanding the available degrees of freedom.

Therefore, combining our findings with up-to-date modulation techniques holds great promise for future applications in the emerging field of ultrafast dynamic nanophotonics. Remarkably, the ultrashort scattering peaks arising at the transient can be used to enhance ultrafast nonlinearities<sup>[74]</sup> (e.g., single-particle lasing) or coded in terms of their intensity as a function of the substrate index to realize light-based computing.<sup>[86]</sup>

Finally, the proposed non-Huygens metasurface can enable the temporal/spectral shaping of fs laser pulses by interfering the latter with the outgoing scattered signal.

### Supporting Information

Supporting Information is available from the Wiley Online Library or from the author.

### Acknowledgements

The research reported in this publication was supported by the Russian Foundation for Basic Research (Project no. 20-02-00086, 20-52-00031) and the Moscow Engineering Physics Institute Academic Excellence Project (agreement with the Ministry of Education and Science of the Russian Federation of 27 August 2013, Project no. 02.a03.21.0005) for the modeling of the resonant light scattering and computer simulation. The contribution of the Russian Science Foundation for the time-domain calculations (Project no. 21-12-00151) and the provision of user facilities (Project no. 19-72-30012) is also acknowledged. A.B.E. acknowledges the support from the Deutsche Forschungsgemeinschaft (DFG, German Research Foundation) within the Cluster of Excellence PhoenixD (EXC 2122, Project ID 390833453). M.R. acknowledges support from the UK Research and Innovation Future Leaders Fellowship (MR/T040513/1).

### Conflict of Interest

The authors declare no conflict of interest.

### Data Availability Statement

The data that supports the findings of this study are available in the Supporting Information of this article.

### Keywords

all-dielectric nanophotonics, dynamic toroidal moments, metasurfaces, nonradiating sources, ultrafast phenomena

Received: February 26, 2021

Revised: May 24, 2021

Published online:

[1] S. M. Kamali, E. Arbabi, A. Arbabi, A. Faraon, *Nanophotonics* **2018**, *7*, 1041.

[2] M. L. Brongersma, *Nanophotonics* **2020**, *10*, 643.  
 [3] D. G. Baranov, D. A. Zuev, S. I. Lepeshov, O. V. Kotov, A. E. Krasnok, A. B. Evlyukhin, B. N. Chichkov, *Optica* **2017**, *4*, 814.  
 [4] S. Liu, M. B. Sinclair, S. Saravi, G. A. Keeler, Y. Yang, J. Reno, G. M. Peake, F. Setzpfandt, I. Staude, T. Pertsch, I. Brener, *Nano Lett.* **2016**, *16*, 5426.  
 [5] R. S. Savelev, D. S. Filonov, P. V. Kapitanova, A. E. Krasnok, A. E. Miroschnichenko, P. A. Belov, Y. S. Kivshar, *Appl. Phys. Lett.* **2014**, *105*, 181116.  
 [6] R. M. Bakker, Y. F. Yu, R. Paniagua-Domínguez, B. Luk'yanchuk, A. I. Kuznetsov, *Nano Lett.* **2017**, *17*, 3458.  
 [7] Y. H. Fu, A. I. Kuznetsov, A. E. Miroschnichenko, Y. F. Yu, B. Luk'yanchuk, *Nat. Commun.* **2013**, *4*, 1527.  
 [8] K. Chen, Y. Feng, F. Monticone, J. Zhao, B. Zhu, T. Jiang, L. Zhang, Y. Kim, X. Ding, S. Zhang, A. Alù, C. W. Qiu, *Adv. Mater.* **2017**, *29*, 1606422.  
 [9] K. Koshelev, S. Kruk, E. Melik-Gaykazyan, J. H. Choi, A. Bogdanov, H. G. Park, Y. Kivshar, *Science* **2020**, *367*, 288.  
 [10] A. S. Shalin, *Quantum Electron.* **2010**, *40*, 1004.  
 [11] P. M. Voroshilov, C. R. Simovski, P. A. Belov, A. S. Shalin, *J. Appl. Phys.* **2015**, *117*, 203101.  
 [12] Y. Cui, D. van Dam, S. A. Mann, N. J. J. van Hoof, P. J. van Veldhoven, E. C. Garnett, E. P. A. M. Bakkers, J. E. M. Haverkort, *Nano Lett.* **2016**, *16*, 6467.  
 [13] P. D. Terekhov, K. V. Baryshnikova, Y. Greenberg, Y. H. Fu, A. B. Evlyukhin, A. S. Shalin, A. Karabchevsky, *Sci. Rep.* **2019**, *9*, 3438.  
 [14] J. Algorri, D. Zografopoulos, A. Ferraro, B. García-Cámara, R. Vergaz, R. Beccherelli, J. Sánchez-Pena, *Nanomaterials* **2018**, *9*, 30.  
 [15] S. Jahani, Z. Jacob, *Nat. Nanotechnol.* **2016**, *11*, 23.  
 [16] H. K. Shamkhi, K. V. Baryshnikova, A. Sayanskiy, P. Kapitanova, P. D. Terekhov, P. Belov, A. Karabchevsky, A. B. Evlyukhin, Y. Kivshar, A. S. Shalin, *Phys. Rev. Lett.* **2019**, *122*, 193905.  
 [17] D. Wang, Q. Fan, J. Wang, Z. Zhang, Y. Liang, T. Xu, *Guangdian Gongcheng/Opto-Electron. Eng.* **2017**, *44*, 103.  
 [18] A. Canós Valero, D. Kislov, E. A. Gurvitz, H. K. Shamkhi, A. A. Pavlov, D. Redka, S. Yankin, P. Zemánek, A. S. Shalin, *Adv. Sci.* **2020**, *7*, 1903049.  
 [19] P. Grahn, A. Shevchenko, M. Kaivola, *New J. Phys.* **2012**, *14*, 093033.  
 [20] R. Alaei, C. Rockstuhl, I. Fernandez-Corbaton, *Opt. Commun.* **2018**, *407*, 17.  
 [21] A. B. Evlyukhin, T. Fischer, C. Reinhardt, B. N. Chichkov, *Phys. Rev. B* **2016**, *94*, 205434.  
 [22] R. E. Raab, O. L. Lange, *Multipole Theory in Electromagnetism*, Oxford Science Publications, New York **2004**.  
 [23] J. D. Jackson, *Classical Electrodynamics*, 3rd ed., Wiley, New York **1999**.  
 [24] N. Papisimakis, V. A. Fedotov, V. Savinov, T. A. Raybould, N. I. Zheludev, *Nat. Mater.* **2016**, *15*, 263.  
 [25] V. M. Dubovik, V. V. Tugushev, *Phys. Rep.* **1990**, *187*, 145.  
 [26] A. T. Góngora, E. Ley-Koo, *Rev. Mex. Fis. E* **2006**, *52*, 188.  
 [27] V. A. Fedotov, A. V. Rogacheva, V. Savinov, D. P. Tsai, N. I. Zheludev, *Sci. Rep.* **2013**, *3*, 2967.  
 [28] N. A. Nemkov, A. A. Basharin, V. A. Fedotov, *Phys. Rev. A* **2018**, *98*, 023858.  
 [29] E. A. Gurvitz, K. S. Ladutenko, P. A. Dergachev, A. B. Evlyukhin, A. E. Miroschnichenko, A. S. Shalin, *Laser Photonics Rev.* **2019**, *13*, 1800266.  
 [30] J. S. Toterogongora, A. E. Miroschnichenko, Y. S. Kivshar, A. Fratallocchi, *Nat. Commun.* **2017**, *8*, 15535.  
 [31] A. A. Basharin, V. Chuguevsky, N. Volsky, M. Kafesaki, E. N. Economou, *Phys. Rev. B* **2017**, *95*, 035104.  
 [32] T. Xiang, T. Lei, X. Huang, Z. Shen, H. Yang, *Appl. Phys. Express* **2018**, *11*, 2.  
 [33] P. D. Terekhov, K. V. Baryshnikova, A. S. Shalin, A. Karabchevsky, A. B. Evlyukhin, *Opt. Lett.* **2017**, *42*, 835.

- [34] A. E. Miroshnichenko, A. B. Evlyukhin, Y. F. Yu, R. M. Bakker, A. Chipouline, A. I. Kuznetsov, B. Luk'yanchuk, B. N. Chichkov, Y. S. Kivshar, *Nat. Commun.* **2015**, 6, 1.
- [35] K. Baryshnikova, D. Filonov, C. Simovski, A. Evlyukhin, A. Kadochkin, E. Nenasheva, P. Ginzburg, A. S. Shalin, *Phys. Rev. B* **2018**, 98, 165419.
- [36] L. Hüttenhofer, F. Eckmann, A. Lauri, J. Cambiasso, E. Pensa, Y. Li, E. Cortés, I. D. Sharp, S. A. Maier, *ACS Nano* **2020**, 14, 2456.
- [37] D. G. Baranov, R. Verre, P. Karpinski, M. Käll, *ACS Photonics* **2018**, 5, 2730.
- [38] R. Verre, D. G. Baranov, B. Munkhbat, J. Cuadra, M. Käll, T. Shegai, *Nat. Nanotechnol.* **2019**, 14, 679.
- [39] L. Xu, M. Rahmani, K. Zangeneh Kamali, A. Lampranidis, L. Ghirardinii, J. Sautter, R. Camacho-Morales, H. Chen, M. Parry, I. Staudé, G. Zhang, D. Neshev, A. E. Miroshnichenko, *Light Sci. Appl.* **2018**, 7, 44.
- [40] G. Grinblat, Y. Li, M. P. Nielsen, R. F. Oulton, S. A. Maier, *Nano Lett.* **2016**, 16, 4635.
- [41] T. Shibamura, G. Grinblat, P. Albella, S. A. Maier, *Nano Lett.* **2017**, 17, 2647.
- [42] S. V. Makarov, M. I. Petrov, U. Zywiets, V. Milichko, D. Zuev, N. Lopantsyna, A. Kuksin, I. Mukhin, G. Zograf, E. Ubyivovk, D. A. Smirnova, S. Starikov, B. N. Chichkov, Y. S. Kivshar, *Nano Lett.* **2017**, 17, 3047.
- [43] A. Kaldun, A. Blättermann, V. Stooß, S. Donsa, H. Wei, R. Pazourek, S. Nagele, C. Ott, C. D. Lin, J. Burgdörfer, T. Pfeifer, *Science* **2016**, 354, 738.
- [44] S. Lepeshov, A. Krasnok, *Optica* **2020**, 7, 1024.
- [45] W. Liu, B. Lei, J. Shi, H. Hu, A. E. Miroshnichenko, *J. Nanomater.* **2015**, 2015, 382.
- [46] W. Liu, J. Zhang, B. Lei, H. Hu, A. E. Miroshnichenko, *Opt. Lett.* **2015**, 40, 2293.
- [47] J. Tian, H. Luo, Y. Yang, F. Ding, Y. Qu, D. Zhao, M. Qiu, S. I. Bozhevolnyi, *Nat. Commun.* **2019**, 10, 1.
- [48] A. K. Osipanova, I. V. Stenishchev, A. A. Basharin, *Laser Photonics Rev.* **2018**, 12, 1800005.
- [49] S. A. Maier, M. P. Nielsen, G. Grinblat, Y. Li, R. F. Oulton, *ACS Nano* **2016**, 11, 953.
- [50] Z.-J. Yang, Y.-H. Deng, Y. Yu, J. He, *Nanoscale* **2020**, 12, 10639.
- [51] B. Luk'yanchuk, R. Paniagua-Domínguez, A. I. Kuznetsov, A. E. Miroshnichenko, Y. S. Kivshar, *Phys. Rev. A* **2017**, 95, 063820.
- [52] A. K. Osipanova, A. Basharin, A. E. Miroshnichenko, B. Luk'yanchuk, *Opt. Mater. Express* **2021**, 11, 23.
- [53] E. A. Gurvitz, K. S. Ladutenko, P. A. Dergachev, A. B. Evlyukhin, A. E. Miroshnichenko, A. S. Shalin, *Laser Photonics Rev.* **2019**, 13, 1800266.
- [54] W. Yan, R. Faggiani, P. Lalanne, *Phys. Rev. B* **2018**, 97, 205422.
- [55] P. Lalanne, W. Yan, K. Vynck, C. Sauvan, J. P. Hugonin, *Laser Photonics Rev.* **2018**, 12, 1700113.
- [56] M. I. Tribelsky, A. E. Miroshnichenko, *Phys. Rev. A* **2019**, 100, 053824.
- [57] O. Ávalos-Ovando, L. V. Besteiro, Z. Wang, A. O. Govorov, *Nanophotonics* **2020**, 9, 3587.
- [58] M. I. Tribelsky, A. E. Miroshnichenko, *Phys. Rev. A* **2016**, 93, 053837.
- [59] L. Wei, Z. Xi, N. Bhattacharya, H. P. Urbach, *Optica* **2016**, 3, 799.
- [60] S. Gladyshev, K. Frizlyuk, A. Bogdanov, *Phys. Rev. B* **2020**, 102, 075103.
- [61] E. Takou, A. C. Tasolamprou, O. Tsilipakos, E. N. Economou, *Phys. Rev. B* **2019**, 100, 085431.
- [62] J. A. Parker, H. Sugimoto, B. Coe, D. Eggema, M. Fujii, N. F. Scherer, S. K. Gray, U. Manna, *Phys. Rev. Lett.* **2020**, 124, 097402.
- [63] V. A. Zenin, S. M. Novikov, Y. Yang, B. N. Chichkov, S. I. Bozhevolnyi, A. B. Evlyukhin, R. Malureanu, A. V. Lavrinenko, *Nano Lett.* **2017**, 17, 7152.
- [64] K. Zhang, D. Li, *Electromagnetic Theory for Microwaves and Optoelectronics*, Springer, Berlin **2008**.
- [65] M. I. Tribelsky, A. E. Miroshnichenko, *Phys. Rev. A* **2019**, 100, 053824.
- [66] M. F. Limonov, M. V. Rybin, A. N. Poddubny, Y. S. Kivshar, *Nat. Photonics* **2017**, 11, 543.
- [67] B. Hopkins, A. N. Poddubny, A. E. Miroshnichenko, Y. S. Kivshar, *Phys. Rev. A* **2013**, 88, 053819.
- [68] Y. Yang, A. E. Miroshnichenko, S. V. Kostinski, M. Odit, P. Kapitanova, M. Qiu, Y. S. Kivshar, *Phys. Rev. B* **2017**, 95, 165426.
- [69] A. A. Bogdanov, K. L. Koshelev, P. V. Kapitanova, M. V. Rybin, S. A. Gladyshev, Z. F. Sadrieva, K. B. Samusev, Y. S. Kivshar, M. F. Limonov, *Adv. Photonics* **2019**, 1, 016001.
- [70] R. F. Harrington, *Time-Harmonic Electromagnetic Fields*, Wiley, New York **2001**.
- [71] C. Gigli, T. Wu, G. Marino, A. Borne, G. Leo, P. Lalanne, *ACS Photonics* **2020**, 7, 1197.
- [72] Y. Qin, B. Ji, X. Song, J. Lin, *Appl. Phys. B Lasers Opt.* **2019**, 125, 1.
- [73] J. Kim, E. G. Carnemolla, C. DeVault, A. M. Shaltout, D. Faccio, V. M. Shalaev, A. V. Kildishev, M. Ferrera, A. Boltasseva, *Nano Lett.* **2018**, 18, 740.
- [74] S. E. Syakhovskiy, V. V. Temovski, M. I. Tribelsky, *Opt. Express* **2019**, 27, 23894.
- [75] N. Maccaferri, S. Meuret, N. Kornienko, D. Jariwala, *Nano Lett.* **2020**, 20, 5593.
- [76] M. Zhang, C. Wang, Y. Hu, A. Shams-Ansari, T. Ren, S. Fan, M. Lončar, *Nat. Photonics* **2019**, 13, 609.
- [77] B. Vial, F. Zolla, A. Nicolet, M. Commandré, *Phys. Rev. A* **2014**, 89, 023829.
- [78] A. I. Kuznetsov, A. E. Miroshnichenko, M. L. Brongersma, Y. S. Kivshar, B. Luk'yanchuk, *Science* **2016**, 354, aag2472.
- [79] H. T. Chen, A. J. Taylor, N. Yu, *Rep. Prog. Phys.* **2016**, 79, 076401.
- [80] P. D. Terekhov, V. E. Babicheva, K. V. Baryshnikova, A. S. Shalin, A. Karabchevsky, A. B. Evlyukhin, *Phys. Rev. B* **2019**, 99, 45424.
- [81] F. J. García de Abajo, *Rev. Mod. Phys.* **2007**, 79, 1267.
- [82] A. M. Shaltout, V. M. Shalaev, M. L. Brongersma, *Science* **2019**, 364, eaat3100.
- [83] S. Lepeshov, A. Krasnok, A. Alù, *ACS Photonics* **2019**, 6, 2126.
- [84] M. Z. Alam, I. De Leon, R. W. Boyd, *Science* **2016**, 352, 795.
- [85] Y. W. Huang, H. W. H. Lee, R. Sokhoyan, R. A. Pala, K. Thyagarajan, S. Han, D. P. Tsai, H. A. Atwater, *Nano Lett.* **2016**, 16, 5319.
- [86] X.-Y. Xu, X.-L. Huang, Z.-M. Li, J. Gao, Z.-Q. Jiao, Y. Wang, R.-J. Ren, H. P. Zhang, X.-M. Jin, *Sci. Adv.* **2020**, 6, eaay5853.

**2-PAPER:** Nanovortex-driven all-dielectric optical diffusion boosting and sorting concept for lab-on-a-chip platforms

Canós Valero A., Kislov D., Gurvitz E.A., Shamkhi H.K., Pavlov A.A., Redka D., Yankin S., Zemánek P., Shalin A.S., “Nanovortex-Driven All-Dielectric Optical Diffusion Boosting and Sorting Concept for Lab-on-a-Chip Platforms”, (2020) *Advanced Science*, 7 (11), art. no. 1903049, DOI: [10.1002/adv.201903049](https://doi.org/10.1002/adv.201903049)

# Nanovortex-Driven All-Dielectric Optical Diffusion Boosting and Sorting Concept for Lab-on-a-Chip Platforms

Adrià Canós Valero,\* Denis Kislov, Egor A. Gurvitz, Hadi K. Shamkhi, Alexander A. Pavlov, Dmitrii Redka, Sergey Yankin, Pavel Zemánek, and Alexander S. Shalin\*

The ever-growing field of microfluidics requires precise and flexible control over fluid flows at reduced scales. Current constraints demand a variety of controllable components to carry out several operations inside microchambers and microreactors. In this context, brand-new nanophotonic approaches can significantly enhance existing capabilities providing unique functionalities via finely tuned light–matter interactions. A concept is proposed, featuring dual on-chip functionality: boosted optically driven diffusion and nanoparticle sorting. High-index dielectric nanoantennae is specially designed to ensure strongly enhanced spin–orbit angular momentum transfer from a laser beam to the scattered field. Hence, subwavelength optical nanovortices emerge driving spiral motion of plasmonic nanoparticles via the interplay between curl–spin optical forces and radiation pressure. The nanovortex size is an order of magnitude smaller than that provided by conventional beam-based approaches. The nanoparticles mediate nanoconfined fluid motion enabling moving-part-free nanomixing inside a microchamber. Moreover, exploiting the nontrivial size dependence of the curled optical forces makes it possible to achieve precise nanoscale sorting of gold nanoparticles, demanded for on-chip separation and filtering. Altogether, a versatile platform is introduced for further miniaturization of moving-part-free, optically driven microfluidic chips for fast chemical analysis, emulsion preparation, or chemical gradient generation with light-controlled navigation of nanoparticles, viruses or biomolecules.

## 1. Introduction

Micro-optofluidics represents one of the most promising and fast growing fields in current state-of-the-art science and engineering.<sup>[1–7]</sup> In particular, the control of fluid flows in micro-sized channels plays an essential role for applications ranging

from the transport of reduced amounts of hazardous or costly substances and DNA biochip technology, to miniaturized analytical and synthetic chemistry.<sup>[8–12]</sup>

The multidisciplinary nature of microfluidics has brought together seemingly unrelated fields, such as electrical and mechanical engineering, biology, chemistry, and optics. For example, in the context of chemical engineering, the utilization of distributed microreactors working in parallel can enhance production significantly and facilitates the design of new products.<sup>[13,14]</sup> However, slow mixing processes constitute a bottleneck that restricts reaction processes, especially when the desired reaction rate is high.<sup>[15,16]</sup> For this purpose, fast mixing is highly required to avoid the reactive process being delayed by this critical step, and to reduce potential side products.<sup>[16]</sup>

Given the low Reynolds numbers at which fluid flow occurs in microreactors, fluid mixing represents a significant challenge.<sup>[4,17,18]</sup> In the most conventional situation where only passive mixing happens, the main driving mechanism corresponds to diffusion (Brownian motion<sup>[4]</sup>), implying mixing to take place at a very low rate. Consequently, the effective distance that the molecules of a fluid need to travel in a mixer before interacting with another fluid (i.e., the mixing length) becomes restrictively long.<sup>[18]</sup> Passive mixers depend solely on decreasing the mixing length by optimizing the flow channel geometry in order to

A. Canós Valero, Dr. D. Kislov, E. A. Gurvitz, H. K. Shamkhi, Dr. A. S. Shalin  
ITMO University  
Kronverksky prospect 49, St. Petersburg 197101, Russia  
E-mail: adria.canos@optomech.ifmo.ru; alexandesh@gmail.com  
Dr. A. A. Pavlov  
Institute of Nanotechnology of Microelectronics of the Russian Academy of Sciences (INME RAS)  
Nagatinskaya Street, House 16A, Building 11, Moscow 119991, Russia

Dr. D. Redka  
Electrotechnical University “LETI” (ETU)  
5 Prof. Popova Street, Saint Petersburg 197376, Russia  
S. Yankin  
LLC COMSOL  
Bolshaya Sadovaya St. 10, Moscow 123001, Russia  
Prof. P. Zemánek  
Czech Academy of Sciences  
Institute of Scientific Instruments  
Královopolská 147, Brno 612 64, Czech Republic

 The ORCID identification number(s) for the author(s) of this article can be found under <https://doi.org/10.1002/adv.201903049>.

© 2020 The Authors. Published by WILEY-VCH Verlag GmbH & Co. KGaA, Weinheim. This is an open access article under the terms of the Creative Commons Attribution License, which permits use, distribution and reproduction in any medium, provided the original work is properly cited.

DOI: 10.1002/adv.201903049

facilitate diffusion.<sup>[4,19]</sup> In contrast, active schemes rely on external sources injecting energy into the flow in order to accelerate mixing and diffusion processes and drastically decrease the mixing lengths.<sup>[17,20]</sup>

Most early studies related to micromixers have been focused on the passive type. Conversely, despite their higher cost and complex fabrication methods, the enhanced efficiency of active micromixers with respect to passive ones has drawn the attention of the scientific community in the recent years.<sup>[17]</sup> Because of the power and size constraints involved in microfluidics, research efforts have been focused on the utilization of mixing principles not involving moving mechanical parts such as surface tension-driven flows,<sup>[21]</sup> ultrasound and acoustically induced vibrations,<sup>[22,23]</sup> and electro- and magnetohydrodynamic action.<sup>[18,24]</sup>

Given the small operation scales of microfluidics, micron-scale focusing of laser beams, as well as different types of light-matter interactions make possible to provide sufficiently strong optical forces to propel particles,<sup>[25–27]</sup> sort objects according to their size or optical properties,<sup>[5,28–31]</sup> or self-arrange colloidal particles into optically bound structures.<sup>[25–27,32,33]</sup> Nowadays the additional degrees of freedom offered by complex shaping of laser beams<sup>[34–38]</sup> have made possible the manipulation and trapping of large amounts of microparticles.<sup>[39]</sup> In particular, they allow to create optical vortices with helical phase front (e.g., Laguerre–Gaussian or higher-order Bessel beams) carrying both linear and angular momentum.<sup>[40,41]</sup> When such an optical microvortex is scattered by particles, it induces an optical torque on them leading to their orbital motion around the focus of the laser beam.<sup>[42]</sup> Due to the angular momentum conservation, elastic scattering of a circularly polarized beam possessing spin–angular momentum (SAM),<sup>[43]</sup> by optically anisotropic<sup>[44–46]</sup> or nonspherical objects<sup>[47,48]</sup> leads to their spinning around the direction of propagation of the incident illumination. Combining both types of optical angular momentum leads to complex spin–orbital interaction<sup>[41,49]</sup> and novel interesting phenomenon, e.g. detection of spin forces.<sup>[50,51]</sup>

At the nanoscale, metal-based plasmonics dominates and provides exciting means for trapping and manipulating nano-

objects.<sup>[52–55]</sup> On the other hand, the recently growing field of all-dielectric nanophotonics<sup>[56]</sup> presents itself as a promising alternative for the integration of optomechanical concepts in microfluidic devices. Properly designed dielectric nanostructures with finely tuned Mie resonant response provide the means for tailoring electric and magnetic components of the scattered light.<sup>[56–58]</sup> They allow to obtain strong near fields, which induce substantial optical forces acting upon other subwavelength scatterers dispersed in the medium surrounding the nanostructure.<sup>[59–63]</sup>

In this work, we focus on the conversion of SAM of an incident circularly polarized plane wave into orbital angular momentum (OAM)<sup>[64,65]</sup> of the scattered field mediated by a specially designed nanostructure constituted of a realistic high refractive index material (silicon). In contrast to the above-mentioned methods, the optical vortex field created in this way is very localized, only reaching a few hundreds of nanometers in diameter. Moreover, the induced optical forces are strong enough to propel gold (Au) nanoparticles of particular sizes along spiral trajectories around the nanostructure. Based on the latter effect, we propose a novel method for mixing fluid in nanovolumes mediated by chemically inert Au nanoparticles (see Figure 1a). In addition, we take advantage of the size sensitivity of the Au polarizability to achieve light-mediated nanoparticle separation by means of the same geometrical configuration (see Figure 1b). The subwavelength size of the investigated optical nanovortex greatly enhances the length scale of interaction in comparison to the more conventional approaches involving Bessel beams,<sup>[66,67]</sup> opening new directions in light-matter interaction via light angular momentum exchange. We believe that the proposed simple geometry for optically driven diffusion boosting and nanoparticle sorting is of high interest for a plethora of applications in microfluidics and lab-on-a-chip devices.

## 2. Formation of an Optical Nanovortex

The spiral motion of nano-objects in an optical nanovortex driven by an out-of-plane light source (Figure 1a) requires, on

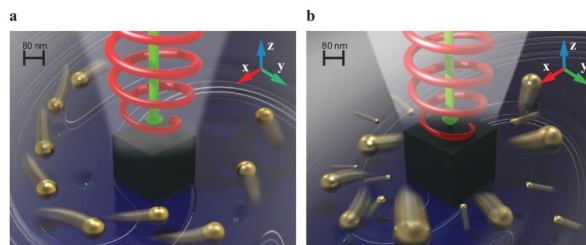


**Figure 1.** An artistic view of the proposed active nanomixing scheme (left) and radial separation of nanoparticles (right). a) A silicon nanocube submerged in a water solution is illuminated by a circularly polarized laser beam coming from the top. The scattered field carries a nonzero tangential component of the pointing vector in the  $xy$  plane, which induces nonzero orbital angular momentum in the negative  $z$  direction. The same effect causes the spiral motion of Au nanoparticles around the nanocube. Viscous friction between the moving nanoparticles and the fluid gives rise to convective fluid motion and enhances fluid mixing. b) Sorting concept. Nanoparticles of different sizes having opposite signs of the real part of polarizability are radially displaced in opposite directions—the smaller ones move toward the nanocube, while larger ones move away from it.

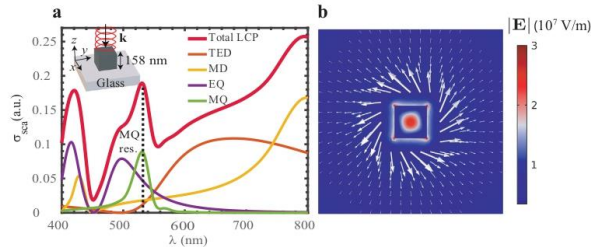


**Figure 2.** a) Cartesian multipole decomposition of the scattering cross-section of the silicon cube deposited on a glass substrate, centered at the origin of the coordinate system; the cube is illuminated by a left-hand circularly polarized plane wave propagating against the  $z$ -axis. The geometry is illustrated in the top inset and the ambient medium is water. The dashed black line indicates the position of the resonant MQ mode [green laser, 532 nm]. The total scattered power with incident LCP illumination (total LCP) is fully reconstructed as the sum of contributions of individual multipoles, respectively, the total electric dipole (TED), magnetic dipole (MD), electric quadrupole (EQ), and the MQ. b) Colorplot denotes the norm of the total electric field at 532 nm wavelength in the transverse  $x$ - $y$  plane at  $z = 70$  nm. The arrows indicate direction and their lengths illustrate the relative size of the transverse part of the scattered Poynting vector. The parameters of the cube are given in Table S1, Supporting Information.

the one hand, efficient transformation of SAM of light to in-plane OAM of the highly confined near fields of the nanocube, which, in turn, should be transferred to the surrounding nanoparticles. Therefore, as a first constraint, sufficient in-plane scattering from the nanocube should take place. This urgent functionality could be enabled, in particular, by the recently observed Transverse Kerker Effect<sup>[66]</sup> allowing for lateral-scattering only. On the other hand, azimuthal forces arising due to helicity inhomogeneities in the scattered near field (curl-spin forces<sup>[69]</sup>) may also enable rotational motion. Hereinafter, we optimize both effects taking into account that we, actually, do not require the total suppression of forward and backward scattering as in<sup>[68]</sup> and, therefore, we can tune the parameters in order to obtain an enhanced optical subwavelength vortex.

A cubical Si nanoantenna with refractive index  $n = 4$  (e.g., silicon at the visible range) and edge 158 nm is illuminated by a circularly polarized plane wave propagating along the negative  $z$ -axis (see inset of Figure 2a). For such an incident field one can calculate the angular momentum flux density using the expressions for paraxial waves.<sup>[70]</sup> Since the wave carries no OAM, the total angular momentum flux density is entirely given by the SAM flux density (see the Supporting Information):

$$J_z^{\text{inc}} = \sigma \frac{I_0}{\omega} \quad (1)$$

where the wave helicity  $\sigma$  takes the values of +1 and -1 for left and right-circular polarization, respectively, and  $I_0$  is the incident light intensity. Since the nanostructure has negligible losses, the total angular momentum of the incident and scattered light is conserved. This conservation law for the total angular momentum implies that part of the incident SAM, given by Equation (1), is transferred to both SAM and OAM of the scattered field leading to spin-orbit coupling phenomena.

The transverse components of the Poynting vector in the field scattered by the nanocube display similar rotating features as for chiral scatterers such as helices or gammadion-like

structures.<sup>[71–73]</sup> however the fabrication process of the first is much less complex and no chirality is required. In order to gain better physical insight, we consider the multipole decomposition for the scattering cross-section of the nanocube deposited over a glass substrate (Figure 2a) and illuminated with LCP light in a water host environment (refractive index  $n_w = 1.335$ ). A careful analysis reveals the most pronounced vortex-like energy flux arises at the magnetic quadrupole (MQ) resonance (Figures 2a,b). Moreover, varying the size of the nanocube, we are able to modify the multipolar response of the resonator in order to position the MQ resonance at the vacuum wavelength 532 nm (399 nm in water) corresponding to the most convenient green laser source (see Table S1, Supporting Information, for the relevant parameters). Hereinafter we will proceed with these values, however, we should note that an even more enhanced MQ response can be obtained in a free space environment (see the Supporting Information).

The MQ mode presents a high signal-to-noise-ratio with respect to the other leading multipoles; the magnetic dipole is almost one order of magnitude smaller and the electric quadrupole is out of resonance. The electric dipole radiation is also strongly suppressed by an anapole state in the vicinity of the MQ resonant frequency. Thus, well-pronounced MQ fields can be obtained driving the vorticity of the Poynting vector<sup>[74]</sup> (Figure 2b) (see also the Supporting Information).

While the numerical results shown in Figure 2 provide a clear link between the enhanced transfer of incident field SAM to scattered field OAM at the MQ resonance, a complete physical picture requires a deeper theoretical insight on the behavior of the fields produced by the MQ mode under the prescribed illumination. For that purpose, we derive in the Supporting Information the expression for the power extracted by the nanocube (referred to as the extinction power,<sup>[75]</sup>  $P_{\text{ext}}$ ) from a circular plane wave propagating against the  $z$ -axis

$$P_{\text{ext}} = -\frac{E_0 k_0^2}{4} \text{Re}\{i\sigma M_{xx} + M_{yy}\} \quad (2)$$

where  $M_{ij}$  is  $ij$ -th component of the MQ tensor. The center of the nanocube is placed at the origin of the coordinate system, with the  $x, y$  and  $z$ -axis oriented perpendicular to its sides. Taking into account symmetry, we obtain the following nonzero tangential component  $S_{\theta}^{[6]}$  of the scattered Poynting vector:

$$S_{\theta}^s = \sigma \frac{3|M_{xy}|^2}{16\pi^2 c \mu_0} \frac{(9+3r^2 k_0^2 + r^4 k_0^4)}{k_0 r^3} \cos(\theta)^2 \sin(\theta) \quad (3)$$

where  $\theta$  is the polar angle in spherical coordinates, and  $r = |\mathbf{r}|$ . In the  $x$ - $y$  plane  $\theta = \pi/2$  and  $S_{\theta}^s = 0$ .

The intuitive physical picture is as follows: during an oscillation period, the incident circularly polarized electric field gradually changes its polarization between the  $x$ - and  $y$ -axis, consequently, the components of the excited MQ tensor oscillate accordingly. In analogy with a rotating electric dipole,<sup>[7]</sup> Equation (2) shows that the scattered near-field at the MQ resonance can be obtained as a superposition of the fields generated by  $M_{xx}$  and a  $\pi\sigma/2$  delayed  $M_{yy}$  component with equal amplitudes. The total Poynting vector outside the scatterer, however, also includes an interference term between the scattered electromagnetic field and the incident one, which leads to nonnegligible curl in the  $x$ - $y$  plane. This is indeed what is observed in the numerical simulations (see Figure 3a, where  $\Gamma_z^s$  is proportional to  $\langle S_{\theta}^s \rangle$ ). Substituting the scattered Poynting vector in Equation (S2), Supporting Information, the time-averaged scattered angular momentum density component in the  $z$ -axis  $J_z$  can be determined as

$$J_z = \sigma \left| \frac{r}{c} S_{\theta}^s \right| \quad (4)$$

Comparing Equation (4) with Equation (1) provides direct evidence that SAM from the incident wave has been transferred

to the scattered field giving rise to the optical vortex shown in Figure 2b. Moreover, since  $J_z$  depends on the choice of origin of the coordinate system<sup>[8]</sup> it can be directly correlated with the extrinsic OAM of the scattered field. Further inspection of Equations (3) and (4) also show that the tangential component of the Poynting vector as well as the angular momentum scale quadratically with the amplitude of the MQ moment enhancing the field vorticity at the MQ resonance. Since the angular momentum scales as  $r^{-n}$  (where  $n$  is a positive integer) in the near field, the vorticity of the Poynting vector is very high close to the particle, but decreases very fast going away from it, as confirmed in Figure 2b. The latter has very important consequences regarding the optical forces governing the motion of plasmonic nanoparticles under the influence of such a field, as mentioned below. Additional analytical and numerical proofs linking the nature of the optical vortex formation to MQ scattering can be found in the Supporting Information.

In this section, we have described the excitation of the MQ mode and proposed an intuitive physical picture explaining the multipolar origin of the tangential component of the Poynting vector giving rise to an optical vortex in the near field of the nanocube.

### 3. Optical Nanovortex-Mediated Forces and Torques

We can now proceed to study the effect of the scattered field on small (dipolar) particles. The time-averaged optical force  $\langle \mathbf{F}_v \rangle$  acting upon such a nanoparticle in the optical nanovortex can be written as<sup>[9]</sup>

$$\langle \mathbf{F}_v \rangle = \frac{\alpha'}{4} \nabla (\mathbf{E}^* \cdot \mathbf{E}) + \frac{ck_0 \alpha''}{\epsilon_0} \left( \frac{1}{c} \langle \mathbf{S} \rangle + \nabla \times \langle \mathbf{L} \rangle \right) \quad (5)$$

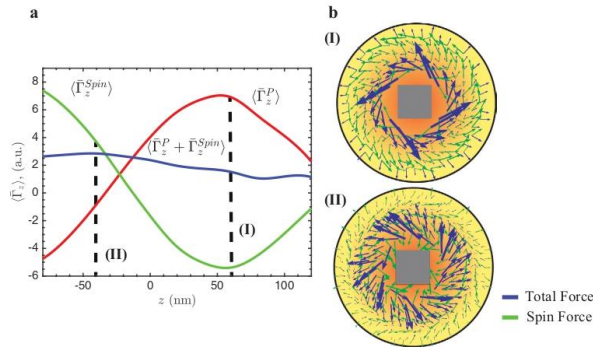


**Figure 3.** a) Optical torque affecting absorbing 40 nm radius nanoparticles with  $n = 2i$  in the near field of the MQ resonance ( $\lambda = 532$  nm). The time-averaged spin ( $\Gamma_z^{Spin}$ ) and radiation pressure ( $\Gamma_z^P$ ) contributions have been spatially averaged (I) in parallel  $x$ - $y$  planes in the near field along the height of the cube ( $z$ -axis). b) Transverse cuts at  $z = 60$  nm (I) and  $z = -40$  nm (II) showing the vector field distributions of total and curl-spin forces around the cube.



where  $n_m$  is the refractive index of the host medium,  $\mathbf{E}$  is the sum of the incident and scattered (by the nanocube) electric fields,  $\langle \mathbf{L} \rangle$  is the average SAM flux density (see the Supporting Information), and  $\alpha'$  and  $\alpha''$  are the real and imaginary parts of the particle dipole polarizability, respectively. The first term on the right-hand side of Equation (5) corresponds to conservative (curl-free) gradient optical forces, which for positive  $\alpha'$  drag the nanoparticle toward the region of maximal field intensity. The terms in round brackets describe nonconservative or "scattering" optical forces, hereinafter noted as  $\langle \mathbf{F}_{sc} \rangle$ . The latter receives contributions from the total Poynting vector ( $\mathbf{S}$ ) and the electric field contribution to the SAM flux density  $\langle \mathbf{L} \rangle$ .<sup>[79]</sup> A MQ mode corresponds to an object of well-defined parity, i.e., a transverse electric (TE) multipole. At the resonance, pure electric or magnetic multipoles strongly break electromagnetic duality, and, consequently, do not present a well-defined helicity.<sup>[74,80]</sup> This effect manifests itself strongly in the near field,<sup>[69]</sup> and implies that the SAM flux density, which is linked to the helicity density,<sup>[74]</sup> features a nonuniform spatial distribution. Therefore, the second term in  $\langle \mathbf{F}_{sc} \rangle$  acknowledged as the curl-spin force<sup>[69]</sup> is not only nonnegligible but also plays an essential role in the dynamics of nanoparticles.

Importantly, due to spin-orbit coupling, the particles will experience an orbital torque oriented along the z-axis,  $\Gamma_z$ , confined in a subwavelength region and directly proportional to the azimuthal component of  $\langle \mathbf{F}_{sc} \rangle$  (see the Supporting Information for the exact expression). The latter depends on the azimuthal components of the time-averaged Poynting vector and the near-field curl-spin forces, as well as on the optical response of the particles themselves ( $\alpha''$ ).

Interestingly, in the case of the MQ, it is possible to show that the contribution of the scattered field to the curl-spin force only has an azimuthal component, i.e., it only induces orbital motion. This result is general to any magnetic (TE) multipole field. The interference with the incident illumination leads, however, to important radial and polar components (see Figure 3).

Currently, very few groups<sup>[69,81]</sup> have investigated optical fields where the effect of spin-curl forces can be visibly appreciated in the dynamics of moving nanoparticles. In contrast, our calculations directly prove that both the spin force and radiation pressure contribute to the induced optical torque in the vicinity of the dielectric cube.

In Figure 3a, we show the optical torque experienced in the near field by an arbitrary absorbing 40 nm radius spherical nanoparticle with  $n = 2i$  calculated with Equation S19, Supporting Information, and averaged over several circular rings on parallel transverse planes (perpendicular to the incident propagation direction). Remarkably, particles whose centers of mass are located at different heights experience different contributions from the curl-spin ( $\Gamma_z^{\text{spin}}$ ) and radiation pressure ( $\Gamma_z^{\text{rad}}$ ) torques, as can be visually appreciated in the force field plots shown in Figure 3b. Moreover, both contributions can be opposite to the helicity of the incident wave if considered separately, but the total scattering force remains helicity locked—a result convenient for our purposes (see Section 5). It is worth noting that  $\Gamma_z^{\text{rad}}$  is nonzero at  $z = 0$ , contrarily to what one might initially expect from Equation (3), but we once more emphasize that the total Poynting vector entering in Equation S19, Supporting

Information, includes an additional interference term between the incident and scattered field yielding a small azimuthal component. As a consequence, the zero of  $\Gamma_z^{\text{rad}}$  is displaced to a lower  $z$  coordinate.

In our setup, the particles are initially pushed toward the glass substrate by the incident beam intensity, where they experience a combination of radiation pressure and curl-spin torques (Figure 3b(II)).

Here, we have introduced analytical expressions for the optical forces and torques induced on dipolar absorbing nanoparticles, which allowed us to unambiguously distinguish the contributions of the radiation pressure and the spin forces. The numerical calculations presented in Figure 3 demonstrate that both the effects mediate the strongly confined (subwavelength) particle rotation with respect to the z-axis (i.e., the direction of the propagation of the incident wave).

#### 4. Nanoparticle Dynamics in the Optical Nanovortex

We now turn our attention toward the potential applicability of the considered effect as a mixing method for microfluidic reactors. In order to illustrate the concept, we consider the water around the nanocube contains a dilute solution of chemically inert, biologically compatible nanoparticles. The dynamics of the latter will be affected by the optical forces arising due to the interaction with the cube's scattered field together with the Brownian and viscous drag forces induced in the fluid. The obvious and most convenient candidates to act as mixing mediators are Au nanoparticles, because they would not interact with the chemical and/or biological compounds dissolved in the solutions and are utilized in a broad range of microfluidics applications.<sup>[82,83]</sup>

In order to increase the mechanical orbital torque transferred to the Au nanoparticles and to prevent them from sticking to the walls of the nanocube due to attractive gradient forces, the ratio  $\langle \mathbf{F}_{sc} \rangle / \langle \mathbf{F}_{sc} \rangle$  should be maximized. For high enough ratios, scattering forces govern the nanoparticle dynamics, causing them to undergo spiral paths around the nanocube and act as stirrers enhancing convective fluid motion and thus diffusive mixing of any admixtures present in the water solution.

The scattering force can be a leading force acting upon the nanoparticle only if the real part of the nanoparticle polarizability is negligible in contrast to the imaginary one (see Equation (5)). For simplicity, we assume a spherical shape so that their dipole polarizability can be evaluated analytically with the exact Mie theory formulae by the method described elsewhere.<sup>[84–86]</sup>

$$\alpha(k_i, R_p) = i \frac{6\pi\epsilon_0 n_m^2}{k_i^3} a_1(m, k_i R_p) \quad (6)$$

where  $k_i$  is the wavenumber in water,  $a_1$  denotes the first electric Mie coefficient,<sup>[75]</sup> which depends on the refractive index contrast between the particle and the medium  $m = \sqrt{\epsilon_{Au}(\omega)}/n_m$  and the dimensionless parameter  $k_i R_p$ , where  $R_p$  is the nanoparticle radius. Details on the model for the permittivity of the nanoparticles  $\epsilon_{Au}$  with appropriate size-dependent corrections

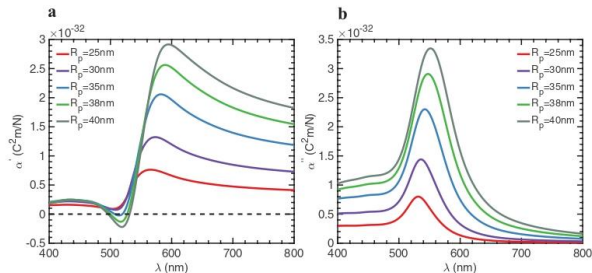


**Figure 4.** a) Real and b) imaginary parts of the dipole polarizability calculated from Equation (6) for Au nanoparticles of different sizes that are dispersed in water. The excitation wavelengths correspond to those in free space. For nanospheres with radius  $R_p \geq 35$  nm, the real part can be equal to zero while the imaginary part is enhanced.

are given in the Supporting Information. Combining Equations (5) and (6) allows for calculating the optical forces on nanoparticles with sizes even beyond the Rayleigh limit (see, e.g., the discussion in refs. [58,87]).

**Figure 4** shows the real and imaginary parts of the polarizability for Au particles of different sizes dispersed in water. We exploit the fact that, in the vicinity of the plasmon resonance, nanoparticles with  $R_p \geq 35$  nm can fulfill the condition  $\alpha' = 0$  with enhanced values of  $\alpha''$ . For example, for particles with  $R_p = 40$  nm, the full suppression of the gradient force occurs at 500 and 530 nm (see Figure 4a). Consequently, only scattering forces are allowed for them, and the ratio  $\langle F_{sc} \rangle / \langle F_g \rangle$  is maximized. Moreover, these wavelengths are in a close proximity to the chosen green source (532 nm).

Large Au nanoparticles with  $R_p \geq 35$  nm could be considered to break the limits of the electric dipole approximation assumed in Equation (5). To prove its validity for quantitative calculations of the optical forces, we have compared our results with exact numerical computations via integrating the Maxwell stress tensor over a 40 nm radius Au nanoparticle and obtained very good agreement (see Supporting Information). Moreover, the electric field distribution in the system plotted in Figure S3B–D, Supporting Information, shows negligible perturbations in the presence of a Au nanoparticle with no backscattering, further confirming the validity of the involved approximations.

In order to determine the trajectories of the Au nanoparticles in water, we assume the system has reached stationary equilibrium in the  $z$  direction, due to the compensation of the  $z$  component of the incident radiation pressure in the presence of the glass substrate. Therefore, the trajectories can be treated as two-dimensional, localized only in the transverse  $x$ - $y$  plane.

Considering scattering force  $\langle F_{sc} \rangle$ , viscous drag force  $F_D$ , commonly given by Stokes law, and stochastic Brownian (thermally activated) forces  $F_B$  acting on the nanoparticle of mass  $m_p$ , the Langevin equation of motion can be written in the following form:

$$\langle F_{sc} \rangle + F_D + F_B = m_p \ddot{\mathbf{r}}_p \quad (7)$$

where  $\ddot{\mathbf{r}}_p$  is the particle instantaneous acceleration vector. Once the scattering force distribution is determined, Equation (7) can be solved in Comsol Multiphysics.<sup>[88]</sup>

To accurately reproduce the motion of the nanoparticles while restricting ourselves to a two-dimensional analysis, the term  $F_D$  needs to take into account the additional drag induced by the walls of the nanocube and the glass substrate. To address this issue, we derive in the Supporting Information a modified Stokes law where the dynamic viscosity of water is replaced by a position-dependent effective viscosity tensor  $\bar{\mu}$ , which we implement in our calculations. When the nanoparticles are sufficiently far away from the nanocube, we demonstrate that our expression corresponds to the well-known Faxen corrections for viscous flow over a planar surface<sup>[89–91]</sup> (see Section 9 in the Supporting Information). We assume the system to be at ambient temperature.

The parameters for the simulations are given in Tables S1 and S2, Supporting Information.

We consider that Au nanoparticles of 40 nm radius are uniformly distributed around the Si nanocube. Their trajectories during a simulation time of 0.1 ms are shown in **Figure 5**. If the nanocube is not illuminated (Figure 5a), Brownian motion induces random displacements of the nanoparticles independently on their position in the simulation domain. Conversely, when the system is illuminated with circularly polarized light with intensities about 50–80 mW  $\mu\text{m}^{-2}$  (corresponding to typical values utilized in conventional optical trapping schemes<sup>[92]</sup>), mechanical orbital torque is transferred to the Au nanoparticles and drives them along spiral trajectories (Figure 5b).

Equation (3) reveals that  $\langle S_z \rangle$  becomes negligible far from the nanocube. Furthermore, the numerical simulations show that the curl-spin force has no longer a significant effect. Consequently, Brownian motion and conventional radiation pressure start to dominate the dynamics (see **Figure 6c**).

In order to characterize the trajectories of the nanoparticles inside the vortex and the enhancement of their diffusional motion, we calculated their mean-squared angular displacements

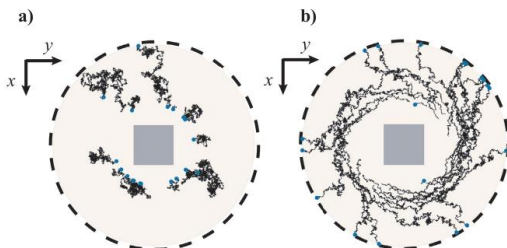


**Figure 5.** Trajectories of Au nanoparticles of 40 nm radius during 0.1 ms of simulations. Illumination wavelength in vacuum was 532 nm (in water 399 nm). a) No incident illumination, only Brownian motion and drag forces act on the particles; b) The nanocube is illuminated with a circularly polarized light, and the optical force contributes significantly. The Au nanoparticles spirally move around the cube. The figures are scaled to the length of the cube side equal to 158 nm.

(MSAD,  $\langle \Delta\phi^2 \rangle$  in Figure 6a), with respect to the center of the nanocube, as explained in Section 10 of the Supporting Information.

Due to the persistent orbital torque inside the vortex, the nanoparticles are actively rotating, as shown by the remarkable increase in the azimuthal angle as a function of time.

The MSAD curves can be fitted with equations of the form  $\langle \phi(t)^2 \rangle = D_g^{\text{eff}} t + \omega_{\text{avg}}^2 t^2$ , where  $D_g^{\text{eff}}$  is an effective rotational diffusion coefficient and  $\omega_{\text{avg}}$  is the average angular speed. This analysis leads, as expected, to  $\omega_{\text{avg}} = 0$  for the case of passive (Brownian) diffusion, and  $\omega_{\text{avg}} = 0.37 \text{ deg}\mu\text{s}^{-1}$ ,  $0.08 \text{ deg}\mu\text{s}^{-1}$  for particles placed, respectively, at 210 and 300 nm from the center of the nanocube. The results confirm that, in the near field of the nanocube, strong rotational motion can be achieved, and the nanoparticles enter a “superdiffusive” regime. Based on the previous information, we introduce the effective radius  $r_m$  which specifies the area of influence of the optical nanovortex (red dashed circle in Figure 6c), the majority of the Au nanoparticles circulate around the nanocube, and the dielectric nanocube acts as an effective optical drive for convective stirring of the fluid around it. The translational mean-squared displacements of the nanoparticles (MSD,  $\langle r^2 \rangle$  in Figure 6b, see Section 10 in the Supporting Information), also show an important increase compared to thermal diffusion in the absence of laser illumination. We remark

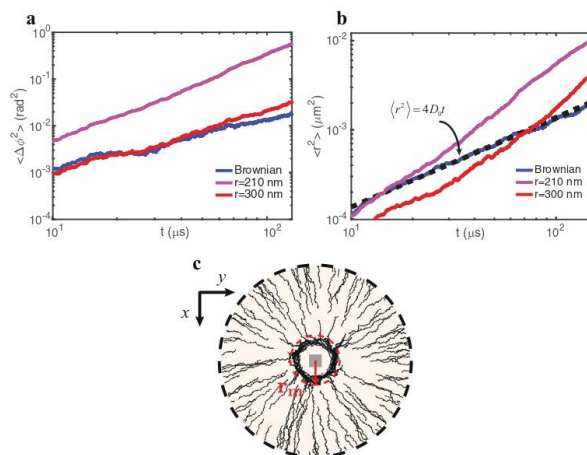


**Figure 6.** a, b) Log-log plots of MSAD and MSD characterizing the diffusional motion of Au nanoparticles under the influence of the optical near fields and allowing the determination of the range of action of the nanovortex,  $r_m$ ; a) Calculated MSAD averaged over 100 Au nanoparticles of 40 nm radius, when the cube is not illuminated (blue), and under LCP illumination at a distance from the center of the nanocube much lower than  $r_m$  (shown in (c)) – violet and at  $r_m$  – red. b) Averaged MSD in the same conditions as in (a). Dashed line corresponds to the fit with Einstein's relation. c) Trajectories of 40 nm radius Au nanoparticles inside and outside the nanovortex region delimited by  $r_m$ . The red dashed circle delimits the effective radius  $r_m$ , which determines the range of action of the tangential optical forces. The optical nanomixing effect is thus achievable at the positions lying inside  $r_m$ .

that the Brownian MSDs are in full agreement with the Einstein–Smoluchowski relation<sup>[93]</sup>  $\langle r(t)^2 \rangle = 4D_0t$ , where  $D_0$  is the diffusion coefficient calculated for spherical particles as  $D_0 = k_B T / 6\pi\eta_{xx}R_p$ , ( $\eta_{xx}$  is the  $xx$  component of the viscosity tensor in Equation S29, Supporting Information) further verifying the correctness of our calculations. Therefore, the proposed light-driven setup strongly boosts diffusion.

The radius  $r_m$  reaches about half of the incident wavelength in water and thus the mechanical effect of optical vortices upon a nanoparticle takes place in the subwavelength region. Such a reduced scale cannot be reached using any focused far field, e.g., radial and Bessel beams.<sup>[66,67,94]</sup> Up to our knowledge, this is the first proposal providing optical nanovortices created in a simple, realizable setup avoiding the need of lossy plasmonic nanoantennas,<sup>[95,96]</sup> short wavelength guided modes,<sup>[97]</sup> or complex chiral structures.<sup>[98]</sup> Such optical nanovortices represent a promising component for on-a-chip OAM exchange driving light–matter interactions (e.g., controlled light emission from quantum dots,<sup>[98]</sup> superresolution,<sup>[99,100]</sup> and nano-object manipulation<sup>[66,94]</sup>).

## 5. Nanovortex-Mediated Liquid Mixing

To study in detail the liquid flow driven by the proposed nanomixing design, we once again utilize direct time-domain simulation in COMSOL Multiphysics. At each time step, the particle position and velocity, as well as the fluid pressure and velocity fields are obtained by solving Equation (7), the Navier–Stokes, and mass balance equations for the fluid.<sup>[100]</sup> We consider simplified forms of the last two equations assuming laminar, incompressible flow, in accordance with the previous results for the particle trajectories. Furthermore, we impose open boundary conditions at the edges and simulate a large fluid domain around the nanocube (usually lab-on-a-chip microchambers are of the order of tens of micrometers).

Figure 7 shows the calculated stresses and velocity fields in the fluid during 200  $\mu\text{s}$ . The particles start with zero initial speed and gradually accelerate under the influence of radiation pressure and spin forces arising from their interaction with the optical nanovortex. Consequently, the fluid environment is also displaced, as Figure 7a demonstrates. At longer times, a single vortex-like velocity distribution is established as shown in Figure 7c.

The velocity streamlines are more inhomogeneous at shorter times, when the nanoparticles start moving. Already at 150  $\mu\text{s}$ , only small fluid distortions take place very close to the nanoparticles and the nanocube. Therefore, a possible way to further enhance the fluid nanomixing would be to realize periodic switching between left- and right-hand circularly

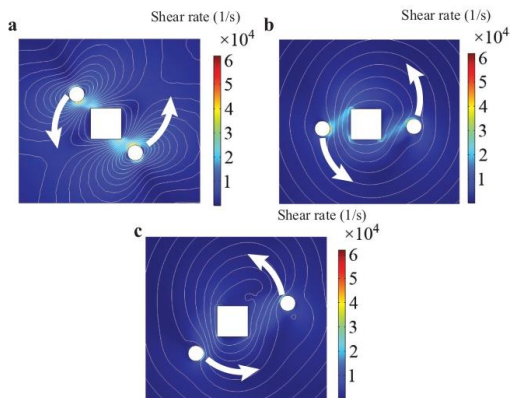


**Figure 7.** Formation of a fluid nanovortex due to the movement of two Au nanoparticles (white circles moving anticlockwise) driven by optical nanovortex formed around the nanocube (white square). Background color map denotes the distribution of stress in the fluid in  $1 \text{ s}^{-1}$  and white contours show the fluid velocity field streamlines of the initially static fluid at different times since the nanoparticles became optically driven. a)  $t = 0.01 \mu\text{s}$ , b)  $t = 150 \mu\text{s}$  and c)  $t = 260 \mu\text{s}$ . The represented domain has dimensions  $800 \times 800 \text{ nm}$ . Parameters of the simulations are given in Table S1, Supporting Information. Open fluid boundary conditions were imposed at a distance of  $1.5 \mu\text{m}$  from the center of the nanocube. For the sake of clarity, thermal motion is not taken into account in the simulation.

polarized incident light, which would reverse the direction of particle motion maintaining a high level of inhomogeneity in the fluid stress field.

Noteworthy that, while all the previous calculations were performed for Au nanoparticles in the visible range, similar dynamics can also be obtained for Ag nanoparticles in the UV range of the spectrum, where  $\alpha' \rightarrow 0$ .<sup>[92]</sup> Nanomixing in the UV region could be advantageously combined with photochemically active processes of the involved chemical compounds.

## 6. Optical Sorting of Au Nanoparticles via the Nanovortex

Hereinafter, we demonstrate the important capability of the proposed configuration to realize optical force-mediated particle on-chip sorting. In this section, we illustrate a novel, dynamical, contact-less size sorting method for Au nanoparticles in liquid solutions addressing one of the most challenging targets of conventional microfluidics with the help of dielectric nanophotonics.

The proposed method is based on the sign switch displayed by  $\alpha'$  close to the plasmon resonance as we demonstrated in Figure 4. The transition reverses the direction of the radial gradient force acting upon the nanoparticle (see the first term in Equation (5)). At a given incident wavelength, we can split

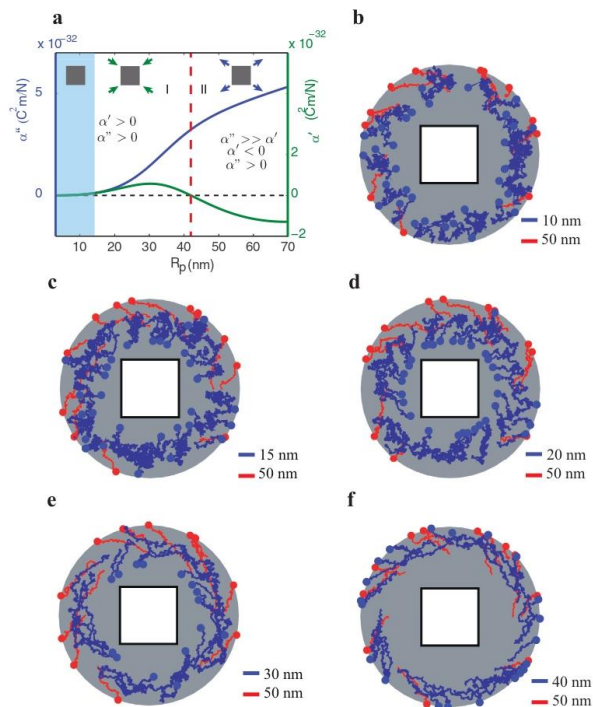


**Figure 8.** a) Real ( $\alpha'$ ), and imaginary ( $\alpha''$ ) parts of the dipole polarizability as a function of the particle radius  $R_p$  for an incident free space wavelength of 532 nm. The black dashed line indicates zero real or imaginary part, while the red dashed line shows the border between region I and II. The blue shaded area corresponds to the size region, where Brownian motion dominates. Insets depict schematically the radial direction of the optical forces exerted on Au nanoparticles inside the different regions. b–f) The blue curves show the calculated trajectories followed by particles with sizes from region I: 10 nm (b), 15 nm (c), 20 nm (d), 30 nm (e), and 40 nm (f), respectively. For comparison, in all the plots (b–f) the red curves correspond to the statistically different trajectories followed by nanoparticles with 50 nm radii corresponding to region II.

the behavior of the Au nanoparticles into regions I and II (see Figure 8a). Smaller nanoparticles from region I with positive  $\alpha'$  are attracted by the radial gradient force toward the nanocube, while larger nanoparticles, from region II, should be repelled outwards (see schematic insets in Figure 8a).

However, in region I, there is a competition between Brownian, gradient, and scattering forces, where the first introduces an unbiased random displacement, and the other two drag the nanoparticles in opposite radial directions. A careful analysis considering the contributions of each force is therefore required to determine the viability of the sorting method.

Figure 8b–f illustrates the proposed approach for nanoparticle separation by comparing the results of the numerical simulations for two sets of Au nanoparticles; the trajectories colored in blue correspond to nanoparticles with increasing size ranging from 10 to 40 nm radii, while the red trajectories in all Figure 8b–f are the paths followed by nanoparticles of 50 nm radius. The smaller particles in blue lie inside region I, while the larger red ones are in region II.

Nanoparticles smaller than 15 nm have very low polarizabilities, resulting in negligible optical forces in comparison with Brownian forces (Figure 8b). However, the numerical simulations show that nanoparticles with radii in the range 15–30 nm

are drawn toward the nanocube tracing inward curved paths (see Figure 8d–f), and thus are primarily affected by gradient forces. The most intense inward forces in region I are experienced by nanoparticles with size 30 nm (Figure 8e) coinciding with the maximum of  $\alpha'$  in Figure 8a, green line. Contrarily, nanoparticles with radii close to 40 nm (i.e., in the vicinity or inside region II), spiral away from the dielectric nanocube due to scattering forces. Larger particles are also repelled by the joint scattering and gradient forces, since the latter changes sign. As we have already mentioned, we performed additional numerical simulations proving the correctness of the dipole approximation for the larger nanoparticles (see Figures S3 and S4, Supporting information).

The results in this section demonstrate that our novel platform can operate as a sorting device for Au nanoparticles by exploiting their inward or outward motion toward the nanocube as a function of their dimension. A precise, in situ size control of Au nanoparticles is a crucial step in many applications, e.g., biological cell uptake rates,<sup>[103,104]</sup> toxicity,<sup>[105]</sup> and Raman signal intensity.<sup>[106]</sup>

## 7. Conclusion

We present conditions for maximal conversion of SAM of the incident light to OAM of the scattered light via the specially designed transversely scattering silicon nanocube. The azimuthal component of the Poynting vector of the scattered field originates from the strong MQ resonance. A Au nanoparticle of appropriate size, illuminated by such optical field and dispersed in the fluid surrounding the nanocube, experiences a combination of spin and radiation pressure forces with non-zero azimuthal component. They are significant only up to a distance of about half of the illuminating wavelength from the silicon nanoantenna. The exceptionally compact optical nanovortex drives the dynamics of the nanoparticles, inducing a convection fluid flow at the nanoscale. The direction of particle motion can be reversed simply by flipping the helicity of the incident circular polarization. Therefore, the proposed mechanism can serve as a nanoscale fluid mixer and diffusion booster driven by light in a contact-less and flexible way. Arrays of the studied dielectric nanoantennae can be easily imprinted on the surface of a microfluidic chip and controllably illuminated in an independent fashion. Hence, we shed light on very exciting perspectives such as light-controlled mixing or even on-chip directional fluid navigation. Employing the dependence of the optical properties of Au nanoparticles on their size, we demonstrate feasibility to drag nanoparticles affected by the optical vortex either toward or outward the nanocube. Thus, smaller nanoparticles (15–30 nm in radius) can be aggregated at the silicon nanoantenna surface, while larger nanoparticles move away from it and drive the fluid flow. This behavior can be utilized to perform in situ size separation directly inside the microfluidic chip.

The proposed, rather simple concept can be extended to nanostructures of different shapes, to an array of such nanostructures and to different types of dispersed nanoparticles, e.g., silver nanoparticles offer an exciting option to combine optical nanovortex with photochemistry at the nanoscale. Our

approach opens a new room of opportunities for the integration of simple, optically driven nanosorting or filtering modules in on-chip platforms paving the way toward more efficient functionalities in micro- and nanofluidic systems.

## Supporting Information

Supporting Information is available from the Wiley Online Library or from the author.

## Acknowledgements

The force calculations were partially supported by Russian Science Foundation (Grant No. 18-72-10127). P.Z. acknowledges support from the Czech Science Agency (19-17765S), the Technology Agency of the Czech Republic (TE01020233), and the Czech Academy of Sciences.

## Conflict of Interest

The authors declare no conflict of interest.

## Keywords

all-dielectric nanophotonics, lab-on-a-chip platforms, nanofluidics, optomechanical manipulations, spin-orbit couplings

Received: October 28, 2019  
Revised: February 10, 2020  
Published online:

- [1] H. Schmidt, A. R. Hawkins, *Nat. Photonics* **2011**, *5*, 598.
- [2] X. Fan, I. M. White, *Nat. Photonics* **2011**, *5*, 591.
- [3] D. Erickson, D. Sinton, D. Psaltis, *Nat. Photonics* **2011**, *5*, 583.
- [4] N. T. Nguyen, S. T. Wereley, *Fundamentals and Applications of Microfluidics*, 2nd ed., Artech House, Boston, MA **2002**.
- [5] Y. Shi, S. Xiong, L. K. Chin, J. Zhang, W. Ser, J. Wu, T. Chen, Z. Yang, Y. Hao, B. Liedberg, P. H. Yap, D. P. Tsai, C.-W. Qiu, A. Q. Liu, *Sci. Adv.* **2018**, *4*, eaao0773.
- [6] D. Gao, W. Ding, M. Nieto-Vesperinas, X. Ding, M. Rahman, T. Zhang, C. Lim, C.-W. Qiu, *Light: Sci. Appl.* **2017**, *6*, e17039.
- [7] Y. Z. Shi, S. Xiong, Y. Zhang, L. K. Chin, Y. Y. Chen, J. B. Zhang, T. H. Zhang, W. Ser, A. Larsson, S. H. Lim, J. H. Wu, T. N. Chen, Z. C. Yang, Y. L. Hao, B. Liedberg, P. H. Yap, K. Wang, D. P. Tsai, C. W. Qiu, A. Q. Liu, *Nat. Commun.* **2018**, *9*, 815.
- [8] E. Livak-Dahl, I. Sinn, M. Burns, *Annu. Rev. Chem. Biomol. Eng.* **2011**, *2*, 325.
- [9] L. Wang, P. C. H. Li, *Anal. Chim. Acta* **2011**, *687*, 12.
- [10] J. S. Kuo, D. T. Chiu, *Annu. Rev. Anal. Chem.* **2011**, *4*, 275.
- [11] P. C. H. Li, *Microfluidic Lab-on-a-chip for Chemical and Biological Analysis and Discovery*, CRC Press, Boca Raton, FL **2005**.
- [12] J. P. Kutter, *Separation Methods in Microanalytical Systems*, CRC Press, Boca Raton, FL **2005**.
- [13] J. Yue, *Catal. Today* **2018**, *308*, 3.
- [14] S. Cattaneo, S. Althabban, S. J. Freakley, M. Sankar, T. Davies, Q. He, N. Dimitratos, C. J. Kiely, G. J. Hutchings, *Nanoscale* **2019**, *11*, 8247.
- [15] E. Yamaguchi, N. Taguchi, A. Itoh, *React. Chem. Eng.* **2019**, *4*, 995.
- [16] J. I. Yoshida, H. Kim, *ChemSusChem* **2011**, *4*, 331.
- [17] V. Hessel, H. Löwe, F. Schönfeld, *Chem. Eng. Sci.* **2005**, *60*, 2479.

- [18] A. Ould El Mocrar, N. Aubry, J. Botton, *Lab Chip* **2003**, 3, 273.
- [19] R. Baber, L. Mazzei, N. T. K. Thanh, A. Gavriilidis, *Nanoscale* **2017**, 9, 14149.
- [20] I. Glasgow, N. Aubry, *Lab Chip* **2003**, 3, 114.
- [21] P. Paik, V. K. Pamula, R. B. Fair, *Lab Chip* **2003**, 3, 253.
- [22] Z. Yang, S. Matsumoto, H. Goto, M. Matsumoto, R. Maeda, *Sens. Actuators, A* **2001**, 93, 266.
- [23] R. H. Liu, R. Lenigk, R. L. Druyor-Sanchez, J. Yang, P. Grodzinski, *Anal. Chem.* **2003**, 75, 1911.
- [24] J. West, B. Karamata, B. Lillis, J. P. Gleeson, J. Alderman, J. K. Collins, W. Lane, A. Mathewson, H. Berney, *Lab Chip* **2002**, 2, 224.
- [25] P. Zemánek, G. Volpe, A. Jonáš, O. Brzobohatý, *Adv. Opt. Photonics* **2019**, 11, 577.
- [26] P. H. Jones, O. M. Maragó, G. Volpe, *Optical Tweezers: Principles and Applications*, Cambridge University Press, Cambridge **2015**.
- [27] P. Y. Chiou, A. T. Ohta, M. C. Wu, *Nature* **2005**, 436, 370.
- [28] A. Jonáš, P. Zemánek, *Electrophoresis* **2008**, 29, 4813.
- [29] M. P. MacDonald, G. C. Spalding, K. Dholakia, *Nature* **2003**, 426, 421.
- [30] M. M. Wang, E. Tu, D. E. Raymond, J. M. Yang, H. Zhang, N. Hagen, B. Dees, E. M. Mercer, A. H. Forster, I. Kariv, P. J. Marchand, W. F. Butler, *Nat. Biotechnol.* **2005**, 23, 83.
- [31] Y. Shi, H. Zhao, K. T. Nguyen, Y. Zhang, L. K. Chin, T. Zhu, Y. Yu, H. Cai, P. H. Yap, P. Y. Liu, S. Xiong, J. Zhang, C.-W. Qiu, C. T. Chan, A. Q. Liu, *ACS Nano* **2019**, 13, 12070.
- [32] O. Brzobohatý, L. Chvátal, A. Jonáš, M. Šiler, J. Kaňka, J. Jezek, P. Zemánek, *ACS Photonics* **2019**, 6, 403.
- [33] W. Singer, M. Frick, S. Bernet, Ritsch-Marte, M. J. *Opt. Soc. Am. B* **2003**, 20, 1568.
- [34] M. Woerdemann, C. Alpmann, M. Esseling, C. Denz, *Laser Photonics Rev.* **2013**, 7, 839.
- [35] K. Dholakia, T. Cizmar, *Nat. Photonics* **2011**, 5, 335.
- [36] D. G. Grier, *Nature* **2003**, 424, 810.
- [37] A. Jesacher, C. Maurer, A. Schwaighofer, S. Bernet, M. Ritsch-Marte, *Opt. Express* **2008**, 16, 4479.
- [38] I. T. Leite, S. Turtaev, X. Jiang, M. Šiler, A. Cuschieri, P. S. J. Russell, T. Cizmar, *Nat. Photonics* **2018**, 12, 33.
- [39] D. Palma, J. Glückstad, *Laser Photonics Rev.* **2013**, 7, 478.
- [40] A. M. Yao, M. J. Padgett, *Adv. Opt. Photonics* **2011**, 3, 161.
- [41] S. Franke-Arnold, L. Allen, M. Padgett, *Laser Photonics Rev.* **2008**, 2, 299.
- [42] K. Ladavac, D. G. Grier, *Opt. Express* **2004**, 12, 1144.
- [43] R. A. Beth, *Phys. Rev.* **1936**, 50, 115.
- [44] T. Wu, T. A. Nieminen, S. Mohanty, J. Miotke, R. L. Meyer, H. Rubinsztein-Dunlop, M. W. Berns, *Nat. Photonics* **2012**, 6, 62.
- [45] J. Leach, H. Mushfique, R. di Leonardo, M. Padgett, J. Cooper, *Lab Chip* **2006**, 6, 735.
- [46] M. E. J. Friese, T. A. Nieminen, N. R. Heckenberg, H. Rubinsztein-Dunlop, *Nature* **1998**, 394, 348.
- [47] T. M. Hoang, Y. Ma, J. Ahn, J. Bang, F. Robicheaux, Z.-Q. Yin, T. Li, *Phys. Rev. Lett.* **2016**, 117, 123604.
- [48] S. Kuhn, A. Kosloff, B. A. Stickler, F. Patolsky, K. Hornberger, M. Arndt, J. Millen, *Optica* **2017**, 4, 356.
- [49] A. V. Arzola, L. Chvátal, P. Ják, P. Zemánek, *Sci. Rep.* **2019**, 9, 4127.
- [50] M. Antognozzi, C. R. Bermingham, R. L. Harniman, S. Simpson, J. Senior, R. Hayward, H. Hoerber, M. R. Dennis, A. Y. Bekshaev, K. Y. Bliokh, F. Nori, *Nat. Phys.* **2016**, 12, 731.
- [51] V. Svak, O. Brzobohatý, M. Šiler, P. Ják, J. Kaňka, P. Zemánek, S. H. Simpson, *Nat. Commun.* **2018**, 9, 5453.
- [52] O. M. Maragó, P. H. Jones, P. G. Gucciardi, G. Volpe, A. C. Ferrari, *Nat. Nanotechnol.* **2013**, 8, 807.
- [53] M. L. Juan, M. Righini, R. Quidant, *Nat. Photonics* **2011**, 5, 349.
- [54] R. Quidant, C. Girard, *Laser Photonics Rev.* **2008**, 2, 47.
- [55] J. Berthelot, S. S. Adimović, M. L. Juan, M. P. Kreuzer, J. Renger, R. Quidant, *Nat. Nanotechnol.* **2014**, 9, 295.
- [56] Y. Kivshar, *Natl. Sci. Rev.* **2018**, 5, 144.
- [57] K. V. Baryshnikova, A. Novitsky, A. B. Evlyukhin, A. S. Shalin, *J. Opt. Soc. Am. B* **2017**, 34, D36.
- [58] M. Nieto-Vesperinas, J. J. Sáenz, R. Gómez-Molina, L. Chantada, *Opt. Express* **2010**, 18, 11428.
- [59] A. S. Shalin, S. V. Sukhov, A. A. Bogdanov, P. A. Belov, P. Ginzburg, *Phys. Rev. A* **2015**, 91, 063830.
- [60] A. S. Shalin, P. Ginzburg, A. A. Orlov, I. Iorsh, P. A. Belov, Y. S. Kivshar, A. V. Zayats, *Phys. Rev. B* **2015**, 91, 125426.
- [61] A. A. Bogdanov, A. S. Shalin, P. Ginzburg, *Sci. Rep.* **2015**, 5, 15846.
- [62] A. Ivinskaya, N. Kostina, A. Proskurnin, M. I. Petrov, A. A. Bogdanov, S. Sukhov, A. V. Krasavin, A. Karabchevsky, A. S. Shalin, P. Ginzburg, *ACS Photonics* **2018**, 5, 4371.
- [63] S. Sukhov, A. Shalin, D. Haefner, A. Dogariu, *Opt. Express* **2015**, 23, 247.
- [64] K. Y. Bliokh, F. J. Rodríguez-Fortuño, F. Nori, A. V. Zayats, *Nat. Photonics* **2015**, 9, 796.
- [65] J. E. Vázquez-Lozano, A. Martínez, F. J. Rodríguez-Fortuño, *Phys. Rev. Appl.* **2019**, 12, 024065.
- [66] V. Garcés-Chávez, K. Volke-Sepulveda, S. Chávez-Cerda, W. Sibbett, K. Dholakia, *Phys. Rev. A* **2002**, 66, 8.
- [67] G. S. Sokolovskii, V. V. Dudulev, S. N. Losev, K. K. Soboleva, A. G. Deryagin, K. A. Fedorova, V. I. Kuchinskii, W. Sibbett, E. U. Rafailov, *Prog. Quantum Electron.* **2014**, 38, 157.
- [68] H. K. Shamkhi, K. V. Baryshnikova, A. Sayansky, P. Kapitanova, P. D. Terekhov, P. Belov, A. Karabchevsky, A. B. Evlyukhin, Y. Kivshar, A. S. Shalin, *Phys. Rev. Lett.* **2019**, 122, 193905.
- [69] S. Albaladejo, M. I. Marqués, M. Laroche, J. J. Sáenz, *Phys. Rev. Lett.* **2009**, 102, 113602.
- [70] A. Dogariu, C. Schwartz, *Opt. Express* **2006**, 14, 8425.
- [71] S. B. Wang, C. T. Chan, *Nat. Commun.* **2014**, 5, 3307.
- [72] E. Hendry, T. Carpy, J. Johnston, M. Popland, R. V. Mikhaylovskiy, A. J. Laphorn, S. M. Kelly, L. D. Barron, N. Gadegaard, M. Kadodwala, *Nat. Nanotechnol.* **2010**, 5, 783.
- [73] A. Y. Zhu, W. T. Chen, A. Zaidi, Y.-W. Huang, M. Khorasaninejad, V. Sanjeev, C.-W. Qiu, F. Capasso, *Light: Sci. Appl.* **2018**, 7, 17158.
- [74] I. Fernandez-Corbaton, X. Zambrana-Puyalto, G. Molina-Terriza, *Phys. Rev. A* **2012**, 86, 042103.
- [75] C. F. Bohren, D. R. Huffman, *Absorption and Scattering of Light by Small Particles*, Wiley, New York **1998**.
- [76] A. B. Evlyukhin, T. Fischer, C. Reinhardt, B. N. Chichkov, *Phys. Rev. B* **2016**, 94, 205434.
- [77] W. Gough, *Eur. J. Phys.* **1986**, 7, 81.
- [78] A. T. O'Neil, I. MacVicar, L. Allen, M. J. Padgett, *Phys. Rev. Lett.* **2002**, 88, 4.
- [79] L. Novotny, B. Hecht, *Principles of Nano-Optics*, Cambridge University Press, Cambridge **2012**.
- [80] I. Fernandez-Corbaton, M. Fruhnert, C. Rockstuhl, *Phys. Rev. X* **2016**, 6, 031013.
- [81] G. Rui, Y. Li, S. Zhou, Y. Wang, B. Gu, Y. Cui, Q. Zhan, *Photonics Res.* **2019**, 7, 69.
- [82] A. Papra, A. Bernard, D. Juncker, N. B. Larsen, B. Michel, E. Delamarque, *Langmuir* **2001**, 17, 4090.
- [83] L. Ge, S. Wang, J. Yu, N. Li, S. Ge, M. Yan, *Adv. Funct. Mater.* **2013**, 23, 3115.
- [84] A. B. Evlyukhin, S. M. Novikov, U. Zywietz, R. L. Eriksen, C. Reinhardt, S. I. Bozhevolnyi, B. N. Chichkov, *Nano Lett.* **2012**, 12, 3749.
- [85] A. B. Evlyukhin, C. Reinhardt, A. Seidel, B. S. Luk'Yanchuk, B. N. Chichkov, *Phys. Rev. B* **2010**, 82, 045404.
- [86] W. T. Doyle, *Phys. Rev. B* **1989**, 39, 9852.

- [87] J. R. Arias-González, M. Nieto-Vesperinas, *J. Opt. Soc. Am. A* **2003**, *20*, 1201.
- [88] M. M. Kim, A. L. Zydney, *J. Colloid Interface Sci.* **2004**, *269*, 425.
- [89] S. Kim, S. J. Karrila, H. Brenner, *Microhydrodynamics: Principles and Selected Applications*, Elsevier Science, Oxford **2013**.
- [90] X. Bian, C. Kim, G. E. Karniadakis, *Soft Matter* **2016**, *12*, 6331.
- [91] G. S. Perkins, R. B. Jones, *Phys. A* **1992**, *189*, 447.
- [92] S. Albaladejo, M. I. Marqués, J. J. Sáenz, *Opt. Express* **2011**, *19*, 11471.
- [93] A. P. Philpse, *Brownian Motion: Elements of Colloid Dynamics. Brownian Motion*, Springer International Publishing, New York **2018**.
- [94] M. Li, S. Yan, B. Yao, Y. Liang, M. Lei, Y. Yang, *Phys. Lett. A* **2015**, *380*, 311.
- [95] J. S. Donner, G. Baffou, D. McCloskey, R. Quidant, *ACS Nano* **2011**, *5*, 5457.
- [96] C. Huang, X. Chen, A. O. Oladipo, N. C. Panoiu, F. Ye, *Sci. Rep.* **2015**, *5*, 13089.
- [97] A. David, B. Gjonaj, G. Bartal, *Phys. Rev. B* **2016**, *93*, 121302.
- [98] A. B. Young, A. B. Young, A. C. T. Thijssen, D. M. Beggs, P. Androvitsaneas, L. Kuipers, J. G. Rarity, S. Hughes, R. Oulton, *Phys. Rev. Lett.* **2015**, *115*, 153901.
- [99] A. David, B. Gjonaj, Y. Blau, S. Dolev, G. Bartal, *Optica* **2015**, *2*, 1045.
- [100] K. I. Willig, R. R. Kellner, R. Medda, B. Hein, S. Jakobs, S. W. Hell, *Nat. Methods* **2006**, *3*, 721.
- [101] G. K. Batchelor, *An Introduction to Fluid Dynamics*, Cambridge University Press, Cambridge **2000**.
- [102] A. S. Ang, S. V. Sukhov, A. Dogariu, A. S. Shalin, *Sci. Rep.* **2017**, *7*, 41014.
- [103] B. D. Chithrani, A. A. Ghazani, W. C. W. Chan, *Nano Lett.* **2006**, *6*, 662.
- [104] B. D. Chithrani, W. C. W. Chan, *Nano Lett.* **2007**, *7*, 1542.
- [105] Y. Pan, S. Neuss, A. Leifert, M. Fischler, F. Wen, U. Simon, G. Schmid, W. Brandau, W. Jahnhen-Dechent, *Small* **2007**, *3*, 1941.
- [106] A. M. Kern, O. J. F. Martin, *Nano Lett.* **2011**, *11*, 482.



**3-PAPER:** Quasibound states in the continuum induced by PT symmetry breaking

Novitsky D.V., Shalin A.S., Redka D., Bobrovs V., Novitsky A.V., “Quasibound states in the continuum induced by PT symmetry breaking”, (2021) *Physical Review B*, 104 (8), art. no. 085126, DOI: [10.1103/PhysRevB.104.085126](https://doi.org/10.1103/PhysRevB.104.085126)

## Quasi-bound states in the continuum induced by $\mathcal{PT}$ -symmetry breaking

Denis V. Novitsky<sup>1</sup>✉, Alexander S. Shalin<sup>2,3,4</sup>, Dmitrii Redka<sup>5,4</sup>, Vjaceslavs Bobrov<sup>4</sup>, and Andrey V. Novitsky<sup>6,2</sup>

<sup>1</sup>*B. I. Stepanov Institute of Physics, National Academy of Sciences of Belarus, Nezavisimosti Avenue 68, 220072 Minsk, Belarus*

<sup>2</sup>*ITMO University, Kronverksky Prospekt 49, 197101 St. Petersburg, Russia*

<sup>3</sup>*Kotel'nikov Institute of Radio Engineering and Electronics,*

*Russian Academy of Sciences (Ulyanovsk branch), Goncharova Str. 48, 432000 Ulyanovsk, Russia*

<sup>4</sup>*Riga Technical University, Institute of Telecommunications, Azenes st. 12, 1048 Riga, Latvia*

<sup>5</sup>*Saint Petersburg Electrotechnical University "LETI" (ETU),*

*Prof. Popova Street 5, 197376 St. Petersburg, Russia*

<sup>6</sup>*Department of Theoretical Physics and Astrophysics, Belarusian State University, Nezavisimosti Avenue 4, 220030 Minsk, Belarus*

(Dated: August 18, 2021)

Bound states in the continuum (BICs) enable unique features in tailoring light-matter interaction on nanoscale. These radiationless localized states drive theoretically infinite quality factors and lifetimes for modern nanophotonics, making room for a variety of emerging applications. Here we use the peculiar properties possessed by the so-called  $\mathcal{PT}$ -symmetric optical structures to propose the novel mechanism for the quasi-BIC manifestation governed by the  $\mathcal{PT}$ -symmetry breaking. In particular, we study regularities of the spontaneous  $\mathcal{PT}$ -symmetry breaking in trilayer structures with the outer loss and gain layers consisting of materials with permittivity close to zero. We reveal singular points on the curves separating  $\mathcal{PT}$ -symmetric and broken- $\mathcal{PT}$ -symmetry states in the parametric space of the light frequency and the angle of incidence. These singularities remarkably coincide with the BIC positions at the frequency of volume plasmon excitation, where the dielectric permittivity vanishes. The loss and gain value acts as an asymmetry parameter that disturbs conditions of the ideal BIC inducing the quasi-BIC. Fascinating properties of these quasi-BICs having ultrahigh quality factors and almost perfect transmission can be utilized in sensing, nonlinear optics, and other applications.

### I. INTRODUCTION

Photonic systems with balanced loss and gain, also known as  $\mathcal{PT}$ -symmetric systems, have attracted much attention over the last decade. Being at first a mere classical analogue of a peculiar quantum-mechanical invariance [1], the  $\mathcal{PT}$  symmetry was soon realized as a powerful tool to manipulate light-matter interaction [2–5]. A number of optical schemes were used to observe the  $\mathcal{PT}$  symmetry including coupled waveguides [6], photonic lattices [7], and two-dimensional crystals [8]. Perhaps, the simplest one is a layered structure with alternating loss and gain materials [9]. Studies of  $\mathcal{PT}$ -symmetric systems initiated rapid development of non-Hermitian photonics devoted to general problems of open photonic systems changing researchers' attitude to loss and gain: loss is more than an attenuation factor to get rid of and gain is more than a means to reach amplification and lasing. As an example of this more general approach, asymmetric, unbalanced distributions of loss and gain have attracted attention recently, e.g., for loss compensation [10] or lasing-threshold tuning [11].

One of the most intriguing features of the  $\mathcal{PT}$  symmetry in various systems exhibits itself in its spontaneous breakdown. This can be achieved by tuning parameters of the system, for example, the level of balanced loss and gain. Under the tuning, one reaches a moment when a modal composition of the system degenerates and the  $\mathcal{PT}$  symmetry gets broken. Such degeneracies called exceptional points (EPs) are important peculiarities of many optical and photonic systems and, generally, correspond to the simultaneous coalescence

of complex eigenvalues and eigenvectors of non-Hermitian Hamiltonians [12]. In particular, the EPs in  $\mathcal{PT}$ -symmetric structures are useful for observing enhanced sensing [13–15], single-mode lasing [16, 17], coherent perfect absorption [18–20], slow light [21], polarization-state conversion [22], non-reciprocal transmission [23], topologically protected states [24, 26, 68], and so on. Note that the  $\mathcal{PT}$ -symmetry breaking at the EP can be treated in terms of transition between the  $\mathcal{PT}$ -symmetric phase and broken- $\mathcal{PT}$ -symmetry phase being one more application of the concept of phase transitions in the laser and optical physics [27, 28].

On the other hand, in the last decade much attention has been paid to the so-called bound states in the continuum (BICs) predicted first in quantum systems [29]. BICs can be considered as point features in reflection or scattering spectra of optical structures, arising, for example, when several resonant responses (modes) are superimposed [30–33]. As a result of such superposition at a certain frequency and angle of light incidence, resonance states having ideally an infinitely high (divergent) quality ( $Q$ ) factors can arise. Such states are characterized by perfect localization of radiation and, as a consequence, cannot be excited by light incident on the structure from outside, i.e., the BICs are dark (trapped) modes decoupled from the continuum of radiation. Although strict BICs are unobservable, slightly deviating from the ideal BIC conditions, it is possible to excite quasi-BICs arising in the form of very narrow (high- $Q$ ) Fano resonances. In the optical context, BICs (although not under this name) were first shown to exist in photonic crystal structures in Refs. [34–36]. Subsequently, BICs have been observed or theoretically discussed in arrays of dielectric and metal-dielectric elements [37–40], waveguide structures [41–43], photonic crystals [44–45], metamaterials and metasurfaces [46–48], and even single dielectric nanoparticles [49, 50]. Potential applications of quasi-BICs

✉ dvnovitsky@gmail.com

include enhancement of nonlinear response [51, 52], lasing [53, 54], generation of optical vortices [53, 56], and sensing [57, 58].

Peculiar BICs appear in non-Hermitian systems and their existence is tightly connected with the EPs. In particular, it was predicted that the BICs can be observed in the broken- $\mathcal{PT}$ -symmetry regime in one- and two-dimensional waveguide systems with loss and gain [59–61]. Another type of BICs was shown to exist in both  $\mathcal{PT}$ -symmetric and broken- $\mathcal{PT}$ -symmetry phases within the coupled-waveguides framework [62]. Specific BIC-like unstable states can exist at the EPs of non-Hermitian defective lattices [63]. Unconventional BICs were reported to appear in the anti- $\mathcal{PT}$ -symmetric phase in the cavity-magnonics systems [64] and open quantum systems with  $\mathcal{PT}$ -symmetric defects [65]. However, the presence of the EP is not a necessary condition for BICs assisted by loss and gain, since the non-Hermiticity can be used for controlling coupling between resonances lying behind the quasi-BIC phenomenon [66, 67]. Finally, a novel mechanism for generation of the BICs outside the scope of the EP physics was proposed in the BIC-supporting systems under  $\mathcal{PT}$ -symmetric perturbation [68].

In this paper, starting with the system supporting a BIC in the Hermitian limit, we study how properties of the BIC alter when loss and gain are introduced. In particular, we consider the  $\mathcal{PT}$ -symmetric layered system containing an epsilon-near-zero (ENZ) material. It was shown recently that the systems with singular (ENZ-like) properties possess BICs caused by coupling between plasmonic and Fabry-Perot resonances [69]. In general, the BIC-supporting one-dimensional (layered) structures require either materials with singular properties or anisotropic media for mixing light of different polarizations [43, 70]. Subsequently, the unique optical, thermal, and topological properties of the ENZ-related BICs have been studied in detail [71–73]. We put these BICs into the context of the  $\mathcal{PT}$  symmetry research by adding balanced loss and gain. This was shown to lead to appearance of the quasi-BIC [74], but the specific mechanism of BIC transformation into quasi-BIC has not been revealed yet. Here, we fill in this gap and show that the high- $Q$  quasi-BIC resonances in the ENZ-containing  $\mathcal{PT}$ -symmetric layered systems are induced by the coincidence of the BIC with a singular point of the  $\mathcal{PT}$ -symmetry breaking phase diagram. The non-Hermiticity magnitude (loss and gain value) takes on the role of the structure asymmetry parameter leading to the peculiar quasi-BIC with symmetric line shape, perfect transmission and strong light localization inside the structure. We note that the distinction between the true BIC and quasi-BIC is important for our discussion, although the quasi-BICs can be often treated just as the BICs in many realistic situations. Thus, the  $\mathcal{PT}$ -symmetry-breaking singularity offers a novel mechanism behind the excitation of quasi-BICs extending the remarkable diversity of BIC physics known nowadays.

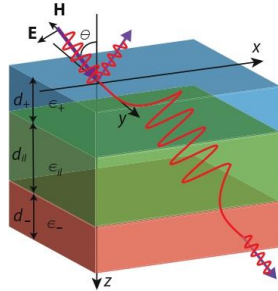


Figure 1. Schematic of a  $\mathcal{PT}$ -symmetric trilayer with outer layers containing lossy and gainy ENZ media and dielectric interlayer in between. The outer layers have the thickness  $d_{\pm} = \lambda_p/2\pi$  (i.e.,  $\omega_p d_{\pm}/c = 1$ , where  $c$  is the speed of light); the interlayer has the thickness  $d_{il} = 10d_{\pm}$  and permittivity  $\epsilon_{il} = 5$ .

## II. $\mathcal{PT}$ -SYMMETRIC TRILAYERS

We start with description of our  $\mathcal{PT}$ -symmetric system and the origin of phase transition there. The simplest  $\mathcal{PT}$ -symmetric layered structure is the bilayer one, which is a well-studied system, see, e.g., our recent analysis [75]. The  $\mathcal{PT}$ -symmetric bilayer consists of just two layers – one with loss (permittivity  $\epsilon_+$ ) and another with gain ( $\epsilon_-$ ). The  $\mathcal{PT}$ -symmetric trilayer has an additional interlayer (spacer) with the real-valued permittivity  $\epsilon_{il}$  located between the loss and gain side layers (see Fig. 1). Trilayers are much less studied and are in the spotlight of this paper. The introduction of the loss-free and gain-free interlayer dramatically changes the phase transition patterns of the system.

We study availability of phase transitions, that is  $\mathcal{PT}$ -symmetry breaking, in trilayers as a function of light-wave angle of incidence. The  $\mathcal{PT}$ -symmetry breaking phenomenon can be described in terms of the scattering matrix eigenvalues and eigenvectors. The scattering matrix of a multilayered structure has the form  $\hat{S} = \begin{pmatrix} t & r_R \\ r_L & t \end{pmatrix}$ , where  $t$  is the transmission coefficient,  $r_L$  and  $r_R$  are the reflection coefficients for the left- and right-incident waves [75]. Eigenvalues  $s_{1,2}$  of the matrix  $\hat{S}$  are known to be both unimodular ( $|s_{1,2}| = 1$ ) in the  $\mathcal{PT}$ -symmetric state and inversely proportional ( $|s_1| = 1/|s_2|$ ) in the broken- $\mathcal{PT}$ -symmetry state. Point of the phase transition where behavior of the eigenvalues  $s_{1,2}$  dramatically changes is the exceptional point. Eigenvectors of the scattering matrix  $\hat{S}$  coincide at the EP, so that the system becomes degenerate there. Transmission and reflection coefficients used in the scattering matrix formulation can be calculated with the well-known transfer-matrix method. We limit our consideration to the TM polarization (see Appendix A for details) to deal with plasmon excitation.

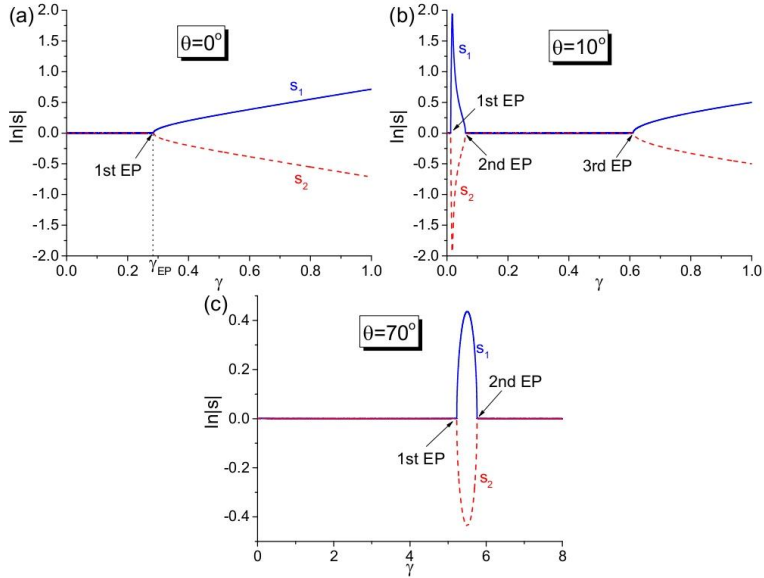


Figure 2. Dependence of the logarithm of the scattering-matrix eigenvalues on the loss and gain coefficient  $\gamma$  for the  $\mathcal{P}$ -symmetric trilayer. The light frequency is  $\omega = \omega_p$ ; three different incidence angles are (a)  $\theta = 0^\circ$ , (b)  $\theta = 10^\circ$ , and (c)  $\theta = 70^\circ$ . We employ parameters of the structure indicated in the caption of Fig. 1.

We take the permittivities  $\varepsilon_+$  and  $\varepsilon_-$  of the loss and gain layers, respectively, as

$$\varepsilon_{\pm} = 1 \pm i\gamma - \frac{\omega_p^2}{\omega^2}, \quad (1)$$

where  $\gamma > 0$  is the loss or gain coefficient (non-Hermiticity magnitude) and  $\omega_p$  is the plasma frequency. We are interested in the ENZ regime observed in the vicinity of  $\omega_p$ , since in this case a trilayer could support a BIC [69]. There are several reasons, why we use Eq. (1) instead of the standard Drude formula as in Ref. [69]. First, the permittivity (1) allows one to separate the effects of ENZ and non-Hermiticity, so that the physical picture becomes as clear as possible. Second, Eq. (1) can be obtained from the Drude formula  $\varepsilon = 1 - \omega_p^2 / (\omega^2 + i\Gamma\omega)$  under  $|\Gamma| \ll \omega$  and  $\gamma \approx \Gamma\omega_p^2 / \omega^3 \approx \Gamma / \omega_p$ , when we are able to neglect dependence of  $\gamma$  on the frequency considering a relatively narrow range near  $\omega_p$ . (See Appendix G for calculations showing that the main results of this paper can be reproduced with the Drude dispersion as well.) Third, since we are interested in determining a dependence of the

system response on the loss and gain level, the easiest way is just to vary  $\gamma$  freely at a given frequency. Such variations are most comprehensible from Eq. (1). Finally, if the first term of  $\varepsilon_{\pm}$  took non-unit values, then it would result only in shifting the ENZ condition to a different frequency. The ENZ media needed can be realized either with the well-known Drude materials [76], such as metals and transparent conducting oxides (although introduction of gain in these materials is not always feasible in practice [73]), or with a low-loss zero-index metamaterial for the ENZ component [69, 77, 79] and the loss or gain material embedded in it. Thus, the choice of the permittivity in the form of Eq. (1) does not limit the generality of our analysis and allows us to consider both ENZ and non-Hermiticity effects in a simple, convenient way. The thicknesses of the loss and gain layers are supposed to be the same,  $d_+ = d_-$ ; the interlayer is characterized with  $\varepsilon_H$  and  $d_H$ ; in the case of a bilayer, one should set  $d_H = 0$ .

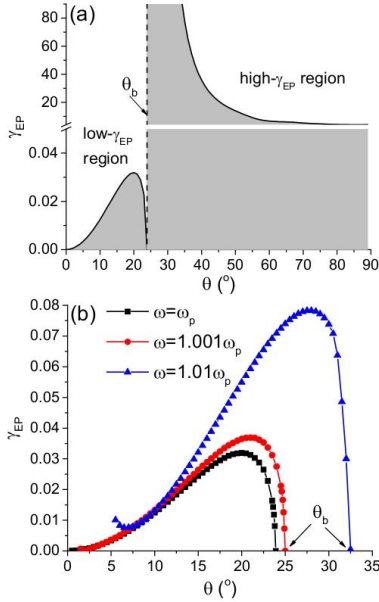


Figure 3. The EP loss and gain level,  $\gamma_{EP}$ , as a function of the angle of incidence for the  $\mathcal{PT}$ -symmetric trilayer. (a) Full angular dependence at  $\omega = \omega_p$ . The gray area corresponds to  $\gamma < \gamma_{EP}$ , where  $\mathcal{PT}$  symmetry is preserved. (b) The low- $\gamma_{EP}$  region for the three different frequencies around  $\omega_p$ . Parameters of the structure are the same as in Fig. 1.

### III. PHASE TRANSITIONS IN $\mathcal{PT}$ -SYMMETRIC TRILAYERS

Let us study behavior of the minimal loss and gain levels corresponding to the first EP (we denote it as  $\gamma_{EP}$ ) as a function of the angle of incidence  $\theta$ . Several examples of curves for scattering matrix eigenvalues  $|s_1|$  and  $|s_2|$  illustrating the  $\mathcal{PT}$ -symmetry breaking are shown in Fig. 2. The point  $\gamma = \gamma_{EP}$ , in which the curves for  $|s_1|$  and  $|s_2|$  diverge is called the exceptional point. One can see that at normal incidence, the  $\mathcal{PT}$ -symmetry breaking occurs for comparatively large non-Hermiticity magnitude,  $\gamma_{EP} \approx 0.285$  [see Fig. 2(a)]. On the contrast, at  $\theta = 10^\circ$ , the loss and gain needed for the EP are much lower,  $\gamma_{EP} \approx 0.0125$  [see Fig. 2(b)]. Finally, at the large incident angle  $\theta = 70^\circ$ , the non-Hermiticity magnitude needed for reaching the first EP gets much larger,  $\gamma_{EP} \approx 5.2$

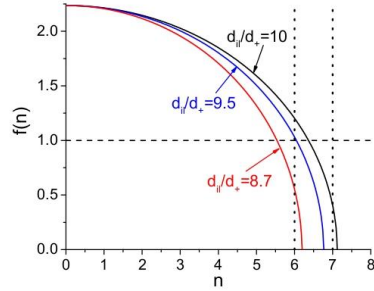


Figure 4. Plot of the function  $f(n) = \sqrt{\epsilon_{il} - \left(\frac{\pi cn}{\omega_p d_{il}}\right)^2}$  for different interlayer thicknesses. The other parameters of the structure are the same as in Fig. 1.

[see Fig. 2(c)]. One can also see in Fig. 2 the second and third EPs at higher levels of the non-Hermiticity parameter. Further, we focus on the first EP and study the transition between the low- $\gamma_{EP}$  and high- $\gamma_{EP}$  regions. The behavior of other EPs is briefly discussed in Appendix B.

In Fig. 3(a), the dependence  $\gamma_{EP}(\theta)$  for the first EP is shown at  $\omega = \omega_p$ . We see that the full angular range is divided into two regions, where  $\gamma_{EP}$  takes on either low or high values. The boundary between these regions denoted as  $\theta_b$  is a peculiar singular point: As we reach  $\theta_b$  from the left,  $\gamma_{EP} \rightarrow 0$  (violation of the  $\mathcal{PT}$  symmetry is easily reached), whereas  $\gamma_{EP} \rightarrow \infty$  just above  $\theta_b$  (the  $\mathcal{PT}$  symmetry is never broken). Even finite, but large values of the loss and gain ( $\gamma_{EP} > 4$ ) needed for breaking the  $\mathcal{PT}$  symmetry at large angles  $\theta > \theta_b$  make the phase transition hardly observable or even impossible. Thus, system's behavior strongly differs in the low- $\gamma_{EP}$  and high- $\gamma_{EP}$  regions.

Using the transfer matrix of the structure, the value of  $\theta_b$  can be estimated analytically at  $\omega = \omega_p$ . Indeed, the singular point corresponds to the condition  $|t| > 1$  for  $\gamma \rightarrow \infty$ , that is the  $\mathcal{PT}$ -symmetry breaking occurs only for very large loss and gain as we reach  $\theta_b$  from the high- $\gamma_{EP}$  side. A simple estimate reads as follows

$$\theta_b(\omega = \omega_p) = \arcsin \sqrt{\epsilon_{il} - \left(\frac{\pi cn}{\omega_p d_{il}}\right)^2}, \quad (2)$$

where  $n$  is an integer number. Derivation of Eq. (2) is discussed in Appendix C. To clearly represent how this estimate can be used, in Fig. 4 we plot the function  $f(n) = \sqrt{\epsilon_{il} - \left(\frac{\pi cn}{\omega_p d_{il}}\right)^2}$ , where  $n$  is assumed to be continuous. In the case of  $d_{il} = 10d_{\pm}$  discussed in Fig. 3(a) there is a single discrete value  $n = 7$  satisfying the sine-value limitation,  $0 \leq f(n) \leq 1$ . So, for  $n = 7$ , we obtain  $\theta_b \approx 23.881^\circ$  which is in perfect agreement with numerical calculations shown in

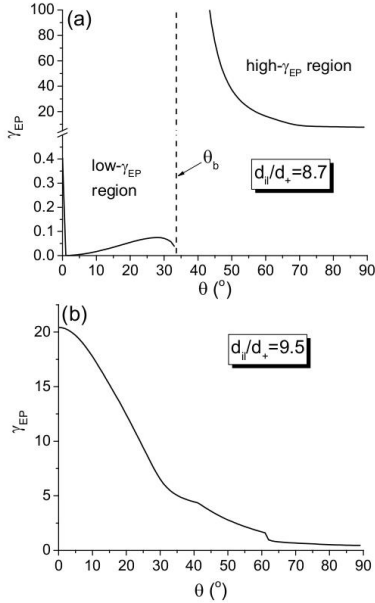


Figure 5. The EP loss and gain level,  $\gamma_{EP}$ , as a function of the incident angle for different interlayer thicknesses (a)  $d_{ij} = 8.7d_{\pm}$  and (b)  $d_{ij} = 9.5d_{\pm}$  of the  $\mathcal{PT}$ -symmetric trilayer. The other parameters of the structure are the same as in Fig. 1.

Fig. 3(a).

To illustrate that this approach works for other situations as well, we consider two other cases. For  $d_{ij} = 8.7d_{\pm}$ , one should take  $n = 6$  to obtain  $\theta_b \approx 33.571^\circ$ . This is supported by numerical calculations of  $\gamma_{EP}$  shown in Fig. 5(a): we again see the low- $\gamma_{EP}$  and high- $\gamma_{EP}$  regions below and above  $\theta_b$ . On the contrary, for  $d_{ij} = 9.5d_{\pm}$ , there is no any suitable discrete  $n$  satisfying  $0 \leq f(n) \leq 1$ . As a result, high- and low- $\gamma_{EP}$  regions are not available in this case [see Fig. 5(b)]:  $\gamma_{EP}$  changes monotonously and there are no any breaks.

The dependencies  $\gamma_{EP}(\theta)$  for several light frequencies in the low- $\gamma_{EP}$  region are demonstrated in Fig. 3(b). In order to make the figure more readable, we do not show the low-angle data with higher  $\gamma_{EP}$  observed in Fig. 3(a). It is clear from Fig. 3(b) that the low- $\gamma_{EP}$  region gets wider and  $\theta_b$  shifts to higher angles, when the frequency is above the plasma one. We would like also to draw attention to the sharp break of the curves near the singular point indicating a potential for

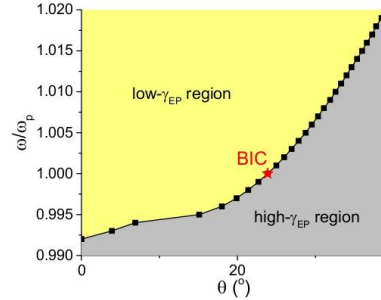


Figure 6. Phase diagram of the  $\mathcal{PT}$ -symmetric trilayer in the “frequency – angle” coordinates. Parameters of the structure are the same as in Fig. 1.

significant modification of the structure response with a tender tuning of the angle of incidence.

As demonstrated in Fig. 6, the full “frequency – angle” plane is divided into two regions possessing different behaviors. In the low(high)- $\gamma_{EP}$  region, the  $\mathcal{PT}$ -symmetry breaking is easily (hardly) achievable. A sharp boundary between the low- and high- $\gamma_{EP}$  regions consists of singular points, in which the value of  $\gamma_{EP}$  is not determined. It is important that changing the permittivity and thickness of the interlayer, we can vary widely these regions in the phase diagram. The brief discussion of the interlayer thickness influence can be found in Appendix D. Thus, the interlayer being just a lossless dielectric strongly influences the response of the  $\mathcal{PT}$ -symmetric trilayer structures, what can be useful in sensing applications.

#### IV. QUASI-BICS VIA THE $\mathcal{PT}$ -SYMMETRY BREAKING

Let us demonstrate how the singular point discussed above can be used for controlling quasi-BICs in ENZ-containing layered structures. It is known that a certain trilayer possesses a BIC at the plasma frequency and a certain incident angle given by  $\theta_{BIC} = \arcsin \sqrt{\epsilon_{ij} - (\pi c n / \omega_p d_{ij})^2}$  with  $n = 0, 1, 2, \dots$  [69]. This type of the BIC is the result of exact destructive interference between the narrowband volume-plasmon resonance in the ENZ layers and the broad Fabry-Perot resonance of the dielectric interlayer. When we detune from the BIC position, the imperfect interference manifests in the spectra as asymmetric Fano profiles. An example is shown in Fig. 7(a): the narrow dips in reflection of lossless structure ( $\gamma = 0$ ) appear as we depart from the BIC angle to  $\theta_{\pm} = \theta_{BIC} \pm 5^\circ$ .

One can see that the BIC given by the above expression coincides with the singular point Eq. (2) of the phase diagram at the plasma frequency, i.e.,  $\theta_{BIC} = \theta_b$ . This fact can be understood in terms of the scattering-matrix poles and zeros whose convergence gives rise to both BICs [69] and singular points

of  $\mathcal{PT}$ -symmetric systems [80, 81]. It should be stressed that the convergence for BICs and EP singularities has different nature. For the BIC in the passive structure without loss and gain, the Hermitian zero and pole coalesce at the real axis. The pole and zero correspond to the volume plasmon and Fabry-Perot modes, respectively. For the EP singularity, the non-Hermitian zero and pole coalesce at the real axis as well. The coalescence is associated with the simultaneous coherent perfect absorption (CPA) and lasing when transmission is simultaneously infinite and zero. This interpretation is confirmed by the sharp Fano profiles seen at  $\theta_{\pm}$  in Fig. 7(c) with a very close dip (absorber) and peak (amplifier). Dip-peak pairs appear at the corresponding points of the singular borderline between the high- $\gamma_{EP}$  and low- $\gamma_{EP}$  regions in Fig. 6 featuring the CPA-lasing effect. The point at  $\omega_p$  and  $\theta_{BIC} = \theta_b$  is a degenerate point (“BIC + CPA-lasing”) emerging due to the very peculiar conditions of the ENZ singularity and volume-plasmon excitation at the plasma frequency and, thus, having very special properties discussed in the rest of this paper. In particular, excitation of the BIC making the radiation to be mostly concentrated inside the structure also suppresses the CPA-lasing and results in the symmetric (Lorentzian) line-shape.

The coincidence of  $\theta_{BIC}$  and  $\theta_b$  has far-reaching consequences. In particular, just below the boundary, the  $\mathcal{PT}$  symmetry can be broken by any loss and gain value, no matter how small. As a result, a sharp resonance appears in the place of BIC as shown in Figs. 7(b) and 7(c), so that the strict BIC transforms into the quasi-BIC. The resonance width reduces, when  $\gamma$  decreases. The side resonances at  $\theta_{\pm}$  which can be also associated with the border between regions in Fig. 6(a) clearly have the Fano profile with the regions of gain-assisted reflection above the unity especially pronounced in Fig. 7(c). The results remain essentially the same for the inverted structure “gainy layer – interlayer – lossy layer” (i.e., when light impinges the gainy layer) with the correction for the Fano profiles inversion.

We would like to emphasize that the quasi-BIC resonance at  $\theta_{BIC}$  is characterized by the transmission which is close to the unity as shown in Fig. 7(d). In other words, this quasi-BIC is effectively free of both absorption and amplification. This property is kept when the non-Hermiticity magnitude increases: the resonance gets wider, but still close to the unity in the transmission peak. We explain this fact with the perfect loss and gain symmetry of the system in conditions of the BIC, what makes our system different from other examples of loss-induced quasi-BICs with resonant increase in absorption as in Refs. [73, 82]. On the contrary, the side resonances at  $\theta_{\pm}$  have rapidly growing transmission and reflection when  $\gamma$  increases. Note that we limit ourselves to relatively low realistic  $\gamma$ s, since for larger ones,  $\gamma \sim 1$ , the effects of instability (such as lasing) are able to violate the perfect transmission.

Figure 8 shows the angular analog of Fig. 7. We see again the absence of the reflection dip at the plasma frequency for the lossless structure [Fig. 8(a)]. Introduction of the loss and gain transforms the BIC into the quasi-BIC at the singular point  $\theta_{BIC}$  with the narrow resonance at  $\omega_p$  and wider Fano resonances at other frequencies [Figs. 8(b) and 8(c)]. Finally,

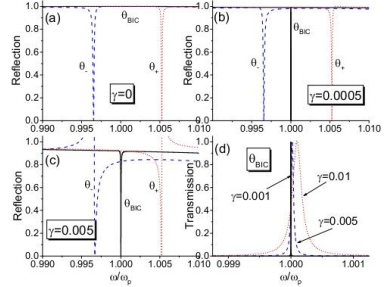


Figure 7. (a)-(c) Reflection and (d) transmission spectra of the  $\mathcal{PT}$ -symmetric trilayer for different loss and gain levels  $\gamma$ . The spectra for the incident angles  $\theta_{BIC}$  and  $\theta_{\pm} = \theta_{BIC} \pm 5^\circ$  are shown. The other parameters are the same as in Fig. 11

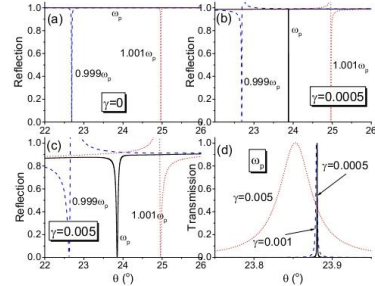


Figure 8. (a)-(c) Reflection and (d) transmission angular spectra of the  $\mathcal{PT}$ -symmetric trilayer for different loss and gain levels  $\gamma$ . The spectra at the frequencies  $\omega_p$ ,  $0.999\omega_p$  and  $1.001\omega_p$  are shown. The other parameters are the same as in Fig. 7

the transmission spectra in Fig. 8(d) demonstrate both widening and shift of the quasi-BIC resonance, when  $\gamma$  increases, the peak transmission being almost equal to the unity. Note that the resonance shifts to the lower angles, that is into the low- $\gamma_{EP}$  region as in Fig. 7.

Symmetric shape of the resonances in Figs. 7(d) and 8(d) is a distinctive feature of some quasi-BICs as verified experimentally for individual nanoparticles [83]. A small blue shift of the quasi-BIC resonance evident from Fig. 7(d) is caused by two reasons: (i) imperfect ENZ condition for a nonzero  $\gamma$  and (ii) availability of low- $\gamma_{EP}$  values above  $\omega_p$ . We also emphasize the necessity of the balanced loss and gain for existing the quasi-BIC discussed, because there are no any resonances at  $\theta_{BIC}$  for loss only as shown in Appendix B. The sustained

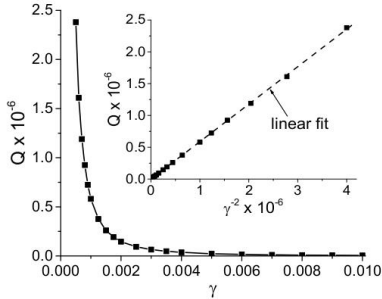


Figure 9. Dependence of the  $Q$  factor of the quasi-BIC resonance on the loss and gain level  $\gamma$ . The  $\mathcal{PT}$ -symmetric trilayer is the same as in Fig. 7. The inset demonstrates the linear dependence of  $Q$  on  $\gamma^{-2}$ .

unity transmission resonance can be of interest for applications in tunable filtering and enhanced sensing, the tunability being caused by the influence of thickness and permittivity of the interlayer on the BIC position.

The narrow quasi-BIC resonances discussed above possess extremely high  $Q$  factors. Due to their symmetry, we can utilize a simple estimate,  $Q = \omega_0 / \Delta\omega$ , where  $\omega_0 \approx \omega_p$  is the resonance central frequency (we take into account its slight shift with increasing  $\gamma$ ),  $\Delta\omega$  is the resonance full-width at half maximum which can be directly estimated from the plots without any fitting. Figure 9 demonstrates a sharp increase of the  $Q$  factor when decreasing loss and gain level  $\gamma$ , so that  $Q$  readily exceeds  $10^6$  for  $\gamma < 10^{-3}$ . Moreover, the inset of Fig. 9 demonstrates a linear dependence of the  $Q$ -factor on the inverse square of  $\gamma$ . Such a behavior is a well-known characteristic of the BIC violated by asymmetry [47]. The asymmetry is often introduced to transform the exact unobservable BIC of the perfect structure to the observable quasi-BIC of the non-ideal system (e.g., the asymmetry may be due to a nonzero angle between elements of the structure as in Ref. [47]). In our case, the non-Hermiticity magnitude  $\gamma$  takes on the role of the structure asymmetry parameter, although the loss and gain are balanced and the shape of the quasi-BIC remains symmetric (so that the Fano asymmetry factor is infinite). This means that the asymmetry inducing the transform of BIC into the quasi-BIC is caused exclusively by breaking  $\mathcal{PT}$  symmetry.

High  $Q$  factors correspond to the strong light localization inside the system as shown directly in our calculations of the intensity distribution inside the  $\mathcal{PT}$ -symmetric trilayer (Fig. 10) using the method described in Appendix B. One can see that the quasi-BIC resonance is characterized by the symmetric intensity distribution due to loss compensation by gain [see Fig. 10(b)]. Note also that the peaks of the stationary interference pattern inside the interlayer have very high intensity in perfect accordance with the large value of the  $Q$  factor. De-

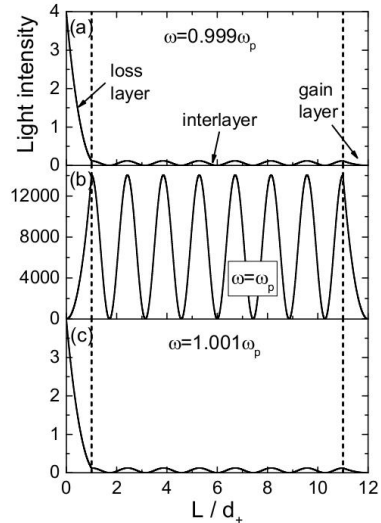


Figure 10. Normalized intensity distributions inside the  $\mathcal{PT}$ -symmetric trilayer for  $\gamma = 0.001$  and  $\theta = \theta_{BIC}$  at the frequencies (a), (d)  $0.999\omega_p$ , (b), (e)  $\omega_p$ , and (c), (f)  $1.001\omega_p$ . The other parameters are the same as in Fig. 7.

tuning from  $\omega_p$  results in asymmetric low-intensity distributions with attenuation in the loss layer uncompensated by the amplification in the gain layer [see Figs. 10(a) and 10(c)]. We would like to mention that the distributions almost do not change, if we swap the loss and gain layers.

## V. CONCLUSION

To sum up, we have studied violation of the  $\mathcal{PT}$  symmetry in trilayer structures with balanced loss and gain. We prove that when the loss and gain layers are ENZ media, an extraordinary singular point of the  $\mathcal{PT}$ -symmetry-breaking phase diagram coincides with the BIC position enabling appearance of the high- $Q$  perfect-transmission resonance with the loss and gain value playing a role of the structure asymmetry parameter. We believe that this new way of quasi-BICs generation induced by  $\mathcal{PT}$ -symmetry breaking is of general interest and applicable in development of non-Hermitian photonics. To observe this effect in more complex structures supporting BICs, one has to tune conditions for the phase-diagram singularity of the  $\mathcal{PT}$ -symmetric system to match it with the BIC position of the same structure without loss and gain. From the



different perspective, the poles and zeros of the lossless and  $\mathcal{PT}$ -symmetric structures should converge at the same point of the parameter space. In our case, this condition is fulfilled at the peculiar point of the ENZ (at the plasma frequency). For sophisticated photonic structures, this condition can be more intricate.

#### ACKNOWLEDGMENTS

The work was supported by the Belarusian Republican Foundation for Fundamental Research (Project No. F20R-158) and the Russian Foundation for Basic Research (Project No. 20-52-00031).

#### Appendix A: Basics of the transfer-matrix method

The transfer-matrix method is a convenient approach for calculation of stationary response of layered structures. We use it in the form presented in the Novotny and Hecht textbook [84]. Let us briefly describe the main points of this method, since they will be used in further derivations. Limiting ourselves to the TM-polarized plane waves, the relation between the amplitudes of the incident wave  $e_0$ , reflected wave  $r$  and transmitted wave  $t$  can be written as follows,

$$\begin{pmatrix} e_0 \\ r \end{pmatrix} = M \begin{pmatrix} t \\ 0 \end{pmatrix}. \quad (\text{A1})$$

The total transfer matrix  $M = T_{01}\Phi_1 T_{12}\Phi_2 \dots \Phi_n T_{n,n+1}$  is the product of the matrices  $T_{i-1,i}$  taking into account light refraction at the interfaces between layers,

$$T_{i-1,i} = \frac{1}{2} \begin{pmatrix} 1 + \kappa_i \eta_i & 1 - \kappa_i \eta_i \\ 1 - \kappa_i \eta_i & 1 + \kappa_i \eta_i \end{pmatrix}, \quad (\text{A2})$$

and the matrices  $\Phi_i$  taking into account light propagation inside layers,

$$\Phi_i = \begin{pmatrix} e^{-ik_{i,z}d_i} & 0 \\ 0 & e^{ik_{i,z}d_i} \end{pmatrix}. \quad (\text{A3})$$

Here  $\kappa_i = k_{i-1,z}/k_{i,z} = \sqrt{(\epsilon_{i-1} - \sin^2 \theta)/(\epsilon_i - \sin^2 \theta)}$  is the ratio of longitudinal components of the wavevector in neighboring layers,  $\eta_i = \epsilon_i/\epsilon_{i-1}$  is the ratio of the adjacent-layers permittivities,  $\theta$  is the light incident angle,  $d_i$  is the  $i$ th layer thickness. The 0th and  $(n+1)$ th layers correspond to the semi-infinite ambient media, which we assume to be the air. Knowing the full transfer matrix of the structure  $M$ , one can easily compute the reflection and transmission coefficients normalized to the incident wave amplitude (i.e.,  $e_0 = 1$  is assumed) as  $t = 1/M_{11}$ ,  $r_L = M_{21}/M_{11}$ , and  $r_R = -M_{12}/M_{11}$ , where  $M_{ij}$  is the corresponding component of the matrix  $M$ .

#### Appendix B: Positions of different EPs

As we have seen in Fig. 2 the system may have several EPs at the same angle of incidence. In the main text, we have

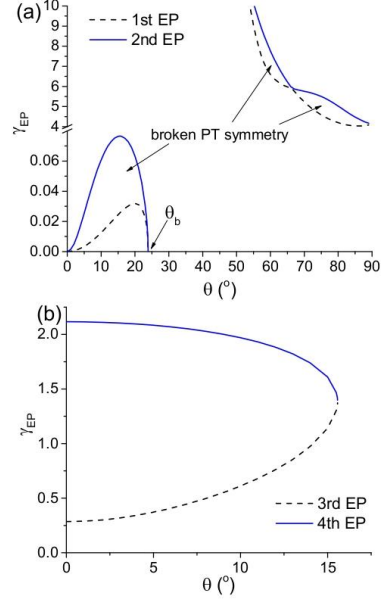


Figure 11. Angular dependencies of the positions of (a) the 1st and 2nd EPs and (b) 3rd and 4th EPs. The frequency is  $\omega = \omega_p$ ; the other parameters are the same as in Fig. 10

focused on the first EP as the most important one for us. In Fig. 11 we show change of positions of different EPs as a function of  $\theta$ . Regions of broken  $\mathcal{PT}$  symmetry lie between the 1st and 2nd EPs as well as between the 3rd and 4th EPs. The latter region exists only at small incident angles. When approaching the singular point  $\theta_b$ , the region of broken  $\mathcal{PT}$  symmetry between the 1st and 2nd EPs gets narrower.

#### Appendix C: Derivation of the boundary angle value for the trilayer

The boundary angle  $\theta_b$  (singular point) can be estimated from the condition of  $|r| > 1$  for  $\gamma \gg 1$ . In terms of the transfer matrix, this means that  $|M_{11}| < 1$  for  $\gamma \gg 1$ . For the three-layer structure discussed in the main text, we can give a relatively simple derivation of the transfer matrix at the plasma frequency. Indeed, for  $\omega = \omega_p$  and  $\gamma \gg 1$ , the following relations are reduced to  $\epsilon_{\pm} = \pm i\gamma$ ;  $\eta_1 =$

$i\gamma = -1/\eta_0$ ,  $\eta_2 = \epsilon_{il}/i\gamma = -1/\eta_3$ ;  $k_{1,z} \approx k_0(1+i)\sqrt{\gamma/2} = -ik_{3,z}$ ,  $k_{2,z} = k_0\sqrt{\epsilon_{il} - \sin^2\theta}$ ;  $\kappa_1 \approx \cos\theta/\sqrt{i\gamma} = i/\kappa_3$ ,  $\kappa_2 \approx \sqrt{i\gamma/(\epsilon_{il} - \sin^2\theta)} = -i/\kappa_3$ , where  $k_0 = \omega_p/c$ . After some algebra, we obtain for the transfer matrix component of interest

$$|M_{11}| \approx 2\gamma e^{\sqrt{2}\gamma} \cos\theta \sqrt{1 - \frac{\sin^2\theta}{\epsilon_{il}}} \left| \sin\left(k_0 d_{il} \sqrt{\epsilon_{il} - \sin^2\theta}\right) \right|, \quad (C1)$$

For arbitrarily large  $\gamma$ , this value remains limited only for arbitrarily small sine term. Thus, for  $\gamma \rightarrow \infty$ , the equation for the boundary angle  $\theta_b$  reads

$$\sin\left(\frac{\omega_p}{c} d_{il} \sqrt{\epsilon_{il} - \sin^2\theta_b}\right) = 0, \quad (C2)$$

which has the solution

$$\theta_b = \arcsin\sqrt{\epsilon_{il} - \left(\frac{\pi cn}{\omega_p d_{il}}\right)^2}, \quad (C3)$$

where  $n = 0, 1, 2, \dots$

#### Appendix D: EP position as a function of the interlayer thickness

Here, we briefly discuss the influence of the interlayer thickness  $d_{il}$  on the response of the structure. In the main text, we have considered mostly the case  $d_{il}/d_{\pm} = 10$  and seen the line of singular points in Fig. 6 and the BIC at the plasma frequency. On the contrary, the bilayer ( $d_{il} = 0$ ) does not support such features. In order to trace the transition between these two cases, we fix  $\omega = \omega_p$  and  $\theta = 0$  and plot the EP position as a function of  $d_{il}$  in Fig. 12(a). We observe a periodic dependence when regions of easy  $\mathcal{P}$ - $\mathcal{T}$ -symmetry breaking take turns to the regions of tough  $\mathcal{P}$ - $\mathcal{T}$ -symmetry breaking. Such a periodicity means that singular points are attainable not for every interlayer thickness, what is supported by Fig. 12(b): the singularity is seen at  $d_{il}/d_{\pm} = 3$ , but not at  $d_{il}/d_{\pm} = 1$  or 2. Thus, tuning the interlayer thickness is important for realizing the necessary regime of light interaction with the structure.

#### Appendix E: The case of the purely absorbing ENZ media

Here we consider the case of purely lossy media used as a model of the ENZ layers. This means that the permittivities of the first and third layers of the trilayer are the same, being equal to  $\epsilon_{\pm} = 1 + i\gamma - \omega_p^2/\omega^2$  with  $\gamma > 0$ . Reflection spectra at the BIC angle  $\theta_{BIC}$  for different  $\gamma$  are shown in Fig. 13. We start from the strict BIC at  $\gamma = 0$  (there are no resonances). Introducing the loss we break the BIC. However, here the BIC breaks in a fundamentally different way in comparison to the case of balanced loss and gain considered in the main text. Loss causes a wide-band decrease of the reflection due to absorption. This results in the low-reflection background with

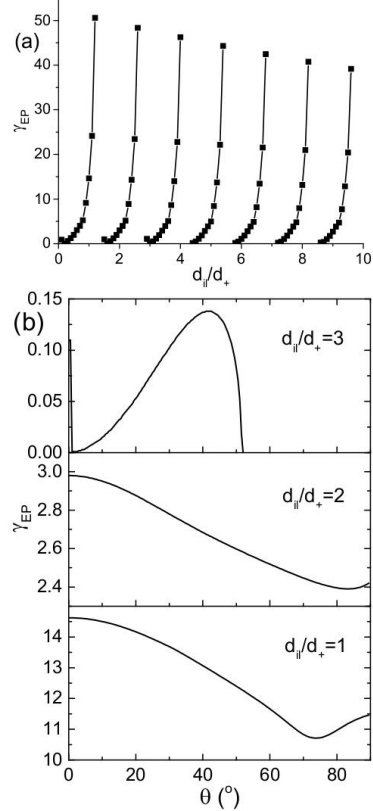


Figure 12. (a) The dependence of  $\gamma_{EP}$  on the interlayer thickness at  $\omega = \omega_p$  and  $\theta = 0$ . (b) The angular dependence of the EP at different interlayer thicknesses at  $\omega = \omega_p$ . The other parameters are the same as in Fig. 11

a peak at the BIC position. In other words, the BIC resists losses and strives for its own preservation. On the contrary, in case of the balanced loss and gain, we see a high-reflection background with a sharp dip due to the easily broken BIC. We can make a conclusion that the loss itself is not the best way to transform a BIC into a quasi-BIC. The balance of the loss

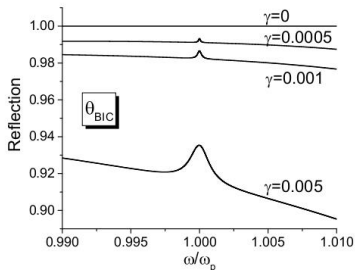


Figure 13. Reflection spectra of the purely lossy trilayer at the incident angle  $\theta_{BIC}$  for different loss levels  $\gamma$  of the first and third layers. The other parameters are the same as in Fig. 7.

and gain is much more efficient.

#### Appendix F: Calculation of intensity distributions inside the trilayer

In order to illustrate features of the perfect-transmission high- $Q$  quasi-BIC at  $\omega = \omega_p$  and  $\theta = \theta_{BIC}$ , we calculate the distributions of the intensity inside the structure at the plasma frequency and neighboring frequencies with the approach described in Ref. [83]. In particular, we divide the layers into many thin sublayers and utilize a partial transfer-matrix  $M^{(i)}$  covering a part of the structure from its input interface to the  $i$ th sublayer as

$$\begin{pmatrix} e_0 \\ r_0 \end{pmatrix} = M^{(i)} \begin{pmatrix} t_i \\ r_i \end{pmatrix}, \quad (F1)$$

where  $r_0$  is the reflection coefficient of the entire structure,  $t_i$  and  $r_i$  are the amplitudes of the forward and backward waves

in the  $i$ th sublayer. Then, we readily get

$$r_i = -\frac{M_{11}^{(i)} r_0 - M_{21}^{(i)} e_0}{M_{11}^{(i)} M_{22}^{(i)} - M_{12}^{(i)} M_{21}^{(i)}}, \quad t_i = \frac{-M_{12}^{(i)} r_0 + M_{22}^{(i)} e_0}{M_{11}^{(i)} M_{22}^{(i)} - M_{12}^{(i)} M_{21}^{(i)}}. \quad (F2)$$

The normalized intensity inside a given sublayer is calculated as  $I_i = |t_i + r_i|^2 / e_0^2$ .

#### Appendix G: Modeling of the ENZ layers permittivity using the Drude model

Here we show that the results obtained in the main text with Eq. (11) are in accordance with analogous calculations performed with the standard Drude formula for the ENZ media,  $\epsilon_{\pm} = 1 - \omega_p^2 / (\omega^2 \pm i\Gamma\omega)$ . Figure 14 corresponds to Fig. 7. Aside from minor changes in the positions of the Fano resonances, the features of the quasi-BICs induced by balanced loss and gain persist in the Drude-model case as well.

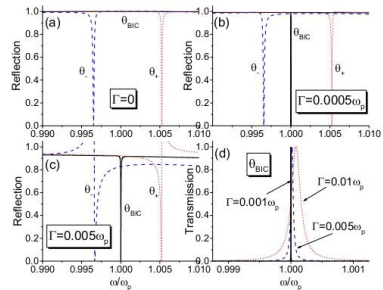


Figure 14. The same as in Fig. 7 but for the loss and gain layers described by the standard Drude formula.

- [1] C. M. Bender and S. Boettcher, Real spectra in non-Hermitian Hamiltonians having  $\mathcal{PT}$  symmetry, Phys. Rev. Lett. **80**, 5243 (1998).
- [2] A. A. Zyablovsky, A. P. Vinogradov, A. A. Pukhov, A. V. Dorofeenko, and A. A. Lisyansky,  $\mathcal{PT}$  symmetry in optics, Phys. Usp. **57**, 1063 (2014).
- [3] L. Feng, R. El-Ganainy, and L. Ge, Non-Hermitian photonics based on parity-time symmetry, Nat. Photon. **11**, 752 (2017).
- [4] R. El-Ganainy, K. G. Makris, M. Khajavikhan, Z. H. Musslimani, S. Rotter, and D. N. Christodoulides, Non-Hermitian physics and  $\mathcal{PT}$  symmetry, Nat. Phys. **13**, 11 (2018).
- [5] S.K. Özdemir, S. Rotter, F. Nori, and L. Yang, Parity-time symmetry and exceptional points in photonics, Nat. Mater. **18**, 783 (2019).

- [6] C. E. Rüter, K. G. Makris, R. El-Ganainy, D. N. Christodoulides, M. Segev, and D. Kip, Observation of parity-time symmetry in optics, Nat. Phys. **6**, 192 (2010).
- [7] A. Regensburger, C. Bersch, M.-A. Miri, G. Onishchukov, D.N. Christodoulides, and U. Peschel, Parity-time synthetic photonic lattices, Nature **488**, 167 (2012).
- [8] M. Kremer, T. Biesenhal, L.J. Maczewsky, M. Heinrich, R. Thomale, and A. Szameit, Demonstration of a two-dimensional  $\mathcal{PT}$ -symmetric crystal, Nat. Commun. **10**, 435 (2019).
- [9] L. Ge, Y. D. Chong, and A. D. Stone, Conservation relations and anisotropic transmission resonances in one-dimensional  $\mathcal{PT}$ -symmetric photonic heterostructures, Phys. Rev. A **85**, 023802 (2012).

- [10] A. V. Hlushchenko, V. I. Shcherbinin, D. V. Novitsky, and V. R. Tuz, Loss compensation symmetry in a multimode waveguide coupler, *Laser Phys. Lett.* **17**, 116202 (2020).
- [11] Y. Liang, Q. Gaimard, V. Klimov, A. Uskov, H. Benisty, A. Ramdane, and A. Lupu, Coupling of nanoantennas in loss-gain environment for application in active tunable metasurfaces, *Phys. Rev. B* **103**, 045419 (2021).
- [12] M.-A. Miri and A. Alù, Exceptional points in optics and photonics, *Science* **363**, eaar7709 (2019).
- [13] W. Chen, S. K. Özdemir, G. Zhao, J. Wiersig, and L. Yang, Exceptional points enhance sensing in an optical microcavity, *Nature (London)* **548**, 192 (2017).
- [14] H. Hodaei, A. U. Hassan, S. Witteck, H. Garcia-Gracia, R. El-Ganainy, D. N. Christodoulides, and M. Khajavikhan, Enhanced sensitivity at higher-order exceptional points, *Nature (London)* **548**, 187 (2017).
- [15] S. Yu, Y. Meng, J.-S. Tang, X.-Y. Xu, Y.-T. Wang, P. Yin, Z.-J. Ke, W. Liu, Z.-P. Li, Y.-Z. Yang, G. Chen, Y.-J. Han, C.-F. Li, and G.-C. Guo, Experimental Investigation of Quantum  $\mathcal{PT}$ -Enhanced Sensor, *Phys. Rev. Lett.* **125**, 240506 (2020).
- [16] L. Feng, Z. J. Wong, R.-M. Ma, Y. Wang, and X. Zhang, Single-mode laser by parity-time symmetry breaking, *Science* **346**, 972 (2014).
- [17] H. Hodaei, M.-A. Miri, M. Heinrich, D. N. Christodoulides, and M. Khajavikhan, Parity-time-symmetric micro-ring lasers, *Science* **346**, 975 (2014).
- [18] S. Longhi,  $\mathcal{PT}$ -symmetric laser absorber, *Phys. Rev. A* **82**, 031801(R) (2010).
- [19] Z. J. Wong, Y.-L. Xu, J. Kim, K. O'Brien, Y. Wang, L. Feng, and X. Zhang, Lasing and anti-lasing in a single cavity, *Nat. Photon.* **10**, 796 (2016).
- [20] D.V. Novitsky, CPA-laser effect and exceptional points in  $\mathcal{PT}$ -symmetric multilayer structures, *J. Opt.* **21**, 085101 (2019).
- [21] T. Goldzak, A. A. Mailybaev, and N. Moiseyev, Light Stops at Exceptional Points, *Phys. Rev. Lett.* **120**, 013901 (2018).
- [22] A. U. Hassan, B. Zhen, M. Soljačić, M. Khajavikhan, and D. N. Christodoulides, Dynamically encircling exceptional points: Exact evolution and polarization state conversion, *Phys. Rev. Lett.* **118**, 093002 (2017).
- [23] D.V. Novitsky, A. Karabchevsky, A.V. Lavrinenko, A.S. Shalin, and A.V. Novitsky,  $\mathcal{PT}$  symmetry breaking in multilayers with resonant loss and gain locks light propagation direction, *Phys. Rev. B* **98**, 125102 (2018).
- [24] S. Weimann, M. Kremer, Y. Plotnik, Y. Lumer, S. Nolte, K. G. Makris, M. Segev, M. C. Rechtsman, and A. Szameit, Topologically protected bound states in photonic parity-time-symmetric crystals, *Nat. Mater.* **16**, 433 (2016).
- [25] A. Y. Song, X.-Q. Sun, A. Dutt, M. Minkov, C. Wójcik, H. Wang, I. A. D. Williamson, M. Orenstein, and S. Fan,  $\mathcal{PT}$ -Symmetric Topological Edge-Gain Effect, *Phys. Rev. Lett.* **125**, 033603 (2020).
- [26] M. Parto, Y. G. N. Liu, B. Bahari, M. Khajavikhan, and D. N. Christodoulides, Non-Hermitian and topological photonics: optics at an exceptional point, *Nanophot.* **10**, 403 (2021).
- [27] V. DeGiorgio and M. O. Scully, Analogy between the Laser Threshold Region and a Second-Order Phase Transition, *Phys. Rev. A* **2**, 1170 (1970).
- [28] F. Xie, M. Ren, W. Wu, D. Yu, W. Cai, and J. Xu, Phase-Transition Optical Activity in Chiral Metamaterials, *Phys. Rev. Lett.* **125**, 237401 (2020).
- [29] J. von Neumann and E. Wigner, Über merkwürdige diskrete Eigenwerte, *Phys. Zeitschrift* **30**, 465 (1929).
- [30] C. W. Hsu, B. Zhen, A. D. Stone, J. D. Joannopoulos, and M. Soljačić, Bound states in the continuum, *Nat. Rev. Mater.* **1**, 16048 (2016).
- [31] S. I. Azzam and A. V. Kildishev, Photonic Bound States in the Continuum: From Basics to Applications, *Adv. Opt. Mater.* **9**, 2001469 (2021).
- [32] K. Koshelev, A. Bogdanov, and Yu. Kivshar, Engineering with Bound States in the Continuum, *Opt. Photon. News* **31(1)**, 38 (2020).
- [33] A. F. Sadreev, Interference traps waves in open system: Bound states in the continuum, *Rep. Prog. Phys.* **84**, 055901 (2021).
- [34] V. N. Astratov, I. S. Culshaw, R. M. Stevenson, D. M. Whitaker, M. S. Skolnick, T. F. Krauss, and R. M. De La Rue, Resonant Coupling of Near-Infrared Radiation to Photonic Band Structure Waveguides, *J. Lightwave Technol.* **17**, 2050 (1999).
- [35] P. Paddon and J. F. Young, Two-dimensional vector-coupled-mode theory for textured planar waveguides, *Phys. Rev. B* **61**, 2090 (2000).
- [36] T. Ochiai and K. Sakoda, Dispersion relation and optical transmittance of a hexagonal photonic crystal slab, *Phys. Rev. B* **63**, 125107 (2001).
- [37] D. C. Marinica, A. G. Borisov, and S. V. Shabanov, Bound states in the continuum in photonics, *Phys. Rev. Lett.* **100**, 183902 (2008).
- [38] E. N. Bulgakov and A. F. Sadreev, Bound states in the continuum in photonic waveguides inspired by defects, *Phys. Rev. B* **78**, 075105 (2008).
- [39] E. N. Bulgakov and D. N. Maksimov, Topological bound states in the continuum in arrays of dielectric spheres, *Phys. Rev. Lett.* **118**, 267401 (2017).
- [40] S. I. Azzam, V. M. Shalaev, A. Boltasseva, and A. V. Kildishev, Formation of Bound States in the Continuum in Hybrid Plasmonic-Photonic Systems, *Phys. Rev. Lett.* **121**, 253901 (2018).
- [41] Y. Plotnik, O. Peleg, F. Dreisow, M. Heinrich, S. Nolte, A. Szameit, and M. Segev, Experimental Observation of Optical Bound States in the Continuum, *Phys. Rev. Lett.* **107**, 183901 (2011).
- [42] S. Weimann, Y. Xu, R. Keil, A. E. Miroshnichenko, A. Tünnermann, S. Nolte, A. A. Sukhorukov, A. Szameit, and Yu. S. Kivshar, Compact Surface Fano States Embedded in the Continuum of Waveguide Arrays, *Phys. Rev. Lett.* **111**, 240403 (2013).
- [43] J. Gomis-Bresco, D. Artigas, and L. Torner, Anisotropy-induced photonic bound states in the continuum, *Nat. Photon.* **11**, 232 (2017).
- [44] J. Lee, B. Zhen, S.-L. Chua, W. Qiu, J. D. Joannopoulos, M. Soljačić, and O. Shapira, Observation and Differentiation of Unique High-Q Optical Resonances Near Zero Wave Vector in Macroscopic Photonic Crystal Slabs, *Phys. Rev. Lett.* **109**, 067401 (2012).
- [45] C. W. Hsu, B. Zhen, J. Lee, S.-L. Chua, S. G. Johnson, J. D. Joannopoulos, and M. Soljačić, Observation of trapped light within the radiation continuum, *Nature (London)* **499**, 188 (2013).
- [46] V. A. Fedotov, M. Rose, S. L. Prosvirnin, N. Papasimakis, and N. I. Zheludev, Sharp Trapped-Mode Resonances in Planar Metamaterials with a Broken Structural Symmetry, *Phys. Rev. Lett.* **99**, 147401 (2007).
- [47] K. Koshelev, S. Leshov, M. Liu, A. Bogdanov, and Yu. Kivshar, Asymmetric Metasurfaces with High-Q Resonances Governed by Bound States in the Continuum, *Phys. Rev. Lett.* **121**, 193903 (2018).
- [48] A. S. Kupriyanov, Y. Xu, A. Sayanskiy, V. Dmitriyev, Yu. S. Kivshar, and V. R. Tuz, Metasurface engineering through bound states in the continuum, *Phys. Rev. Appl.* **12**, 014024 (2019).

- [49] A. A. Bogdanov, K. L. Koshelev, P. V. Kapitanova, M. V. Rybin, S. A. Gladyshev, Z. F. Sadrieva, K. B. Samusev, Yu. S. Kivshar, and M. F. Limonov, Bound states in the continuum and Fano resonances in the strong mode coupling regime, *Adv. Photon.* **1**, 016001 (2019).
- [50] L. Huang, L. Xu, M. Rahmani, D. N. Neshev, and A. E. Miroshnichenko, Pushing the limit of high-Q mode of a single dielectric nanocavity, *Adv. Photon.* **3**, 016004 (2021).
- [51] K. Koshelev, S. Kruk, E. Melik-Gaykazyan, J.-H. Choi, A. Bogdanov, H.-G. Park, and Yu. Kivshar, Subwavelength dielectric resonators for nonlinear nanophotonics, *Science* **367**, 288 (2020).
- [52] E. N. Bulgakov and D. N. Maksimov, Nonlinear response from optical bound states in the continuum, *Sci. Rep.* **9**, 7153 (2019).
- [53] A. Kodigala, T. Lepetit, Q. Gu, B. Bahari, Y. Fainman, and B. Kanté, Lasing action from photonic bound states in continuum, *Nature (London)* **541**, 196 (2017).
- [54] J. S. Toterogongora and A. Fratolocchi, Integrated nanolasers via complex engineering of radiationless states, *J. Phys. Photonics* **3**, 011001 (2021).
- [55] C. Huang, C. Zhang, S. Xiao, Y. Wang, Y. Fan, Y. Liu, N. Zhang, G. Qu, H. Ji, J. Han, L. Ge, Yu. Kivshar, and Q. Song, Ultrafast control of vortex microlasers, *Science* **367**, 1018 (2020).
- [56] B. Wang, W. Liu, M. Zhao, J. Wang, Y. Zhang, A. Chen, F. Guan, X. Liu, L. Shi, and J. Zi, Generating optical vortex beams by momentum-space polarization vortices centred at bound states in the continuum, *Nat. Photon.* **14**, 623 (2020).
- [57] D. N. Maksimov, V. S. Gerasimov, S. Romano, and S. P. Polyutov, Refractive index sensing with optical bound states in the continuum, *Opt. Express* **28**, 38907 (2020).
- [58] Y. Wang, Z. Han, Y. Du, and J. Qin, Ultrasensitive terahertz sensing with high-Q toroidal dipole resonance governed by bound states in the continuum in all-dielectric metasurface, *Nanophot.* **10**, 1295 (2021).
- [59] A. Regensburger, M.-A. Miri, C. Bersch, J. Näger, G. Onishchukov, D.N. Christodoulides, and U. Peschel, Observation of Defect States in  $\mathcal{PT}$ -Symmetric Optical Lattices, *Phys. Rev. Lett.* **110**, 223902 (2013).
- [60] M. I. Molina and Yu. S. Kivshar, Embedded States in the Continuum for  $\mathcal{PT}$ -Symmetric Systems, *Stud. Appl. Math.* **133**, 337 (2014).
- [61] Ya. V. Kartashov, C. Milián, V. V. Konotop, and L. Torner, Bound states in the continuum in a two-dimensional  $\mathcal{PT}$ -symmetric system, *Opt. Lett.* **43**, 575 (2018).
- [62] S. Longhi, Bound states in the continuum in  $\mathcal{PT}$ -symmetric optical lattices, *Opt. Lett.* **39**, 1697 (2014).
- [63] S. Longhi and G. Della Valle, Optical lattices with exceptional points in the continuum, *Phys. Rev. A* **89**, 052132 (2014).
- [64] Y. Yang, Yi-Pu Wang, J. W. Rao, Y. S. Gui, B. M. Yao, W. Lu, and C.-M. Hu, Unconventional Singularity in Anti-Parity-Time Symmetric Cavity Magnonics, *Phys. Rev. Lett.* **125**, 147202 (2020).
- [65] S. Garmon, M. Gianfreda, and N. Hatano, Bound states, scattering states, and resonant states in  $\mathcal{PT}$ -symmetric open quantum systems, *Phys. Rev. A* **92**, 022125 (2015).
- [66] H. K. Gandhi, D. Rocco, L. Carletti, and C. De Angelis, Gain-loss engineering of bound states in the continuum for enhanced nonlinear response in dielectric nanocavities, *Opt. Express* **28**, 3009 (2020).
- [67] H. K. Gandhi, A. Laha, and S. Ghosh, Ultrasensitive light confinement: Driven by multiple bound states in the continuum, *Phys. Rev. A* **102**, 033528 (2020).
- [68] Q. Song, J. Hu, S. Dai, C. Zheng, D. Han, J. Zi, Z. Q. Zhang, and C. T. Chan, Coexistence of a new type of bound state in the continuum and a lasing threshold mode induced by PT symmetry, *Sci. Adv.* **6**, eabc1160 (2020).
- [69] F. Monticone, H. M. Doeleman, W. Den Hollander, A. F. Koenderink, and A. Alù, Trapping Light in Plain Sight: Embedded Photonic Eigenstates in Zero-Index Metamaterials, *Laser Photon. Rev.* **12**, 1700220 (2018).
- [70] P. S. Pankin, B.-R. Wu, J.-H. Yang, K.-P. Chen, I. V. Timofeev, and A. F. Sadreev, One-dimensional photonic bound states in the continuum, *Comm. Phys.* **3**, 91 (2020).
- [71] R. Duggan, Y. Ra’di, and A. Alù, Temporally and spatially coherent emission from thermal embedded eigenstates, *ACS Photon.* **6**, 2949 (2019).
- [72] Z. Sakotic, A. Krasnok, N. Cselusyzka, N. Jankovic, and A. Alù, Berreman embedded eigenstates for narrow-band absorption and thermal emission, *Phys. Rev. Appl.* **13**, 064073 (2020).
- [73] Z. Sakotic, A. Krasnok, A. Alù, and N. Jankovic, Topological scattering singularities and embedded eigenstates for polarization control and sensing applications, *Photon. Res.* **9**, 1310 (2021).
- [74] Z. Sakotic, A. Krasnok, N. Cselusyzka, N. Jankovic, and A. Alù, Coherent Virtual Absorption and Embedded Eigenstates in non-Hermitian  $\mathcal{PT}$ -Symmetrical Systems, in *Conference on Lasers and Electro-Optics, OSA Technical Digest* (Optical Society of America, 2019) FW4D.5.
- [75] A. Novitsky, D. Lyakhov, D. Michels, A. A. Pavlov, A. S. Shalin, and D. V. Novitsky, Unambiguous scattering matrix for non-Hermitian systems, *Phys. Rev. A* **101**, 043834 (2020).
- [76] N. Kinsey, C. DeVault, A. Boltasseva, and V. M. Shalaev, Near-zero-index materials for photonics, *Nat. Rev. Mater.* **4**, 742 (2019).
- [77] A. S. Shalin, Broadband blooming of a medium modified by an incorporated layer of nanocavities, *JETP Lett.* **91**, 636 (2010).
- [78] P. D. Terekhov, H. K. Shamkhi, E. A. Gurvitz, K. V. Baryshnikova, A. B. Evlyukhin, A. S. Shalin, and A. Karabchevsky, Broadband forward scattering from dielectric cubic nanoantenna in lossless media, *Opt. Express* **27**, 10924 (2019).
- [79] P. D. Terekhov, K. V. Baryshnikova, Y. Galutin, Y. H. Fu, A. B. Evlyukhin, A. S. Shalin, and A. Karabchevsky, Enhanced absorption in all-dielectric metasurfaces due to magnetic dipole excitation, *Sci. Rep.* **9**, 3438 (2019).
- [80] Y. D. Chong, L. Ge, and A. D. Stone,  $\mathcal{PT}$ -Symmetry Breaking and Laser-Absorber Modes in Optical Scattering Systems, *Phys. Rev. Lett.* **106**, 093902 (2011).
- [81] A. Krasnok, D. Baranov, H. Li, M.-A. Miri, F. Monticone, and A. Alù, Anomalies in light scattering, *Adv. Opt. Photon.* **11**, 892 (2019).
- [82] Q. Ren, F. Feng, X. Yao, Q. Xu, M. Xin, Z. Lan, J. You, X. Xiao, and W. E. I. Sha, Multiplexing-oriented plasmon-MoS<sub>2</sub> hybrid metasurfaces driven by nonlinear quasi bound states in the continuum, *Opt. Express* **29**, 5384 (2021).
- [83] E. Melik-Gaykazyan, K. Koshelev, J.-H. Choi, S. S. Kruk, A. Bogdanov, H.-G. Park, and Yu. Kivshar, From Fano to Quasi-BIC Resonances in Individual Dielectric Nanoantennas, *Nano Lett.* **21**, 1765 (2021).
- [84] L. Novotny and B. Hecht, *Principles of Nano-Optics* (Cambridge University Press, New York, 2006).
- [85] D. V. Novitsky and S. Yu. Mikhnevich, Bistable behavior of reflection and transmission of a one-dimensional photonic crystal with a dense resonant medium as a defect, *J. Opt. Soc. Am. B* **25**, 1362 (2008).

#### **4-PAPER:** Magnetic octupole response of dielectric quadrumers

Terekhov P.D., Evlyukhin A.B., Redka D., Volkov V.S., Shalin A.S., Karabchevsky A.,  
“Magnetic Octupole Response of Dielectric Quadrumers”, (2020) *Laser and Photonics  
Reviews*, 14 (4), art. no. 1900331, DOI: [10.1002/lpor.201900331](https://doi.org/10.1002/lpor.201900331)

# Magnetic Octupole Response of Dielectric Quadrumers

Pavel D. Terekhov,\* Andrey B. Evlyukhin,\* Dmitrii Redka, Valentyin S. Volkov, Alexander S. Shalin, and Alina Karabchevsky

The development of new approaches to tuning the resonant magnetic response of simple all-dielectric nanostructures is very important in modern nanophotonics. Here, it is shown that a resonant magnetic octupole (MOCT) response can be obtained by dividing a solid rectangular silicon block to a quadramer structure with the introduction of narrow gaps between four nanocubes. The spectral position of the MOCT resonance is controlled and tuned by varying the distance between the nanocubes. It is demonstrated that several magnetic hot-spots related to the MOCT resonance can be located in the gaps creating a strong magnetic field gradient in free space. It is observed that the resonant excitation of the MOCT moment leads to a significant enhancement of light absorption in the system at the spectral region, where light absorption in bulk silicon is weak. The results of this work can be applied to design new composite antennas and metamaterials based on complex building blocks, energy harvesting devices, and molecular trapping with magnetic hot-spots.

## 1. Introduction

Dielectric nanophotonics is one of the most actively developing fields in photonics research.<sup>[1–3]</sup> A variety of applications of dielectric nanostructures in technological devices has led to a growing interest of scientific groups over the globe. One very important property of dielectric structures in comparison to their metal counterparts is the opportunity to control electric and magnetic components of light due to the excitation of electric and magnetic multipole resonances<sup>[4–6]</sup> with the simultaneous accumulation

of electromagnetic energy.<sup>[6–8]</sup> Additionally, dielectric high-index particles have commercial value due to low resonant absorption in optical range,<sup>[9]</sup> while plasmonic structures experience significant Ohmic losses.<sup>[10–12]</sup> To study scattering of light by dielectric nanostructures one can use the multipole decomposition approach, already widespread in scientific investigations<sup>[13–26]</sup> including different spectral ranges.<sup>[27,28]</sup> State-of-the-art literature reports that the multipole responses can be tuned by changing particles' geometry,<sup>[29]</sup> size, aspect ratio, material dispersion, and the refractive index of surrounding media. Several recent studies have focused on high-order multipole excitations.<sup>[30–34]</sup>

Owing to the large value of refractive index and low losses in near-infrared<sup>[35]</sup> silicon is the most suitable material for

the resonant dielectric nanophotonics<sup>[4]</sup> and structures development.<sup>[36–39]</sup> For instance, silicon nanostraps placed on optical waveguide allows for probing forbidden overtone transitions.<sup>[40]</sup> If placed on top of a lossy plasmonic material, silicon nanostrap allows for the realization of the cloaking effect and manipulation with waveguide's evanescent fields.<sup>[41]</sup>

Dimers, oligomers, and other dielectric nanostructures (fabricated from silicon) are used for magnetic field concentration and enhancement.<sup>[42,43]</sup> In this work we study the optical properties of the silicon quadramer which supports the resonant excitation of a magnetic octupole moment and allows it to be controlled using structure parameters. We show that a solid block of crystalline silicon does not support magnetic octupole resonances, and that simply cutting it enables a resonant magnetic octupole response of the resulting silicon quadramer.

This effect leads to both the magnetic field enhancement inside the structure's slits and to increased light absorption by the structure. The suggested structures can be used to design modern optical devices and for efficient light control using magnetic octupole excitation. It is worth noting, that the achieved magnetic octupole response appears in an unusual part of the spectrum: for a bulk structure of comparable size, it would appear at far shorter wavelengths.

Modern optics actively studies metasurfaces and metamaterials, which require advanced meta-atoms supporting a specially tuned optical response. High-order multipole excitations feature specific radiation patterns and distributions of near fields. Therefore, involving high-order multipoles in an optical response of metasurfaces can expand their functional properties.<sup>[44]</sup> Usually,

P. D. Terekhov, Dr. A. Karabchevsky  
School of Electrical and Computer Engineering  
Ben-Gurion University  
Beer-Sheva 8410501, Israel  
E-mail: terekhovpd@gmail.com

P. D. Terekhov, Dr. A. B. Evlyukhin, Dr. A. S. Shalin  
Department of Physics and Engineering  
ITMO University  
49 Kronversky Ave. St. Petersburg 197101, Russia  
E-mail: a.b.evlyukhin@daad-alumni.de

Dr. A. B. Evlyukhin, Dr. V. S. Volkov  
Moscow Institute of Physics and Technology  
9 Institutsky Lane Dolgoprudny 141700, Russia  
Dr. D. Redka  
Department of Photonics

Saint Petersburg Electrotechnical University LETI  
5 Prof. Popova Street St. Petersburg 197376, Russia

The ORCID identification number(s) for the author(s) of this article can be found under <https://doi.org/10.1002/lpor.201900331>

DOI: 10.1002/lpor.201900331

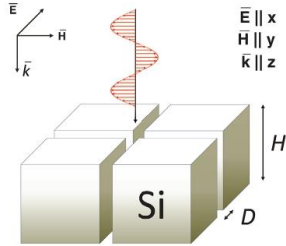


Figure 1. The artistic representation of the quadrumer of silicon cubes.

one needs to increase particles volume to excite high-order multipoles (magnetic octupole, electric 16-pole, etc.). However, exploiting bigger particles as building blocks is complicated because their size and, consequently, interparticle spacing can surpass resonant wavelengths. That results in a diffraction, which crucially restricts the functionality of metasurfaces making them to become simple diffraction lattices. Here we pave a way to overcoming this challenge and demonstrate the possibility to resonantly excite high-order multipoles via artificial nanostructuring of a scatterer, so that its total size remains nearly unchanged and effectively smaller than the resonant wavelength. This approach can find wide application for the development of new types of metasurfaces, compact nanoantennas with unique high-order multipole response, and other nanostructures for multiscale light governing. In general, tailoring the resonant response of high-order multipole moments over the optical spectral range opens new opportunities in practical applications, for example, sensors, detectors, and selective or directive nanoantennas.

## 2. Theoretical Background

Here, we use multipole decomposition approach described in refs. [13,45–47] including multipole moments up to the magnetic octupole (MOCT) term. To study the multipole contributions to a scattering cross section of full quadrumer structure presented in Figure 1 we consider it as an unite system. The origin of the Cartesian coordinate system is located at the center of mass (center of symmetry) of the structure, and, for the incident wave, the electric field is polarized along  $x$ -axis, and  $k$ -vector is directed along  $z$ -axis (see Figure 1).

In our approximation a scattering cross section of a particle in a homogeneous host medium can be presented as (see ref. [47] for details)

$$C_{\text{scat}} \approx \frac{k_0^4}{6\pi\epsilon_0^2|\mathbf{E}_{\text{inc}}|^2}|\mathbf{D}|^2 + \frac{k_0^6\epsilon_d\mu_0}{6\pi\epsilon_0|\mathbf{E}_{\text{inc}}|^2}|\mathbf{m}|^2 + \frac{k_0^6\epsilon_d}{720\pi\epsilon_0^2|\mathbf{E}_{\text{inc}}|^2}|\hat{\mathbf{Q}}|^2 + \frac{k_0^6\epsilon_d^2\mu_0}{80\pi\epsilon_0|\mathbf{E}_{\text{inc}}|^2}|\hat{\mathbf{M}}|^2 + \frac{k_0^8\epsilon_d^2}{1890\pi\epsilon_0^2|\mathbf{E}_{\text{inc}}|^2}|\hat{\mathbf{O}}|^2 + \frac{k_0^8\epsilon_d^2\mu_0}{1890\pi k_0^8\epsilon_0|\mathbf{E}_{\text{inc}}|^2}|\hat{\mathbf{O}}_m|^2 \quad (1)$$

where  $\mathbf{E}_{\text{inc}}$  is the electric field amplitude of the incident light wave,  $\epsilon_d = n_d^2$  is the dielectric permittivity of the surrounding medium,  $\epsilon_0$  is the vacuum electric permittivity, and  $v_d = c/\sqrt{\epsilon_d}$  is the light speed in the surrounding medium;  $k_0$  and  $k_d$  are the wavenumbers in vacuum and in the surrounding medium, correspondingly.  $\mathbf{m}$  is the magnetic dipole moment (MD) of a particle;  $\mathbf{D}$  is the total electric dipole moment (TED);  $\hat{\mathbf{Q}}$ ,  $\hat{\mathbf{M}}$ ,  $\hat{\mathbf{O}}$ , and  $\hat{\mathbf{O}}_m$  are the electric quadrupole tensor (EQ), the magnetic quadrupole tensor (MQ), the tensor of electric octupole (OCT), and the tensor of magnetic octupole (MOCT), respectively. Here  $||$  denotes the sum of squared tensor components. Note that these tensors are symmetric and traceless, and in tensor notation, for example,  $\hat{\mathbf{Q}}$  is equal to  $Q_{\alpha\beta}$  (for quadrupole moments) and  $\hat{\mathbf{O}}$  is equal to  $O_{\alpha\beta\gamma}$  (for octupole moments), where subscript indices denote components (e.g.,  $\alpha = x, y, z$ ).<sup>[45]</sup> Let us also show the expressions used here for the Cartesian electric and magnetic octupole moments, expanding the multipole decomposition at ref. [46]

$$\hat{\mathbf{O}} = \frac{15i}{\omega} \int_{V_s} \frac{j_2(k_d r')}{(k_d r')^2} (\mathbf{j}'r' + r'\mathbf{j}'r' + r'r'\mathbf{j}' - \hat{\mathbf{A}}) dr' \quad (2)$$

$$\hat{\mathbf{O}}_m = \frac{105}{4} \int_{V_s} \frac{j_3(k_d r')}{(k_d r')^3} ((\mathbf{r}' \times \mathbf{j})r' + r'[\mathbf{r}' \times \mathbf{j}]r' + r'r'[\mathbf{r}' \times \mathbf{j}] - \hat{\mathbf{A}}') dr' \quad (3)$$

where vector  $\mathbf{j}(r')$  is the electric polarization current density depending on the position inside the scatterer and induced by an incident light wave,  $r'$  is the radius vector of a point inside the scatterer,  $\omega$  is the angular frequency of the incident wave;  $j_2(k_d r')$ ,  $j_3(k_d r')$  are the spherical Bessel functions,  $V_s$  is a scatterer volume, and the tensors  $\hat{\mathbf{A}}$  and  $\hat{\mathbf{A}}'$  are

$$A_{\beta\gamma\tau} = \delta_{\beta\tau} V_\tau + \delta_{\beta\tau} V_\tau + \delta_{\tau\tau} V_\beta \quad (4)$$

$$A'_{\beta\gamma\tau} = \delta_{\beta\tau} V'_\tau + \delta_{\beta\tau} V'_\tau + \delta_{\tau\tau} V'_\beta \quad (5)$$

where  $\beta = x, y, z$ ;  $\gamma = x, y, z$ ;  $\tau = x, y, z$ ;  $\delta_{\beta\tau}$  is the Kronecker delta,

$$\mathbf{V} = \frac{1}{5} [2(\mathbf{r}' \cdot \mathbf{j})\mathbf{r}' + r'^2\mathbf{j}] \quad (6)$$

$$\mathbf{V}' = \frac{1}{5} r'^2 [\mathbf{r}' \times \mathbf{j}] \quad (7)$$

The combinations of three vectors (like  $\mathbf{j}'r'$ ) in Equations (2) and (3) are the tensor products of the corresponding vectors, the sign  $\times$  stands for the vector product and the sign  $\cdot$  stands for the scalar product of two vectors. Detailed derivations are presented in ref. [47].

The polarization currents inside the dielectric structure are calculated using the total electric field obtained from the full-wave simulations in the commercial package COMSOL Multiphysics.<sup>[48]</sup> The details of the methods involved can be found, for example, in ref. [49]. Electric fields  $\mathbf{E}(r')$  and polarization currents are related by the Equation  $\mathbf{j}(r') = -i\omega\epsilon_0(\epsilon_s - \epsilon_d)\mathbf{E}(r')$ , where  $\epsilon_s$  is the dielectric permittivity of the silicon scatterers.<sup>[35]</sup> These currents are then used to obtain multipole contributions to the scattering cross section. To compare, the total



scattering cross section is also obtained through the direct integration of the Poynting vector over a closed surface in the far-field zone and the normalization to the incident field intensity.

### 3. Results and Discussion

In this work, we study previously unrevealed MOCT-induced optical properties of silicon quadrumers. We learn how to use controllable resonant MOCT excitation to tailor magnetic hot-spots and resonant energy absorption. The considered systems are the silicon block with dimensions equal to  $500 \times 500 \times 250$  nm, which represents zero distance between silicon cubes in Figure 1 and silicon quadrumers composed of four Si cubes ( $250 \times 250 \times 250$  nm) with distance between them  $D = 25, 50,$  and  $100$  nm. These structures are illuminated with a linearly polarized monochromatic plane wave with time-dependence  $e^{-i\omega t}$  as shown in Figure 1. Material data for silicon has been taken from ref. [35]. To investigate scattering cross section spectral resonances, we apply the multipole decomposition technique which shows good performance in all cases considered (Figure 2). The almost perfect agreement between the sum of the multipole contributions and the directly calculated scattered cross section proves that the multipole approach is sufficiently accurate. Figure 2a shows the scattering cross section spectrum calculated for the solid silicon block. One can note that both the resonant multipole contributions and the total scattering cross section in this case significantly differ from the spectra in Figure 2b–d due to the introduction of inhomogeneity to the system.

In this way, the conversion of the solid block to the quadrumer structure leads to a strong reconfiguration of electric and magnetic fields in the system and to a higher order multipole excitation. Surprisingly, the presence of narrow air gaps in the quadrumer leads to the excitation of the MOCT moment in the considered spectral range. Note that this is not related to the increase in the total structure size, since our calculations for solid blocks with the edge of  $525$  nm do not show MOCT resonances in the considered spectral range. To visualize this, we show the total scattering cross section of  $525 \times 525 \times 250$  nm silicon block (dashed line in Figure 2b) in order to compare it with the case of the corresponding quadrumer. It can be seen that there is no resonant response between  $\lambda = 850$  nm and  $\lambda = 900$  nm; small resonant peak at  $\lambda = 840$  nm corresponds to EQ.

Let us consider in detail the resonant excitation of the magnetic octupole moment at the wavelengths of  $850$ – $900$  nm. Cutting the solid block enables MOCT resonance weakening with increasing the intercube distance. The resonant MOCT peak occurs at  $\lambda = 874$  nm in Figure 2b, at  $\lambda = 863$  nm in Figure 2c, and at  $\lambda = 852$  nm in Figure 2d. While attenuating, the resonant peak also experiences a blue shift. Moreover, the multipole decomposition and scattering cross section do not depend on rotation of the incident plane wave polarization by  $45^\circ$  (not demonstrated in figures).

Figure 3 shows the distribution of normalized (to the magnetic field amplitude of the incident wave) magnetic field at the MOCT resonance. It is important for practical applications to be able to create the so-called magnetic hot-spots in free space.<sup>[42]</sup> Due to structuring, the total magnetic field in the gaps can be enhanced (comparing to the incident one) up to  $\approx 10$  times for  $D = 50$  nm (Figure 3a) and  $\approx 14$  times for  $D = 25$  nm (Figure 3b). Strong

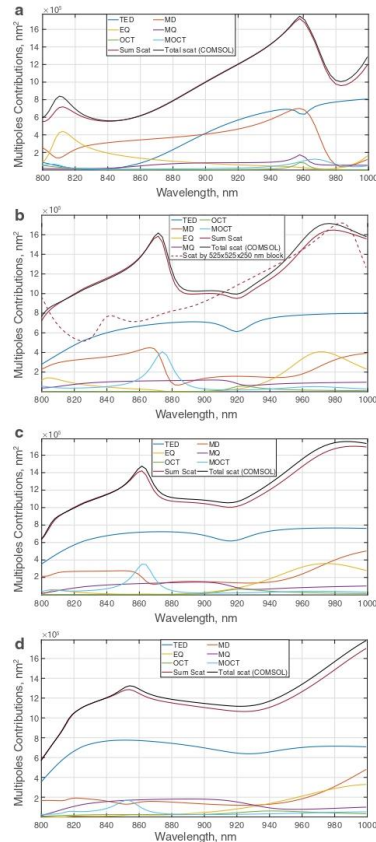


**Figure 2.** Scattering cross-section spectra and corresponding multipoles' contributions calculated for a) the single silicon block of height  $H = 250$  nm and base edge  $500$  nm; b–d) the quadrumer of silicon cubes. The distance between cubes in the quadrumer is b)  $D = 25$  nm c)  $D = 50$  nm d)  $D = 100$  nm. 'Sum Scat' states for the scattering cross section as the sum of the multipole contributions; 'Total scat (COMSOL)' states for the total scattering cross sections calculated directly in COMSOL.

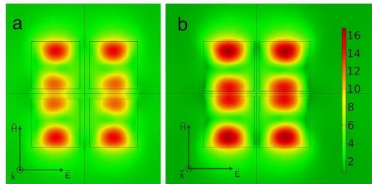


**Figure 3.** a) Distribution of the normalized magnetic field in  $(xy)$ -plane ( $z = 0$ ) of the silicon quadrumer with a)  $D = 50$  nm,  $\lambda = 863$  nm, b)  $D = 25$  nm,  $\lambda = 874$  nm. Color bar is the same for both pictures.

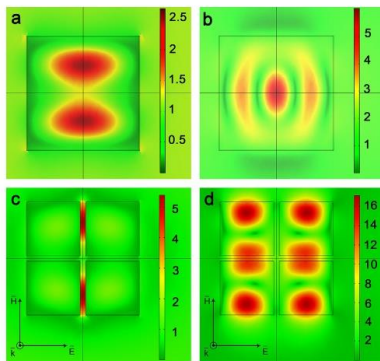


**Figure 4.** The absolute value of a,c)  $E_x$  and b,d)  $H_y$  in a,b) the solid silicon block and c,d) the silicon quadrumer with  $D = 25$  nm at  $\lambda = 874$  nm.

local magnetic fields can be used to control or detect small quantum objects (quantum dots, atoms, and molecules) supporting magnetic optical transitions.<sup>[50]</sup> Magnetic hot-spots are also useful for spectroscopy,<sup>[51]</sup> better enhancement of Raman scattering, fluorescence, and circular dichroism of molecules,<sup>[52]</sup> sensing,<sup>[53]</sup> and other applications.

The location of obtained hot-spots can also be tuned using the incident light polarization. The hot-spots move to another air gaps if the polarization is rotated by  $90^\circ$  (i.e., if electric field is polarized along perpendicular axis). It is possible to exploit this effect to design magnetic switchers at the nanoscale.

It is important to go in details with the physics of the considered process. **Figure 4a,c** show the absolute value of the  $x$ -component of the electric field ( $E_x$ ) in the solid block and in the quadrumer, respectively. Following Maxwell's equations, in the oligomer structure the electric field enhancement appears in the slits along the polarization of the incident wave due to the discontinuity of the normal component. In addition, **Figure 4b,d** show the absolute value of the  $y$ -component of the magnetic field ( $H_y$ ) and the crucial redistribution of the magnetic field because of the structuring. This leads to six different field concentration zones

in the quadrumer structure constructing magnetic octupole near-field pattern.<sup>[34]</sup> The magnetic field does not undergo a discontinuity in the gaps along  $H_y$  ( $\mu = 1$  in the both media) that is why the magnetic hot-spots take place between the cubes too.

In addition to the magnetic field enhancement, MOCT resonance can provide a strong electromagnetic absorption in the quadrumer. **Figure 5a** shows the comparison of absorbed power for  $\lambda$  between 850 and 900 nm for the solid silicon block and the quadrumer with the distance  $D = 25$  nm between the cubes. **Figure 5b** proves that the discovered energy absorption peak spectrally corresponds to the MOCT resonance. It is worth noting that in this spectral range natural light absorption by silicon is small. Therefore, air gaps in the quadrumer structure cause strong absorption in silicon, despite its very small  $\text{Im}(n) \approx 0.08$ . **Figure 5c** compares the electric field inside the silicon block and quadrumer structure. Clearly, resonant magnetic octupole response leads to a strong electric field concentration and, therefore, to the resonant absorption in the silicon quadrumer. The spectral position of the MOCT resonance and, hence, the position of the absorption peak can be changed by varying the distance between the cubes. Such the tunable absorption can be widely used to control the energy concentration by dielectric structures and to design modern optical devices.

Here, we note that the substrate influence on this effect is yet to be studied. It is known that dielectric substrates with low refractive index almost does not change the optical response,<sup>[7,54]</sup> however, to take into account more reflective materials more complex formalism should be introduced. The principal demonstration paved the way to future theoretical and experimental investigations of magnetic octupole excitations in quadrumers placed on different metal and dielectric substrates.

#### 4. Conclusion

In this work we study resonant MOCT excitation which leads to controlled magnetic hot-spots and resonant absorption by a nanostructure. We analyze the multipole contributions to the scattering cross section and reveal the excitation of magnetic octupole due to the coupling effects in this structure as compared to the single cube. In this work, the resonant excitation of a magnetic octupole moment in dielectric quadrumers is demonstrated and analyzed in detail. We show how to control MOCT resonant excitation and its spectral position. In addition, we reveal its possible application to obtain magnetic hot-spots and to absorb electromagnetic energy in the nanostructure. The magnetic field in the air gap between the nanocubes can be 14 times larger in comparison with incident one, and is even stronger inside the nanostructure. Use of quadrumers as building blocks for metasurfaces promises even higher magnetic field enhancement due to potential excitation of so-called trapped modes. It is very important to note that an excitation of high-order multipole moments exploiting nanostructuring of small particles is the powerful approach to avoid diffraction restriction in designing of advanced metasurfaces and metamaterials. Moreover, after being scaled to the microwave region the considered structure could be very perspective for magnetic resonance imaging applications, where a strong concentration of magnetic fields is necessary to increase the contrast and quality of the pictures.<sup>[55,56]</sup> Besides,

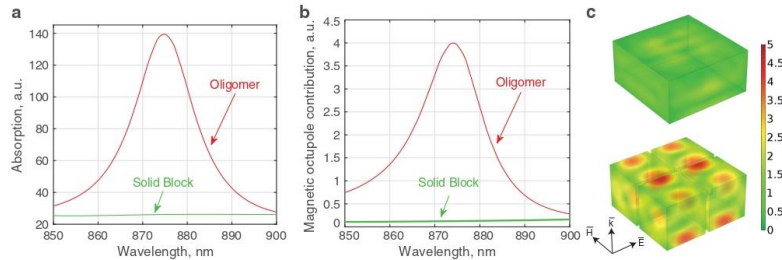


**Figure 5.** Spectra of the a) absorption power and b) MOCT contribution to the scattering cross section calculated for a single silicon block of height  $H = 250$  nm and base edge  $500$  nm (green lines) and the quadrumer of silicon cubes with the distance between cubes  $D = 25$  nm (red lines). The absorption peak in the structure clearly corresponds to the resonant excitation of MOCT moment. c) Normalized electric field inside the solid block (top) and quadrumer (bottom) at  $\lambda = 874$  nm. One can see that resonant MOCT response provides strong electric field concentration leading to the resonant absorption in the silicon quadrumer.

resonant magnetic octupole response can be widely used for spectroscopy, sensing, small quantum objects detection, and many other promising applications.<sup>[57–61]</sup>

### Acknowledgements

The authors thank Svetlana Korinfskaya for help with the artistic work. This work was supported by the Israel Innovation Authority-Kamin Program, Grant No. 62045 (Year 2). A.S.S. acknowledges the support of the Russian Fund for Basic Research within the projects 18-02-00414, 18-52-00005. The development of the analytical approach was partially supported by the Russian Science Foundation Grant No. 18-19-00684. Support from the Russian Fund for Basic Research within the projects 18-29-02089 is acknowledged as well. Contribution of P.D.T. in the research was performed as a part of the joint Ph.D. program between the BGU and ITMO.

### Conflict of Interest

The authors declare no conflict of interest.

### Keywords

magnetic hot-spots, magnetic octupole, oligomers, quadrumers, silicon photonics

Received: October 1, 2019  
Revised: January 26, 2020  
Published online:

- [1] I. Staude, J. Schilling, *Nat. Photonics* **2017**, *11*, 274.
- [2] Y. Kivshar, *Natl. Sci. Rev.* **2018**, *5*, 144.
- [3] S. M. Kamali, E. Arbabi, A. Arbabi, A. Faraon, *Nanophotonics* **2018**, *7*, 1041.
- [4] A. B. Evlyukhin, C. Reinhardt, A. Seidel, B. S. Luk'yanchuk, B. N. Chichkov, *Phys. Rev. B* **2010**, *82*, 045404.

- [5] A. B. Evlyukhin, C. Reinhardt, B. N. Chichkov, *Phys. Rev. B* **2011**, *84*, 235429.
- [6] A. B. Evlyukhin, S. M. Novikov, U. Zywietz, R. L. Eriksen, C. Reinhardt, S. I. Bozhevolnyi, B. N. Chichkov, *Nano Lett.* **2012**, *12*, 3749.
- [7] U. Zywietz, A. B. Evlyukhin, C. Reinhardt, B. N. Chichkov, *Nat. Commun.* **2014**, *5*, 3402.
- [8] A. E. Miroshnichenko, A. B. Evlyukhin, Y. F. Yu, R. M. Bakker, A. Chipouline, A. I. Kuznetsov, B. Luk'yanchuk, B. N. Chichkov, Y. S. Kivshar, *Nat. Commun.* **2015**, *6*, 8069.
- [9] A. A. Basharin, M. Kafesaki, E. N. Economou, C. M. Soukoulis, V. A. Fedotov, V. Savinov, N. I. Zheludev, *Phys. Rev. X* **2015**, *5*, 011036.
- [10] J. B. Khurgin, *Nat. Nanotechnol.* **2015**, *10*, 2.
- [11] A. Karabchevsky, A. Mosayebi, A. V. Kavokin, *Light: Sci. Appl.* **2016**, *5*, e16164.
- [12] A. Karabchevsky, O. Krasnykov, M. Auslender, B. Hadad, A. Goldner, I. Abdulhalim, *Plasmonics* **2009**, *4*, 281.
- [13] R. Alaei, C. Rockstuhl, I. Fernandez-Corbaton, *Adv. Opt. Mater.* **2019**, *7*, 1800783.
- [14] Y. Yang, A. E. Miroshnichenko, S. V. Kostinski, M. Odit, P. Kapitanova, M. Qiu, Y. S. Kivshar, *Phys. Rev. B* **2017**, *95*, 165426.
- [15] I. Staude, A. E. Miroshnichenko, M. Decker, N. T. Fofang, S. Liu, E. Gonzales, J. Dominguez, T. S. Luk, D. N. Neshev, I. Brener, Y. Kivshar, *ACS Nano* **2013**, *7*, 7824.
- [16] P. D. Terekhov, K. V. Baryshnikova, A. S. Shalin, A. Karabchevsky, A. B. Evlyukhin, *Opt. Lett.* **2017**, *42*, 835.
- [17] W. Chen, Y. Chen, W. Liu, *Laser Photonics Rev.* **2019**, *13*, 1900067.
- [18] P. Grah, A. Shevchenko, M. Kaivola, *New J. Phys.* **2012**, *14*, 093033.
- [19] P. D. Terekhov, V. E. Babicheva, K. V. Baryshnikova, A. S. Shalin, A. Karabchevsky, A. B. Evlyukhin, *Phys. Rev. B* **2019**, *99*, 045424.
- [20] S. Mühlig, C. Menzel, C. Rockstuhl, F. Lederer, *Metamaterials* **2011**, *5*, 64.
- [21] M.-T. Suzuki, T. Nomoto, R. Arita, Y. Yanagi, S. Hayami, H. Kusunose, *Phys. Rev. B* **2019**, *99*, 174407.
- [22] I. M. Hancu, A. G. Curto, M. Castro-López, M. Kuttge, N. F. van Hulst, *Nano Lett.* **2013**, *14*, 166.
- [23] H. K. Shamkhi, K. V. Baryshnikova, A. Sayansky, P. Kapitanova, P. D. Terekhov, P. Belov, A. Karabchevsky, A. B. Evlyukhin, Y. Kivshar, A. S. Shalin, *Phys. Rev. Lett.* **2019**, *122*, 193905.
- [24] B. Luk'yanchuk, R. Paniagua-Dominguez, A. I. Kuznetsov, A. E. Miroshnichenko, Y. S. Kivshar, *Phys. Rev. A* **2017**, *95*, 063820.

- [25] V. Savinov, V. Fedotov, N. I. Zheludev, *Phys. Rev. B* **2014**, *89*, 205112.
- [26] D. A. Powell, *Phys. Rev. Appl.* **2017**, *7*, 034006.
- [27] P. Terekhov, K. Baryshnikova, A. Evlyukhin, A. Shalin, *J. Phys.: Conf. Ser.* **2017**, *929*, 012065.
- [28] M. Balezin, K. V. Baryshnikova, P. Kapitanova, A. B. Evlyukhin, *J. Appl. Phys.* **2018**, *124*, 034903.
- [29] P. D. Terekhov, K. V. Baryshnikova, Y. A. Artemyev, A. Karabchevsky, A. S. Shalin, A. B. Evlyukhin, *Phys. Rev. B* **2017**, *96*, 035443.
- [30] A. Y. Zhu, W. T. Chen, A. Zaidi, Y.-W. Huang, M. Khorasaninejad, V. Sanjeev, C.-W. Qiu, F. Capasso, *Light: Sci. Appl.* **2018**, *7*, 17158.
- [31] W. Liu, A. E. Miroshnichenko, *ACS Photonics* **2017**, *5*, 1733.
- [32] P. Terekhov, H. Shamkhi, E. Gurvitz, K. Baryshnikova, A. Evlyukhin, A. Shalin, A. Karabchevsky, *Opt. Express* **2019**, *27*, 10924.
- [33] R. Alaei, M. Albooyeh, S. Tretyakov, C. Rockstuhl, *Opt. Lett.* **2016**, *41*, 4099.
- [34] E. A. Gurvitz, K. S. Ladutenko, P. A. Dergachev, A. B. Evlyukhin, A. E. Miroshnichenko, A. S. Shalin, *Laser Photonics Rev.* **2019**, *13*, 1800266.
- [35] E. D. Palik, *Handbook of Optical Constants of Solids: Handbook of Thermo-Optic Coefficients of Optical Materials with Applications*, Elsevier, New York **1997**.
- [36] L. Wang, Y. Rho, W. Shou, S. Hong, K. Kato, M. Eliceiri, M. Shi, C. P. Grigoropoulos, H. Pan, C. Carraro, D. Qi, *ACS Nano* **2018**, *12*, 2231.
- [37] F. Deng, H. Liu, M. Panmai, S. Lan, *Opt. Express* **2018**, *26*, 20051.
- [38] P. D. Terekhov, K. V. Baryshnikova, Y. Greenberg, Y. H. Fu, A. B. Evlyukhin, A. S. Shalin, A. Karabchevsky, *Sci. Rep.* **2019**, *9*, 3438.
- [39] P. M. Voroshilov, C. R. Simovski, P. A. Belov, A. S. Shalin, *J. Appl. Phys.* **2015**, *117*, 203101.
- [40] A. Katiyi, A. Karabchevsky, *ACS Sens.* **2018**, *3*, 618.
- [41] Y. Galutin, E. Falek, A. Karabchevsky, *Sci. Rep.* **2017**, *7*, 12076.
- [42] K. V. Baryshnikova, A. Novitsky, A. B. Evlyukhin, A. S. Shalin, *J. Opt. Soc. Am. B* **2017**, *34*, D36.
- [43] R. M. Bakker, D. Permyakov, Y. F. Yu, D. Markovich, R. Paniagua-Dominguez, L. Gonzaga, A. Samusev, Y. Kivshar, B. Luk'yanchuk, A. I. Kuznetsov, *Nano Lett.* **2015**, *15*, 2137.
- [44] A. Rahimzadegan, D. Arslan, D. Dams, A. Groner, X. Garcia-Santiago, R. Alaei, I. Fernandez-Corbaton, T. Pertsch, I. Staudte, C. Rockstuhl, *Nanophotonics* **2020**, *9*, 75.
- [45] A. B. Evlyukhin, T. Fischer, C. Reinhardt, B. N. Chichkov, *Phys. Rev. B* **2016**, *94*, 205434.
- [46] R. Alaei, C. Rockstuhl, I. Fernandez-Corbaton, *Opt. Commun.* **2018**, *407*, 17.
- [47] A. B. Evlyukhin, B. N. Chichkov, *Phys. Rev. B* **2019**, *100*, 125415.
- [48] COMSOL Multiphysics® v5.4. www.comsol.com. COMSOL AB, Stockholm, Sweden.
- [49] W. B. Zimmerman, *Multiphysics Modeling with Finite Element Methods*, Vol. 18, World Scientific, Singapore **2006**.
- [50] C. L. Degen, F. Reinhard, P. Cappellaro, *Rev. Mod. Phys.* **2017**, *89*, 035002.
- [51] M. Sadrara, M. Miri, *Sci. Rep.* **2019**, *9*, 2926.
- [52] Z. Naeimi, M. Miri, *Opt. Lett.* **2018**, *43*, 462.
- [53] Z. Yong, S. Zhang, C. Gong, S. He, *Sci. Rep.* **2016**, *6*, 24063.
- [54] P. Spinelli, M. Verschuuren, A. Polman, *Nat. Commun.* **2012**, *3*, 692.
- [55] A. Andreychenko, H. Kroeze, D. W. Klomp, J. J. Lagendijk, P. R. Luitjen, C. A. van den Berg, *Magn. Reson. Med.* **2013**, *70*, 875.
- [56] A. A. Mikhailovskaya, A. V. Shchelokova, D. A. Dobrykh, I. V. Sushkov, A. P. Slobozhanyuk, A. Webb, *J. Magn. Reson.* **2018**, *291*, 47.
- [57] M. Kasprzyk, S. Person, D. Ananias, L. D. Carlos, L. Novotny, *Phys. Rev. Lett.* **2015**, *114*, 163903.
- [58] T. H. Taminiau, S. Karaveli, N. F. Van Hulst, R. Zia, *Nat. Commun.* **2012**, *3*, 979.
- [59] H. Giessen, R. Vogelgesang, *Science* **2009**, *326*, 529.
- [60] M. Burrelli, D. Van Oosten, T. Kampfrath, H. Schoenmaker, R. Heide-man, A. Leinse, L. Kuipers, *Science* **2009**, *326*, 550.
- [61] O. Borovkova, D. Ignatyeva, S. Sekatskii, A. Karabchevsky, V. Belotelov, *Photonics Res.* **2020**, *8*, 57.

**5-PAPER:** Controlling wave fronts with tunable disordered non-Hermitian multilayers

Novitsky D.V., Lyakhov D., Michels D., Redka D., Pavlov A.A., Shalin A.S.,  
“Controlling wave fronts with tunable disordered non-Hermitian multilayers”, (2021)  
*Scientific Reports*, 11 (1), art. no. 4790, DOI: [10.1038/s41598-021-84271-0](https://doi.org/10.1038/s41598-021-84271-0)



## OPEN Controlling wave fronts with tunable disordered non-Hermitian multilayers

Denis V. Novitsky<sup>1</sup>✉, Dmitry Lyakhov<sup>2</sup>, Dominik Michels<sup>2</sup>, Dmitrii Redka<sup>3</sup>, Alexander A. Pavlov<sup>4</sup> & Alexander S. Shalin<sup>4,5</sup>

Unique and flexible properties of non-Hermitian photonic systems attract ever-increasing attention via delivering a whole bunch of novel optical effects and allowing for efficient tuning light-matter interactions on nano- and microscales. Together with an increasing demand for the fast and spatially compact methods of light governing, this peculiar approach paves a broad avenue to novel optical applications. Here, unifying the approaches of disordered metamaterials and non-Hermitian photonics, we propose a conceptually new and simple architecture driven by disordered loss-gain multilayers and, therefore, providing a powerful tool to control both the passage time and the wave-front shape of incident light with different switching times. For the first time we show the possibility to switch on and off kink formation by changing the level of disorder in the case of adiabatically raising wave fronts. At the same time, we deliver flexible tuning of the output intensity by using the nonlinear effect of loss and gain saturation. Since the disorder strength in our system can be conveniently controlled with the power of the external pump, our approach can be considered as a basis for different active photonic devices.

Recently, the studies of open optical systems containing loss and gain attract increased attention. Although such systems are well-known for many years, the recent trend of non-Hermitian photonics provides the second breath to the investigations of lasers, waveguides, resonators, etc. This is not only due to a different language borrowed from quantum mechanics, but also because of a number of novel phenomena found in loss-gain structures. We name here only a few examples, such as the effects of  $\mathcal{P}$ - $\mathcal{T}$  symmetry<sup>1-3</sup> and exceptional points<sup>4,5</sup>. These effects include unidirectional invisibility<sup>6,7</sup>, sensors<sup>8,9</sup> and gyroscopes<sup>10,11</sup> with enhanced sensitivity, loss-induced<sup>12</sup> and asymmetric<sup>13</sup> lasing, novel single-mode<sup>14-16</sup> and vortex<sup>17</sup> lasers, coherent perfect absorbers<sup>18-21</sup>, and topological bulk-boundary correspondence<sup>22-25</sup>.

Disordered photonics is another spotlight of modern research<sup>26</sup>. It deals with light propagation in the presence of random fluctuations of the medium parameters such as refractive index or unit cell dimensions. The rich physics of such systems rooted in multiple scattering allows to realize a number of unusual features; the scattering properties of single particles and complex structures are well-studied in literature<sup>27-29</sup>. The most prominent feature of disordered systems is the Anderson localization of light<sup>30-32</sup> appearing as a result of multiple path interference of waves scattering on random inclusions. Multiple scattering can also lead to the peculiar statistical properties of light violating usual diffusion (sub- and superdiffusion) like in optical Levy flights<sup>33-35</sup>. The situation becomes even more complicated when the interplay between disorder and nonlinearity occurs with the subsequent suppression of Anderson localization or promotion of diffusion<sup>36-38</sup>.

There is a recent trend combining together disorder and non-Hermiticity in the random systems with loss and gain. One of the main aims of such combinations is the enhancement of transmission which is usually strongly suppressed due to multiple scattering<sup>39</sup>. For example, this problem can be solved with the help of the concept of so-called constant-intensity waves in specially designed loss-gain profiles<sup>39-43</sup>. The non-Hermitian disorder due to random fluctuations of loss and gain can be a source of novel-type localized states<sup>44-46</sup>. Another interesting direction is the effects of asymmetric hopping on many-body localization predicted for dynamics

<sup>1</sup>B. I. Stepanov Institute of Physics, National Academy of Sciences of Belarus, Nezavisimosti Avenue 68, 220072 Minsk, Belarus. <sup>2</sup>Visual Computing Center, King Abdullah University of Science and Technology, Thuwal 23955-6900, Kingdom of Saudi Arabia. <sup>3</sup>Saint Petersburg Electrotechnical University "LETI" (ETU), Prof. Popova Street 5, 197376 St. Petersburg, Russia. <sup>4</sup>Institute of Nanotechnology of Microelectronics of the Russian Academy of Sciences, Leninsky Prospekt 32A, 119991 Moscow, Russia. <sup>5</sup>Kotel'nikov Institute of Radio Engineering and Electronics of the Russian Academy of Sciences (Ulyanovsk Branch), Goncharova Str. 48, 432000 Ulyanovsk, Russia. ✉email: dnovitsky@gmail.com

of the quantum particles<sup>44,47</sup>. Such effects can have an optical analogue realized, e.g., due to nonreciprocity via utilization of magnetic or nonlinear materials. There is also a very active subfield of random lasing obtained in disordered amplifying media<sup>48–51</sup>. However, the *dynamics* of light interaction with structures containing both loss/gain and disorder are still poorly studied.

In this paper, we analyze the propagation of wave fronts through the disordered loss-gain non-Hermitian multilayer structures. The problem is aimed to be as realistic as possible: The fronts are the monochromatic waveforms having finite switching time, the loss and gain are due to resonant media and not merely a phenomenological imaginary part of permittivity, and the disorder can be controlled with external pump and change in time due to gain depletion and loss saturation. We have previously reported the study of short pulse propagation and localization in such media<sup>52</sup> with the possibility to slow down or even stop the pulse. Here, we deal with the opposite case of continuous radiation with the emphasis on the transient process of steady-state establishment for the light intensities large enough to saturate the medium and give substantial transmission. This process can have different dynamics depending on the sharpness of the incident wave switching. In particular, we distinguish two regimes, when switching is slow (adiabatic) and fast (non-adiabatic). For these switching regimes, we show that the introduction of disorder changes the characteristic time of the transient process, whereas the resulting intensity of the signal is governed by saturation-limited input intensity. In particular, for the first time we demonstrate how the disorder can be used to switch on and off kinks at the output of the system. Thus, the non-Hermitian approach to disorder-induced control of propagation time, wave-front shape and transmitted intensity proposed in this paper opens new possibilities for ultrafast (picosecond or subnanosecond) multifunctional manipulation of optical signals.

## Results

**Problem statement.** Hereinafter, we consider a host dielectric doped with two-level atoms. Light propagation in such a medium is described by the well-known semiclassical Maxwell-Bloch equations for the dimensionless electric-field amplitude  $\Omega = (\mu/h\omega)E$  (normalized Rabi frequency), complex amplitude of the atomic polarization  $\rho$ , and population difference between the ground and excited states  $w$ <sup>53–55</sup>:

$$\frac{d\rho}{d\tau} = i\Omega w + i\rho\delta - \gamma_2\rho, \quad (1)$$

$$\frac{dw}{d\tau} = 2i(l^* \Omega^* \rho - \rho^* l \Omega) - \gamma_1(w - 1), \quad (2)$$

$$\frac{\partial^2 \Omega}{\partial \xi^2} - n_d^2 \frac{\partial^2 \Omega}{\partial \tau^2} + 2i \frac{\partial \Omega}{\partial \xi} + 2im_d^2 \frac{\partial \Omega}{\partial \tau} + (n_d^2 - 1)\Omega = 3\epsilon l \left( \frac{\partial^2 \rho}{\partial \tau^2} - 2i \frac{\partial \rho}{\partial \tau} - \rho \right), \quad (3)$$

where  $\tau = \omega t$  and  $\xi = kz$  are the dimensionless time and distance,  $\mu$  is the dipole moment of the quantum transition,  $\hbar$  is the reduced Planck constant,  $\delta = \Delta\omega/\omega = (\omega_0 - \omega)/\omega$  is the normalized frequency detuning,  $\omega$  is the carrier frequency,  $\omega_0$  is the frequency of the quantum transition,  $\gamma_1 = 1/(\omega T_1)$  and  $\gamma_2 = 1/(\omega T_2)$  are the normalized relaxation rates of population and polarization respectively, and  $T_1$  ( $T_2$ ) is the longitudinal (transverse) relaxation time;  $\epsilon = \omega_l/\omega = 4\pi\mu^2 C/3\hbar\omega$  is the light-matter coupling strength with  $C$  the density of two-level atoms and  $\omega_l$  the Lorentz frequency;  $l = (n_d^2 + 2)/3$  is the local-field enhancement factor due to the polarization of the host dielectric with refractive index  $n_d$  by the embedded two-level particles. We numerically solve Eqs. (1)–(3) using the finite-difference approach described in Refs.<sup>56,57</sup> well-proven in solving such tasks.

The parameters used for calculations are characteristic, e.g., for semiconductor quantum dots as the active particles. We suppose the exact resonance ( $\delta = 0$ ). The host refractive index is  $n_d = 1.5$ . Incident monotonically switching cw field has the central wavelength  $\lambda = 0.8 \mu\text{m}$  and the envelope as follows,

$$\Omega(t) = \frac{\Omega_0}{1 + e^{-(t-t_0)/t_p}}, \quad (4)$$

where  $\Omega_0$  is the amplitude of the resulting cw field (plateau),  $t_p$  is the switching time,  $t_0 = 5t_p$  is the offset time. The disorder is introduced to the system through the periodical random variations of the initial population difference  $w_0 = w(t=0)$  along the light propagation direction. One can say that the population difference shows which part of two-level atoms in the medium are excited. We use here the two-valued quadratic model of disorder described in Ref.<sup>58</sup>. In fact, we have the multilayer structure with the initial population difference in the  $j$ th layer of the medium corresponding to the distance  $(j-1)\delta L < z \leq j\delta L$  given by

$$w_0^{(j)} = \text{sgn}(1 - 2r[(2\zeta_j - 1)(r - 1) + 1]), \quad (5)$$

where  $\zeta_j$  is the random number uniformly distributed in the range  $[0; 1]$ ,  $r$  is the parameter of the disorder strength,  $\text{sgn}$  is the sign function, and  $\delta L = \lambda/4$  is the layer thickness. When  $r = 0$ , we have the trivial case of purely absorbing medium (all  $w_0^{(j)} = 1$ , Fig. 1a). For  $r \geq 0.3$ , the gain layers with  $w_0^{(j)} = -1$  become possible (Fig. 1b,c). The case of the maximal disorder,  $r = 1$ , corresponds to the purely amplifying medium (all  $w_0^{(j)} = -1$ , Fig. 1d). Thus, the parameter  $r$  not only governs deviation from the ordered case of pure loss, but also takes on the role of pumping strength resulting in appearance of gain. In general, the different layers of the structure are under different, randomly distributed pumping and can be lossy or gainy with a certain probability. This can be realized in a side-pumping scheme similar to that utilized in Ref.<sup>20</sup> or with the adaptive-pumping approach<sup>58</sup>.

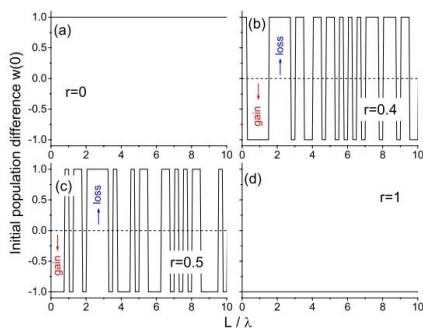


**Figure 1.** The example of initial population difference distributions for different disorder strengths  $r$ .

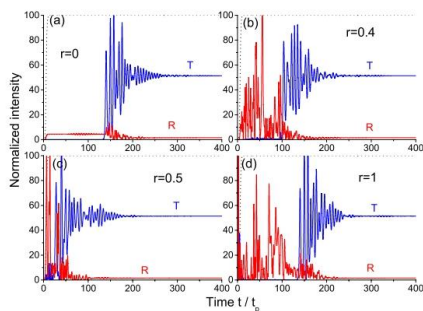


**Figure 2.** Intensity profiles for the transmitted and reflected light in the case of incident *non-adiabatic* front. Different panels show the results for different disorder strengths  $r$ .

Note that the quadratic model of disorder (Eq. 5) gives essentially the same results as the linear  $e^{\pm 2}$ , but is more convenient for symmetric representation of gain and loss. The similar linear model was experimentally realized recently in the context of random lasing<sup>49</sup>.

**Non-adiabatic fronts.** In this section, we consider the case of non-adiabatically switching field (Eq. 4), when  $t_p \ll T_2$ . In particular, we take the relaxation times  $T_1 = 1$  ns and  $T_2 = 0.1$  ns and the switching time  $t_p = 5$  ps. The Lorentz frequency is  $\omega_L^0 = 10^{10}$  s<sup>-1</sup>. The full thickness of the medium is  $L = 100\lambda$ . The final amplitude is  $\Omega_0 = 10\gamma_2$ .

Figure 2 shows the results of transmitted and reflected intensities calculations for different values of the disorder strength  $r$ . The initial population difference used in calculations is the same as in Fig. 1. Note that we consider here a single realization of disorder, since the observed features of interest for us are the same for different realizations at a certain level of disorder  $r$ : the specific oscillations of output intensity can differ, but the time needed for steady-state establishment and the final intensity are essentially the same for every realization. In the ordered system ( $r = 0$ , see Fig. 2a), which is the uniform resonantly absorbing medium, the time needed for the front to pass through ( $\sim 150t_p$ ) is much longer due to dispersion than the free propagation time ( $Lt_d/c \sim 0.08t_p$ ) and, in fact, is governed by the relaxation time  $T_2 = 20t_p$ . The stationary response of the medium is established after its saturation and is seen from  $\sim 300t_p$  on.



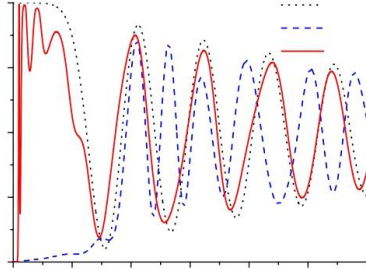


**Figure 3.** Dynamics of population difference at the entrance of non-adiabatic front in the medium with different disorder strengths  $r$ .

Increasing disorder strength  $r$  results in larger number of gain layers. As a result of stimulated emission in these layers, saturation needs less time and the stationary level is established faster. This is especially obvious for  $r = 0.5$  (Fig. 2c). For even larger  $r$ , the number of gain layers becomes so large that amplified emission in the form of powerful bursts happens in the very first instants of time effectively returning most two-level particles to the ground level. Therefore, the propagation time of the front through the highly-amplifying system is similar to that in the case of purely absorbing medium (compare Fig. 2d and a).

The difference in the response time can be illustrated with the dynamics of population difference at the entrance of the structure shown in Fig. 3. This figure demonstrates the initial stage of medium saturation with the oscillations converging to the very low (almost zero) value. These are the well-known Rabi oscillations with the frequency given by the so-called Rabi frequency and, hence, dependent on the incident radiation amplitude. Note that for these oscillations to appear, the Rabi frequency should be larger than the medium relaxation rate that is easily satisfied in our calculations ( $\Omega_0 = 10\gamma_2$ ). It is seen that although the dynamics for the amplifying ( $r = 1$ ) and the absorbing medium ( $r = 0$ ) start from absolutely different levels ( $w = -1$  and  $w = 1$ , respectively), the oscillations of population difference very closely follow each other. On the contrary, for  $r = 0.5$ , we also start from  $w = -1$  (the first layer with gain), but the subsequent dynamics strongly differs from those for  $r = 0$  and  $r = 1$ . This confirms that similarity of the transmitted intensity profiles in Fig. 2d.a is not accidental.

An additional corroboration of this conclusion is given in Fig. 4, which shows the distribution of population difference for different disorder strengths  $r$  at the time instant  $t = 20t_0$ , corresponding to the initial stage of radiation interaction with the medium (before the steady-state is established). It is seen that we have the random variations at  $r = 0.4$  (Fig. 4b) and  $r = 0.5$  (Fig. 4c) which can be treated as the variations of population difference around zero value. In other words, the medium can be considered as saturated on average. The light-matter interaction is comparatively weak in this case (there is no loss and gain on average) resulting in the increased speed of signal propagation, especially for  $r = 0.5$ . On the contrary, the distributions for the purely absorbing ( $r = 0$ , Fig. 4a) and purely amplifying media ( $r = 1$ , Fig. 4d) are very similar, except for some local excitation due to random wanderings of light inside the medium. This confirms the rapid relaxation of amplifying medium due to spontaneous emission, so that the incident wave front propagates further in such effectively de-inverted medium giving the response analogous to that for  $r = 0$ .

We see from Fig. 2 that the stationary level of transmission is around 51.5% and reflection is only about 1.5%. The rest (almost half the energy of the wave) is absorbed by the saturated medium. How realistic is it? Let us estimate the level of stationary population difference necessary for this value of absorption. In the steady-state approximation, the two-level medium can be described with the effective dielectric permittivity as follows<sup>62</sup>

$$\epsilon_{eff} = \epsilon'_{eff} + i\epsilon''_{eff} = n_s^2 + \frac{K(-\delta + i\gamma_2)}{1 + |\Omega|^2/\Omega_{sat}^2}, \tag{6}$$

where  $\Omega_{sat}^2 = \gamma_1(\gamma_2^2 + \delta^2)/4l^2\gamma_2$  is the saturation intensity,  $K = 3\omega_L l^2/\omega(\gamma_2^2 + \delta^2)$ . In the exact resonance ( $\delta = 0$ ), we have  $\epsilon'_{eff} = n_s^2$  and  $\epsilon''_{eff} = 3\omega_L T_2 w_{eff}$ , where  $w_{eff} = (1 + |\Omega|^2/\Omega_{sat}^2)^{-1}$  is the sought-for effective population difference. Since  $\epsilon_{eff} = (n + i\kappa)^2$ , we can easily connect  $w_{eff}$  with the effective absorption coefficient  $\kappa$ , which, in turn, can be linked to the transmission as  $T = \exp(-4\pi\kappa l/\lambda)$ . For the parameters used in our calculations, one should take  $w_{eff} \approx 5.5 \cdot 10^{-4}$  to reach the transmission of 50%. This value of effective population difference is close to zero (i.e. the medium is indeed saturated) and has the same order of magnitude as the stationary population difference obtained in our numerical calculations.

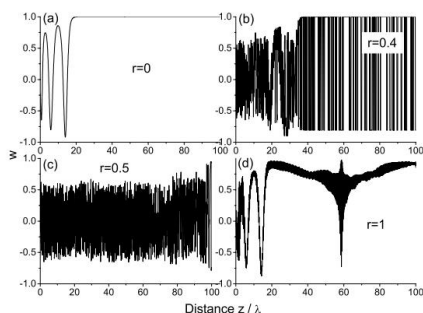


**Figure 4.** Distributions of population difference along the medium with different disorder strengths  $r$  at the time instant  $t = 20t_p$ . The medium is excited by the non-adiabatic wave front.

Note that in our estimation, we have neglected reflection which is indeed very low as seen in Fig. 2. This can be easily explained with a simple calculation of transmission and reflection of light from a uniform layer with the effective permittivity having small imaginary part. Finally, we see from the expression  $w_{eff} = (1 + |\Omega|^2 / \Omega_{sat}^2)^{-1}$  that it should depend on the incident wave intensity: increasing intensity, we can make absorption smaller due to saturation. In other words, the low-intensity waves are almost entirely absorbed, whereas the high-intensity ones are mostly transmitted. The effect of disorder on the propagation time can be conveniently observed at the intermediate intensities, not very low and not very high (e.g.,  $\Omega_0 = 10\gamma_2$  as in Fig. 2).

The features discussed in this section are also valid for two interacting wave fronts as shown in Supplementary Information.

**Adiabatic fronts.** In this section, we consider the case of adiabatically switching field (Eq. 4), when  $t_p \gg T_2$ . In particular, we take the relaxation times  $T_1 = 1$  ns and  $T_2 = 0.1$  ps and the switching time  $t_p = 30T_2$ . The Lorentz frequency is  $\omega_0^j = 10^{11}$  s $^{-1}$ . The full thickness of the medium is  $L = 200\lambda$ , which is long enough for a kink to form and can be traversed after  $Lna/c \sim 0.27t_p$  in the case of dispersion-free medium. The final amplitude is  $\Omega_0 = 0.3\gamma_2$ , so that there are no Rabi oscillations and the light-matter interaction is quasi-stationary in this case<sup>60</sup>.

It is known that the adiabatically switching waveform (Eq. 4) undergoes self-steepening resulting in the kink (shock wave) formation after some distance passed through the resonantly absorbing medium<sup>61,62</sup>. Such a kink is seen in Fig. 5a for the disorder strength  $r = 0$ , when all the layers are the same absorbing medium. For increased disorder, we still obtain the kink at the exit (Fig. 5b at  $r = 0.4$ ), although the system is now non-uniform and contains both loss and gain layers. Note the increased speed of this kink. For  $r = 0.5$ , when both loss and gain are equally probable, the kink formation is totally suppressed as shown in Fig. 5c. Moreover, the transmitted intensity grows ahead of the incident intensity (at early times  $t < 4t_p$ ). These features are due to the large number of gain layers providing the proper amplification of the signal and fast saturation of the medium, so that the wave can almost freely propagate through the structure in later times. For even stronger disorders, the portion of gain layers becomes so large that even tiny impinging radiation rapidly stimulates a powerful burst of energy as seen in Fig. 5d for  $r = 1$  (uniform gain medium). After this burst, the most part of the particles return to the ground state, so that the medium remains only weakly excited and gets saturated by the incident wave front. Although the kink is not formed in this case, the transmitted profile is closer to a kink than for  $r = 0.5$ , manifesting a characteristic offset time between input and output signals.

Thus, disorder gives us an opportunity to control the shape of the output wave switching on and off kink formation. As shown in Supplementary Information, a similar effect disorder has on a pair of interacting adiabatic fronts.

## Conclusion

In summary, we have proposed a novel approach for wave-front velocity and shape governing in the multi-layer structure with disorderly distributed resonant loss and gain. This concept involves functionalities of both non-Hermitian system and disordered multilayer providing several new optical effects. The two types of fronts were considered—the adiabatic (slowly switching) and non-adiabatic (rapidly switching) ones. These two cases have different dynamic features—kinks and Rabi oscillations, respectively,—which condition the propagation characteristics of the wave fronts. Introduction of disorder governed by external pumping results in a number of easily noticeable novel features, such as kink suppression and propagation time shortening. These disorder-induced effects together with the transmitted intensity determined by the medium saturation give us a tool to

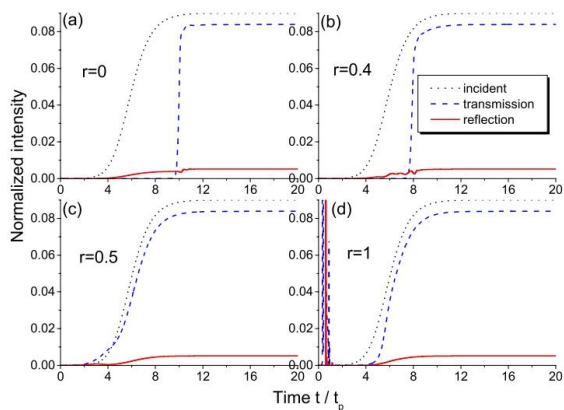


**Figure 5.** Intensity profiles for the transmitted and reflected light in the case of incident adiabatic front. Different panels show the results for different disorder strengths  $r$ .

control transmission, shape and propagation time of the waves with the finite switching time. Such possibilities are extremely important for manipulation of light produced by realistic laser sources and can be used in optical switching and data processing among other applications.

#### Data availability

The datasets generated during and/or analysed during the current study are available from the corresponding author on reasonable request.

Received: 13 October 2020; Accepted: 15 February 2021

Published online: 26 February 2021

#### References

- Zyablovsky, A. A., Vinogradov, A. P., Pukhov, A. A., Dorofeenko, A. V. & Lisjansky, A. A.  $\mathcal{PT}$  symmetry in optics. *Phys. Usp.* **57**, 1063–1082 (2014).
- Feng, L., El-Ganainy, R. & Ge, L. Non-Hermitian photonics based on parity-time symmetry. *Nat. Photon.* **11**, 752–762 (2017).
- El-Ganainy, R. *et al.* Non-Hermitian physics and  $\mathcal{PT}$  symmetry. *Nat. Phys.* **13**, 11–19 (2018).
- Ozdemir, S. K., Rotter, S., Nori, F. & Yang, L. Parity-time symmetry and exceptional points in photonics. *Nat. Mater.* **18**, 783–798 (2019).
- Miri, M.-A. & Alu, A. Exceptional points in optics and photonics. *Science* **363**, eaar7709 (2019).
- Lin, Z. *et al.* Unidirectional invisibility induced by  $\mathcal{PT}$ -symmetric periodic structures. *Phys. Rev. Lett.* **106**, 213901 (2011).
- Feng, L. *et al.* Experimental demonstration of a unidirectional reflectionless parity-time metamaterial at optical frequencies. *Nat. Mater.* **12**, 108–113 (2013).
- Chen, W., Ozdemir, S. K., Zhao, G., Wiersig, J. & Yang, L. Exceptional points enhance sensing in an optical microcavity. *Nature (London)* **548**, 192–196 (2017).
- Hodaie, H. *et al.* Enhanced sensitivity at higher-order exceptional points. *Nature (London)* **548**, 187–191 (2017).
- Hokmabadi, M. P., Schumer, A., Christodoulides, D. N. & Khajavikhan, M. Non-Hermitian ring laser gyroscopes with enhanced Sagnac sensitivity. *Nature (London)* **576**, 70–74 (2019).
- Lai, Y.-H., Lu, Y.-K., Suh, M.-G., Yuan, Z. & Vahala, K. Observation of the exceptional-point-enhanced Sagnac effect. *Nature (London)* **576**, 65–69 (2019).
- Peng, B. *et al.* Loss-induced suppression and revival of lasing. *Science* **346**, 328–332 (2014).
- Novitsky, D. V., Karabchevsky, A., Lavrinenko, A. V., Shalin, A. S. & Novitsky, A. V.  $\mathcal{PT}$  symmetry breaking in multilayers with resonant loss and gain locks light propagation direction. *Phys. Rev. B* **98**, 125102 (2018).
- Feng, L., Wong, Z. J., Ma, R.-M., Wang, Y. & Zhang, X. Single-mode laser by parity-time symmetry breaking. *Science* **346**, 972–975 (2014).
- Hodaie, H., Miri, M.-A., Heinrich, M., Christodoulides, D. N. & Khajavikhan, M. Parity-time-symmetric microring lasers. *Science* **346**, 975–978 (2014).
- Gu, Z. *et al.* Experimental demonstration of  $\mathcal{PT}$ -symmetric stripe lasers. *Laser Photon. Rev.* **10**, 588–594 (2016).
- Zhang, Z. *et al.* Tunable topological charge vortex microlaser. *Science* **368**, 760–763 (2020).
- Longhi, S.  $\mathcal{PT}$ -symmetric laser absorber. *Phys. Rev. A* **82**, 031801(R) (2010).
- Chong, Y. D., Ge, L. & Stone, A. D. Symmetry breaking and laser-absorber modes in optical scattering systems. *Phys. Rev. Lett.* **106**, 093902 (2011).

20. Wong, Z. J. *et al.* Lasing and anti-lasing in a single cavity. *Nat. Photon.* **10**, 796–801 (2016).
21. Novitsky, D. V. CPA-laser effect and exceptional points in  $\mathcal{PT}$ -symmetric multilayer structures. *J. Opt.* **21**, 085101 (2019).
22. Leykam, D., Bliokh, K. Y., Huang, C., Chong, Y. D. & Nori, F. Edge modes, degeneracies, and topological numbers in non-Hermitian systems. *Phys. Rev. Lett.* **118**, 040401 (2017).
23. Takata, K. & Notomi, M. Photonic topological insulating phase induced solely by gain and loss. *Phys. Rev. Lett.* **121**, 213902 (2018).
24. Ni, X. *et al.*  $\mathcal{PT}$  phase transitions of edge states at  $\mathcal{PT}$  symmetric interfaces in non-Hermitian topological insulators. *Phys. Rev. B* **98**, 165129 (2018).
25. Zhao, H. *et al.* Non-Hermitian topological light steering. *Science* **365**, 1163–1166 (2019).
26. Wiersma, D. S. Disordered photonics. *Nat. Photon.* **7**, 188–196 (2013).
27. Zhigunov, D., Evlyukhin, A. B., Shalin, A. S., Zywieta, U. & Chichkov, B. N. Femtosecond laser printing of single Ge and SiGe nanoparticles with electric and magnetic optical resonances. *ACS Photon.* **5**, 977–983 (2018).
28. Baryshnikova, K. *et al.* Giant magnetoelectric field separation via anapole-type states in high-index dielectric structures. *Phys. Rev. B* **98**, 165419 (2018).
29. Ivinskaya, A. *et al.* Optomechanical manipulation with hyperbolic metasurfaces. *ACS Photon.* **5**, 4371–4377 (2018).
30. Segev, M., Silberberg, Y. & Christodoulides, D. N. Anderson localization of light. *Nat. Photon.* **7**, 197–204 (2013).
31. Gredeskul, S. A. *et al.* Anderson localization in metamaterials and other complex media. *Low Temp. Phys.* **38**, 570–602 (2012).
32. Sheinfux, H. H. *et al.* Observation of Anderson localization in disordered nanophotonic structures. *Science* **356**, 953–956 (2017).
33. Chabanov, A. A., Zhang, Z. Q. & Genack, A. Z. Breakdown of diffusion in dynamics of extended waves in mesoscopic media. *Phys. Rev. Lett.* **90**, 203903 (2003).
34. Sarma, R., Golubev, T., Yamilov, A. & Cao, H. Control of light diffusion in a disordered photonic waveguide. *Appl. Phys. Lett.* **105**, 041104 (2014).
35. Naraghi, R. R. & Dogariu, A. Phase transitions in diffusion of light. *Phys. Rev. Lett.* **117**, 263901 (2016).
36. Conti, C., Angelani, L. & Ruocco, G. Light diffusion and localization in three-dimensional nonlinear disordered media. *Phys. Rev. A* **75**, 033812 (2007).
37. Lahini, Y. *et al.* Anderson localization and nonlinearity in one-dimensional disordered photonic lattices. *Phys. Rev. Lett.* **100**, 013906 (2008).
38. Sharabi, Y., Sheinfux, H. H., Sagi, Y., Eisenstein, G. & Segev, M. Self-induced diffusion in disordered nonlinear photonic media. *Phys. Rev. Lett.* **121**, 233901 (2018).
39. Makris, K. G., Musslimani, Z. H., Christodoulides, D. N. & Rotter, S. Constant-intensity waves and their modulation instability in non-Hermitian potentials. *Nat. Commun.* **6**, 7257 (2015).
40. Makris, K. G., Brandstötter, A., Ambichl, P., Musslimani, Z. H. & Rotter, S. Wave propagation through disordered media without backscattering and intensity variations. *Light Sci. Appl.* **6**, e17035 (2017).
41. Brandstötter, A., Makris, K. G. & Rotter, S. Scattering-free pulse propagation through invisible non-Hermitian media. *Phys. Rev. B* **99**, 115402 (2019).
42. Tzortzakakis, A. F., Makris, K. G., Rotter, S. & Economou, E. N. Shape-preserving beam transmission through non-Hermitian disordered lattices. [arXiv:2005.06414](https://arxiv.org/abs/2005.06414) (2020).
43. Makris, K. G., Krešić, I., Brandstötter, A. & Rotter, S. Scattering-free channels of invisibility across non-Hermitian media. *Optica* **7**, 619–623 (2020).
44. Hamazaki, R., Kawabata, K. & Ueda, M. Non-Hermitian many-body localization. *Phys. Rev. Lett.* **123**, 090603 (2019).
45. Tzortzakakis, A. F., Makris, K. G. & Economou, E. N. Non-Hermitian disorder in two-dimensional optical lattices. *Phys. Rev. B* **101**, 014202 (2020).
46. Huang, Y. & Shklovskii, B. I. Anderson transition in three-dimensional systems with non-Hermitian disorder. *Phys. Rev. B* **101**, 014204 (2020).
47. Zhai, L.-J., Yin, S. & Huang, G.-Y. Many-body localization in a non-Hermitian quasiperiodic system. *Phys. Rev. B* **102**, 064206 (2020).
48. Noginov, M. A. *Solid-State Random Lasers* (Springer, New York, 2005).
49. Turitsyn, S. K. *et al.* Random distributed feedback fibre laser. *Nat. Photon.* **4**, 231–235 (2010).
50. Liu, J. *et al.* Random nanolasing in the Anderson localized regime. *Nat. Nanotech.* **9**, 285–289 (2014).
51. Abaie, B. *et al.* Random lasing in an Anderson localizing optical fiber. *Light Sci. Appl.* **6**, e17041 (2017).
52. Novitsky, D. V., Redka, D. & Shalin, A. S. Different regimes of ultrashort pulse propagation in disordered layered media with resonant loss and gain. *Ann. Phys. (Berlin)* **531**, 1900080 (2019).
53. Allen, L. & Eberly, J. H. *Optical Resonance and Two-Level Atoms* (Wiley, New York, 1975).
54. Crenshaw, M. E. Comparison of quantum and classical local-field effects on two-level atoms in a dielectric. *Phys. Rev. A* **78**, 053827 (2008).
55. Novitsky, D. V. Femtosecond pulses in a dense two-level medium: Spectral transformations, transient processes, and collisional dynamics. *Phys. Rev. A* **84**, 013817 (2011).
56. Crenshaw, M. E. Quasadiabatic approximation for a dense collection of two-level atoms. *Phys. Rev. A* **54**, 3559–3575 (1996).
57. Novitsky, D. V. Compression of an intensive light pulse in photonic-band-gap structures with a dense resonant medium. *Phys. Rev. A* **79**, 023828 (2009).
58. Bachelard, N., Gigan, S., Noblin, X. & Sebbah, P. Adaptive pumping for spectral control of random lasers. *Nat. Phys.* **10**, 426–431 (2014).
59. Lee, M., Callard, S., Seassal, C. & Jeon, H. Taming of random lasers. *Nat. Photon.* **13**, 445–448 (2019).
60. Novitsky, D. V. & Shalin, A. S. Kink-based mirrorless quasi-bistability in resonantly absorbing media. *Opt. Lett.* **45**, 137–140 (2020).
61. Ponomarenko, S. A. & Haghgoo, S. Self-similarity and optical kinks in resonant nonlinear media. *Phys. Rev. A* **82**, 051801(R) (2010).
62. Novitsky, D. V., Tuz, V. R., Prosvirnin, S. L., Lavrinenko, A. V. & Novitsky, A. V. Transmission enhancement in loss-gain multilayers by resonant suppression of refection. *Phys. Rev. B* **96**, 235129 (2017).
63. Novitsky, D. V. Optical kinks and kink-kink and kink-pulse interactions in resonant two-level media. *Phys. Rev. A* **95**, 053846 (2017).

### Acknowledgements

The work was supported by the Belarusian Republican Foundation for Fundamental Research (Project No. F20R-158) and the Russian Foundation for Basic Research (Project No. 20-52-00031). Numerical simulations of the nonlinear interaction of light with resonant media have been supported by the Russian Science Foundation (Project No. 18-72-10127). D.M. and D.L. are partially supported by KAUST baseline funding.

### Author contributions

D.V.N. performed calculations and wrote the draft, A.S.S. analysed the results, D.L., D.M., D.R. and A.A.P. participated in the problem formulation and discussion of the results. All authors reviewed the manuscript.

**6-PAPER:** Nanoscale tunable optical binding mediated by hyperbolic metamaterials

Kostina N.A., Kislov D.A., Ivinskaya A.N., Proskurin A., Redka D.N., Novitsky A., Ginzburg P., Shalin A.S., “Nanoscale Tunable Optical Binding Mediated by Hyperbolic Metamaterials”, (2020) *ACS Photonics*, 7 (2), pp. 425 - 433, DOI: [10.1021/acsp Photonics.9b01378](https://doi.org/10.1021/acsp Photonics.9b01378)

## Nanoscale Tunable Optical Binding Mediated by Hyperbolic Metamaterials

Natalia A. Kostina,<sup>\*,†</sup> Denis A. Kislov,<sup>‡</sup> Aliaksandra N. Ivinskaya,<sup>†,□</sup> Alexey Proskurin,<sup>‡</sup> Dmitrii N. Redka,<sup>‡</sup> Andrey Novitsky,<sup>§,⊙</sup> Pavel Ginzburg,<sup>||,⊙,¶</sup> and Alexander S. Shalin<sup>\*,†,||</sup>

<sup>†</sup>Department of Physics and Engineering, ITMO University, Kronverksky pr., 49, 197101 St. Petersburg, Russia

<sup>‡</sup>Saint Petersburg Electrotechnical University "LETI" (ETU), Prof. Popova Street, 5, 197376 St. Petersburg, Russia

<sup>§</sup>Department of Theoretical Physics and Astrophysics, Belarusian State University, Nezavisimosti Avenue, 4, 220030 Minsk, Belarus

<sup>||</sup>School of Electrical Engineering, Tel Aviv University, Ramat Aviv, 69978 Tel Aviv, Israel

<sup>⊙</sup>Light-Matter Interaction Centre, Tel Aviv University 69978, Tel Aviv, Israel

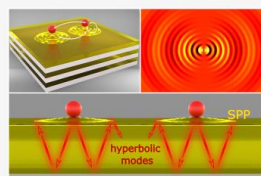
<sup>□</sup>Center for Photonics and 2D Materials, Moscow Institute of Physics and Technology, Institutskiy per., 9, 141700 Dolgoprudny, Russia

<sup>¶</sup>Ulyanovsk State University, Lev Tolstoy Street 42, 432017 Ulyanovsk, Russia

### Supporting Information

**ABSTRACT:** Carefully designed nanostructures can inspire a new type of optomechanical interactions and allow surpassing limitations set by classical diffractive optical elements. Apart from strong near-field localization, a nanostructured environment allows controlling scattering channels and might tailor many-body interactions. Here we investigate an effect of optical binding, where several particles demonstrate a collective mechanical behavior of bunching together in a light field. In contrast to classical binding, where separation distances between particles are diffraction limited, an auxiliary hyperbolic metasurface is shown here to break this barrier by introducing several controllable near-field interaction channels. Strong material dispersion of the hyperbolic metamaterial along with high spatial confinement of optical modes, which it supports, allows achieving superior tuning capabilities and efficient control over binding distances on the nanoscale. In addition, a careful choice of the metamaterial slab's thickness enables decreasing optical binding distances by orders of magnitude compared to free space scenarios due to the multiple reflections of volumetric modes from the substrate. Auxiliary tunable metamaterials, which allow controlling collective optomechanical interactions on the nanoscale, open a venue for new investigations including collective nanofluidic interactions, triggered biochemical reactions, and many others.

**KEYWORDS:** optical forces, optical tweezers, hyperbolic metamaterials, surface plasmons, optical binding



Optomechanical manipulation<sup>1</sup> is a widely used technique across many disciplines,<sup>2,3</sup> where it is utilized for many fundamental and applied investigations. The capability to manipulate small objects with focused light beams and measure pico- and even femto-<sup>4,5</sup> Newton-scale forces opens a venue for studies of new light–matter interaction regimes<sup>6,7</sup> and biomolecular processes<sup>8,9</sup> to name just a few. Conventional optical tweezer realizations rely on diffractive optical elements and, as a result, have limited trapping capabilities in application to nanoscale particles. As a promising paradigm solution, auxiliary nanostructures have been introduced. So-called plasmonic tweezers<sup>10,11</sup> utilize the capability of noble metal structures to confine light beyond the diffraction limit<sup>12,13</sup> and provide improved trap stiffness with relatively low optical powers. While the majority of plasmonic tweezer configurations utilize nanoantenna arrays, optomechanical surfaces,<sup>14,15</sup> metasurfaces,<sup>16</sup> and metamaterials<sup>17,18</sup> have been recently proposed. These types of configurations with less structured

features (in comparison to antenna arrays) might provide additional capabilities, such as optical attraction,<sup>19</sup> and are less sensitive to accurate positioning of trapping beams with respect to a structure.

In general, functionalities of auxiliary structures can be split into three main categories. The first one is related to the ability of near-field concentration beyond the diffraction limit, which is traced back to the first generation of plasmonic tweezers.<sup>20–22</sup> Here the main tool for analysis is based on dipolar approximation, where the manipulated particle's size is small compared with the fastest spatial intensity variation. It is also important that this model assumes the local field to remain unperturbed by a small particle. The next level of sophistication in auxiliary structure design is to account for a modified density of photonic states, which governs scattering channels from the

Received: September 23, 2019

Published: December 16, 2019

particle. For example, if a nearby structure significantly modifies a scattering pattern, the particle takes the recoil in order to conserve the entire linear momentum. One of the main functions of metasurfaces and metamaterials<sup>6–18</sup> is to tailor scattering into high density of states modes. Apparently, the most complex approach to optomechanical manipulation utilizes active feedback, where a Brownian particle in an optical field modifies the trapping potential dynamically and experiences a back action effect.<sup>23</sup>

An important niche in the field of the optomechanical manipulation is devoted to the investigation of many-body interactions mediated by self-consistent optical fields. Light-induced binding of micro- and nanosized objects can provide stable configurations of particles due to light rescattering and their self-organization under external illumination.<sup>24,25</sup> Capabilities to achieve simultaneous sorting and ordering of particle clusters without a need to structure the incident beam makes optical binding advantageous over holographic tweezing techniques.<sup>3,26,27</sup> Various binding scenarios have been investigated and include studies of interactions under Gaussian- and Bessel-shaped beam illumination,<sup>28,29</sup> pattern creation with several interfering beams,<sup>30,31</sup> evanescent field excitations, and self-organization of several optically interacting plasmonic particles.<sup>32</sup> However, those methods rely on either high-field intensities or specific particles' materials, which may limit their generality. Increasing optical trap stiffness without a need to use high-intensity illumination, flexible control over interparticle distances, and anisotropic optical binding in different directions are among the long-standing challenges, valuable from both fundamental and practical standpoints.<sup>33</sup> Parameters of optical binding can be significantly influenced by introducing a nearby interface. It modifies both the incident field due to Fresnel reflection and effective particle polarizabilities owing to near-field interactions, qualitatively understood with the help of the image theory.<sup>34,35</sup> It was shown that metal–dielectric interfaces supporting the propagation of surface plasmon-polariton modes (SPPs) can increase optical trapping stiffness and reduce particle–interface separation distances owing to strong interactions with SPPs.<sup>10,36–38</sup>

Structured interfaces can provide an additional flexibility in tailoring scattering channels via a predesigned dispersion of surface and bulk modes. Anisotropic response is one among many possibilities. Generally, extremely anisotropic metamaterials<sup>39–41</sup> proved to be useful in various types of applications, i.e., cloaking,<sup>42–44</sup> super-resolution,<sup>45,46</sup> and energy transfer.<sup>47–49</sup> and recently have opened a venue for flexible optomechanical control. Furthermore, it has been shown that hyperbolic dispersion of bulk modes causes optical pulling forces,<sup>17</sup> can lead to levitation<sup>50</sup> and repulsion,<sup>51</sup> and can even generate negative lateral optical forces along the surface.<sup>16</sup>

Here we investigate capabilities of hyperbolic metamaterial substrates in application to optical binding. A typical scenario is depicted in Figure 1, where a pair of small particles are linked together by an optical field, mediated by a structured surface. In contrary to free space binding scenarios, a layered metal–dielectric substrate opens additional interaction channels, mediated by surface and volumetric modes. As it will be shown, the interplay between the surface geometry and the modes within the bulk will allow achieving optical binding with deeply subwavelength separation distances and even efficiently tune the latter by exploiting strong chromatic dispersion of the metamaterial.

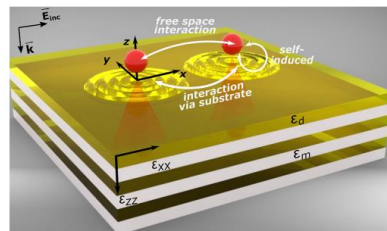


**Figure 1.** General concept of optical binding above a metamaterial slab. Highly confined optical modes inside the layered hyperbolic metamaterial open additional interaction channels and allow for the formation of dimers and chains with separation distances below the diffraction limit.

This article is organized as follows: Green's function approach to optomechanical interactions is revised first, followed by the analysis of optical binding next to semi-infinite hyperbolic substrate and finite thickness slab.

#### ■ GREEN'S FUNCTION FORMALISM IN APPLICATION TO OPTICAL BINDING NEAR INTERFACES

The considered scenario is depicted in Figure 1, where a plane wave illuminates two subwavelength nanoparticles placed in the vicinity of an anisotropic substrate. Particles' locations in Cartesian coordinates are  $(0, 0, a)$  and  $(x, y, a)$ , where  $a = \lambda_0/30$  is the radius of the particles and  $\lambda_0$  is the incident light wavelength. Light–matter interactions with the particles will be analyzed under the dipolar approximation. There are three types of channels, which govern the binding phenomenon: (i) particle–particle interaction via the substrate modes, (ii) particle–particle interaction via free space modes, and (iii) individual coupling between each particle and the substrate.

Optical force on a particle in the dipolar approximation can be written as follows:

$$\vec{F} = \frac{1}{2} \text{Re} \left[ \sum_i (\alpha(\omega) E_i(\vec{r}, \omega))^* \nabla E_i(\vec{r}, \omega) \right] \quad (1)$$

where  $E_i$  corresponds to the  $i$ th component of the self-consistent electric field,  $i = x, y, z$  are coordinates, and  $\alpha(\omega)$  is the dipolar particle's polarizability in vacuum, including the radiation correction  $\alpha = \frac{\alpha_{ns}}{1 - i \frac{3\alpha_{ns}}{4\pi\epsilon_0}}; \alpha_{ns} = 4\pi\epsilon_0 a^3 \frac{\epsilon_p - \epsilon_0}{\epsilon_p + 2\epsilon_0}$ ,  $\epsilon_0$  is the vacuum permittivity,  $\epsilon_p$  is the permittivity of the particle (we consider  $\epsilon_p = 3$ ), and  $\epsilon_1$  is the permittivity of the surrounding media.

In our notations, where  $\vec{r}_1 = (0, 0, a)$  and  $\vec{r}_2 = (x, y, a)$ , the self-consistent electric field is given by

$$\begin{aligned} \vec{E}(\vec{r}) &= \vec{E}_{inc}(\vec{r}) + \frac{k_0^2}{\epsilon_0} \vec{G}(\vec{r}_1, \vec{r}_1) \alpha_1 \vec{E}(\vec{r}_1) \\ &+ \frac{k_0^2}{\epsilon_0} \vec{G}(\vec{r}_1, \vec{r}_2) \alpha_2 \vec{E}(\vec{r}_2), \quad j = 1, 2 \end{aligned} \quad (2)$$

The first term here represents the incident field with the substrate reflection taken into account; the second and the third terms are the contributions of the dipoles. The Green's function

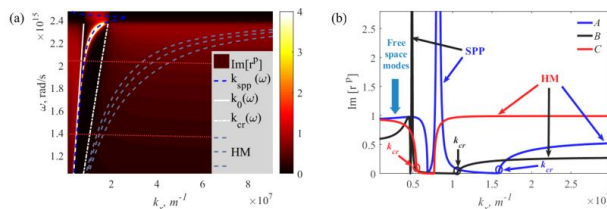


**Figure 2.** (a) Color map of the imaginary part of the reflection coefficient as a function of the wavevector's  $x$ -component and incident wave frequency. From this graph one can, for example, pick out frequencies  $\omega = 2.05 \times 10^{15}$  and  $\omega = 1.4 \times 10^{15}$  rad/s as points A and B, correspondingly (shown with dotted red lines). A corresponds to  $\lambda_0 = 920$  nm and effective medium parameters  $\epsilon_{xx} = -1.714 + 0.075i$ ,  $\epsilon_{zz} = 5.392 + 0.0084i$  and for B  $\lambda_0 = 1350$  nm,  $\epsilon_{xx} = -8.94 + 0.33i$ ,  $\epsilon_{zz} = 5.19 + 0.0118i$ . (b) Imaginary part of the reflection coefficient as a function of the wavevector  $x$ -component. The dependence is plotted for three sets of parameters: A with blue, B with black, and C (ideal case without the SPP contribution for  $\lambda_0 = 920$  nm,  $\epsilon_{xx} = -2 + 0.066i$ ,  $\epsilon_{zz} = 0.5 + 0.0084i$ ) with red lines. Characteristic regions to underline the contributions of different interaction channels are  $k_x \in [0; k_c]$  for propagating free-space modes,  $k_x \in (k_0; k_c]$  for SPP,  $k_x \in (k_c, \infty)$  for hyperbolic modes.

$\vec{G}$  encapsulates the entire information on the interaction of the dipole with the substrate.<sup>34</sup> Substituting the solution of self-consistently formulated eq 2 into eq 1 allows for calculating the optical force.

#### ■ TAILORING GREEN'S FUNCTIONS NEAR HYPERBOLIC SUBSTRATES

Investigation of different particle–substrate interaction channels can be performed by analyzing the corresponding Green's function in reciprocal space ( $k$ -space). This integral representation, as it will be shown hereinafter, can be split into three parts corresponding to the interaction channels with different physical origin. In particular, propagating (nonevanescent in the upper half-space) modes, surface plasmons, and bulk hyperbolic modes can be involved.<sup>16,44,52–54</sup> Further, we will consider layered realization of the metamaterial depicted in Figure 1. The permittivity tensor linked to the chosen set of layers is diagonal and obtained via standard homogenization theory<sup>55,56</sup> with  $\epsilon_{xx} = \epsilon_{yy} \neq \epsilon_{zz}$  where hyperbolic dispersion occurs when  $\text{Re}[\epsilon_{xx}] < 0$  and  $\text{Re}[\epsilon_{zz}] > 0$ . Those components also have strong chromatic dispersion, which will be subsequently used for achieving tunability in binding parameters (see section Chromatic Tuning of Binding).

In order to split the spectral integral representing Green's function in  $k$ -space, dispersion of the contributing modes should be derived first. The longitudinal component of the wavevector of bulk metamaterial mode has the form<sup>54</sup>

$$k_{z2} = \sqrt{(k_0^2 \epsilon_{zz} - k_x^2) \frac{\epsilon_{xx}}{\epsilon_{zz}}} \quad (3)$$

where  $k_0$  is the wavenumber of an incident wave and  $k_x$  is the component of the wavevector of a bulk mode along the substrate surface (transversal component). While  $\frac{\text{Re}[\epsilon_{xx}]}{\text{Re}[\epsilon_{zz}]} < 0$ , the wave propagation in a bulk hyperbolic material is possible as long as  $k_x$  surpasses a critical value

$$k_{cr} = k_0 \sqrt{\epsilon_{zz}} \quad (4)$$

and  $k_z$  becomes real.

In order to reveal the contribution of different types of modes (free space, plasmons, hyperbolic modes), Fresnel coefficients should be analyzed.<sup>54</sup> The reflection coefficient from a semi-

infinite hyperbolic substrate for  $s$ - and  $p$ -polarized waves is given by

$$r^p = \frac{\epsilon_{xx} k_{z1} - \epsilon_1 k_{z2}}{\epsilon_{xx} k_{z1} + \epsilon_1 k_{z2}}, \quad r^s = \frac{k_{z1} - k_{z2}}{k_{z1} + k_{z2}} \quad (5)$$

here  $\epsilon_1$  denotes the dielectric permittivity of the upper half-space and  $k_{z2}$ ,  $k_{z1}$  are longitudinal (perpendicular to the substrate) wavevector components in the hyperbolic metamaterial and in the upper half-space, respectively.

Examination of the Fresnel coefficients allows identifying conditions for excitation of two types of modes in the structure: volumetric hyperbolic modes in a metamaterial and surface plasmon-polaritons on its interface. From the reflection coefficient for  $p$ -polarization it is possible to obtain the SPP propagation constant (note that SPP is naturally  $p$ -polarized):

$$k_x^{\text{SPP}} = k_0 \sqrt{\frac{\epsilon_1(\epsilon_{xx} - \epsilon_1)}{\epsilon_{xx} - \epsilon_1^2 \epsilon_{zz}^{-1}}} \quad (6)$$

SPP exists only if  $\text{Re}[\epsilon_{zz}] > \text{Re}[\epsilon_1]$ , resulting in imaginary  $z$  and real  $x$  components of the SPP wavevector. The surface plasmon-polariton resonance condition corresponds to the zero denominator of eq 6, but it is not satisfied as far as  $\text{Re}[\epsilon_{zz}] < 0$ ,  $\text{Re}[\epsilon_{zz}] > 0$ . The minimal value of the denominator corresponds to the  $\text{Re}[\epsilon_{xx}] \rightarrow 0$  and  $\text{Re}[\epsilon_{zz}] \rightarrow \infty$ , which is close to the surface plasmon-polariton excitation. For the opposite case  $\text{Re}[\epsilon_{xx}] > 0$ ,  $\text{Re}[\epsilon_{zz}] < 0$  surface plasmon-polariton does not exist, as perpendicular to the surface wavevector component is real.

Let us consider in detail the hyperbolic case of  $\text{Re}[\epsilon_{xx}] < 0$ ,  $\text{Re}[\epsilon_{zz}] > 0$ . Figure 2(a) is presented to provide a better understanding of the modal structure of the system. The imaginary part of the reflection coefficient contains information about all of the modes.<sup>54</sup> Here the dispersion for homogenized multilayered  $\text{Ag}/\text{Ta}_2\text{O}_5$  is presented (filling factor of the structure is 0.133). The imaginary part of the reflection coefficient as a function of the parallel to substrate wavevector component and frequency  $\omega$  is presented. White lines (solid and dash-dotted) correspond to the light line ( $k_0(\omega) = \omega/c$ ) and critical wavevector  $k_{cr}(\omega)$  from eq 4; the dark blue line illustrates the dispersion characteristic of the surface plasmon-polariton  $k_x^{\text{SPP}}(\omega)$  from eq 6, and hyperbolic modes are marked with blue



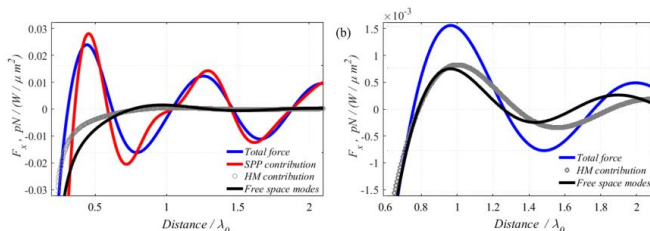


**Figure 3.** Dependence of the optical binding force on the distance between the particles. (a) is for A from Figure 2(b). (b) is for line C. The blue line corresponds to the total optical binding force near the anisotropic substrate, the red line is for the surface plasmon-polariton mode contribution, the grey circles depict contribution of hyperbolic modes, and the black lines show contribution of free-space propagating modes.

dashed lines (just a few examples). The behavior of the  $\text{Im}[r^p]$  is in perfect agreement with the dispersion characteristics.

Therefore, there are three important regions governing the interaction of a nanoparticle with the hyperbolic metamaterial. Hyperbolic modes are contributing for  $k_x > k_{cs}$  and surface plasmon-polaritons are supported between  $k_0$  and  $k_{cp}$ , so the distance between them defines the overall contribution of SPPs. The free-space modes are allowed at  $0 \leq k_x \leq k_0$ . In the particular case of  $k_{cs} \rightarrow k_0$  the SPP is negligible while hyperbolic modes and free-space modes play the main role. This scenario (among many others) is considered in Figure 2(b) (red line) to underline the contribution of hyperbolic modes in the absence of SPPs.

Thus, Green's function for particles–substrate interaction can be decomposed as follows:

$$\begin{aligned} \vec{G}^{\text{subs}}(\vec{r}_j, \vec{r}_i) = & \int_0^{k_0} \vec{M}^{\text{subs}}(k_x) dk_x + \int_{k_0}^{k_{cp}} \vec{M}^{\text{subs}}(k_x) dk_x \\ & + \int_{k_{cs}}^{\infty} \vec{M}^{\text{subs}}(k_x) dk_x, \quad j = 1, 2; \quad i = 1, 2 \end{aligned} \quad (7)$$

The integrand matrix  $\vec{M}^{\text{subs}}$  in the Green's function is presented in the Supporting Information (Section Green's Function Formalism).

In accordance with the aforementioned:  $I = \int_0^{k_0}$ , the free-space propagating mode contribution,  $II = \int_{k_0}^{k_{cp}}$ , the surface plasmon-polariton contribution (if SPPs are supported  $\epsilon_{zz} > \epsilon_1$ ), and  $III = \int_{k_{cs}}^{\infty}$ , volumetric (hyperbolic) modes of the substrate.

The hyperbolic mode contribution is usually estimated with the approximation  $k_x/k_0 \rightarrow \infty$ , where reflection from a substrate depends only on the dielectric permittivities, as long as  $k_x > k_0$ .<sup>16,50,51</sup> Moreover, the interplay between plasmonic and hyperbolic contributions could be efficiently tailored via adjusting material parameters ( $\epsilon_{zz}$ ) and, consequently,  $k_{cs}$ .

In order to demonstrate this capability, the imaginary part of the reflection coefficient for a p-polarized wave as a function of  $k_x$  has been plotted in Figure 2(b) for different material parameters: line A ( $\lambda_0 = 920$  nm,  $\epsilon_{xx} = -1.714 + 0.075i$ ,  $\epsilon_{zz} = 5.392 + 0.0084i$ ), where  $k_{cs}$  is quite large and the SPP contribution is dominating. Line B ( $\lambda_0 = 1350$  nm,  $\epsilon_{xx} = -8.94 + 0.33i$ ,  $\epsilon_{zz} = 5.10 + 0.0118i$ ), where SPPs peak is much narrower and bulk mode contribution is more pronounced, and line C for arbitrary metamaterial with ( $\lambda_0 = 920$  nm,  $\epsilon_{xx} = -2 +$

$0.066i$ ,  $\epsilon_{zz} = 0.5 + 0.0084i$ ), where  $k_{cs}$  is less than  $k_0$ , the SPP contribution is absent, and, consequently, the interaction is governed by free space modes and bulk hyperbolic modes (magnitudes are related as  $III = 2.5I$ ). These particular scenarios will be further investigated in terms of optical forces. We should stress that each of these integrals is taken into account twice via effective field eq 1, so the overall difference in force is bigger.

Noteworthy, the interval-based integration given by eq 7 is valid only for a standalone particle. Introducing another particle involves cross-coupling between different terms; for example, the SPP generated by the first particle could be scattered by another one into bulk hyperbolic modes and vice versa. This effect will be considered in the next section and shown to have a minor impact on the overall trapping and binding efficiency.

## RESULTS

Having identified the contribution of different interaction channels to the Green's function, we can proceed with the self-consistent scattering problem (eq 2).

**Semi-infinite Substrate.** The influence of a semi-infinite anisotropic multilayered metamaterial on optical binding will be analyzed next. The most significant parameters for binding are the period and stiffness, allowing for effective structuring of nanoparticles in many different 2D and even 3D architectures.<sup>25,31,57</sup> Recently, we revealed the possibility to bind nanoparticles with subwavelength separation distances via the interference of surface plasmon-polaritons.<sup>34</sup> Introducing additional metamaterial bulk modes seems promising for the further enhancement of binding capabilities.

Let us consider a pair of nanoparticles, one of which is fixed at the origin of the coordinates as in the previous scenario. For the sake of simplicity, we consider the second particle to have the same parameters as the first one. Effective field at the nanoparticle follows from eq 2 and is given in the Supporting Information (Section Expressions for the Effective Fields).

The period of optical binding can now be defined as a distance between two nearest stable equilibrium positions, and the stiffness is the ratio of the restoring force to the particle's displacement  $\kappa = -\Delta F_x / \Delta x$  (in close vicinity to a stable position, where  $F_x(x)$  has approximately a linear profile). Hereinafter the period  $L_{\text{bind}}$  and distances will be normalized over the incident wavelength  $\lambda_0$ , and the optical forces are given in pN over intensity ( $W/\mu\text{m}^2$ ).

The material parameters are taken to be the same as for lines A and C in Figure 2(b), corresponding to the dominating

contributions of SPPs (A) and hyperbolic modes (C). In Figure 3 the optical forces for both principally different scenarios are shown. The blue lines correspond to the total optical force, and the black lines correspond to the contribution of modes with  $k_x \leq k_0$  (propagating free-space modes in the upper half-space). The SPP contribution for A is given by the red line (it is zero for the C case by definition; see the previous section). Hyperbolic mode (HM) contribution is depicted by gray circles.

In case A, the optical forces are fully driven by surface waves, and the contribution of other modes is negligible. In case C despite the predominating influence of the hyperbolic modes, optical binding has almost nothing special in comparison with the free-space scenario. In this case, the HM contribution just increases the force almost twice (which is still two orders of magnitude less than that of SPPs) and slightly shifts the equilibrium positions, almost not affecting  $L_{\text{bind}}$ . In this case of a semi-infinite metamaterial for normally incident light the hyperbolic modes excited by the first particle just propagate symmetrically in the volume, not interacting with the second particle, and vice versa.

However, the existing nonzero contribution of the HMs can be explained via the aforementioned cross-terms, when modes excited by one particle are scattered by another one, giving rise to additional HMs with broken symmetry, which, in turn, leads to the optical force shift.<sup>16</sup>

Thus, the hyperbolic modes even being dominating in the interaction with the semi-infinite metamaterial do not provide a sufficient contribution to binding in this case.

**Finite Thickness Metamaterial Slabs.** The main reason for the weak influence of HMs on binding is the lack of a feedback from the bulk modes, which propagate away from the particles to infinity. However, as it will be shown hereinafter, strong optical binding can be obtained utilizing an anisotropic finite thickness slab due to reflections of hyperbolic modes from the boundaries. The structure under consideration appears in Figure 4.

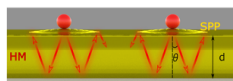


**Figure 4.** Scheme of optical binding near an anisotropic hyperbolic metamaterial (HMM) slab. Reflections from the boundaries of the slab form high-intensity regions and result in optical binding with separation distances  $L_{\text{bind}}$  below the diffraction limit.

In contrast to conventional waveguides,  $k_x$  in hyperbolic slabs can achieve rather high values, which, together with the highly confined shape of the modes, could allow for very small distances between the hot-spots driven by multiple reflections. This, in turn, paves the way for strong subwavelength binding of nanoparticles and also provides tunability via changing material parameters, slab thickness, excitation wavelength, etc.

The formalism developed for the semi-infinite substrate is also applicable for the finite-thickness slab. The main difference is in the Fresnel reflection coefficient, which in the latter case is given by

$$r_{\text{slab}} = \frac{r - r \exp(2ik_2d)}{1 - (r)^2 \exp(2ik_2d)} \quad (8)$$

where  $d$  represents the thickness of the slab. It is clearly seen that additional periodical maxima will be present in  $r_{\text{slab}}(k_x)$  (reflection of a p-polarized wave). These peaks are related to the additional boundary, which causes multiple reflections between the upper and lower interfaces. The distance between hot-spots at the interface and, thus, between the bound particles depends on the parameter  $d$  and angle between the group velocity of the hyperbolic modes and the normal to the surface. Noteworthy, hyperbolic modes are not usual "geometric" rays; thus exact calculations are needed to find the actual binding period  $L_{\text{bind}}$ .

Let us consider the optical binding force near an anisotropic slab with parameters A and C (from Figure 2(b)) and thicknesses  $d = \lambda_0/2$  and  $d = \lambda_0/8$ ,  $\lambda_0 = 920$  nm. Figure 5 represents the imaginary part of the reflection coefficient (left column (a, c)) and optical force (right column (b, d)). Noteworthy, additional peaks corresponding to the multiple reflections appear in the reflection coefficient. Here we show  $\text{Im}[r^p]$  only for  $k_x/k_0 \leq 10$ , because the next peaks are much weaker due to the absorption and are not necessary for subsequent qualitative analysis. However, the force calculations take into account all possible  $k_x$  ( $0 \leq k_x/k_0 < \infty$ ) to provide accurate values. The distance between the reflection peaks increases (in  $k$ -space) with decreasing thickness and leads to the optical force period decrease.

Comparing Figure 2(b) and Figure 5(a) we find SPP contribution to become much less pronounced (magnitudes of integrals from formula (6)  $II \approx 3I$  for a semi-infinite case,  $II \approx 2.3I$  for  $d = \lambda_0/2$ , and  $II \approx 2I$  for  $d = \lambda_0/8$  (Figure 5(a))) (where  $I$  is the integral contribution of the free-space modes from eq 7). For a thin slab  $d = \lambda_0/8$  the contribution of SPPs  $k_x/k_0 = 1.044$  and  $k_y/k_0 = 1.84$  can be considered as negligible for small distances and almost does not influence the optical forces (Figure 5(b)) governed predominantly by the hyperbolic mode with  $k_x/k_0 = 8.8$  ( $III \approx 7I$ ) and  $L_{\text{bind}} \approx 1/8.8 \approx 0.114$ . For  $d = \lambda_0/2$ , however, we have more supported modes, e.g., SPPs ( $k_x/k_0 = 1.17$  and  $k_y/k_0 = 1.2$ ) together with a set of hyperbolic modes. This leads to the peculiar behavior of the optical forces: HM with  $k_x/k_0 \geq 3.08$  enables subwavelength binding with  $L_{\text{bind}} \approx 1/3.08 \approx 0.32$  modulated by SPPs' overall envelope (schematically shown with a gray dotted line) with the period  $\sim 0.85$ . Note, all the distances are normalized over the wavelength of the incident wave  $\lambda_0$ .

For the parameters C (Figure 5(c,d)) there is no surface plasmon-polariton contribution by definition (we have chosen the appropriate parameters in the first section especially to emphasize the influence of hyperbolic modes in both semi-infinite and finite cases), because  $k_{cr}/k_0 = 0.7 < 1$ , so the optical forces are completely dependent on the free-space and volumetric modes. For the half-wavelength hyperbolic slab the forces are governed by free-space propagating waves ( $II = 0$ ,  $III \approx I$ ) with small  $k_x$  and low-amplitude HMs (high  $k_x$  ones are effectively absorbed via a rather large thickness); thus, the dependence is close to optical binding in free space in terms of both period and force magnitude. For the thin slab the force is almost 2 orders of magnitude increased (Figure 5(d)), and the periodicity now is fully driven by the two most pronounced peaks  $k_x/k_0 = 1.33$  ( $L_{\text{bind}} \approx 0.75$ ), shown by a gray envelope, and  $k_x/k_0 = 3.11$ , corresponding to  $L_{\text{bind}} \approx 0.32$  (overall integral  $III \approx 6.3I$ ). The total force in both cases reaches 30 fN for intensities of  $\sim 100$  mW/ $\mu\text{m}^2$ .

Here the stability of equilibrium positions along the  $x$ -direction is discussed; however, these positions are stable along

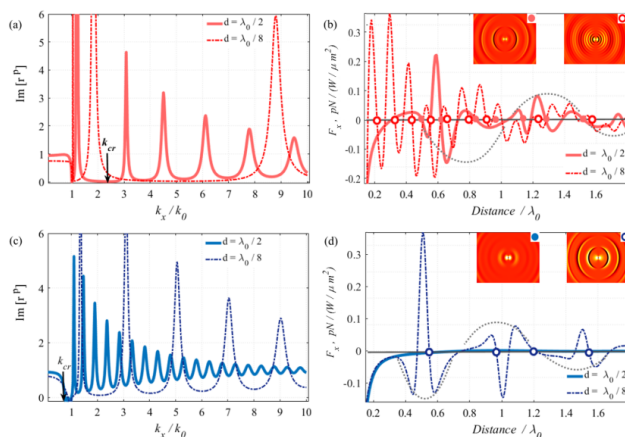


**Figure 5.** Imaginary part of the reflection coefficient over relative transversal wavevector component (a, c) and optical binding force (b, d). The dependence is plotted for two sets of parameters: (a) and (b) correspond to the parameters A from Figure 2. (c) and (d) correspond to C from Figure 2. The solid lines depict the reflection coefficient and optical binding force for a slab with thickness  $d = \lambda_0/2$ ; the dash-dotted lines depict the reflection coefficient for a slab with the thickness  $d = \lambda_0/8$ , where  $\lambda_0 = 920$  nm is the incident wavelength. The black arrows in (a) and (c) show the position of the  $k_x$ . One can see that for C it is placed before  $k_0$ . Gray dotted lines represent envelopes (see text). The insets in (b) and (d) show electric component  $E_x$  of the field scattered by the particle above the homogeneous hyperbolic substrate with thickness  $d = \lambda_0/2$  (left column) and  $d = \lambda_0/8$  (right column).

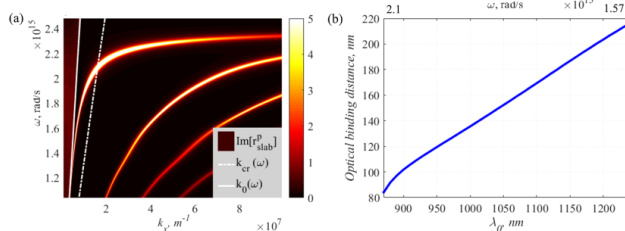


**Figure 6.** Chromatic tuning for the multilayered structure of silver and  $\text{Ta}_2\text{O}_5$  layers with a slab thickness 115 nm and filling factor of 0.133. (a) Imaginary part of the reflection coefficient (dispersion diagram). (b) Optical binding period over the frequency.

the  $y$ -direction too (see Supporting Information Figure S3). The trapping potential of optical binding approaches  $3k_B T$  at room temperature for both A and C parameters and moderate intensities usually involved in optical trapping of nanoparticles;<sup>32</sup> thus it is stable against Brownian motion. Considering the overall vertical force, we should take into account van der Waals forces attracting the particles to the substrate together with the optical forces. Therefore, the overall force tends to adpress the particles to the surface. However, we should mention here that it can be suppressed or even reversed (if necessary) via, for example, a nanometer-thick dielectric spacer, electrostatic charging,<sup>58</sup> or one more light source, enabling additional optical traps above the surface.

The aforementioned qualitative mode analysis of optical forces and binding period is an approximation. Often, several

peaks contribute to the optical force and form a unique signature, either with SPP or not (e.g., curved and asymmetric Figure 5(b,d)). However, it allows for a better understanding of the binding scenarios in the presence of such complicated structures as hyperbolic metamaterials and even for some quantitative estimations provided above. It should be stressed that the existence of higher multipoles in the case of bigger particles leads to more complicated field distribution; therefore, the maxima of the field are less pronounced.

Moreover, comparing two principally different scenarios (with and without SPP contributions), we find a new possibility to obtain optical binding forces, which are several orders of magnitude higher than in the free-space binding scenarios (and about one order of magnitude stronger than that delivered by plasmonic metals<sup>59</sup>). Furthermore, tuning the distance between

bound particles beyond the diffraction limit is also possible. These characteristics are strongly enhanced in the case of thin slabs, allowing for better utilizing hyperbolic mode feedback, and the proved great tolerance to the metamaterial parameters paves the way to a plethora of highly demanded applications.

**Chromatic Tuning of Binding.** In the previous sections we have considered semi-infinite and finite slabs of hyperbolic metamaterials consisting of Ag<sup>59</sup> and Ta<sub>2</sub>O<sub>5</sub><sup>60</sup> layers, allowing for effective tuning via adjusting material and geometrical parameters. Hereinafter let us consider another important degree of freedom: chromatic tuning of the metamaterial-assisted optical binding.

Figure 6(a) shows the dependence of the reflection coefficient on the incident wave frequency and  $k_x/k_0$  for a slab thickness of 115 nm. It can be seen that the number of HM peaks governed by the reflections (equal to Fabry–Perot resonances for hyperbolic modes) and contributing to optical binding is increased with lower frequency ( $d/\lambda_0$  decrease), so the optical force dependence becomes more complicated.

The distance between the bound particles (Figure 6(b)) is now a function of the frequency; thus the material dispersion plays a key role here. The binding period is proportional to the relations of the thickness of the slab and incident wavelength and  $\epsilon_{xx}(\omega)$  and  $\epsilon_{zz}(\omega)$ . In this case the permittivities are monotonically dependent on the frequency;<sup>39</sup> thus the dependence of the optical binding distance is more or less monotonic. However, in other wavelength regions additional HMs and nonmonotonic dispersion of optical constants could displace the stable equilibrium positions and change the dependence shown in Figure 6(b). This additional degree of freedom opens room for opportunities for tuning optical binding via a “noninvasive” way and fabricate novel designs and architectures of nanostructures on metamaterial substrates by adjusting optically induced forces with hyperbolic modes.

Moreover, in the Supporting Information (Section The Impact of the Topmost Layer) we consider the dependence of the optical binding force on the topmost layer of the slab (metal or dielectric), which also can be useful in a plethora of applications.

## CONCLUSION

In this work we describe the transverse optical binding of two particles near a hyperbolic metamaterial. High- $k$  volumetric modes can provide additional channels of the particles' interaction with substrates and, therefore, drastically enhance capabilities of optomechanical manipulation schemes. For a semi-infinite (or rather thick) metamaterial slab the hyperbolic modes even being dominating in scattering do not contribute to optical binding because of the almost absent feedback (hyperbolic modes excited by one particle do not interact with the second one). In contrast, thin metamaterial slabs provide multiple reflections from boundaries, forming a set of strongly localized hot-spots with huge intensity gradients governing nanoparticle motion at the nanoscale. Furthermore, mode analysis shows the predominant impact of HMs on binding giving rise to several orders of magnitude increased optical forces and deeply subwavelength nanoparticle positioning. Moreover, the principal realization of this phenomenon appears to be rather tolerant to the metamaterial parameters, enabling strongly enhanced performance for a whole set of designs and driving broadband chromatic tuning. Novel auxiliary carefully designed metamaterials and metasurfaces featuring superior optomechanical mechanisms are nowadays extremely demanded in a variety

of applications, such as microfluidics, lab-on-a-chip devices, and biology and medicine to name just a few.

## ASSOCIATED CONTENT

### Supporting Information

The Supporting Information is available free of charge at <https://pubs.acs.org/doi/10.1021/acsp Photonics.9b01378>.

1. Green's function formalism; 2. Expressions for the effective fields; 3. The impact of the topmost layer; 4. Spatial distribution of the electromagnetic field above the thin slab; 5. The stability along the  $y$  directions (PDF)

## AUTHOR INFORMATION

### Corresponding Authors

\*E-mail: natalia.kostina@metalab.ifmo.ru.

\*E-mail: alexandesh@gmail.com.

### ORCID

Denis A. Kislov: 0000-0003-0478-1855

Aliaksandra N. Ivinskaya: 0000-0002-0262-6459

Andrey Novitsky: 0000-0001-9553-7318

### Present Address

□Silicon Photonics Technologies Department, Interuniversity Microelectronics Center, Kapeldreef 75, Leuven 3001, Belgium.

### Author Contributions

N.K. designed the model and the computational framework and analyzed the data. A.P. and D.K. performed finite element simulations. A.S.S. and P.G. wrote the manuscript and supervised the work. All authors contributed to the research activities.

### Notes

The authors declare no competing financial interest.

## ACKNOWLEDGMENTS

The work has been supported in part by ERC StG “In Motion” and the PAZY Foundation. A.S.S. acknowledges the support of the Russian Fund for Basic Research within the projects 18-02-00414 and 18-52-00005. Simulations of the optical forces have been supported by the Russian Science Foundation (Project No. 18-72-10127). A.N. thanks the Belarusian Republican Foundation for Fundamental Research (Project No. F18R-021).

## REFERENCES

- (1) Ashkin, A. Acceleration and Trapping of Particles by Radiation Pressure. *Phys. Rev. Lett.* **1970**, *24* (4), 156–159.
- (2) Neuman, K. C.; Block, S. M. Optical Trapping. *Rev. Sci. Instrum.* **2004**, *75* (9), 2787–2809.
- (3) MacDonald, M. P.; Paterson, L.; Volke-Sepulveda, K.; Arlt, J.; Sibbett, W.; Dholakia, K. Creation and Manipulation of Three-Dimensional Optically Trapped Structures. *Science* **2002**, *296* (5570), 1101–1103.
- (4) Jonás, A.; Zemánek, P. Light at Work: The Use of Optical Forces for Particle Manipulation, Sorting, and Analysis. *Electrophoresis* **2008**, *29*, 4813–4851.
- (5) Damková, J.; Chvátal, L.; Ježek, J.; Oulehla, J.; Brzobohatý, O.; Zemánek, P. Enhancement of the “tractor-Beam” Pulling Force on an Optically Bound Structure. *Light: Sci. Appl.* **2018**, *7* (1), 17135.
- (6) Novotny, L.; Bian, R. X.; Xie, X. S. Theory of Nanometric Optical Tweezers. *Phys. Rev. Lett.* **1997**, *79* (4), 645–648.
- (7) Juan, M. L.; Gordon, R.; Pang, Y.; Eftekhari, F.; Quidant, R. Self-Induced Back-Action Optical Trapping of Dielectric Nanoparticles. *Nat. Phys.* **2009**, *5* (12), 915–919.
- (8) Grier, D. G. A Revolution in Optical Manipulation. *Nature* **2003**, *424* (6950), 810–816.

- (9) Moffitt, J. R.; Chemla, Y. R.; Smith, S. B.; Bustamante, C. Recent Advances in Optical Tweezers. *Annu. Rev. Biochem.* **2008**, *77* (1), 205–228.
- (10) Juan, M. L.; Righini, M.; Quidant, R. Plasmon Nano-Optical Tweezers. *Nat. Photonics* **2011**, *5*, 349–356.
- (11) Righini, M.; Volpe, G.; Girard, C.; Petrov, D.; Quidant, R. Surface Plasmon Optical Tweezers: Tunable Optical Manipulation in the Femtonewton Range. *Phys. Rev. Lett.* **2008**, *100* (18), 186804.
- (12) Gramotnev, D. K.; Bozhovly, S. I. Plasmonics beyond the Diffraction Limit. *Nat. Photonics* **2010**, *4* (2), 83–91.
- (13) Berkovitch, N.; Ginzburg, P.; Orenstein, M. Nano-Plasmonic Antennas in the near Infrared Regime. *J. Phys.: Condens. Matter* **2012**, *24*, 073202.
- (14) Shilkina, D. A.; Lyubin, E. V.; Soboleva, I. V.; Fedyanin, A. A. Trap Position Control in the Vicinity of Reflecting Surfaces in Optical Tweezers. *JETP Lett.* **2014**, *98* (10), 644–647.
- (15) Ivinskaya, A.; Petrov, M. I.; Bogdanov, A. A.; Shishkin, I.; Ginzburg, P.; Shalin, A. S. Plasmon-Assisted Optical Trapping and Anti-Trapping. *Light: Sci. Appl.* **2017**, *6* (5), No. e16258.
- (16) Ivinskaya, A.; Kostina, N.; Proskurin, A.; Petrov, M. I.; Bogdanov, A. A.; Sukhov, S.; Krasavin, A. V.; Karabchevsky, A.; Shalin, A. S.; Ginzburg, P. Optomechanical Manipulation with Hyperbolic Metasurfaces. *ACS Photonics* **2018**, *5* (11), 4371–4377.
- (17) Bogdanov, A. A.; Shalin, A. S.; Ginzburg, P. Optical Forces in Nanorod Metamaterial. *Sci. Rep.* **2015**, *5*, 15846.
- (18) Shalin, A. S.; Sukhov, S. V.; Bogdanov, A. A.; Belov, P. A.; Ginzburg, P. Optical Pulling Forces in Hyperbolic Metamaterials. *Phys. Rev. A: At., Mol., Opt. Phys.* **2015**, *91* (6), DOI: 10.1103/PhysRevA.91.063830.
- (19) Chen, J.; Ng, J.; Lin, Z.; Chan, C. T. Optical Pulling Force. *Nat. Photonics* **2011**, *5* (9), 531–534.
- (20) Shalin, A. S.; Sukhov, S. V. Plasmonic Nanostructures as Accelerators for Nanoparticles: Optical Nanocannon. *Plasmonics* **2013**, *8* (2), 625–629.
- (21) Shalin, A. S.; Ginzburg, P.; Belov, P. A.; Kivshar, Y. S.; Zayats, A. V. Nano-Opto-Mechanical Effects in Plasmonic Waveguides. *Laser Photonics Rev.* **2014**, *8* (1), 131–136.
- (22) Baryshnikova, K. V.; Novitsky, A.; Evlyukhin, A. B.; Shalin, A. S. Magnetic Field Concentration with Coaxial Silicon Nanocylinders in the Optical Spectral Range. *J. Opt. Soc. Am. B* **2017**, *34*, D36.
- (23) Descharmes, N.; Dharamipathy, U. P.; Diao, Z.; Tonin, M.; Houdré, R. Observation of Backaction and Self-Induced Trapping in a Planar Hollow Photonic Crystal Cavity. *Phys. Rev. Lett.* **2013**, *110* (12), 123601.
- (24) Burns, M. M.; Fournier, J. M.; Golovchenko, J. A. Optical Binding. *Phys. Rev. Lett.* **1989**, *63* (12), 1233–1236.
- (25) Dholakia, K.; Zemánek, P. Colloquium: Grippled by Light: Optical Binding. *Rev. Mod. Phys.* **2010**, *82* (2), 1767–1791.
- (26) Sukhov, S.; Shalin, A.; Haefner, P.; Dogariu, A. Actio et Reactio in Optical Binding. *Opt. Express* **2015**, *23* (1), 247.
- (27) Grzegorzczak, T. M.; Kemp, B. A.; Kong, J. A. Stable Optical Trapping Based on Optical Binding Forces. *Phys. Rev. Lett.* **2006**, *96* (11), 1–4.
- (28) Taylor, J. M.; Love, G. D. Optical Binding Mechanisms: A Conceptual Model for Gaussian Beam Traps. *Opt. Express* **2009**, *17* (17), 15381.
- (29) Chen, J.; Ng, J.; Wang, P.; Lin, Z. Analytical Partial Wave Expansion of Vector Bessel Beam and Its Application to Optical Binding: Erratum. *Opt. Lett.* **2011**, *36* (7), 1243.
- (30) Simpson, S. H.; Zemánek, P.; Maragó, O. M.; Jones, P. H.; Hanna, S. Optical Binding of Nanowires. *Nano Lett.* **2017**, *17* (6), 3485–3492.
- (31) Donato, M. G.; Brzobohatý, O.; Simpson, S. H.; Irrera, A.; Leonardi, A. A.; Lo Faro, M. J.; Svak, V.; Maragó, O. M.; Zemánek, P. Optical Trapping, Optical Binding, and Rotational Dynamics of Silicon Nanowires in Counter-Propagating Beams. *Nano Lett.* **2019**, *19* (1), 342–352.
- (32) Demergis, V.; Florin, E. L. Ultrastrong Optical Binding of Metallic Nanoparticles. *Nano Lett.* **2012**, *12* (11), 5756–5760.
- (33) Taylor, J. M. *Optical Binding Phenomena: Observations and Mechanisms*; 2011; DOI: 10.1007/978-3-642-21195-9.
- (34) Kostina, N.; Petrov, M.; Ivinskaya, A.; Sukhov, S.; Bogdanov, A.; Toftul, I.; Nieto-Vesperinas, M.; Ginzburg, P.; Shalin, A. Optical Binding via Surface Plasmon Polariton Interference. *Phys. Rev. B: Condens. Matter Mater. Phys.* **2019**, *99* (12), DOI: 10.1103/PhysRevB.99.125416.
- (35) Chaumet, P. C.; Nieto-Vesperinas, M. Optical Binding of Particles with or without the Presence of a Flat Dielectric Surface. *Phys. Rev. B: Condens. Matter Mater. Phys.* **2001**, *64* (3), DOI: 10.1103/PhysRevB.64.035422.
- (36) Quidant, R. Plasmonic Tweezers-The Strength of Surface Plasmons. *MRS Bull.* **2012**, *37* (8), 739–744.
- (37) Song, Y. G.; Han, B. M.; Chang, S. Force of Surface Plasmon-Coupled Evanescent Fields on Mie Particles. *Opt. Commun.* **2001**, *198* (1–3), 7–19.
- (38) Quidant, R.; Girard, C. Surface-Plasmon-Based Optical Manipulation. *Laser Photonics Rev.* **2008**, *2* (1–2), 47–57.
- (39) Shekhar, P.; Atkinson, J.; Jacob, Z. Hyperbolic Metamaterials: Fundamentals and Applications. *Nano Converg.* **2014**, *1* (1), DOI: 10.1186/s40580-014-0014-6.
- (40) Ginzburg, P.; Fortuño, F. J. R.; Wurtz, G. A.; Dickson, W.; Murphy, A.; Morgan, F.; Pollard, R. J.; Iorsh, I.; Atarshchenko, A.; Belov, P. A.; et al. Manipulating Polarization of Light with Ultrathin Epsilon-near-Zero Metamaterials. *Opt. Express* **2013**, *21* (12), 14907.
- (41) Ferrari, L.; Wu, C.; Lepage, D.; Zhang, X.; Liu, Z. Hyperbolic Metamaterials and Their Applications. *Prog. Quantum Electron.* **2015**, *40*, 1–40.
- (42) Milton, G. W.; Nicorovici, N. A. P. On the Cloaking Effects Associated with Anomalous Localized Resonance. *Proc. R. Soc. London, Ser. A* **2006**, *462* (2074), 3027–3059.
- (43) Schurig, D.; Mock, J. J.; Justice, B. J.; Cummer, S. A.; Pendry, J. B.; Starr, A. F.; Smith, D. R. Metamaterial Electromagnetic Cloak at Microwave Frequencies. *Science* **2006**, *314* (5801), 977–980.
- (44) Shalin, A. S.; Ginzburg, P.; Orlov, A. A.; Iorsh, I.; Belov, P. A.; Kivshar, Y. S.; Zayats, A. V. Scattering Suppression from Arbitrary Objects in Spatially Dispersive Layered Metamaterials. *Phys. Rev. B: Condens. Matter Mater. Phys.* **2015**, *91* (12), DOI: 10.1103/PhysRevB.91.125426.
- (45) Liu, Z.; Lee, H.; Xiong, Y.; Sun, C.; Zhang, X. Far-Field Optical Hyperlens Magnifying Sub-Diffraction-Limited Objects. *Science* **2007**, *315* (5819), 1686.
- (46) Rho, J.; Ye, Z.; Xiong, Y.; Yin, X.; Liu, Z.; Choi, H.; Bartal, G.; Zhang, X. Spherical Hyperlens for Two-Dimensional Sub-Diffraction Imaging at Visible Frequencies. *Nat. Commun.* **2010**, *1* (9), DOI: 10.1038/ncomms1148.
- (47) Tumkur, T. U.; Kitur, J. K.; Bonner, C. E.; Poddubny, A. N.; Narimanov, E. E.; Noginov, M. A. Control of Förster Energy Transfer in the Vicinity of Metallic Surfaces and Hyperbolic Metamaterials. *Faraday Discuss.* **2015**, *178*, 395–412.
- (48) Biehs, S. A.; Tschikina, M.; Ben-Abdallah, P. Hyperbolic Metamaterials as an Analog of a Blackbody in the near Field. *Phys. Rev. Lett.* **2012**, *109* (10), DOI: 10.1103/PhysRevLett.109.104301.
- (49) Roth, D. J.; Nasir, M. E.; Ginzburg, P.; Wang, P.; Le Marois, A.; Suhling, K.; Richards, D.; Zayats, A. V. Förster Resonance Energy Transfer inside Hyperbolic Metamaterials. *ACS Photonics* **2018**, *5* (11), 4594–4603.
- (50) Rodríguez-Fortuño, F. J.; Vakil, A.; Engheta, N. Electric Levitation Using  $\mu$ -near-Zero Metamaterials. *Phys. Rev. Lett.* **2014**, *112* (3), DOI: 10.1103/PhysRevLett.112.033902.
- (51) Rodríguez-Fortuño, F. J.; Zayats, A. V. Repulsion of Polarised Particles from Anisotropic Materials with a Near-Zero Permittivity Component. *Light: Sci. Appl.* **2016**, *5*, e16022.
- (52) Zhukovskiy, S. V.; Kidwai, O.; Sipe, J. E. Physical Nature of Volume Plasmon Polaritons in Hyperbolic Metamaterials. *Opt. Express* **2013**, *21* (12), 14982.
- (53) Zhukovskiy, S. V.; Andriyevskiy, A.; Sipe, J. E.; Lavrinenko, A. V. From Surface to Volume Plasmons in Hyperbolic Metamaterials: General Existence Conditions for Bulk High- $k$  Waves in Metal-

Dielectric and Graphene-Dielectric Multilayers. *Phys. Rev. B: Condens. Matter Mater. Phys.* **2014**, *90* (15), DOI: 10.1103/PhysRevB.90.155429.

(54) Kidwai, O.; Zhukovsky, S. V.; Sipe, J. E. Effective-Medium Approach to Planar Multilayer Hyperbolic Metamaterials: Strengths and Limitations. *Phys. Rev. A: At, Mol, Opt. Phys.* **2012**, *85* (5), No. 053842.

(55) Poddubny, A.; Iorsh, I.; Belov, P.; Kivshar, Y. Hyperbolic Metamaterials. *Nat. Photonics* **2013**, *7* (12), 948–957.

(56) Tschikin, M.; Biels, S. A.; Messina, R.; Ben-Abdallah, P. On the Limits of the Effective Description of Hyperbolic Materials in the Presence of Surface Waves. *J. Opt. (Bristol, U. K.)* **2013**, *15* (10), 105101.

(57) Brzobohatý, O.; Čížmár, T.; Karásek, V.; Šiler, M.; Dholakia, K.; Zemánek, P. Experimental and Theoretical Determination of Optical Binding Forces. *Opt. Express* **2010**, *18* (24), 25389.

(58) Wang, K.; Schonbrun, E.; Crozier, K. B. Propulsion of Gold Nanoparticles with Surface Plasmon Polaritons: Evidence of Enhanced Optical Force from Near-Field Coupling between Gold Particle and Gold Film. *Nano Lett.* **2009**, *9* (7), 2623–2629.


(59) Johnson, P. B.; Christy, R. W. Optical Constants of the Noble Metals. *Phys. Rev. B* **1972**, *6* (12), 4370–4379.

(60) Rodríguez-de Marcos, L. V.; Larroquet, J. I.; Méndez, J. A.; Aznárez, J. A. Self-Consistent Optical Constants of SiO<sub>2</sub> and Ta<sub>2</sub>O<sub>5</sub> Films. *Opt. Mater. Express* **2016**, *6* (11), 3622.

**7-PAPER:** Towards macroporous phononic crystal based structures for FBAR applications. Theoretical investigation of technologically competitive solutions

Oseev A., Mukhin N.V., Lucklum R., Zubtsov M., Schmidt M.-P., Redka D., Kozyrev A., Hirsch S., “Towards macroporous phononic crystal based structures for FBAR applications. Theoretical investigation of technologically competitive solutions”, (2018) *Microsystem Technologies*, 24 (5), pp. 2389 - 2399, DOI: [10.1007/s00542-017-3616-1](https://doi.org/10.1007/s00542-017-3616-1)

## Towards macroporous phononic crystal based structures for FBAR applications. Theoretical investigation of technologically competitive solutions

Aleksandr Oseev<sup>1</sup>  · Nikolay V. Mukhin<sup>1,2</sup> · Ralf Lucklum<sup>1</sup> · Mikhail Zubtsov<sup>1</sup> · Marc-Peter Schmidt<sup>1</sup> · Dmitrii Redka<sup>2</sup> · Andrey Kozyrev<sup>2</sup> · Soeren Hirsch<sup>3</sup>

Received: 18 August 2017 / Accepted: 28 October 2017  
© Springer-Verlag GmbH Germany 2017

**Abstract** The research work of current contribution is focused on the study of periodic macroporous arrangements, their designs scaling ability and performance depending on a possible technological imperfection. The studied in this work phononic structures are designed for a subsequent integration into the new class of integrated solutions on a basis of solid mounted film bulk acoustic resonators (SMR FBARs). Devices completed on a basis of developed solutions are intended for front-ends of telecommunication and radar systems applications. The main purpose of the research is an initial step towards enabling an efficient operation of integrated FBAR devices in a broad band or in several frequency bands using a multiple bandgap reflecting solid arrangements that ensure the isolation of acoustic energy within the piezoelectric layer for selected operation bands. The possibility of technological integration of periodic structures into the FBAR platform is a main critical point that limits the application of certain approach. Proposed in current work phononic crystal macroporous arrangements can be applied to improve an isolation of film bulk acoustic modes for SMR at specific frequencies; improve isolation and spatial separation of FBAR filter banks; enable an efficient operation of switchable and tunable SMR FBARs.

### 1 Introduction

New front-ends of mobile devices are developed for the single chip integration of multiple frequency bands and operating modes while simultaneously minimizing a power consumption and size. Banks of microwave filters based on thin film bulk acoustic resonators (FBAR) are currently utilized for that purposes and exhibit certain limits of miniaturization. Nowadays, FBAR devices demonstrate significant advantages in comparison to surface acoustic wave (SAW) devices. Their ultra-small dimensions and ability to work at frequencies up to tens of gigahertz make them a convenient replacement of the SAW based devices. They are widely used in miniaturized filters for communication, radar and navigation systems.

Modern microwave FBARs are multilayer thin film structures containing in most cases a single piezoelectric layer (AlN, ZnO) (Lakin et al. 1993; Ueda et al. 2008; Hashimoto 2009). The piezoelectric layer thickness is a micrometer order, and it is required to utilize a resonator handling substrate to provide a mechanical support for the films. The acoustic energy of FBAR resonator, however, should be concentrated within the thin piezoelectric layer. Nowadays, two different concepts are applied for this purpose. In a membrane type of the film resonator, the isolation of acoustic vibrations is achieved by means of the under-etched membrane that limits the acoustic energy dissipation only at the membrane clamping boundaries. Feature of membrane based structures is an existence of supporting membrane eigenmodes that should be suppressed. Another type of the film resonators utilizes acoustic mirrors to isolate the acoustic vibrations from scattering into the bulk of a substrate. This type of the resonators is known as solidly mounted resonators (SMR). SMRs use a reflective structure made of subsequently

✉ Aleksandr Oseev  
aleksandar.oseev@ovgu.de

<sup>1</sup> Institute of Micro and Sensor Systems (IMOS), Otto-von-Guericke-University, Magdeburg, Germany

<sup>2</sup> St. Petersburg Electrotechnical University ("LETI"), St. Petersburg, Russia

<sup>3</sup> Department of Engineering, University of Applied Sciences Brandenburg, Brandenburg, Germany



deposited layers of materials with a high acoustic contrast. The thickness of those layers is defined as a quarter of a wavelength. The layers thickness reproducibility plays a significant role in a resonator performance. Deviations in the Bragg reflector layers cause a dissipation of acoustic energy into the structure volume that deteriorates the resonator performance. Considering high frequency FBAR applications, the fabrication of efficient Bragg reflectors becomes rather challenging due to finite tolerances of a thin films reproducibility.

General trends towards the integrated solutions and the structures miniaturization have currently led to the development of another type of FBAR devices that utilize the induced piezoelectric effect for the selective excitation of normal acoustic modes of the resonator and as a result gain an access to the resonator frequency switching (Kozryev et al. 2011; Gevorgian et al. 2013; Kalkur and Mansour 2015). These devices are currently only at the initial state of development but in the future they can gain a significant interest. Therefore, the necessity to ensure the operation within several frequency band is one of the requirements that has to be satisfied developing a novel SMR devices.

In current contribution, the ability to implement two-dimensional periodic composite arrangements (phononic crystal structures) is discussed in order to obtain an efficient isolation of piezoelectric film resonances. Considering the direction of propagating wave, the isolation can be completed in different ways. The phononic crystal based structure can be considered as a replacement of a standard Bragg reflector or as an arrangement that separate the neighboring resonators in a lateral direction. In current contribution we focus our work on the possible ways of phononic structures implementation as an alternative to currently utilized Bragg reflectors. Although the subject of decoupling of separate resonators in a lateral direction is an important task, we mostly focus on the structures design where the isolation of main thickness shear mode is discussed. Therefore the PnC structure is positioned under the piezoelectric film. The phononic structures of a certain design can exhibit complete bandgaps that ensure the isolation of the acoustic energy within the piezoelectric layer regardless of the polarization of acoustic modes. The fabrication of periodic structures can be completed even for higher frequency structures applying developed technological approaches.

Periodic structures attracted a great attention since the development of a theory of the electronic band for solid materials. Similarly to the periodic potential of the crystal lattice, composite materials with a periodic spatial modulation of the dielectric constant on the scale of the optical wavelength, so-called photonic crystals, were introduced several decades ago (Joannopoulos et al. 2011). Scattering centers with dielectric properties that differ from a

homogeneous matrix surrounding the scatters are arranged in a typical photonic structure. Due to the destructive interference of multiple scattered waves, these structures are featured by regions of wave lengths, where an incident electromagnetic wave cannot propagate through the structure. These ranges of wavelengths with respective frequencies were called the photonic band gaps (Joannopoulos et al. 2011).

In comparison to propagation of transversal electromagnetic waves through the photonic structure, the propagation of acoustic waves in solid periodic composite materials is featured by much richer and at the same time more complicated behavior. It is defined by a simultaneous propagation of transversal and longitudinal components of an incident acoustic wave. As an equivalent of photonic crystals, acoustic periodic composites materials with a spatial modulation of elasticity, a mass density and longitudinal and transverse velocities of elastic waves were called Phononic Crystals (PnC). As it was demonstrated for electromagnetic waves, the destructive/constructive interference of elastic waves in phononic structures features band gaps in certain wavelength regions (Sigalas and Economou 1992; Kushwaha et al. 1993).

The existence of a band gap in a certain frequency (wavelength) range can be advocated in the same way as it was originally shown for electron spectrum in a solid material. The band gap can be considered as a region of a very low density of states for propagation of the acoustic wave through the structure with a periodic variation of mechanical properties of a medium. By analogy with solid materials, the acoustic wave propagation behavior in phononic structures can be described by the Bloch's theorem as a wave function in a periodical environment.

During the last decade, the reports on micrometre wavelength scale studies of periodical phononic structures that are mostly applicable for radio frequency communication devices were published. Unique properties of phononic structures, such as an ability to exhibit bandgaps in a certain frequency range that is predefined by the structure design, made them attractive for surface acoustic wave devices applications (such as filters, resonators etc.). Wu et al. (2005) reported on a silicon based phononic structure fabricated under standard MEMS technology as well as acoustic wave excitation and detection with a help of piezoelectric ZnO layer with a system of slanted IDTs. PnC structure scatters are performed as air filled holes with a square lattice. The experimental confirmation of existence of the complete bandgap for surface acoustic waves was demonstrated later by Benchabane et al. (2006). The square-lattice two-dimensional phononic structure was directly etched in a lithium niobate waveguide. In this case, surface acoustic waves were excited with standard IDTs. The complete bandgap was experimentally found at

frequency around 200 MHz. Afterwards, scattering and propagation of surface acoustic waves through the square-lattice phononic structure was experimentally investigated with optical methods in (Kokkonen et al. 2007; Profunser et al. 2009). The bandgap properties of the investigated 2D arrangement were vividly demonstrated as measured wave fields at different frequencies. Considering the phononic structures as an efficient acoustic wave reflector, the two-port SAW devices were combined with phononic reflective gratings (Wu et al. 2009). The experimental structure was completed as layered ZnO/Si SAW device with a square lattice phononic structure performed as an array of cylindrical scatters (holes) in the silicon waveguide. The achieved results demonstrated that phononic structures can act as an efficient acoustic wave reflector with significantly reduced number of lattice periods in comparison to the conventional metal reflective gratings.

The investigation of two-dimensional solid/solid binary composite systems showed that the square array of carbon fibres embedded in an epoxy matrix can exhibit rather large absolute bandgaps or multiple bandgaps (Vasseur et al. 1994). In current case, it is beneficial to obtain the composite arrangement that is able to exhibit several bandgaps in order to perform an isolation of multiple acoustic resonances in ferroelectric films of switchable FBARs. In previous works, two-dimensional boron-nitride arrays of infinite cylinders of two different radii that are periodically distributed in an infinite matrix were studied (Pennec et al. 2010). The structure constituted with carbon cylinders that are built in the epoxy matrix showed an ability of such composite arrangement to exhibit five separate complete bandgaps. It was shown that contrast between the diameters of two cylinders significantly influences the acoustic band gaps determining the width and appearance in a certain frequency range. A variation of the scatters material has shown that the bandgaps width can be significantly improved. Thus, the performance of cylindrical scatters made of tungsten arranged in boron-nitride arrays in an epoxy background allowed to obtain considerably large absolute multiple bandgaps. Demonstrated bandgaps broadening can be explained by a contrast between the densities of tungsten and carbon (Pennec et al. 2010). The variation of scatters arrangement, geometry and material allows to design the required spectral behavior of the composite periodical arrangement defining the regions of absolute bandgaps.

However, in order to utilize previously demonstrated theoretical results in certain applications, the technological aspects of composite arrangements fabrication should be taken into consideration. The fabricated structures should be technologically designed with respect to the wavelength that predetermines arrangement geometrical parameters. Depending on the structure dimensions, the fabrication

approaches vary and significantly limit possible arrangement designs.

Depending on the structure design, various technological approaches can be undertaken. Previous works have reported about the fabrication of periodic phononic arrangements in the micrometer wavelength range for the surface acoustic wave devices application. The structures were etched directly within a piezoelectric substrate as a periodic arrangement of etched holes and trenches.

Initial results of periodic arrangement fabrication with  $\text{CHF}_3/\text{Ar}$ ,  $\text{CF}_4/\text{O}_2$  and  $\text{CF}_4/\text{Ar}$  dry etching demonstrate extremely low etching rates and poor selectivity (Ronggui and Righini 1991). Deep reactive ion etching of microstructures in Pyrex glass applying SF6 plasma was investigated in (Li et al. 2001), and considerably high etch ratio of 0.6  $\mu\text{m}/\text{min}$  has been achieved. It has been found that physical sputter-etching significantly improves the etching process by assisting the removal of etch residuals providing an access of the etching medium to the targeting surface. By application of this approach it became possible to reach the reduction of the nonvolatile product redepositing on sidewalls and improve the structuring of periodic microarrangements. Further technology improvement was completed using a SF6/Ar gas mixture in order to avoid trenches formation at the bottom during the etching process (Park et al. 2005). In a contrast to SAW structures application, FBAR devices operate at the higher frequency utilizing the film bulk acoustic waves. The structure design in this case has to be adjusted to the type of the excited wave within the piezoelectric film, and the dimensions of microfabricated structures have to be scaled to the respective wavelength region.

## 2 Results

The prime aim of the current contribution is to investigate the most optimal solutions of the periodic structure design considering the technological aspects of the structure fabrication. The study was performed with the help of finite element method using COMSOL Multiphysics FEM software. The prime requirement is that the periodic structure should exhibit an existence of bandgaps at several frequency regions of the switchable FBAR.

The current work is focused on the consideration of periodic structure designs that are technologically achievable for sub-micrometer dimensions using standard microfabrication approaches. With regard to that, the application of macroporous structures is proposed. Macroporous silicon based structure can be fabricated utilizing standard masked electrochemical etching with the structure design that is predetermined by the photolithography (Lehmann and Föll 1990). Nowadays, macroporous

silicon structures have found various applications including photonic crystals (Wehrspohn and Schilling 2003), sensors (Kurowski et al. 2002), optical filters (Lehmann et al. 2001) and etc. The fabrication of porous structures with electrochemical etching in a HF solution is currently the developed micromachining process (Barillaro et al. 2002). The micrometer size porous structures can be achieved (Smith and Collins 1992) with the use of the p-doped type of anodized silicon substrates. The initial structuring of the wafer surface will allow to predefine areas of the micrometer size pore formation (Lehmann and Grüning 1997). The process of the macropores fabrication of defined geometry can be achieved adjusting the technological parameter and can reach the wafer thickness in depth (Lehmann and Ronnebeck 1999). The technological results of sub-micrometer structure fabrication (Matthias et al. 2005) as well as the lateral direction nanostructures fabrication (Liang et al. 2002) provide a significant basis that ensures the technological feasibility of the proposed in current contribution designs.

In the current work we found optimal solutions for pore arrangements of different symmetry that are completed as arrays of air filled cylindrical inclusions in the silicon host material. 2D square, triangular and honeycomb arrangements of holes were used for this study as shown in Fig. 1.

The propagation of acoustic waves in the elastic medium is governed by:

$$\rho \frac{\partial^2 u_i(\mathbf{r}, t)}{\partial t^2} = \sum_{j,m,n} \frac{\partial}{\partial x_j} \left[ C_{ijmn} \frac{\partial u_n(\mathbf{r}, t)}{\partial x_m} \right],$$

where  $u_i(\mathbf{r}, t)$  is a component of the elastic displacement field;  $C_{ijmn}$  is a component of the elastic stiffness tensor;  $\rho$  is the mass density;  $\mathbf{r} = (x, y, z)$  denotes the position vector.

The silicon based porous artificial periodic structures were modeled as arrays of air filled cylinders for three different symmetry cases. This arrangement is obtained by translating the unit cells for each case respectively as it is shown in Fig. 1. The cylinders are assumed to be parallel to the  $z$  axis; thus, in this paper we consider only the elastic waves that propagate in the  $x$ - $y$  plane.

According to the Floquet–Bloch wave theory, the displacement vector can be represented as a product of periodic function and exponential factor:

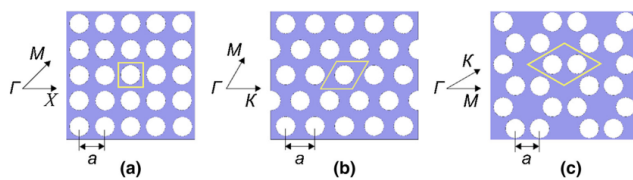
$$\mathbf{u}(\mathbf{r}, \mathbf{k}) = \mathbf{u}_{\mathbf{k}}(\mathbf{r}) \exp(i\mathbf{k}\mathbf{r}),$$

where  $\mathbf{u}_{\mathbf{k}}(\mathbf{r})$  is a periodic function of  $\mathbf{r}$  with the same periodicity as the structure;  $\mathbf{k} = (k_x, k_y)$  is the wave vector.

For square 2D structures, the irreducible Brillouin zone spans from  $\Gamma$  to  $X$  to  $M$  and back to  $\Gamma$ . The results of the band diagram computation for the infinite periodic arrangement with lattice constant  $0.94 \mu\text{m}$ , square symmetry and holes filling factor of 76% are demonstrated in Fig. 2a. The filling factor was defined as a percentage ratio of the area of the holes per unit cell square. The dependence of absolute bandgap boundaries from the filling factor is demonstrated in Fig. 2b.

Demonstrated in Fig. 2b computational results of bandgaps variation depending on the filling factor show that the increase of the holes diameter for the same lattice constant causes a broadening of the low frequency bandgap and appearance of higher frequency stop bands. At the same time, it can be seen that a relatively narrow high frequency bandgap that is found for low filling factors completely vanishes with an increase of the diameter of holes. It should be mentioned that at relatively high filling factor, the square symmetry arrangement exhibits a rather broad complete bandgap at lower frequency range and a narrower bandgap at higher frequency that is advantageous for the case of switchable FBAR applications. The displacement distribution and the analysis of frequency dependence of the structure reflection for the shear component of displacement are demonstrated in Fig. 3. In comparison to complete FBAR structure, the simulation model should be extended with top and bottom electrodes and piezoelectric film in between. However, in order to simplify the calculations and obtain the results that determine the behavior of the periodic structure separately from the piezoelectric film, the model was reduced to the prescribed shear displacement at the boundary of the presumable FBAR reflector. In contrast to that simplified model, the finite FBAR structure will be extended with the piezoelectric layer and electrodes with certain dimensions. Despite that fact the most of piezoelectric films have an efficient coupling to shear acoustic mode, the appearance of normal components is unavoidable as a result of mode conversion at the structure boundaries. Appearance of resonant modes different from the horizontally polarized

**Fig. 1** Square (a), triangular (b) and honeycomb (c) arrangements of cylindrical holes in the silicon host material and propagation directions for 2D phononic crystals based on them



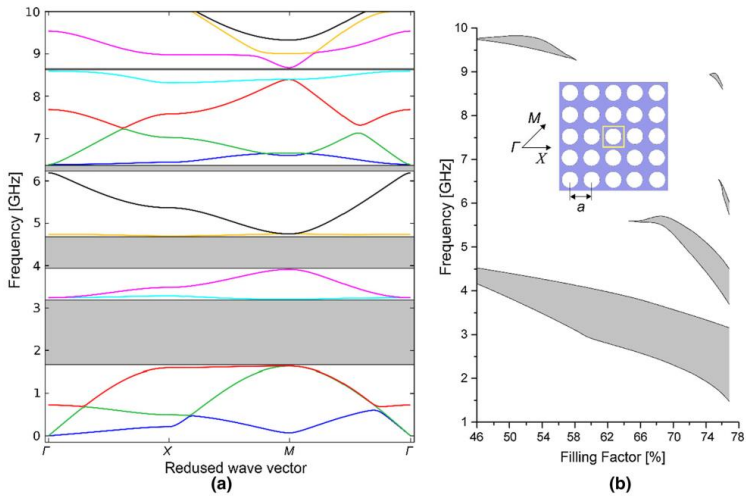


**Fig. 2** Band diagram for the pore silicon infinite square arrangement, filling factor 76% (a), and the dependence of the width of the absolute bandgaps from the filling factor (b) for fixed value of lattice constant of 0.94  $\mu\text{m}$

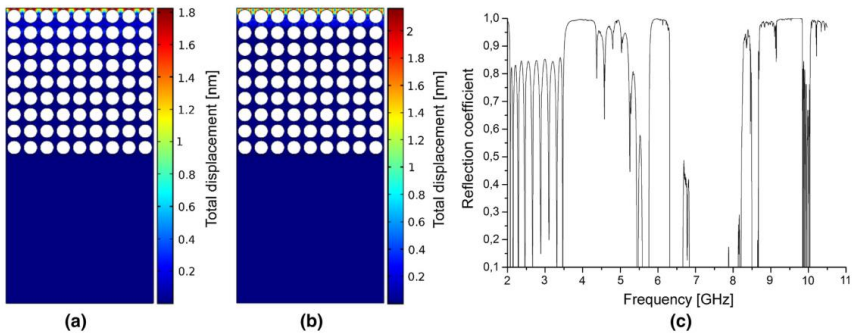


**Fig. 3** Simulation results of square arrangement of air filled cylinders in the silicon matrix (filling factor 54%). Displacement distribution of the structure excited with a shear displacement applied

to the top structure boundary taken at frequency of 4 GHz (a) and 9.5 GHz (b), and the structure reflection coefficient (c)

can introduce the leakage of acoustic energy and as a result the deterioration of the resonator performance. In order to diminish those effects, it is beneficial when near to the resonance mode the reflecting phononic structure has a complete bandgap and isolate the top piezoelectric structure modes independent on their polarization. Eventhough the unwanted resonance modes should be suppressed by the

finite FBAR design, the leakage of acoustic energy is ensured by the efficient complete bandgap reflector. More detailed consideration of possible effects appearing in 3D arrangement should be addressed at the stage of final device developing and are a subject of separate study.

The completed analysis of the finite structure reflection for the case of horizontally polarized excitation of the top

structure boundary demonstrates an efficient isolation of the surface displacement at several relatively narrow frequency ranges. Despite the fact that the complete bandgaps for the structure filling factor of 54% exist only around 4 and 10 GHz, the efficient isolation of shear displacement component is also achievable at the frequency around 6 GHz.

The analysis of triangular symmetry arrangement demonstrates the absence of complete bandgap at low filling factor and several rather narrow complete bandgaps for the higher filling ratios. The band diagram computed for the infinite periodic arrangement with the lattice constant 6.3  $\mu\text{m}$  and the filling factor of 65% is demonstrated in Fig. 4a. The structure shows several rather narrow complete bandgaps that do not improve with the increase of filling factor, as it is demonstrated in Fig. 4b. The reduced wave vector in this case spans in direction of  $\Gamma$ -K-M- $\Gamma$ , according to directions shown in Fig. 1b.

The computational results of triangular arrangement demonstrate the possibility to achieve several rather narrow bandgaps at the relatively high filling factor. From the practical point, that arrangement is not optimal, since the achievable bandgaps are relatively narrow for multiple operation bands applications and support the frequency switching within very narrow regions. The analysis of the finite structure reflection for the shear excited top boundary shows that an efficient isolation can be achieved only at

narrow frequency ranges that coincide with the complete bandgap computation results. The structure displacement distribution for the frequencies of high reflection and the computed reflection coefficient for the broad frequency range are demonstrated in Fig. 5.

The honeycomb arrangement was theoretically investigated as an alternative solution for the periodic arrangement design. The results of completed band diagram computations for the filling factor of 58% and a lattice constant of 0.9  $\mu\text{m}$  are demonstrated in Fig. 6a. As it can be seen, the honeycomb structure design supports the appearance of the broad bandgap at lower frequency and several middle broad bandgaps at higher frequencies. In terms of FBAR application, the computed structure allows the operation of switchable FBARs and operation of several isolated bands within the frequency region of the broad bandgap. The dependence of the structure response on the filling factor of cylindrical scatters (for fixed lattice constant of 0.9  $\mu\text{m}$ ) is demonstrated in Fig. 6b.

The obtained computational results show that for the low filling factor, the lower frequency bandgap becomes narrower and the higher frequency bandgaps vanish, when the filling factor is lower than 52%. The most promising in the described structure design is ability of the structure to sustain the relatively broad bandgap for the wide filling factor range. The honeycomb structure design appeared to be the most promising in terms of switchable FBARs

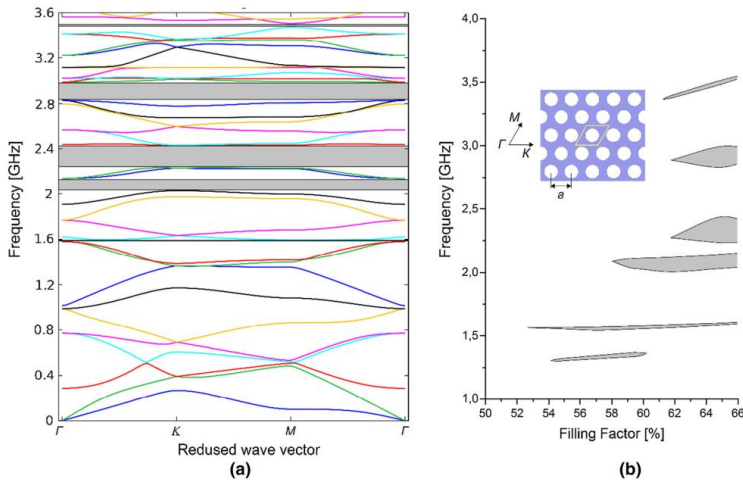


**Fig. 4** Band diagram for the pore silicon infinite trigonal arrangement, filling factor 65% (a) and the dependence of the width of the absolute forbidden acoustic bands on the filling factor (b) for fixed lattice constant of 6.3  $\mu\text{m}$

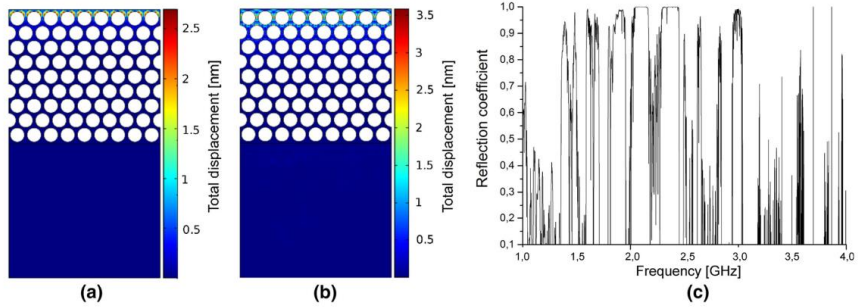


**Fig. 5** Simulation results of trigonal arrangement of air filled cylinders in the silicon matrix (filling factor 65%). Displacement distribution of the structure excited with a shear displacement applied to the top structure boundary taken at frequency of 2.1 GHz (a) and 3 GHz (b), and the structure reflection coefficient (c)

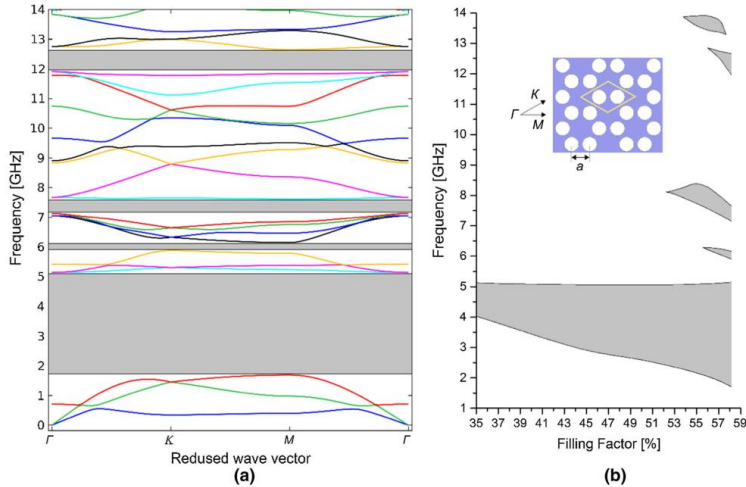


**Fig. 6** Band diagram for the pore silicon infinite graphite arrangement, filling factor 58% (a) and the dependence of the width of the absolute forbidden acoustic bands on the filling factor (b) for the distance between neighboring scatters  $a = 0.9 \mu\text{m}$

applications that can isolate the resonance modes of several switchable resonators or support an efficient operation of FBAR filters in several neighboring frequency bands. The computation results completed for the structure reflection with the horizontally excited top boundary confirm the structure bandgap behavior. The structure displacement distribution and the frequency dependence of the finite

arrangement reflection coefficient are demonstrated in Fig. 7.

The obtained computation results of the structure reflection coefficient demonstrate two well defined frequency regions, where the arrangement is able to efficiently isolate mechanical deformations. At lower frequencies, the structure has a rather broad region from almost 2 GHz till 5 GHz that is beneficial for switchable FBARs and

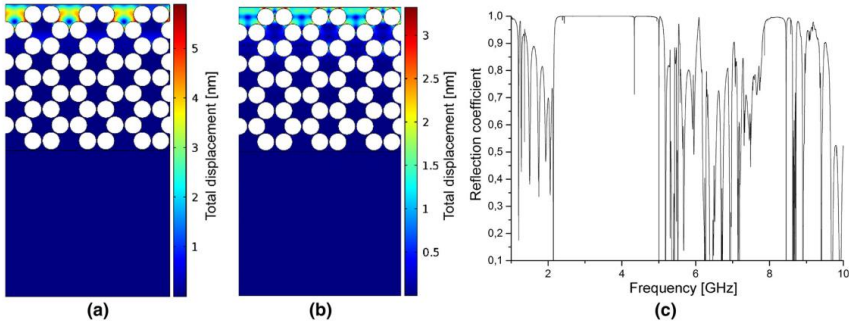


**Fig. 7** Simulation results of graphite arrangement of air filled cylinders in the silicon matrix (filling factor 55%). Displacement distribution of the structure excited with a shear displacement applied

to the top structure boundary taken at frequency of 4 GHz (a) and 8 GHz (b), and the structure reflection coefficient (c)

multiple band arrangements. The displacement distribution simulations show a high level of the displacement localization at the structure surface with relatively low penetration of the mechanical displacement into the volume. Relatively narrow high frequency bandgap that appears in the structure reflection spectrum is beneficial considering the application for the FBAR structures, where the efficient operation within multiple frequency bands have to be ensured. Among the demonstrated structures designs, the honeycomb arrangement demonstrates the most promising response as an acoustic reflector for FBAR devices on a basis of the microporous technological approach. Further investigations of the structure response depending on the deviation of technological parameters were performed for the honeycomb symmetry arrangement.

### 3 Discussion

The respective structure dimensions, as it was demonstrated in performed simulations, are micrometer and sub-micrometer order. In most cases, theoretically achieved structure designs are rather challenging to fabricate in micrometer and sub-micrometer dimensions. In previous works (Gorisse and Reinhardt 2016), the fabrication process of the 2D phononic structure for the purpose of a lateral coupling reduction between neighboring resonators was demonstrated. The fabrication of periodic arrangements was completed by means of hydrogen implantation into the LiNbO<sub>3</sub> piezoelectric material forming Li<sub>1-x</sub>NbO<sub>3</sub> inclusions. Another work has demonstrated the design and fabrication of the silicon carbide/air periodic arrangement that was utilized as a Bragg acoustic mirror to confine the acoustic energy in a resonance cavity (Ziaei-

Moayyed et al. 2010). Most works underline the complexity of microstructures fabrication with standard approaches. In current contribution, the realization of the periodic arrangement within sub-micrometer dimensions is considered to be realized within subsequent steps on a basis of the macroporous structures fabrication technology.

Previously demonstrated results of complete bandgaps were addressed to the infinite periodic arrangement. In order to estimate the structures performance within finite dimensions, the analysis of reflection coefficient depending on the number of structure periods was completed. The analysis was completed for the honeycomb arrangement. Summarized computation results are demonstrated in Fig. 8. The reflection coefficient was computed for the frequency of 4 GHz.

The obtained results demonstrate that the structure with 8 periods already exhibits the reflection behavior comparable to the infinite case. Considering this observation, the required minimal number of the arrangement periods for the honeycomb symmetry can be reduced to the value where the maximal structure reflection coefficient is already achieved.

The ability to design the structure for certain frequency bands is the subject of geometry variation with respect to the wavelength. The theoretical investigations of variable lattice constant and pore dimensions demonstrate the ability to adjust the structure for the required frequency ranges. The computation results of the honeycomb structure bandgap variation depending on the wavelength structure scaling are summarized in Fig. 9.

The obtained computation results show that the increase of the structure wavelength shifts the bandgaps towards lower frequency regions as expected. The change of

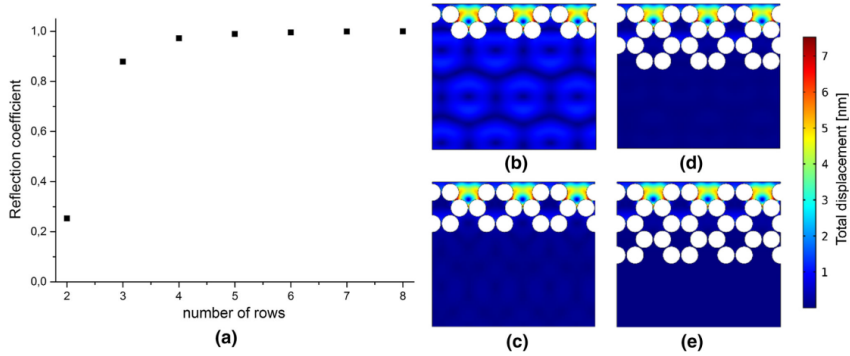


**Fig. 8** Dependence of the structure reflection coefficient on the number of rows of the arrangement (a) and the simulation results of displacement distribution for number of rows equal 2 (b), 3 (c), 4 (d), 5 (e), 6 (f), taken at frequency of 4 GHz

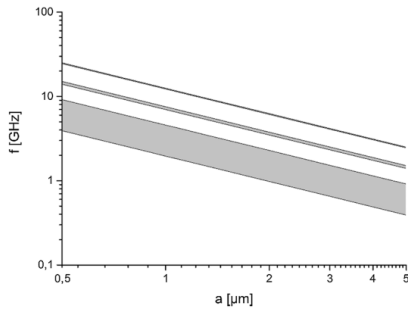


**Fig. 9** Honeycomb arrangement bandgap variation depending on the structure lattice constant for fixed filling factor of 55%

structure wavelength causes an equal relative shift of both bandgap edges keeping the number of bandgap regions.

The structure performance and reproducibility of geometry play a significant role in order to obtain the theoretically predicted results. The estimation of influences of the structure dimensions deviation on the periodic arrangement reflection coefficient is demonstrated in Fig. 10. Random fluctuations of the holes diameter were modeled using the normal law, according to which the distribution function of the holes diameters by sizes can be presented in a following way:

$$f(d) = \frac{1}{\sigma\sqrt{2\pi}} \exp\left[-\frac{(d-\bar{d})^2}{2\sigma^2}\right],$$

where  $d$  is the diameter of the holes,  $\bar{d}$  is the average diameter of the holes, and  $\sigma$  is dispersion.

Figure 10a shows the distribution of the holes diameters by sizes for different values of the dispersion. The results of modeling the reflection coefficient from the structure shown in Fig. 7a with the corresponding fluctuations of the diameter of the holes ( $\sigma = 0, \sigma = 0.0015 \bar{d}, \sigma = 0.03 \bar{d}$ , where  $\bar{d} = 0.495 \mu\text{m}$ ) are shown in Fig. 10b–d.

The results show that the deviation of structure dimensions can cause an appearance of narrow vibration modes as a result of disruption of the structure periodicity that enriches the number of possible transmission modes within the bandgap. The most significant impact is observed for the higher frequency bandgaps. The increase of dimensions fluctuations deteriorates the reflection coefficient for the low deviations and completely vanishes for the higher values, Fig. 10. Technologically, it is more likely to obtain a rather slight distribution of the dimensions deviation that should not cause a significant deterioration of the periodic structure within the certain spatial area of the FBAR structure. Nevertheless, as it can be seen, it is advantageous to have a rather broad bandgap than several narrow ones to reduce influences of possible fabrication tolerances.

#### 4 Conclusions

In current contribution we have demonstrated the results of the theoretical research work focused on the study of technologically competitive solutions of phononic structures performance for the FBAR devices purposes. We proposed to consider the established technological platform



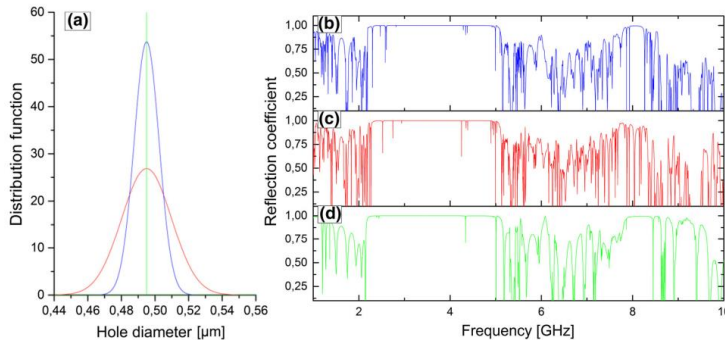


**Fig. 10** Influence of deviation of inclusions geometry on spectral properties of periodic arrangement. Distribution function **(a)** and respective reflection coefficient for  $\sigma = 0.0015 \bar{d}$  **(b)**,  $\sigma = 0.03 \bar{d}$  **(c)** and  $\sigma = 0$  **(d)**

for the macroporous structures fabrication as an approach that allows to realize the phononic based acoustic reflectors for FBAR SMR devices and to study appropriate periodic structure solutions with numerical methods. We have shown that the application of macroporous periodic arrangements can enable the efficient operation of SMR FBARs within broad frequency ranges without necessity to utilize a membrane type of the piezoelectric film isolation. The work presented the computation results for square, triangular and honeycomb arrangements showing the achievable bandgap responses. It was found that the honeycomb arrangement is the most advantageous in terms of bandgap performance that presumably should allow to operate the FBAR structures within the broad frequency range. The completed work is an initial step towards the phononic crystal based FBAR devices fabrication that is the subject of ongoing research.

**Acknowledgements** The research work of current contribution was supported by German Research Foundation under LU 605/16-1 and HI 1261/5-1 grants, by the Federal Ministry of Education and Research (BMBF) within MEMSonMID (03IPT518X) project and by the DAAD program “Mikhail Lomonosov” (Project no. 3.10001.2017/DAAD).

## References

- Barillaro G, Nannini A, Piotto M (2002) Electrochemical etching in HF solution for silicon micromachining. *Sens Actuators A* 102:195–201
- Benchabane S, Khelif A, Rauch J, Robert L, Laude V (2006) Evidence for complete surface wave band gap in a piezoelectric phononic crystal. *Phys Rev E* 73:65601
- Gevorgian S, Tagantsev AK, Vorobiev A (2013) FBARs utilizing induced piezoelectric effect. In: *Tuneable film bulk acoustic wave resonators*. Springer, New York, pp 117–131
- Gorisse M, Reinhardt A (2016) Laterally coupled BAW filter employing phononic crystals
- Hashimoto K (2009) RF bulk acoustic wave filters for communications. Artech House, London
- Joannopoulos JD, Johnson SG, Winn JN, Meade RD (2011) *Photonic crystals: molding the flow of light*. Princeton University Press, Princeton
- Kalkur TS, Mansour A (eds) (2015) *Tunable and switchable resonators and filters based on ferroelectric BST thin films for wireless communications*. IEEE, New York
- Kokkonen K, Kaivoila M, Benchabane S, Khelif A, Laude V (2007) Scattering of surface acoustic waves by a phononic crystal revealed by heterodyne interferometry. *Appl Phys Lett* 91:83517
- Kozyrev AB, Mikhaylov AK, Ptashnik SV, Zinoviev SV, Petrov PK, Alford NM, Wang T (2011) Electronically switchable bulk acoustic wave resonator based on paraelectric state ferroelectric films. *Electron Lett* 47:1326–1327
- Kurowski A, Schultze JW, Lüth H, Schöning MJ (2002) Micro- and nanopatterning of sensor chips by means of macroporous silicon. *Sens Actuators B Chem* 83:123–128
- Kushwaha MS, Halevi P, Dobrzynski L, Djafari-Rouhani B (1993) Acoustic band structure of periodic elastic composites. *Phys Rev Lett* 71:2022
- Lakin KM, Kline GR, McCarron KT (1993) High-Q microwave acoustic resonators and filters. *IEEE Trans Microw Theory Tech* 41:2139–2146
- Lehmann V, Föll H (1990) Formation mechanism and properties of electrochemically etched trenches in n-type silicon. *J Electrochem Soc* 137:653–659
- Lehmann V, Grüning U (1997) The limits of macropore array fabrication. *Thin Solid Films* 297:13–17
- Lehmann V, Ronnebeck S (1999) The physics of macropore formation in low-doped p-type silicon. *J Electrochem Soc* 146:2968–2975
- Lehmann V, Stengl R, Reisinger H, Detempe R, Theiss W (2001) Optical shortpass filters based on macroporous silicon. *Appl Phys Lett* 78:589–591
- Li X, Abe T, Esashi M (2001) Deep reactive ion etching of Pyrex glass using SF<sub>6</sub> plasma. *Sens Actuators A* 87:139–145
- Liang J, Chik H, Yin A, Xu J (2002) Two-dimensional lateral superlattices of nanostructures: nonlithographic formation by anodic membrane template. *J Appl Phys* 91:2544–2546

- Matthias S, Müller F, Schilling J, Gösele U (2005) Pushing the limits of macroporous silicon etching. *Appl Phys A Mater Sci Process* 80:1391–1396
- Park JH, Lee N, Lee J, Park JS, Park HD (2005) Deep dry etching of borosilicate glass using SF<sub>6</sub> and SF<sub>6</sub>/Ar inductively coupled plasmas. *Microelectron Eng* 82:119–128
- Pennec Y, Vasseur JO, Djafari-Rouhani B, Dobrzyński L, Deymier PA (2010) Two-dimensional phononic crystals: examples and applications. *Surf Sci Rep* 65:229–291
- Profunser DM, Muramoto E, Matsuda O, Wright OB, Lang U (2009) Dynamic visualization of surface acoustic waves on a two-dimensional phononic crystal. *Phys Rev B* 80:14301
- Ronggui S, Righini GC (1991) Characterization of reactive ion etching of glass and its applications in integrated optics. *J Vac Sci Technol A Vac Surf Films* 9:2709–2712
- Sigalas MM, Economou EN (1992) Elastic and acoustic wave band structure. *J Sound Vib* 158:377–382
- Smith RL, Collins SD (1992) Porous silicon formation mechanisms. *J Appl Phys* 71:R1–R22
- Ueda M, Hara M, Taniguchi S, Yokoyama T, Nishihara T, Hashimoto K, Satoh Y (2008) Development of an X-band filter using air-gap-type film bulk acoustic resonators. *Jpn J Appl Phys* 47:4007
- Vasseur JO, Djafari-Rouhani B, Dobrzyński L, Kushwaha MS, Halevi P (1994) Complete acoustic band gaps in periodic fibre reinforced composite materials: the carbon/epoxy composite and some metallic systems. *J Phys Condens Matter* 6:8759
- Wehrspohn RB, Schilling J (2003) A model system for photonic crystals: macroporous silicon. *Phys Status Solidi A* 197:673–687
- Wu T, Wu L, Huang Z (2005) Frequency band-gap measurement of two-dimensional air/silicon phononic crystals using layered slanted finger interdigital transducers. *J Appl Phys* 97:94916
- Wu T, Wang W, Sun J, Hsu J, Chen Y (2009) Utilization of phononic-crystal reflective gratings in a layered surface acoustic wave device. *Appl Phys Lett* 94:101913
- Ziaei-Moayyed M, Su MF, Reinke CM, El-Kady I, Olsson RH (eds) (2010) Silicon carbide phononic crystals for high fQ micromechanical resonators. IEEE, New York

**8-PAPER:** Different regimes of ultrashort pulse propagation in disordered layered media with resonant loss and gain

Novitsky D.V., Redka D., Shalin A.S., “Different Regimes of Ultrashort Pulse Propagation in Disordered Layered Media with Resonant Loss and Gain”, (2019) *Annalen der Physik*, 531 (9), art. no. 1900080, DOI: [10.1002/andp.201900080](https://doi.org/10.1002/andp.201900080),

# Different Regimes of Ultrashort Pulse Propagation in Disordered Layered Media with Resonant Loss and Gain

Denis V. Novitsky,\* Dmitrii Redka, and Alexander S. Shalin

Different optical nanostructures containing both loss and gain components attract ever-increasing attention as novel advanced materials and building blocks for a variety of nanophotonic and plasmonic applications. Unique tunable optical signatures of the so-called active metamaterials support their utilization for sensing, imaging, and signal processing on micro- and nanoscales. However, this tunability requires flexible control over the metamaterial parameters, which could be provided by involving a set of nonlinear interactions. In this paper, a method of governing ultrashort pulses is proposed by varying the level of a population difference disorder in a random active metamaterial. This enables us to deliver three different interaction regimes: self-induced transparency (low disorder), localization regime (moderate disorder), and light amplification (strong disorder) corresponding to strongly different light pulse speeds. Since this control could be realized via rather plain tools, like simple pump tuning, the proposed disordered medium opens a room of opportunities for designing a peculiar active component for a whole set of highly demanded optical applications.

## 1. Introduction

Since the first optical metamaterials utilized plasmonic effects and were based on metal-containing nanostructures, the problem of losses has arisen from the very beginning of this field. The idea to add active (gain) components to nanoplasmic metamaterials to compensate losses was a natural next step.<sup>[1]</sup> This concept was successfully applied to negative-refractive-index metamaterials<sup>[2,3]</sup> which were of primary interest in the early investigations in nanophotonics. The topic of active metamaterials

has gained great momentum since then. Both the number of active structures considered and the list of effects in these structures increased dramatically. For example, widely utilized hyperbolic metamaterials<sup>[4–10]</sup> supplemented with gain material allows us to reach simultaneously spontaneous emission enhancement and outcoupling of high-wavenumber modes,<sup>[11]</sup> strong coupling,<sup>[12]</sup> and loss compensation.<sup>[13]</sup> Other active nanostructured systems include magnetic metamaterials for tunable reflection,<sup>[14]</sup> graphene-based random metamaterials,<sup>[15]</sup> and hybrid metal-semiconductor metasurfaces for polarization switching and light-beam steering.<sup>[16]</sup> There are a multitude of studies on novel laser sources based on active metamaterials, from dark-state lasing in metal-dielectric systems<sup>[17]</sup> to metastructures utilizing superconducting qubits<sup>[18]</sup> and randomly dispersed graphene flakes.<sup>[15]</sup> The fruitfulness of studies devoted to photonic systems containing both loss and gain is vividly illustrated by the great attention to the so-called PT-symmetric structures in recent years. Although such systems are often developed on the basis of waveguides and cavities (see, e.g., recent reviews<sup>[19,20]</sup>), there are also proposals of PT-symmetric metamaterials.<sup>[21,22]</sup>

In this paper, we modify the usual loss-gain setting by introducing another variable into system – disorder. Since the seminal paper by P. W. Anderson<sup>[23]</sup> who predicted the localization of matter waves in disordered lattices, the concept of Anderson localization was transferred to optics and became the starting point of the fruitful field of disordered photonics.<sup>[24,25]</sup> It turned out recently that disordered metamaterials are of great interest not only due to Anderson localization,<sup>[26,27]</sup> but also can serve for observation of topological state transitions,<sup>[28]</sup> transmission enhancement,<sup>[29]</sup> and wavefront shaping.<sup>[30]</sup>

Although we are concerned here with metamaterial-like structures, it should be mentioned that disordered photonics with active materials has a long history. The main concern of these studies was perhaps random lasing based on multiple scattering of light in amplifying disordered media. The standard approach to reach random lasing is to use solid-state powders,<sup>[31]</sup> including semiconductors,<sup>[32]</sup> and dye solutions with scatterers.<sup>[33]</sup> More advanced variant is a fiber laser with random distributed feedback.<sup>[34–36]</sup> Recently, random lasing in the Anderson localized regime was reported both in 2D disordered photonic crystals<sup>[37]</sup>

Dr. D. V. Novitsky  
B. I. Stepanov Institute of Physics  
National Academy of Sciences of Belarus  
68 Nezavisimosti Avenue, Minsk 220072, Belarus  
E-mail: d.novitsky@ifanbel.bas-net.by  
Dr. D. V. Novitsky, Dr. A. S. Shalin  
ITMO University  
49 Kronverksky Prospekt, St. Petersburg 197101, Russia  
Dr. D. Redka  
Saint Petersburg Electrotechnical University "LETI" (ETU)  
5 Prof. Popova Street, St. Petersburg 197376, Russia  
Dr. A. S. Shalin  
Ulyanovsk State University  
42 Lev Tolstoy Street, Ulyanovsk 432017, Russia

The ORCID identification number(s) for the author(s) of this article can be found under <https://doi.org/10.1002/andp.201900080>

DOI: 10.1002/andp.201900080

and disordered optical fibers.<sup>[38]</sup> Random lasing systems can be also utilized for switching<sup>[39]</sup> and nonlinearity-induced modification and competition of laser modes.<sup>[40,41]</sup>

We study the disordered 1D layered structure with resonant loss and gain. Another feature of our consideration is the emphasis on the dynamics of a short pulse propagation. Therefore, our results belong not only to the fields of active and disordered photonics, but also continue the long chain of investigations devoted to the coherent pulse propagation in resonant media.<sup>[42]</sup> In particular, our analysis is naturally connected to the studies of self-induced transparency (SIT)<sup>[43,44]</sup> and related coherent effects such as the formation of population density gratings<sup>[45,46]</sup> and collisions between solitonic pulses.<sup>[47–49]</sup>

In the pioneering work by Folli and Conti,<sup>[50]</sup> the interplay between SIT and localization was studied for the first time. They considered the disordered multilayer formed by randomly changing layer thicknesses with incorporated two-level particles. In other words, the disorder was in the background medium of the structure, so that the commonly known localized states of light form then interact with the SIT pulses supported by the nonlinearity due to the two-level particles. Here we are interested in the systems with disorder in the parameters of the resonant part of the system, whereas the background is uniform. In our recent paper,<sup>[51]</sup> we have proposed the concept of a disordered resonant medium which is the realization of such a system. It can be considered as a multilayer metamaterial with the density of active particles randomly varying from layer to layer. We have studied pulse localization in this model and analyzed the transition from SIT to localization as a function of a number of parameters, such as disorder parameter, mean particle density, total length, and the thickness of constant-density layers. Localization in this framework results in a strong suppression of the transmission and enhancement of both the reflection and absorption. In a further study,<sup>[52]</sup> these observations were used to propose a transmission modulation scheme based on disorder-induced inelasticity of pulse–pulse collisions.

In contrast to those *passive* systems, here we assume that the density of active particles is uniform and study another class of disordered resonant media with randomly varying initial population difference. Such a medium can be viewed as a sort of *active* disordered metamaterial and represents a set of layers with different levels of loss and/or gain. The ordered case is just the uniform resonantly absorbing medium, whereas the introduction of a disorder means appearance of excited layers: the stronger the disorder, the larger the excitation. Since it is not obvious how such systems respond to the external pulsed excitation, we analyze several concrete models of disorder and demonstrate three different regimes of pulse interaction with the system: the SIT regime, the localization regime, and the amplification regime. The first one is observed at a low disorder and is characterized by almost unperturbed slow soliton propagation. The localization regime occurring at an intermediate disorder implies low output and strong absorption of a radiation inside the structure. At a large disorder, the signal rapidly appears at the back end of the structure, and the total energy of the transmitted and reflected light is amplified. One can switch between these regimes by changing disorder parameter, for example, via change of pumping. This allows us to obtain dramatically different responses (transmission and reflec-

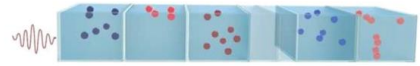


**Figure 1.** Schematic depiction of the system under consideration. Different shades of blue and red denote different levels of loss and gain, respectively.

tion) at different levels of disorder that can be used as a basis for tunable optical devices.

## 2. Governing Equations

The system considered in this paper consists of a background dielectric doped with active (two-level) atoms (**Figure 1**). Light propagation in this medium can be described in the semiclassical approximation by the well-known Maxwell–Bloch equations. Namely, we have differential equations for the dimensionless electric-field amplitude  $\Omega = (\mu/\hbar\omega)E$  (normalized Rabi frequency), complex amplitude of the atomic polarization  $\rho$ , and population difference between the ground and excited state  $w$ <sup>[42]</sup> (see also ref. [49]):

$$\frac{d\rho}{d\tau} = i\Omega w + i\rho\delta - \gamma_2\rho \quad (1)$$

$$\frac{dw}{d\tau} = 2i(l^*\Omega^*\rho - \rho^*l\Omega) - \gamma_1(w - 1) \quad (2)$$

$$\begin{aligned} \frac{\partial^2\Omega}{\partial\xi^2} - n_d^2\frac{\partial^2\Omega}{\partial\tau^2} + 2i\frac{\partial\Omega}{\partial\xi} + 2in_d^2\frac{\partial\Omega}{\partial\tau} + (n_d^2 - 1)\Omega \\ = 3el\left(\frac{\partial^2\rho}{\partial\tau^2} - 2i\frac{\partial\rho}{\partial\tau} - \rho\right) \end{aligned} \quad (3)$$

where  $\tau = \omega t$  and  $\xi = kz$  are the dimensionless time and distance,  $\mu$  is the dipole moment of the quantum transition,  $\hbar$  is the reduced Planck constant,  $\delta = \Delta\omega/\omega = (\omega_0 - \omega)/\omega$  is the normalized frequency detuning,  $\omega$  is the carrier frequency,  $\omega_0$  is the frequency of the quantum transition,  $\gamma_1 = 1/(\omega T_1)$  and  $\gamma_2 = 1/(\omega T_2)$  are the normalized relaxation rates of population and polarization respectively, and  $T_1$  ( $T_2$ ) is the longitudinal (transverse) relaxation time. The dimensionless parameter  $\epsilon = \omega_l/\omega = 4\pi\mu^2 C/3\hbar\omega$  is responsible for the light-matter coupling, where  $C$  is the density of two-level atoms and  $\omega_l$  is the normalized Lorentz frequency. Quantity  $l = (n_d^2 + 2)/3$  is the local-field enhancement factor due to the polarization of the background dielectric with refractive index  $n_d$  by the embedded active particles.<sup>[53]</sup> Further we numerically solve Equations (1)–(3) using the finite-difference approach described in ref. [54].

We limit our analysis to the 1D system described above as it is usually done in analysis of SIT and similar effects. The parameters used for calculations are characteristic, for example, for semiconductor quantum dots as the active particles:<sup>[55,56]</sup> the relaxation times  $T_1 = 1$  ns and  $T_2 = 0.1$  ns (much larger than light pulse duration, that is, we are in the coherent regime), the Lorentz frequency  $\omega_l^0 = 10^{12}$  s<sup>-1</sup> (if not stated otherwise), and the exact resonance ( $\delta = 0$ ). The full thickness of the medium

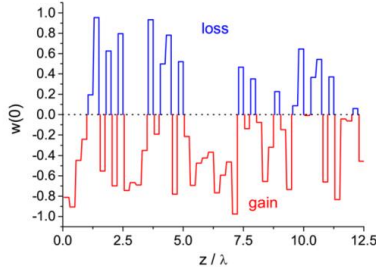


**Figure 2.** Examples of initial population difference  $w_0$  distributed along the medium for the model of disorder given by Equation (4). The thickness of the layer with constant  $w_0$  is  $\delta L = \lambda/4$  and the disorder strength is  $r = 1$ .

$L = 1000\lambda$ . Incident light pulses have the central wavelength  $\lambda = 0.8 \mu\text{m}$  and the Gaussian envelope  $\Omega = \Omega_p \exp(-t^2/2t_p^2)$  with the pulse duration of  $t_p = 50$  fs. For pulses of such short duration, we can safely neglect the influence of the near dipole-dipole interactions between the two-level emitters<sup>[57]</sup> as well as the inhomogeneous broadening.<sup>[58]</sup> The peak Rabi frequency is given by  $\Omega_p = \Omega_0 = \lambda/\sqrt{2\pi}ct_p$ , which corresponds to the pulse area of  $2\pi$  (the  $2\pi$  SIT pulse). Without loss of generality, we take  $n_d = 1$ ; similar results can be obtained for other values of background refractive index as will be shown directly.

The disorder is introduced through the periodical random variations of the initial population difference  $w_0 = w(t=0)$  along the light propagation direction (see Figure 1). Further we consider the concrete model of disorder, which is the simplest example of a general class of disorder allowing to study its influence on the system's response. The model considered implies that the initial population difference in a given layer can take on any possible value. In Supporting Information, our findings are backed with calculations for the two other models of disorder – the two-valued one with layers either fully inverted or totally unexcited and the generalized one which is a straightforward modification of the previous two. We believe that the behavior of light pulses will be qualitatively the same for different specific models of disorder, so that we can limit ourselves to the simplest ones used in this paper.

### 3. Results

The model of disorder considered here implies that the initial population difference in the  $j$ th layer of the medium corresponding to the distance  $(j-1)\delta L < z \leq j\delta L$  is given by

$$w_0^{(j)} = 1 - 2\zeta_j r \quad (4)$$

where  $\zeta_j$  is the random number uniformly distributed in the range  $[0; 1]$  and  $r$  is the parameter of the disorder strength. When  $r = 0$ , we have the trivial case of purely absorbing (lossy) medium (all  $w_0^{(j)} = 1$ ). On the contrary,  $r = 1$  corresponds to the maximal

disorder, when loss and gain have equal probability to appear. In other words, the system can be considered as a multilayer (total thickness  $L$ ) consisting of slabs (thickness  $\delta L$ ) with different initial population differences, that is, different parts of the medium are under different pumping (see Figure 1). For  $r > 0.5$ , the gain layers with  $w_0^{(j)} < 0$  become possible. Thus, the parameter  $r$  not only governs deviation from the ordered case of pure loss, but also takes on the role of pumping strength resulting in appearance of gain. An example of distribution governed by Equation (4) is depicted in Figure 2 for the period of random density variations  $\delta L = \lambda/4$  and maximal disorder  $r = 1$ .

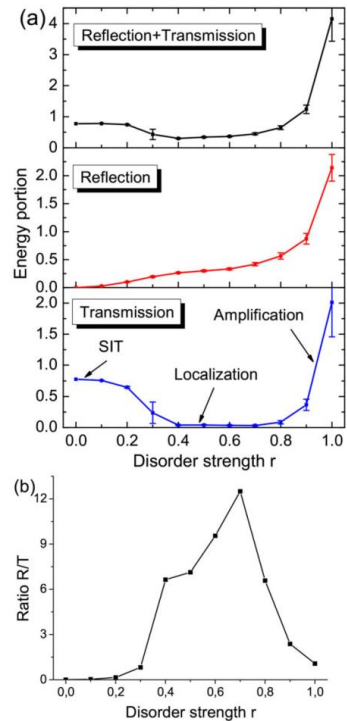


**Figure 3.** a) Average output energy of transmitted (bottom) and reflected (middle) light as well as their sum (top) as a function of the disorder parameter  $r$  calculated within the model of disorder given by Equation (4). Energy averaged over 100 realizations was calculated for the time interval  $500t_p$  and was normalized on the input energy. The layer thickness is  $\delta L = \lambda/4$ . The error bars show the unbiased standard deviations for the corresponding average values. b) The ratio of average values of reflection and transmission as a function of  $r$ .

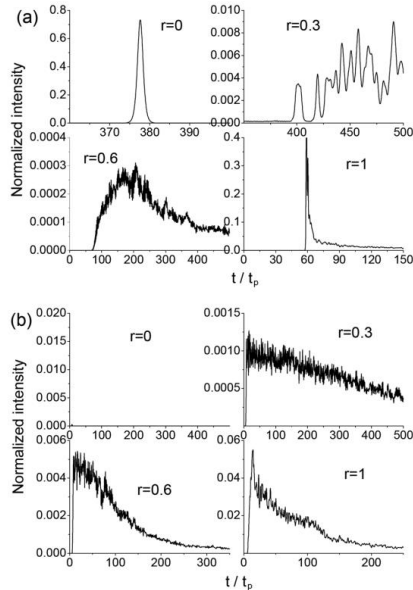


**Figure 4.** Profiles of a) transmitted and b) reflected intensity for different values of the disorder parameter  $r$  calculated within the model of disorder given by Equation (4). Profiles are averaged over 100 realizations, the layer thickness is  $\delta L = \lambda/4$ .

Figure 3a shows the mean values of transmission and reflection for different levels of disorder calculated in the framework of the model (4). One can distinguish three different regimes of a pulse interaction with the disordered resonant medium. At low disorder ( $r \leq 0.2$ ), we have the *SIT regime* with high transmission and the resulting pulse corresponding to a SIT soliton [see the profile in Figure 4a at  $r = 0$ ]. Remind that SIT is the nonlinear effect of high-intensity ultrashort pulse transmission through the resonantly absorbing medium.<sup>[42–44]</sup> The pulse duration should be much shorter than relaxation times of the medium ( $t_p \ll T_1, T_2$ ), so that the energy absorbed at the front edge of the pulse can be coherently returned to the pulse at its trailing edge. As a result, the solitonic pulse of a specific form can be observed propagating through the medium with low attenuation. This is exactly what we see in Figure 4a.

For  $r > 0.2$ , the transition to localization occurs with gradual decrease of transmission and increase of reflection and absorption. In this case, localization means that the radiation gets trapped inside the structure in the form of population inversion.<sup>[50,51]</sup> This trapping happens closer to the entrance as disorder grows, so that the slowing down SIT pulses and almost standing population inversion can be observed as

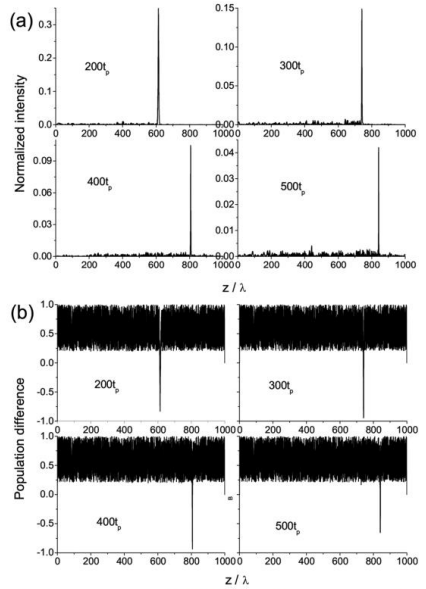


**Figure 5.** The distributions of a) light intensity and b) population difference at different moments of time for a realization of disorder with  $r = 0.4$ .

shown in Figure 5 for a realization with  $r = 0.4$ . Another sign of transition to localization is the increase of variance<sup>[59]</sup> – the statistical value related to the standard deviation shown in figures with the error bars. It is indeed seen that the standard deviation (hence, variance) increases near the transition to the localization regime ( $r = 0.3$  in Figure 3a), which means strong fluctuations of response from realization to realization.

The average transmission profile at the point of this transition [Figure 4a at  $r = 0.3$ ] contains several residual peaks due to the presence of strongly attenuated pulses at the output in some realizations, whereas the average reflection profile [Figure 4b] has an almost linear slope. For  $0.4 \leq r \leq 0.7$ , we have the *localization regime* with very low and almost uniform transmission and reflection slowly growing with  $r$ . The average intensity profiles (Figure 4 at  $r = 0.6$ ) have sharp leading edge and exponentially decaying trailing edge.

For  $r > 0.7$ , the second transition occurs, from localization to *amplification regime*, with the rapidly growing transmission and reflection. The large standard deviations in this regime indicate that individual realizations of a disorder can strongly deviate from the mean response, but the amplification is relatively large in all realizations. The average profiles (Figure 4 at  $r = 1$ ) have sharp peaks and flat tails. It is interesting that the transmission peak

in this case appears at the back end much faster than the SIT soliton at  $r = 0$ . The simple estimation shows that the peak corresponds to the time needed for photons to almost freely pass through the medium ( $\Delta t_{\text{pass}} \approx L/c \approx 50t_p$ ), in contrast to SIT regime with slowly moving solitons ( $\Delta t_{\text{pass}} \approx 380t_p$ ). Thus, varying the degree of disorder, we have the possibility to control the response time of the medium via registering the transmitted signal: from relatively long times (SIT regime, slow pulse) to infinite time (localization regime, no pulse) to relatively short times (amplification regime, fast pulse).

Another feature is that changing the disorder parameter (e.g., by changing pumping) allows us to switch between the regimes with the prevailing transmission and reflection. Indeed, as we see in Figure 3b, the transition from SIT to localization regime means that the cumulative reflected energy is much higher than the transmitted one, the optimal ratio being at  $r = 0.7$ , at the edge of the localization regime. If we do not compare the total energetic characteristics, but the signal levels shown in Figure 4, we can see essentially the same behavior: from the almost zero reflected signal due to SIT ( $r = 0$ ) to the prevailing reflected signal ( $r = 0.6$ ) and back to the transmitted signal an order of magnitude stronger than the reflected one ( $r = 1$ ). Thus, varying the degree of disorder, we have the possibility to control the reflection-to-transmission ratio back and forth.

The results reported above were obtained for  $\delta L = \lambda/4$  as the thickness of layers with constant initial population difference. Let us now discuss the influence of this parameter on the performance of the disordered medium. We choose the value  $r = 0.5$  sitting in the middle of the localization regime and calculate the average transmission and reflection for different  $\delta L$  as shown in Figure 6. (Note that we use smaller number of realizations – 25 instead of 100, – since our experience evidences that such number is quite enough to make reliable conclusions). We see that the optimum for localization (i.e., minimum of total output) is in the range  $0.1\lambda \leq \delta L \leq 0.25\lambda$  that is in a very good accordance with the results on the problem reported in ref. [51].

In Supporting Information, we show that similar results can be obtained for two other models of disorder. In particular, in the framework of the so-called two-valued model, we analyze the importance (and optimization) of the medium thickness and the average concentration of active particles. It is also demonstrated that the same regimes discussed above can be observed in the more realistic structures with non-vacuum host medium.

As to possible experimental implementation, the random distributions of the population difference can be created, for example, in a side-pumping scheme similar to that utilized in ref. [60]. According to our model of disorder, Equation (4), the random numbers  $\zeta_i$  set the random variations of population difference along the radiation propagation direction. This disorder can be introduced into our system within a side-pumping scheme through periodic placing absorbing strips of random thickness on the structure. Different strips will block different portions of pump, so that different regions of the medium will be differently and randomly excited. The disorder parameter  $r$ , which governs the strength (or degree) of disorder, shows, how large the variations of population difference are. It can be tuned simply by changing pump intensity, so that at the same distribution of random numbers  $\zeta_i$ , stronger pumping results in larger amplitude of population-difference variations. Within this conceptual

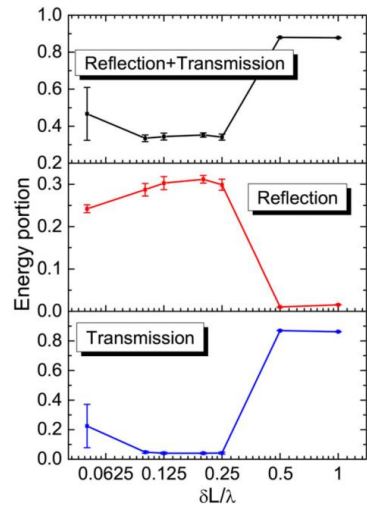


Figure 6. Average output energy of transmitted (bottom) and reflected (middle) light as well as their sum (top) as a function of the layer thickness  $\delta L$ . The disorder parameter is  $r = 0.5$ . Energy averaged over 25 realizations was calculated for the time interval  $500t_p$  and was normalized on the input energy.

scheme, one can create the distributions of loss and gain with different disorder strengths on demand.

#### 4. Conclusion

In conclusion, we have studied the propagation of ultrashort pulses in the resonant multilayered medium with initial population difference randomly varying along the propagation direction. In contrast to previous considerations of SIT and localization,<sup>[50,51]</sup> we deal with not passive, but active system with disordered loss-gain distribution and uniform background. Calculations performed for three possible models of the disorder reveal two transitions (and, correspondingly, three different regimes) as the disorder in such a system grows and the medium starts to strongly deviate from the uniform absorbing medium. The transitions are: from the SIT regime to the localization regime and then to the amplification regime. The latter appears, only when the population difference can take negative values and the disorder parameter is large enough. Coexistence of the three regimes in the same system opens a room of opportunities for a flexible control over the optical response of the medium. In particular, we show the possibility to govern the reflection-to-transmission ratio and the speed of a pulse propagation through the medium by changing the disorder parameter via, for example, utilizing tunable pumping. Thus, we propose the active



multilayered disordered metamaterial-like system (e.g., quantum-dot-based) enabling us to switch between different light-interaction regimes, which is of high demand for a variety of applications, such as imaging, signal processing, and as a basis for ultracompact light absorbers (localization regime).

### Supporting Information

Supporting Information is available from the Wiley Online Library or from the author.

### Acknowledgements

The work was supported by the Belarusian Republican Foundation for Fundamental Research (Project No. F18-049), the Russian Foundation for Basic Research (Projects No. 18-02-00414, 18-52-00005, and 18-32-00160), and Government of Russian Federation (Grant No. 08-08). Numerical simulations of the nonlinear interaction of light with resonant media have been supported by the Russian Science Foundation (Project No. 17-72-10098). The investigation of the profiles of transmitted and reflected intensity for different values of the disorder is partially supported by the Russian Science Foundation (Project No. 18-72-10127).

### Conflict of Interest

The authors declare no conflict of interest.

### Keywords

amplification of light, disordered metamaterials, localization of light, resonant medium, self-induced transparency

Received: March 4, 2019  
Revised: May 29, 2019  
Published online:

- [1] O. Hess, J. B. Pendry, S. A. Maier, R. F. Oulton, J. M. Hamm, K. L. Tsakmakidis, *Nat. Mater.* **2012**, *11*, 573.
- [2] S. Wuestner, A. Pusch, K. L. Tsakmakidis, J. M. Hamm, O. Hess, *Phys. Rev. Lett.* **2010**, *105*, 127401.
- [3] S. Xiao, V. P. Drachev, A. V. Kildishev, X. Ni, U. K. Chettiar, H.-K. Yuan, V. M. Shalaev, *Nature* **2010**, *466*, 735.
- [4] D. R. Smith, D. Schurig, *Phys. Rev. Lett.* **2003**, *90*, 077405.
- [5] P. A. Belov, *Microwave Opt. Technol. Lett.* **2003**, *37*, 259.
- [6] A. Poddubny, I. Iorsh, P. Belov, Yu. Kivshar, *Nat. Photon.* **2013**, *7*, 958.
- [7] A. S. Shalin, P. Ginzburg, A. A. Orlov, I. Iorsh, P. A. Belov, Yu. S. Kivshar, A. V. Zayats, *Phys. Rev. B* **2015**, *91*, 125426.
- [8] A. V. Chebykin, A. A. Orlov, A. S. Shalin, A. N. Poddubny, P. A. Belov, *Phys. Rev. B* **2015**, *91*, 205126.
- [9] A. S. Shalin, S. V. Sukhov, A. A. Bogdanov, P. A. Belov, P. Ginzburg, *Phys. Rev. A* **2015**, *91*, 063830.
- [10] A. Ivinskaya, N. Kostina, A. Proskurin, M. I. Petrov, A. A. Bogdanov, S. Sukhov, A. V. Krasavin, A. Karabchevsky, A. S. Shalin, P. Ginzburg, *ACS Photonics* **2018**, *5*, 4371.
- [11] T. Galfsky, H. N. S. Krishnamoorthy, W. Newman, E. E. Narimanov, Z. Jacob, V. M. Menon, *Optica* **2015**, *2*, 62.
- [12] F. Vaianella, J. M. Hamm, O. Hess, B. Maes, *ACS Photon.* **2018**, *5*, 2486.
- [13] D. V. Novitsky, V. R. Tuz, S. L. Prosvirnin, A. V. Lavrinenko, A. V. Novitsky, *Phys. Rev. B* **2017**, *96*, 235129.
- [14] T. Deng, R. Huang, M.-C. Tang, P. K. Tan, *Opt. Express* **2014**, *22*, 6287.
- [15] A. Marini, F. J. Garcia de Abajo, *Phys. Rev. Lett.* **2016**, *116*, 217401.
- [16] L. Cong, Y. K. Srivastava, H. Zhang, X. Zhang, J. Han, R. Singh, *Light Sci. Appl.* **2018**, *7*, 28.
- [17] S. Droulias, A. Jain, T. Koschny, C. M. Soukoulis, *Phys. Rev. Lett.* **2017**, *118*, 073901.
- [18] H. Asai, S. Savelev, S. Kawabata, A. M. Zagorskin, *Phys. Rev. B* **2015**, *91*, 134513.
- [19] L. Feng, R. El-Ganainy, L. Ge, *Nat. Photon.* **2017**, *11*, 752.
- [20] R. El-Ganainy, K. G. Makris, M. Khajavikhan, Z. H. Musslimani, S. Rotter, D. N. Christodoulides, *Nat. Phys.* **2018**, *13*, 11.
- [21] H. Alaeian, J. A. Dionne, *Phys. Rev. A* **2014**, *89*, 033829.
- [22] D. V. Novitsky, A. Karabchevsky, A. V. Lavrinenko, A. S. Shalin, A. V. Novitsky, *Phys. Rev. B* **2018**, *98*, 125102.
- [23] P. W. Anderson, *Phys. Rev.* **1958**, *109*, 1492.
- [24] D. Wiersma, *Nat. Photon.* **2013**, *7*, 188.
- [25] M. Segev, Y. Silberberg, D. N. Christodoulides, *Nat. Photon.* **2013**, *7*, 197.
- [26] S. A. Gredeskul, Yu. S. Kivshar, A. A. Asatryan, K. Y. Bliokh, Yu. P. Bliokh, V. D. Freilikher, I. V. Shadrivov, *Low Temp. Phys.* **2012**, *38*, 570.
- [27] H. H. Scheinflux, Y. Lumer, G. Ankonina, A. Z. Genack, G. Bartal, M. Segev, *Science* **2017**, *356*, 953.
- [28] C. Liu, W. Gao, B. Yang, S. Zhang, *Phys. Rev. Lett.* **2017**, *119*, 183901.
- [29] H. H. Scheinflux, I. Kaminker, A. Z. Genack, M. Segev, *Nat. Commun.* **2016**, *7*, 12927.
- [30] M. Jang, Y. Horie, A. Shibukawa, J. Brake, Y. Liu, S. M. Kamali, A. Arbabi, H. Ruan, A. Faraon, C. Yang, *Nat. Photon.* **2018**, *12*, 84.
- [31] M. A. Noginov, *Solid-State Random Lasers*, Springer, New York, NY **2005**.
- [32] H. Cao, Y. G. Zhao, S. T. Ho, E. W. Seelig, Q. H. Wang, R. P. H. Chang, *Phys. Rev. Lett.* **1999**, *82*, 2278.
- [33] N. M. Lawandy, R. M. Balachandran, A. S. L. Gomes, E. Sauvain, *Nature* **1994**, *368*, 436.
- [34] S. K. Turitsyn, S. A. Babin, A. E. El-Taher, P. Harper, D. V. Churkin, S. I. Kablukov, J. D. Ania-Casta non, V. Karalekas, E. V. Podivilov, *Nat. Photon.* **2010**, *4*, 231.
- [35] S. K. Turitsyn, S. A. Babin, D. V. Churkin, I. D. Vatnik, M. Nikulin, E. V. Podivilov, *Phys. Rep.* **2014**, *542*, 133.
- [36] X. Du, H. Zhang, H. Xiao, P. Ma, X. Wang, P. Zhou, Z. Liu, *Ann. Phys.* **2016**, *528*, 649.
- [37] J. Liu, P. D. Garcia, S. Ek, N. Gregersen, T. Suhr, M. Schubert, J. Mark, S. Stobbe, P. Lodahl, *Nat. Nanotech.* **2014**, *9*, 285.
- [38] B. Abaie, E. Mobini, S. Karbasi, T. Hawkins, J. Ballato, A. Mafi, *Light Sci. Appl.* **2017**, *6*, e17041.
- [39] M. Leonetti, C. Conti, C. Lopez, *Nat. Commun.* **2013**, *4*, 1740.
- [40] B. Liu, A. Yamilov, Y. Ling, J. Y. Xu, H. Cao, *Phys. Rev. Lett.* **2003**, *91*, 063903.
- [41] P. Stano, P. Jacquod, *Nat. Photon.* **2013**, *7*, 66.
- [42] L. Allen, J. H. Eberly, *Optical Resonance and Two-Level Atoms*, Wiley, New York **1975**.
- [43] S. L. McCall, E. L. Hahn, *Phys. Rev.* **1969**, *183*, 457.
- [44] I. A. Poluektov, Yu. M. Popov, V. S. Roitberg, *Sov. Phys. Usp.* **1975**, *17*, 673.
- [45] R. M. Arkhipov, M. V. Arkhipov, I. Babushkin, A. Demircan, U. Morgner, N. N. Rosanov, *Opt. Lett.* **2016**, *41*, 4983.
- [46] R. M. Arkhipov, A. V. Pakhomov, M. V. Arkhipov, I. Babushkin, A. Demircan, U. Morgner, N. N. Rosanov, *Sci. Rep.* **2017**, *7*, 12467.
- [47] A. A. Afanas'ev, V. M. Volkov, V. V. Dritz, B. A. Samson, *J. Mod. Opt.* **1990**, *37*, 165.
- [48] M. J. Shaw, B. W. Shore, *J. Opt. Soc. Am. B* **1991**, *8*, 1127.
- [49] D. V. Novitsky, *Phys. Rev. A* **2011**, *84*, 013817.

- [50] V. Follis, C. Conti, *Opt. Lett.* **2011**, *36*, 2830.  
[51] D. V. Novitsky, *Phys. Rev. A* **2018**, *97*, 013826.  
[52] D. V. Novitsky, A. S. Shalin, *Ann. Phys.* **2019**, *531*, 1800405.  
[53] M. E. Crenshaw, *Phys. Rev. A* **2008**, *78*, 053827.  
[54] D. V. Novitsky, *Phys. Rev. A* **2009**, *79*, 023828.  
[55] *Handbook of Optical Constants of Solids* (Ed: E. D. Palik), Academic Press, San Diego, CA **1998**.  
[56] J.-C. Diels, W. Rudolph, *Ultrashort Laser Pulse Phenomena*, 2nd ed., Academic Press, San Diego, CA **2006**.  
[57] D. V. Novitsky, *Phys. Rev. A* **2010**, *82*, 015802.  
[58] D. V. Novitsky, *J. Phys. B* **2014**, *47*, 095401.  
[59] A. A. Chabanov, M. Stoytchev, A. Z. Genack, *Nature* **2000**, *404*, 850.  
[60] Z. J. Wong, Y.-L. Xu, J. Kim, K. O'Brien, Y. Wang, L. Feng, X. Zhang, *Nat. Photon.* **2016**, *10*, 796.

**9-PAPER:** Diffusion-inspired time-varying phosphorescent decay in a nanostructured environment

Kislov D., Novitsky D., Kadochkin A., Redka D., Shalin A.S., Ginzburg P. “Diffusion-inspired time-varying phosphorescent decay in a nanostructured environment”, (2020) *Physical Review B*, 101 (3), art. no. 035420, DOI: [10.1103/PhysRevB.101.035420](https://doi.org/10.1103/PhysRevB.101.035420)

**Diffusion-inspired time-varying phosphorescent decay in a nanostructured environment**Denis Kislov,<sup>1,\*</sup> Denis Novitsky,<sup>1,2</sup> Alexey Kadochkin,<sup>3</sup> Dmitrii Redka,<sup>4</sup> Alexander S. Shalin,<sup>1</sup> and Pavel Ginzburg<sup>5,6</sup><sup>1</sup>*ITMO University, 49 Kronverksky Pr., St. Petersburg 197101, Russia*<sup>2</sup>*B.I. Stepanov Institute of Physics, National Academy of Sciences of Belarus, 68 Nezavisimosti Avenue, Minsk 220072, Belarus*<sup>3</sup>*Ulyanovsk State University, Ulyanovsk 432017, Russia*<sup>4</sup>*Saint Petersburg, Electrotechnical University "LETI" (ETU) 5 Prof. Popova Street, St. Petersburg 197376, Russia*<sup>5</sup>*Center for Photonics and 2D Materials, Moscow Institute of Physics and Technology, Dolgoprudny 141700, Russia*<sup>6</sup>*Tel Aviv University, Ramat Aviv, Tel Aviv 69978, Israel*

(Received 1 October 2019; published 22 January 2020)

Structured environment controls dynamics of light-matter interaction processes via modified local density of electromagnetic states. In typical scenarios, where nanosecond-scale fluorescent processes are involved, mechanical conformational changes of the environment during the interaction processes can be safely neglected. However, slow decaying phosphorescent complexes (e.g., lanthanides) can efficiently probe micro- and millisecond scale motion via near-field interactions with nearby structures. As the result, lifetime statistics can inherit information about nanoscale mechanical motion. Here we study light-matter interaction dynamics of phosphorescent dyes, diffusing in a proximity of a plasmonic nanoantenna. The interplay between time-varying Purcell enhancement and stochastic motion of molecules is considered via a modified diffusion equation, and collective decay phenomena is analysed. Fluid properties, such as local temperature and diffusivity, are mapped on phosphorescent lifetime distribution and then extracted with the help of inverse Laplace transformation. The presented photonic platform enables performing contactless all-optical thermometry and diffusion measurements, paving a way for a range of possible applications. In particular, detailed studies of nanofluidic processes in lab-on-a-chip devices, challenging for analysis with other optical methods, can be performed with time-dependent phosphorescence.

DOI: [10.1103/PhysRevB.101.035420](https://doi.org/10.1103/PhysRevB.101.035420)**I. INTRODUCTION**

Light-matter interaction processes strongly depend on both internal structure of quantum systems and surrounding environments [1]. While the first factor in a vast majority of scenarios is pre-defined by nature, the latter one can be modified by carefully designed nanostructuring [2–6]. Purcell enhancement of spontaneous emission rates with plasmonic nanoantennae is one among prominent examples of tailoring first-order light-matter interaction, e.g., Refs. [7,8]. The essence of structuring-inspired manipulation can be understood via local density of electromagnetic states (LDOS), which enter interaction Hamiltonians governing quantum processes of any order [9,10]. LDOS is directly related to a classical Green's function, which allows formulating quantum problems in terms of pure classical electromagnetic quantities.

Common approach to address light-emission processes is based on time-dependent perturbation theory in the case of weak coupling regime, or on the complete solution of dynamic equations in more advanced strong coupling scenarios. In both cases, however, strength of the fundamental interaction parameter is time independent. This approach is well justified in cavity quantum electrodynamics, where the environment is static and does not change during the interaction. In colloidal applications, where a solution of particles can undergo either

ordered or random motion, dynamical changes of the environment can be also neglected under certain and commonly met approximations. For example, fast virtual level assisted non-linear processes and even dipole-allowed nanosecond scale fluorescent decays are orders of magnitude faster than slow microsecond-scale changes in fluidic environment.

In a sharp contrast to dipole-allowed fluorescent transitions, phosphorescent dyes are characterized by micro- and milli- second slow decays, which originate from fundamentally different quantum process – spin flip followed by the photon emission transition. In particular, phosphorescent (e.g., Ref. [11]) and rare earth (e.g., Ref. [12]) luminescent molecules have characteristic decay times in a range of micro and even milliseconds scales. Those properties can be employed for different imaging techniques, such as gated photoluminescence microscopy [13], and also can be affected by nanostructuring [14–17]. In terms of fundamental light-matter interaction processes, phosphorescent timescales can be comparable with conformational changes inside colloidal environment. For example, a spherical molecule in water at room temperature has an average drift of several hundreds of nm during the time period of 100  $\mu$ s. This nanoscale displacement between an emitter and a nanoantenna is enough to dramatically change the decay rate, as it will be shown hereafter. It is worth noting that conformational changes are still significantly slower than the optical carrier frequency and allow applying time-scale separation approach for the theoretical treatment. This approach has been recently applied

\*denis.a.kislov@gmail.com

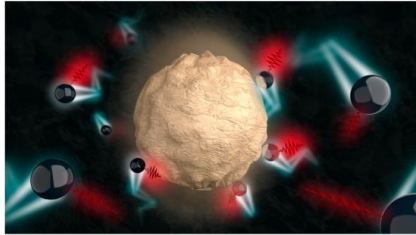


FIG. 1. The schematics of the system—diffusion of slow-decaying phosphorescent dyes next to a resonant nanoantenna.

to velocimetry mapping with phosphorescent emitters [18] and for analysis of rotational micro-Doppler effects [19,20].

Here we develop a theoretical framework for treating diffusion processes of slow-decaying phosphorescent compounds in a solution of resonant optical antennae (Fig. 1). An assembly of emitters, dissolved in a liquid mixed with metal nanoparticles, is pumped with an external illumination. Slow-decaying dyes diffuse in the vicinity of resonating nanoparticles and change their emission on the timescale, comparable with the spontaneous decay. As the result of this interaction, the information on the fluid dynamics is imprinted in the photon statistics.

The manuscript is organized as follows: the basic diffusion model with an additional decay term associated with the position-dependent Purcell effect is introduced in Sec. II. Contrary to traditional description of diffusion processes, the overall number of excited emitters is kept as a variable. Orientation-averaged and position-dependent Purcell factor is calculated next. The analysis is based on the evaluation of classical Green's functions via Mie series expansion. Solution of the diffusion equation with the position-dependent Purcell-driven decay factor comes as the main result in Sec. II D, followed by the conclusions in Sec. IV.

## II. THEORETICAL FORMALISM

### A. Diffusion model

The proposed diffusion model describes the density of excited and time-decaying molecules, undergoing Brownian motion in a proximity of metal or dielectric nanoparticles (Fig. 1). Since the later objects have significantly higher mass, they can be assumed to be static during the interaction (however, the reference frame can be linked directly to the resonator, which is static in its rest frame). The concentration of excited molecules is  $n(\mathbf{r}, t)$  and it depends not only on the diffusion in a solvent, but also on time via Purcell-enhanced interactions with a nearby nanoantenna. This position-dependent decay rate can be written as  $\gamma(\mathbf{r}) = \gamma_0 F(\mathbf{r})$ , where  $F(\mathbf{r})$  is the Purcell factor and  $\mathbf{r}$  stays for the distance between the nanoparticle and the excited molecule. In free space, without a particle present, the characteristic decay time is  $\tau_0 = 1/\gamma_0$ . For lanthanide complexes it can vary from

$\mu$ s to ms depending on an internal structure and surrounding solvent, which can quench the radiation.

The diffusion equation for this type of a process can be written as

$$\frac{\partial n}{\partial t} = D\Delta n - \gamma(\mathbf{r})n, \quad (1)$$

where  $D$  is the diffusion coefficient of phosphorescent molecules. Purcell effect introduces an additional spatially dependent decay channel. Diffusion coefficient ( $D$ ) generally depends on temperature and other parameters of an environment, which can be related to each other via Stokes–Einstein relation:

$$\frac{D_{T_1}}{D_{T_2}} = \frac{T_1 \mu_{T_2}}{T_2 \mu_{T_1}}, \quad (2)$$

where  $\mu$  is a solvent's dynamic viscosity and subindices correspond to different local temperatures [21]. This dependence can provide a new methodology for local temperature sensing via Purcell-effect-induced luminescence modification, as it will be shown with forthcoming analysis.

Hereinafter, the model will concentrate on the interaction dynamics with a single spherical particle by assuming radial symmetry of the entire scenario. It means that the pumping mechanism is also isotropic (unpolarized) and it induces a spatially dependent excitation of molecules in the region under consideration. While the antenna effect for pump can be also introduced, here for the sake of simplicity we assume a Gaussian initial distribution of the form  $n(r, 0) = n_0 e^{-2r^2/R_b^2}$ , where  $R_b$  is the waist radius of a tightly focused pump laser beam. Under the simplifying conditions, we can neglect the angular dependence of concentration and recast Eq. (1) in spherical coordinates by leaving only the radial component:

$$\frac{\partial n}{\partial t} = D \frac{\partial^2 n}{\partial r^2} + 2 \frac{D}{r} \frac{\partial n}{\partial r} - \gamma(r)n. \quad (3)$$

We will solve Eq. (3) numerically in a range of  $r$  from the radius of the nanoparticle ( $a$ ) to a certain value  $R \gg a$ . This allows us to set the boundary conditions as an absence of molecular flow near the surface and far away from the nanoparticle  $\frac{\partial n(0,t)}{\partial r} = \frac{\partial n(R,t)}{\partial r} = 0$ . This assumption relies on relatively low density of nanoparticles in the liquid. To obtain the solution of Eq. (3), position-dependent Purcell Factor should be estimated, which will be done next.

While the proposed model assumes low concentration of plasmonic nanoparticles, it can be extended to scenarios that are more complex. Increase in the concentration can lead to emergence of several effects. For example, dye molecule can drift from one resonator to another—in this case, boundary conditions for Eq. (3) should be modified. For dense nanoparticle solutions, antenna-antenna interaction start playing a role, giving rise to collective modes. In this case, LDOS based on Green's functions formalism should be revised. The general model for the case of high concentration should address both of the beforehand mentioned aspects and cannot utilize the radial symmetry, assumed for deriving Eq. (3). To justify the low concentration assumption, the volumetric fraction of gold nanoparticles should be less than a single one per focal volume of a collecting objective. Also, the mean-squared displacement of diffusing molecules during

their decay time should be smaller than an averaged spacing between gold nanoparticles. Furthermore, high concentration of emitting molecules can lead to additional decay channels (concentration quenching), which can complicate the overall dynamics beyond the proposed model. Optimal concentration values around  $100 \mu\text{M}$  [22] and other beforehand mentioned conditions can be met in a possible experimental realization.

### B. Position and orientation averaged Purcell enhancement

Electromagnetic Green's function of a radiating dipole next to spherical dielectric particle has a closed form analytical solution based on Mie theory. This allows to obtain analytical expressions for Purcell factor, describing the enhancement of spontaneous emission rates in the vicinity of nanoparticles as follows [23,24]:

$$F_{\perp}^{\text{rad}}(r) = \frac{3}{2} \sum_{m=1}^{\infty} m(m+1)(2m+1) \times \left| \frac{\psi_m(kr\sqrt{\varepsilon_d})}{(kr\sqrt{\varepsilon_d})^2} + A_m \frac{\xi_m(kr\sqrt{\varepsilon_d})}{(kr\sqrt{\varepsilon_d})^2} \right|^2, \\ F_{\parallel}^{\text{rad}}(r) = \frac{3}{4} \sum_{m=1}^{\infty} (2m+1) \left( \left| \frac{\psi_m(kr\sqrt{\varepsilon_d})}{kr\sqrt{\varepsilon_d}} + B_m \frac{\xi_m(kr\sqrt{\varepsilon_d})}{kr\sqrt{\varepsilon_d}} \right|^2 + \left| \frac{\psi'_m(kr\sqrt{\varepsilon_d})}{kr\sqrt{\varepsilon_d}} + A_m \frac{\xi'_m(kr\sqrt{\varepsilon_d})}{kr\sqrt{\varepsilon_d}} \right|^2 \right), \quad (4)$$

where  $F_{\perp}^{\text{rad}}$  and  $F_{\parallel}^{\text{rad}}$  stay for *radiative* enhancement of the emission in the case, when the dipole moment of a molecule is either perpendicular or parallel to the nanosphere surface. In the case, when the molecules are randomly oriented in respect to the sphere, the average enhancement is given by  $F^{\text{rad}}(r) = \frac{2}{3} F_{\parallel}^{\text{rad}}(r) + \frac{1}{3} F_{\perp}^{\text{rad}}(r)$ . Corresponding *total* rate enhancements are given by

$$F_{\parallel}^{\text{tot}}(r) = 1 + \frac{3}{4} \sum_{m=1}^{\infty} (2m+1) \times \text{Re} \left[ B_m \left( \frac{\xi_m(kr\sqrt{\varepsilon_d})}{kr\sqrt{\varepsilon_d}} \right)^2 + A_m \left( \frac{\xi'_m(kr\sqrt{\varepsilon_d})}{kr\sqrt{\varepsilon_d}} \right)^2 \right], \\ F_{\perp}^{\text{tot}}(r) = 1 + \frac{3}{2} \sum_{m=1}^{\infty} m(m+1)(2m+1) \times \text{Re} \left[ A_m \left( \frac{\xi_m(kr\sqrt{\varepsilon_d})}{(kr\sqrt{\varepsilon_d})^2} \right)^2 \right]. \quad (5)$$

In Eqs. (4) and (5)  $\varepsilon_d$  is the dielectric permittivity of the environment,  $k$  - wavenumber in vacuum,  $A_m$  and  $B_m$  are Mie coefficients (widely used notions have been used [23,24]),  $m$  - number of multipole terms,  $\psi_m(x) = x j_m(x)$ ,  $\xi_m(x) = x h_m^{(1)}(x)$ , where  $j_m(x)$  and  $h_m^{(1)}(x)$  are, respectively, spherical Bessel and Hankel functions of the first kind.

Radiative and nonradiative enhancements should be distinguished, as they influence the light-matter interaction in different ways. Total radiative lifetime governs the decay dynamics, while the radiative contribution is responsible for

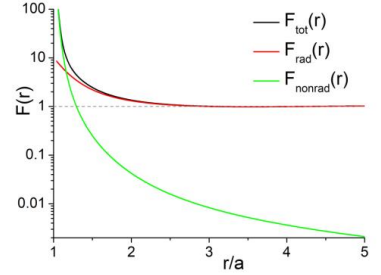


FIG. 2. Purcell enhancement next to a gold (50-nm-radius) nanoparticle. Orientation-averaged total, radiative, and nonradiative enhancements (black, red, and green lines, respectively) as a function of the normalized distance (to the particle's radius) between the dipole and particle's surface. Detailed parameters are given in the main text.

a number of photons detected at the far field. The difference between radiative and total rates is the result of losses within the particle [25]. While in a majority of optoelectronic applications only the radiative enhancement is a factor for maximization, our diffusion model requires the knowledge of the total decay rate. The information about local properties of the fluid, however, can be analyzed via collecting emitted photons. Separation into radiative and nonradiative channels, based on Green's functions formalism, can be also preformed [26].

Radiative and total enhancements are plotted as the function of the distance between the emitter and the gold nanoparticle (Fig. 2). The following typical parameters have been used—the radius of the spherical particle is 50 nm, the optical properties of gold were taken from [27]. The phosphorescent emission central wavelength is 690 nm. It can be seen that nonradiative channels prevail the decay dynamics in the close proximity of the particle, while at distances larger than 100 nm the influence of the particle is minor, and Purcell enhancement approaches unity (no enhancement). Qualitatively, it means that far-situated fluorophores will contribute to the background radiation and will decay with the rate of  $\gamma_0$ . Those contributions can be factorized by applying lifetime distribution post-processing techniques [28]. The most relevant region for observing the diffusion dynamics via photon counting is situated at distances of 20–100 nm from the nanoparticle surface.

### C. Temperature dependence of the diffusion coefficient

Taking into account the spatial distribution of the Purcell enhancement and low density of the dissolved nanoparticles, electromagnetic coupling between neighboring nanoantennas can be ignored. Furthermore, contributions of the emitters situated far apart from the particle are neglected, since their lifetimes are unmodified during the diffusion process, as it was previously discussed.

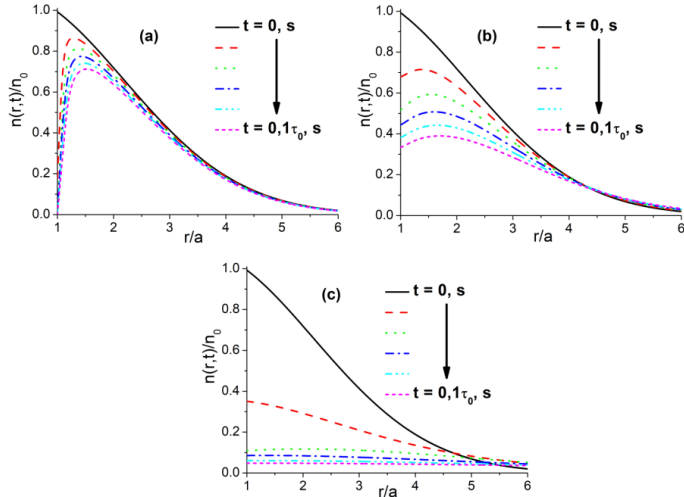


FIG. 3. Radial distribution of excited dye molecules density in a vicinity of the particle. Different times, elapsed from the pump pulse are represented with color lines (in captions  $[0 : 6 : 0.1\tau_0]$  the interval is equidistantly divided into six sections). Diffusion coefficients ( $D$  [ $\mu\text{m}^2/\text{ms}$ ]) are: (a) 0, (b) 0.2, (c) 1.6. Other parameters:  $a = 50$  nm,  $R_b = 4.8a$ ,  $\tau_0 = 300$   $\mu\text{s}$ .

The diffusion coefficient of emitters is given by the Stokes-Einstein relation assuming spherical shapes of the molecules and low Reynolds numbers, which are justified in the case of nanoscale objects dissolved in water [29]:

$$D(T) = \frac{k_B T}{6\pi\mu(T)R_{\text{mol}}}, \quad (6)$$

where  $\mu$  is the dynamical viscosity of the solvent,  $T$  is absolute temperature, and  $R_{\text{mol}}$  is the radius of the light-emitting complex.  $R_{\text{mol}} \approx 0.5\text{-}1$  nm for the molecules, which are discussed here [29]. There are empirical models relating dynamical viscosity and local temperature. For example, distilled water obeys  $\mu(T) = A_0 10^{B_0/T - C_0}$ , where  $A_0 = 2.4 \times 10^{-5}$  Pa s,  $B_0 = 247.8$  K and  $C_0 = 140$  K. In this case, the diffusion coefficient for a range of organic compounds (e.g., eosin, rose bengal, erythrosine), which possess relevant phosphorescent properties [30], will fall in the following range:  $0.2 \div 1.6$   $\mu\text{m}^2/\text{ms}$  (from 273 to 373 K).

#### D. Analysis of the diffusion-inspired emission dynamics

Having the values of the diffusion coefficient and the position-dependent Purcell factor, the entire model can be solved now. Figure 3 shows the density of the excited molecules as a function of the distance from the particle at different instances of time. Color lines correspond to different times elapsed from the instance of the pulsed pump excitation.

It can be seen from Fig. 3 that when the diffusion coefficient is very small (panel a) the population of excited dyes drops down fast next to the particle and there is no

Brownian inflow towards it. However, when the diffusion is efficient, slow decaying molecules (unaffected by Purcell enhancement) flow in and start sensing the presence of the antenna. As the result, they become decaying faster. This dynamical behavior is clearly seen by comparing panels a, b, and c. The diffusion kinetics has a direct replica on the lifetime distribution, which can be measured at the far field.

Intensity, collected at the far field, has the following time dependence:

$$I(t) \sim \int_a^{R_{\text{collection}}} \int_0^\pi \int_0^{2\pi} F^{\text{rad}}(r) \gamma_0 n(r, t) r^2 \sin^2(\vartheta) dr d\vartheta d\varphi. \quad (7)$$

$R_{\text{collection}}$  here corresponds to the focal volume of a collecting objective and it is supposed to be much larger than the spot size of the exciting beam  $R_b$  (this assumption does not affect the main result, however). Note that the time dependence solely originates from  $n(r, t)$ . While  $n(r, t)$  is governed by the total decay rate, the emitted intensity in Eq. (7) also depends explicitly on the radiative Purcell enhancement. Figure 4(a) demonstrates the time-dependent intensity decay for different values of the diffusion constant. It is clearly seen that in the chosen range of parameters the intensity drops faster with the increase of the diffusivity. When the molecules are randomly moving around the antenna, they have larger probability to be found in its vicinity and, as a result, they experience larger Purcell enhancement.

The kinetics of the collected intensity can be used as a tool for diffusion and, hence, temperature detection. To demonstrate this, we apply the inverse Laplace transformation

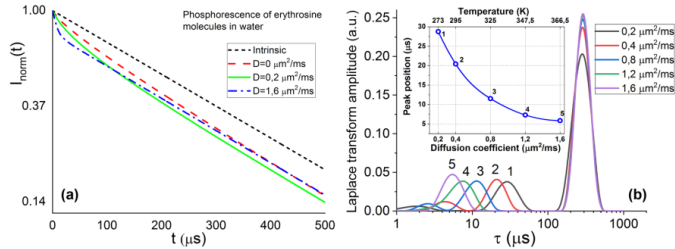


FIG. 4. (a) Normalized intensity (log-scale) decay of the dye molecules in a vicinity of the particle for different diffusion coefficient values: Intrinsic phosphorescence of erythroine molecules in water (no particle present) and with the particle present for  $D$  [ $\mu\text{m}^2/\text{ms}$ ] = 0, 0.2, and 1.6. (b) Lifetime distribution analysis of the collected luminescence signal. Color lines correspond to different diffusion coefficients and, hence, temperatures. The inset shows the position of the secondary (numbered) peak as a function of the diffusion coefficient. The decay time is derived from the regularized inverse Laplace transformation. The radius of the collecting objective focal volume is  $R_{\text{collection}} = 10a$ .

on the function  $I(t)$  given by Eq. (7). Namely, the intensity can be represented as

$$I(t) = \int_0^{\infty} g(s)e^{-st} ds, \quad (8)$$

where  $s = 1/\tau$  is the inverse relaxation time. We solve this equation using the numerical approach similar to that reported in Ref. [28] and get the distribution  $g(s)$  for different exponential contributions to the total luminescence kinetics. The result is shown in Fig. 4(b), where the nonexponential response of the system is clearly seen. The right strongest peak corresponds to the free-space relaxation time of the molecules ( $\tau_0 = 300 \mu\text{s}$ ). The secondary peak on the left is associated to the Purcell effect and contains the information on the diffusion characteristics. Indeed, it is seen that the increase in the diffusion coefficient results in further shift of this secondary peak towards shorter lifetimes due to increasing probability for molecules to approach to the metal nanoparticle. The position of this peak as a function of the diffusion coefficient and, consequently the temperature, is shown in the inset. Therefore, it becomes possible to measure temperature and diffusion coefficient in a liquid via the proposed photonic contactless design. This pronounced dependence of the optical signature of phosphorescent molecules on surroundings can be extremely useful for remote all-optical temperature control.

### III. OUTLOOK

Quite a few spectroscopic methods have been developed for thermometry applications. For example, different types of vacancies in nanodiamonds were shown to serve as an excellent platform for high-resolution temperature mapping [31,32]. Micro-photoluminescence measurements of quantum well structures can be used for mapping cryogenic temperatures [33]. Quite a few proposals and demonstrations have been developed for measuring temperatures in microchannels [34–37] and diffusion coefficients of reagents in microfluidic cells [38,39]. Monitoring and control of fluid properties, such as temperatures and viscosities, as well as associated mass transfer processes (including diffusion), is crucial in many biochemical, biological and medical applications.

For example, several degrees deviations significantly affect efficiencies of polymerase chain reactions [40], the heating mode in the Reimer–Tiemann reaction [41], crystallization process of quantum dots formation [42], and many others. Environmental control is especially important for protein-based biotherapeutic drugs, which are very sensitive to temperature fluctuations (for example, insulin [43] and monoclonal antibodies), which are a new class of biotherapeutic drugs used to treat various diseases, such as autoimmune diseases and cancer [44,45]. Therefore, microanalysis methods provide significant benefits for characterizing the degradation of such drugs, because native protein solutions have different viscosities in comparison to degraded samples [46,47].

Our approach for measuring the diffusion coefficient and temperature offers flexible solutions for the beforehand mentioned applications. Under experimental constraints, resonant metal nanoparticles can be mixed with a fluid within a channel. However, nanoantennae array can be directly deposited on channel boundaries (e.g., Ref. [48]). Analyte solution is then mixed with slow-decaying molecules. Erythroine, eosin, bengal rose, and rare-earth metal ion complexes are among the candidates that can be employed in the experiment. This versatility provides flexibly in choosing certain spectral range for analysis as well as identifying characteristic decay times, most suitable for a desirable range of solvent's viscosity. Relevant concentration, antennae spacing and other conditions, which simplify data interpretation, have been discussed after Eq. (3). High numerical objective should be used for pumping the dyes and for collecting the emission. While time-correlated single photon counting (TCSPC) techniques should be used for retrieving time-dependent intensity decay, slow decaying phosphorescence can be detected with sensitive photodiodes, capable to resolve the signal in time.

### IV. CONCLUSIONS

Lab-on-a-chip architectures, capable to accommodate several sensing functions within in a miniature device, is a fast-growing field attracting ever-increasing attention. However, hardware realizations of many important functionalities are often face challenges, especially in cases when nanoscale



resolution is required. Here we developed a novel concept for contactless all-optical temperature and diffusion measurements, which are enabled by dynamic time-dependent Purcell effect in a solution of phosphorescent molecules interfacing resonant nanoantennae. Dynamics of the long lifetime phosphorescent molecules decay is shown to be strongly dependent on the Brownian motion next to a resonator. This special interaction is described with temperature-dependent diffusion coefficient of the surrounding liquid. Subsequently, far-field radiation emitted from diffusing molecules is analyzed via the inverse Laplace transform and exploited to recover local properties of a fluid environment. As the result, an efficient contact-free approach to measure required hydrodynamical characteristics of a liquid in a broad temperature range with

nanoscale spatial resolution is demonstrated. Moreover, the proposed method can utilize biologically compatible compounds demonstrating new capabilities in a variety of lab-on-a-chip realizations and expanding the range of microfluidics applications.

#### ACKNOWLEDGMENTS

The work has been supported in part by ERC StG “In Motion” and PAZY Foundation. A.S.S. acknowledges the support of the Russian Fund for Basic Research within Projects No. 18-02-00414 and No. 18-52-00005. Numerical simulations of the particles dynamics and lifetimes have been supported by the Russian Science Foundation (Project No. 18-72-10127).

- 
- [1] L. Novotny and B. Hecht, *Principles of Nano-Optics*, 2nd ed. (Cambridge University Press, Cambridge, 2012).
- [2] K. V. Baryshnikova, A. Novitsky, A. B. Evlyukhin, and A. S. Shalin, *J. Opt. Soc. Am. B* **34**, D36 (2017).
- [3] P. D. Terekhov, V. E. Babicheva, K. V. Baryshnikova, A. S. Shalin, A. Karabchevsky, and A. B. Evlyukhin, *Phys. Rev. B* **99**, 045424 (2019).
- [4] E. A. Gurvitz, K. S. Ladutenko, P. A. Dergachev, A. B. Evlyukhin, A. E. Miroshnichenko, and A. S. Shalin, *Laser Photonics Rev.* **13**, 1800266 (2019).
- [5] H. K. Shamkhi, K. V. Baryshnikova, A. Sayanskiy, P. Kapitanova, P. D. Terekhov, P. Belov, A. Karabchevsky, A. B. Evlyukhin, Y. Kivshar, and A. S. Shalin, *Phys. Rev. Lett.* **122**, 193905 (2019).
- [6] K. Baryshnikova, D. Filonov, C. Simovski, A. Evlyukhin, A. Kadochkin, E. Nenasheva, P. Ginzburg, and A. S. Shalin, *Phys. Rev. B* **98**, 165419 (2018).
- [7] L. Novotny and N. Van Hulst, *Nat. Photonics* **5**, 83 (2011).
- [8] J. J. Greffet, *Science* **308**, 1561 (2005).
- [9] G. Milburn, *Quantum Optics*, 3rd ed. (Wiley-VCH, Weinheim, Germany, 2012).
- [10] P. Ginzburg, *Rev. Phys.* **1**, 120 (2016).
- [11] K. J. Morris, M. S. Roach, W. Xu, J. N. Demas, and B. A. DeGraff, *Anal. Chem.* **79**, 9310 (2007).
- [12] D. Liu, Z. Wang, H. Yu, and J. You, *Eur. Polym. J.* **45**, 2260 (2009).
- [13] W. A. W. Razali, V. K. A. Sreenivasan, C. Bradac, M. Connor, E. M. Goldys, and A. V. Zvyagin, *J. Biophotonics* **9**, 848 (2016).
- [14] D. J. Roth, P. Ginzburg, L. M. Hirvonen, J. A. Levitt, M. E. Nasir, K. Suhling, D. Richards, V. A. Podolskiy, and A. V. Zayats, *Laser Photon. Rev.* **13**, 1900101 (2019).
- [15] M. G. Kucherenko and D. A. Kislov, *J. Photochem. Photobiol. A Chem.* **354**, 25 (2018).
- [16] S. V. Izmodenova, D. A. Kislov, and M. G. Kucherenko, *Colloid J.* **76**, 683 (2014).
- [17] D. A. Kislov and M. G. Kucherenko, *Opt. Spectrosc. (English Transl. Opt. i Spektrosk.)* **117**, 784 (2014).
- [18] A. S. Kadochkin, I. I. Shishkin, A. S. Shalin, and P. Ginzburg, *Laser Photonics Rev.* **12**, 1800042 (2018).
- [19] V. Kozlov, D. Filonov, Y. Yankelevich, and P. Ginzburg, *J. Quant. Spectrosc. Radiat. Transf.* **190**, 7 (2017).
- [20] D. Filonov, B. Z. Steinberg, and P. Ginzburg, *Phys. Rev. B* **95**, 235139 (2017).
- [21] I. Shishkin, T. Alon, R. Dagan, and P. Ginzburg, *MRS Adv.* **2**, 2391 (2017).
- [22] D. Ross, M. Gaitan, and L. E. Locascio, *Anal. Chem.* **73**, 4117 (2001).
- [23] S. V. Gaponenko, P.-M. Adam, D. V. Guzatov, and A. O. Muravitskaya, *Sci. Rep.* **9**, 7138 (2019).
- [24] D. V. Guzatov, S. V. Vaschenko, V. V. Stankevich, A. Y. Lunevich, Y. F. Glukhov, and S. V. Gaponenko, *J. Phys. Chem. C* **116**, 10723 (2012).
- [25] P. Ginzburg, *Ann. Phys.* **528**, 571 (2016).
- [26] A. N. Poddubny, P. Ginzburg, P. A. Belov, A. V. Zayats, and Y. S. Kivshar, *Phys. Rev. A At. Mol. Opt. Phys.* **86**, 033826 (2012).
- [27] P. B. Johnson and R. W. Christy, *Phys. Rev. B* **6**, 4370 (1972).
- [28] P. Ginzburg, D. J. Roth, M. E. Nasir, P. Segovia, A. V. Krasavin, J. Levitt, L. M. Hirvonen, B. Wells, K. Suhling, D. Richards, V. A. Podolskiy, and A. V. Zayats, *Light Sci. Appl.* **6**, e16273 (2017).
- [29] Y. Chenyakin, A. D. Ullmann, E. Evoy, L. Renbaum-Wolff, S. Kamal, and K. A. Bertram, *Atmos. Chem. Phys.* **17**, 2423 (2017).
- [30] A. Penzkofer, A. Tyagi, E. Slyusareva, and A. Szyzkh, *Chem. Phys.* **378**, 58 (2010).
- [31] X. Meng, S. Liu, J. I. Dadap, and R. M. Osgood, *Phys. Rev. Mater.* **1**, 015202 (2017).
- [32] C. Bradac, W. Gao, J. Forneris, M. E. Trusheim, and I. Aharonovich, *Nat. Commun.* **10**, 5625 (2019).
- [33] V. S. Krivobok, S. N. Nikolaev, E. E. Onishchenko, A. A. Pruchkina, S. I. Chentsov, A. Y. Klovov, S. V. Sorokin, and I. V. Sedova, *J. Lumin.* **213**, 273 (2019).
- [34] G. D. Brinatti Vazquez, O. E. Martínez, and J. Martín Cabaleiro, *Appl. Opt.* **58**, 5556 (2019).
- [35] J. Wu, T. Y. Kwok, X. Li, W. Cao, Y. Wang, J. Huang, Y. Hong, D. Zhang, and W. Wen, *Sci. Rep.* **3**, 3321 (2013).
- [36] R. G. Geitenbeek, J. C. Vollenbroek, H. M. H. Weijgertze, C. B. M. Tregouet, A. E. Nieuwelink, C. L. Kennedy, B. M. Weckhuysen, D. Lohse, A. Van Blaaderen, A. Van Den Berg, M. Odijk, and A. Meijerink, *Lab Chip* **19**, 1236 (2019).
- [37] I. Wegrzyn, A. Ainla, G. D. M. Jeffries, and A. Jesorka, *Sensors (Switzerland)* **13**, 4289 (2013).

- [38] C. T. Culbertson, S. C. Jacobson, and J. Michael Ramsey, *Talanta* **56**, 365 (2002).
- [39] C. Peters, L. Wolff, S. Haase, J. Thien, T. Brands, H. J. Koß, and A. Bardow, *Lab Chip* **17**, 2768 (2017).
- [40] A. M. Chaudhari, T. M. Woudenberg, M. Albin, and K. E. Goodson, *J. Microelectromech. Syst.* **7**, 345 (1998).
- [41] A. Iles, R. Fortt, and A. J. de Mello, *Lab Chip* **5**, 540 (2005).
- [42] E. M. Chan, A. P. Alivisatos, and R. A. Mathies, *J. Am. Chem. Soc.* **127**, 13854 (2005).
- [43] J. Brange and L. Langkjær, in *Pharmaceutical Biotechnology* (Springer, Berlin, 1993), pp. 315–350.
- [44] A. Vennepureddy, P. Singh, R. Rastogi, J. Atallah, and T. Terjanian, *J. Oncol. Pharm. Pract.* **23**, 525 (2017).
- [45] V. de Zwart, S. C. Gouw, and F. A. Meyer-Wentrup, *Cochrane Database Syst. Rev.* **1**, CD011181 (2016).
- [46] L. L. Josephson, E. M. Furst, and W. J. Galush, *J. Rheol. (N.Y.)* **60**, 531 (2016).
- [47] J. A. Pathak, R. R. Sologuren, and R. Narwal, *Biophys. J.* **104**, 913 (2013).
- [48] H. Markovich, I. I. Shishkin, N. Hendler, and P. Ginzburg, *Nano Lett.* **18**, 5024 (2018).

**10-PAPER:** Superscattering emerging from the physics of bound states in the continuum

Canós Valero A., Shamkhi H.K., Kupriianov A.S., Weiss T., Pavlov A.A., Redka D., Bobrovs V., Kivshar Y., Shalin A.S., “Superscattering emerging from the physics of bound states in the continuum”, (2023) *Nature Communications*, 14 (1), art. no. 4689, DOI: [10.1038/s41467-023-40382-y](https://doi.org/10.1038/s41467-023-40382-y)



# Superscattering emerging from the physics of bound states in the continuum

Received: 10 January 2022

Accepted: 25 July 2023

Published online: 04 August 2023

Check for updates

Adrià Canós Valero<sup>1,2</sup> , Hadi K. Shamkhi<sup>2,3</sup>, Anton S. Kupriianov<sup>4</sup>,  
Thomas Weiss<sup>1</sup>, Alexander A. Pavlov<sup>5</sup>, Dmitrii Redka<sup>6</sup>,  
Vjaceslavs Bobrovs<sup>7</sup>, Yuri Kivshar<sup>8</sup> & Alexander S. Shalin<sup>9,10</sup>

We study the Mie-like scattering from an open subwavelength resonator made of a high-index dielectric material, when its parameters are tuned to the regime of interfering resonances. We uncover a novel mechanism of superscattering, closely linked to strong coupling of the resonant modes and described by the physics of bound states in the continuum (BICs). We demonstrate that the enhanced scattering occurs due to constructive interference described by the Friedrich-Wintgen mechanism of interfering resonances, allowing to push the scattering cross section of a multipole resonance beyond the currently established limit. We develop a general non-Hermitian model to describe interfering resonances of the quasi-normal modes, and study subwavelength dielectric nonspherical resonators exhibiting avoided crossing resonances associated with quasi-BIC states. We confirm our theoretical findings by a scattering experiment conducted in the microwave frequency range. Our results reveal a new strategy to boost scattering from non-Hermitian systems, suggesting important implications for metadevices.

Non-Hermitian physics offers a wide range of unusual phenomena not accessible for purely Hermitian systems<sup>1</sup>. In recent years, there has been tremendous progress in the implementations of non-Hermitian platforms in optics, with discoveries of many intriguing effects that may occur in lossy or gain-compensated optical structures. Being motivated by the studies of parity-time ( $\mathcal{PT}$ ) -symmetric systems, a novel field of non-Hermitian photonics emerged<sup>2</sup>, taking advantage of new degrees of freedom offered by complex energy landscapes<sup>3–6</sup>. The advancements are particularly exciting for subwavelength photonics, allowing to study of unconventional regimes of light-matter interaction such as exceptional points<sup>7–9</sup> and dark states<sup>10–11</sup>.

Importantly, the eigenvalues of an isolated optical resonator with uncompensated radiative losses are always complex.

Nevertheless, they can be controlled by engineering the resonator parameters to achieve the regime of bound states in the continuum (BIC) with ultrahigh quality factors ( $Q$ -factors) and strong energy localization<sup>12</sup>. This regime arises due to the destructive interference within the modes of the same radiation channel, as a consequence of the Friedrich-Wintgen (FW) mechanism of interfering resonances<sup>13</sup>. While a bimodal system coupled to one channel of the continuum is well understood, the subtleties underlying multiple-channel interactions are yet to be exploited in photonics. Destructive interference leads to a quasi-BIC regime and the suppression of radiation in one channel. Here, we pose the question, of whether constructive interference of a quasi-BIC state and a low- $Q$  mode in a multi-channel structure can boost radiation beyond the limit for an isotropic

<sup>1</sup>Institute of Physics, University of Graz, and NAWI Graz, 8010 Graz, Austria. <sup>2</sup>ITMO University, St. Petersburg 197101, Russia. <sup>3</sup>Institute of Materials Research and Engineering, Agency for Science, Technology and Research, 2 Fusionopolis Way, Innovis #08-03, Singapore 138634, Republic of Singapore. <sup>4</sup>College of Physics, Jilin University, Changchun 130012, China. <sup>5</sup>Institute of Nanotechnology of Microelectronics, Moscow 119991, Russia. <sup>6</sup>Electrotechnical University LETI, St. Petersburg 197376, Russia. <sup>7</sup>Riga Technical University, Institute of Telecommunications, Riga 1048, Latvia. <sup>8</sup>Nonlinear Physics Centre, Research School of Physics, Australian National University, Canberra, ACT 2601, Australia. <sup>9</sup>Center for Photonics and 2D Materials, Moscow Institute of Physics and Technology, Dolgoprudny 141700, Russia. <sup>10</sup>MSU, Faculty of Physics, Moscow 119991, Russia. e-mail: [adria.canos5@gmail.com](mailto:adria.canos5@gmail.com); [yuri.kivshar@anu.edu.au](mailto:yuri.kivshar@anu.edu.au); [alexandesh@gmail.com](mailto:alexandesh@gmail.com)

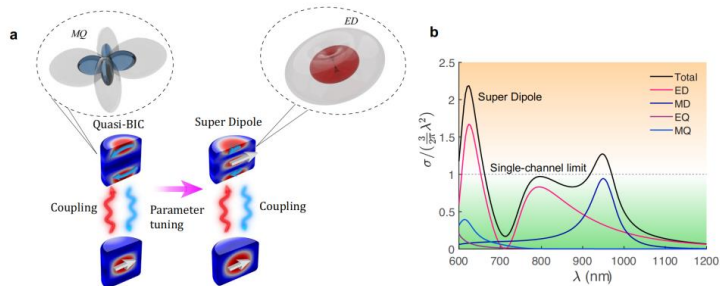


**Fig. 1 | Superscattering from the physics of BICs.** **a** Concept of BIC-inspired superscattering in an isolated resonator. Strong coupling of two modes reshapes both their near fields and scattering patterns as a function of a tuning parameter. The interfering resonances lead to a quasi-BIC state (destructive interference) and induce power redistribution between multipolar scattering channels leading to super-dipole radiation (constructive interference). **b** Super-dipole resonance

arising in the scattering cross-section of a dielectric cylinder with refractive index  $n_p \sim 3.8$ , radius 130 nm, and height 180 nm. The scattering cross-section of the electric dipole channel significantly exceeds the single-channel limit. This is in contrast with conventional superscattering, where several multipole resonances need to be overlapped.

scatterer, realizing superscattering<sup>44,45</sup>. Until now, superscattering was known to originate only from a degeneracy of multipolar resonances<sup>44–22</sup>, which, when spectrally overlapped, exceeded the single-channel cross-section.

In this work, we demonstrate that strong coupling between two modes can lead to a previously unknown regime of superscattering in subwavelength resonators, in addition to the quasi-BIC states (see Fig. 1a). We reveal that mode coupling induces power redistribution between two scattering channels, allowing to overcome the single-channel scattering limit and control not only the  $Q$ -factor, but also enhance the power scattered by a multipole, (e.g., the electric dipole) beyond the limit, as demonstrated in Fig. 1b. Unlike the recent proposal in<sup>23</sup>, there is no need to introduce gain in the resonator. We first formulate a general phenomenological model and later employ rigorous perturbation theory for quasi-normal modes (QNMs) of non-Hermitian resonators<sup>24,25</sup> to design several examples of subwavelength cavities with broken spherical symmetry.

## Results

### Enhancing scattering by finite objects

We start our analysis by overviewing how superscattering arises through the mechanism originally proposed in<sup>6</sup>. Consider a particle possessing either spherical symmetry, or dimensions much smaller than the incident wavelength, illuminated along the  $z$  axis by an incident plane wave. In all that follows, we consider its center of mass is taken as the origin of the coordinate system.

In or outside the smallest spherical region surrounding such particle, the electromagnetic fields can be expressed as a combination of multipolar waves, i.e.,  $\mathbf{E}(r) = \sum_{\tau} c_{\tau} \mathbf{W}_{\tau}(r)$ . The triplet  $(\tau) \equiv (l, m, p)$  represents a scattering ‘channel’, through which the particle can exchange power with the environment. The first number indicates the total angular momentum, so that  $l=1$  is a dipole,  $l=2$  a quadrupole, and so forth. The second is the absolute value of the projection of angular momentum to the  $z$ -axis, while  $p$  denotes the magnetic or electric character of the multipole ( $p=1$  for electric or  $p=2$  magnetic). Each multipolar wave can be decomposed further into an outgoing (–) and an incoming (+) wave, so that the field in one channel is alternatively expressed as  $\mathbf{E}_{\tau}(r) = s_{\tau}^{+} \mathbf{W}_{\tau}^{+}(r) + s_{\tau}^{-} \mathbf{W}_{\tau}^{-}(r)$ .  $s_{\tau}^{\pm}$  are the incoming (outgoing) coefficients in channel  $\tau$ . With a suitable normalization,  $|s_{\tau}^{\pm}|^2$  corresponds to the power carried towards or away from the particle in every multipole channel.

The effect of the scatterer is completely described by the ‘reflection’ coefficients  $R_{\tau} \equiv s_{\tau}^{-} / s_{\tau}^{+}$ . Furthermore, energy conservation dictates  $|R_{\tau}| \leq 1$  for passive scatterers. The scattering cross section for each channel is then given by

$$\sigma_{\tau} = \frac{2l+1}{8\pi} \lambda^2 |1 - R_{\tau}|^2 \quad (1)$$

The limit is attained for  $R_{\tau} = -1$ , and yields  $\sigma_{\tau, \text{Max}} = (2l+1)\lambda^2 / 2\pi$ . For example, in the case of a dipole (electric or magnetic), the limit is  $\sigma_{\text{Max}} = 3\lambda^2 / 2\pi$ . In a scatterer with negligible absorption losses, this limit can be achieved at a multipolar resonance<sup>6</sup>. To each resonance, one can associate an underlying quasinormal mode (QNM), with a complex eigenfrequency  $\tilde{\omega}_m = \omega_m - i\gamma_m$ . For small  $\gamma_m$ , a multipolar resonance appears in the real frequency spectrum, centered around  $\omega_m$  and having a linewidth of  $2\gamma_m$ .

To design a superscatterer, the resonant frequencies of several QNMs associated to different multipolar channels must be brought together by a smart design of the particle geometry, so that the total scattering cross section, given by the sum of their contributions, exceeds the limit. This is typically done so by adding material layers of different thickness to a sphere or an elongated rod<sup>14,21,26</sup>. The superscattering regime was very recently experimentally verified for the first time<sup>14</sup>.

What happens in the absence of spherical symmetry? Intriguingly, it was shown that larger bounds on total extinction could be attained for lossy nonspherical shapes<sup>27</sup>, even for deeply subwavelength plasmonic particles. The enhancement, however, was mostly delivered by absorption from such particles, and still remained significantly below the single-channel limit (for a detailed comparison, we refer the reader to the Supplementary Information S12 and Figure S6). Finite plasmonic nanorods were also numerically investigated<sup>28</sup>, exhibiting enhanced cross-sections for some well-chosen geometrical parameters (Figure S6). Despite these works, focused in plasmonic cavities with large absorption cross-sections, there appeared to be no qualitative differences between a spherical shape and the general case.

In fact, scattering by nonspherical objects, even with sub-wavelength dimensions, is described by a matrix  $R$  with potentially nonzero off-diagonal components of the form  $R_{\tau\tau'} \equiv s_{\tau}^{-} / s_{\tau'}^{+}$ . They relate the incoming wave in channel  $\tau'$ , to the outgoing wave in channel  $\tau$ . This has an important consequence: since the limit in Eq. (1) relies on

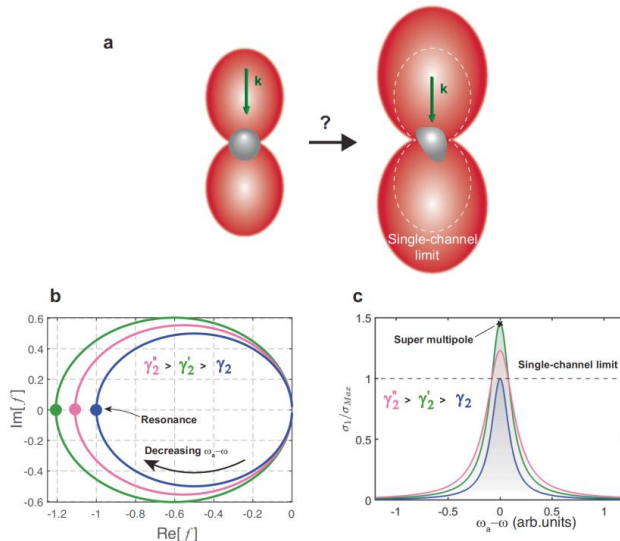


**Fig. 2 | Boosting scattering of a multipolar resonance.** **a** Artistic picture illustrating the question at hand: can symmetry break enhance the scattering cross-section of a multipole beyond the limit? Red lobes represent the scattering pattern characteristic of an electric or magnetic dipole. On the left-hand side, a spherical scatterer is illuminated by a plane wave with momentum  $k$ . On the right-hand side, a nonspherical scatterer displays a similar dipolar scattering pattern, but significantly enhanced. **b**, **c** General model of a single QNM  $|a\rangle$  compatible with two scattering channels  $\tau = 1, 2$ . **b** Shows the evolution of the real and imaginary parts of  $f(\omega)$ , whose modulus determines the scattering enhancement (see details in text), as a

function of the detuning  $\omega_a - \omega$ , for fixed  $\gamma_1 = 1$  (radiation rate to channel 1 in normalized units) and increasing  $\gamma_2$  (radiation rate to channel 2). Dark blue:  $\gamma_2 = 0$ , green:  $\gamma_2 = 0.017$ , pink:  $\gamma_2 = 0.06$ . Resonance takes place when  $\omega_a - \omega = 0$ . A maximum of  $f(\omega)$  occurs for a critical value of radiation rate to the second channel (green curve), and then progressively decreases. **c** Scattering cross section to channel 1 for the same cases studied in **b**, normalized by the single-channel limit, denoted as  $\sigma_{1\text{max}}$ . When  $\gamma_2 > 0.017$ , the scattering cross section of the channel significantly exceeds the limit, leading to a ‘super’ multipole resonance.

the  $R$ -matrix being diagonal, (i.e., there is no power exchange between the multipole channels), the latter, in principle, ceases to be valid.

We realize that, in general, depending on the symmetry of the object, the scattering cross section of one multipole can receive contributions from other multipoles. Intriguingly, this suggests that the strength of a multipole could, in theory, be boosted beyond the conventionally accepted limit, as depicted in Fig. 2a. In stark contrast with conventional superscattering, by being able to enhance the cross section of a single multipole, we could not only enhance overall scattering, but also manipulate the radiation pattern, for instance making it larger without significantly altering its shape, as illustrated in Fig. 2a. So far, this effect has proven to be elusive, and has not been reported in the literature.

### Super-multipole resonances

To verify this possibility, we assume only two scattering channels (multipoles)  $\tau = 1, 2$  are important, and, after some assumptions we derive an ad-hoc expression for the scattering cross section of channel 1 (derivation provided in the Supplementary Information S3):

$$\sigma_1/\sigma_{1\text{max}} = \frac{1}{4} |1 - R_{11} - R_{12}|^2 \equiv |f(\omega)|^2 \quad (2)$$

The function  $f(\omega)$  can be complex, and its modulus will determine the ultimate limit for scattering in this case. Namely, if  $|f(\omega)| > 1$ , the

single-channel limit could be exceeded, since  $\sigma_1$  would then be larger than  $\sigma_{1\text{max}}$ . To derive an analytical expression for it, we investigate a hypothetical structure supporting a single QNM  $|a\rangle$  which, due to an a priori unknown mechanism, is coupled to the two scattering channels. The radiation rate of is the sum of radiation rates to the two channels, i.e.,  $\gamma_a = \gamma_1 + \gamma_2$ . According to temporal coupled mode theory<sup>25,28</sup> (TCMT), we get  $f(\omega) = i \frac{\sqrt{\gamma_1 \gamma_2} + \gamma_1}{\omega_a - \omega - i(\gamma_1 + \gamma_2)}$  (refer to Supplementary Information S4 for details).

What happens when the radiation rate to the second channel increases? Fixing  $\gamma_1 = 1$  (in normalized units), we plot  $f(\omega)$  as a function of detuning from resonance  $\omega_a - \omega$ , for different values of  $\gamma_2$  (Fig. 2b). In all cases, the maximum occurs at resonance (zero detuning). If  $\gamma_2 = 0$ ,  $|f(\omega)| = 1$ , since the QNM can only radiate to one channel. This is the conventional case. Strikingly, there exists a critical  $\gamma_2$  for which  $|f(\omega)|$  reaches a maximum exceeding 1 (green curve in Fig. 2b). Interestingly, for radiation rates larger than the critical (pink curve in Fig. 2b) we observe a progressive degradation of the enhancement, confirming that there indeed exists an optimal, small  $\gamma_2$  where the cross section is maximized beyond the limit.

To provide more insight, the scattering cross section of channel 1 is displayed in Fig. 2c, for the different cases shown in Fig. 2b. It can be clearly seen that the green spectrum exceeds the limit by almost 1.5 times. It should be noted that this is the case despite a clear broadening of the resonance due to the additional losses. Thus, contrary to what is

widely accepted, radiation losses can contribute to an enhancement of the channel cross section, instead of degrading it. We refer to this novel regime as a ‘super-multipole’, in contrast with conventional superscattering, where several QNMs need to be overlapped in the spectrum.

With this first model, we have predicted the existence of super-multipole resonances capable of enhancing the cross section of one channel beyond the limit. Symmetry breaking is a necessary but not sufficient condition for their formation. In particular, a careful control of the radiation rate to each of the multipoles involved is required for their realization. It is not evident how this control can be achieved in practice.

In the following section, we show that, in the vicinity of a quasi-BIC, symmetry breaking has a strong impact on the scattering cross section. QNMs belonging to different multipoles can couple strongly in the near field, leading to an avoided crossing and acquiring a mixed multipolar character, which allows to easily modify their radiation rates. Then, defying conventional intuition, a single super-multipole resonance can drive the scattering cross section of a multipole beyond the single-channel limit (as well as the total scattering cross section). Super-multipoles exist as a natural counterpart of a quasi-BIC, where the contribution of a QNM to one or more scattering channels is forbidden.

### Super-multipoles emerging from quasi-BICs

We now extend our TCMT model above to the case of a structure supporting two QNMs  $|a\rangle, |b\rangle$ , each compatible, respectively, with a single scattering channel  $\tau = 1, 2$ . These can be, for instance, two multipolar QNMs of a suitably designed spherical scatterer (e.g., the electric dipole and magnetic quadrupole modes). In a real system, there might also be contributions from non-resonant QNMs forming a ‘background’, as shown later. These are, however, neglected in our preliminary analysis. The model is used solely for illustration purposes. Later, the results are verified with rigorous cavity perturbation theory in a realistic nanoresonator, as well as with microwave experiments.

After breaking the spherical symmetry in some fashion, the two QNMs can couple in the near field, leading to an ‘effective’ Hamiltonian of the form (refer to the Supplementary Information S2):

$$\mathcal{H}_0(\zeta) = \begin{pmatrix} \tilde{\omega}_a(\zeta) & \kappa(\zeta) \\ \kappa(\zeta) & \tilde{\omega}_b(\zeta) \end{pmatrix} \quad (3)$$

Diagonalizing  $\mathcal{H}_0(\zeta)$  results in two new hybrid QNMs  $|u\rangle, |d\rangle$  that are a combination of the original ones. Thus, the new modes have a mixed multipolar nature. Accidentally, (or due to symmetry), the coupling coefficient can vanish, and the hybrid QNMs become  $|u\rangle = |a\rangle$  and  $|d\rangle = |b\rangle$ . We consider that, in general, the uncoupled eigenfrequencies and the coupling coefficient (here assumed to be real), are a function of a geometrical parameter  $\zeta$ . In our first example in the next section,  $\zeta$  will be related to the ellipticity of the particle.

In general, Eq. (3) does not only describe the hybridization of the QNMs of a sphere, but that of any particle without spherical symmetry, such as a finite cylinder, as shown later. If we assume that channel 1 is a low order multipole (for instance a dipole), while channel 2 is a higher order one, (for instance a quadrupole), radiative losses in channel 2 are significantly lower. Then, for  $\kappa = 0$ , QNM  $|b\rangle$  corresponds to a quasi-BIC with high  $Q$ -factor. This is because  $|b\rangle$  is, by assumption in our model, completely unmatched from the lowest order multipoles<sup>22,29</sup>.

Assuming time-harmonic dependence of all fields in the form  $e^{-i\omega t}$ , we can derive an expression for the  $R$ -matrix<sup>28,30</sup>, (in the remainder of this work, unless written explicitly, we omit the  $\zeta$  dependence for the sake of brevity):

$$\mathcal{R}(\omega) = \mathbb{I}_2 + 2T(\omega) \quad (4)$$

$$T(\omega) = iD[\mathcal{H}_0(\zeta) - \mathbb{I}_2\omega]^{-1}D^T \quad (5)$$

where  $\mathbb{I}_2$  is the  $2 \times 2$  identity matrix, and  $D$  is a matrix connecting the QNMs to the multipole fields<sup>31</sup>. In the absence of any scatterer,  $\mathbb{I}_2$  guarantees the incoming waves are perfectly reflected to the outgoing ones.

In this first scenario,  $D = \text{diag}(d_1, d_2)$ . This ensures that the original QNMs are matched to different multipolar channels. In particular,  $|a\rangle$  is matched only with multipole 1, and  $|b\rangle$  with 2. The radiative losses of each uncoupled mode are given by  $\gamma_{a,b} = d_{1,2}^2$ . Emulating a realistic situation (as shown in the next section), we consider channel 1 corresponds to a dipole (electric or magnetic), and channel 2 to a quadrupole (magnetic or electric). Since dipolar QNMs leak strongly to the far field,  $d_1 \gg d_2$ , hence it follows that  $\gamma_a \gg \gamma_b$ . Due to this, as mentioned earlier, when  $\kappa = 0$ , QNM  $|d\rangle = |b\rangle$  and displays a peak in its  $Q$ -factor, which corresponds to a quasi-BIC.

Based on the model [Eq. (4)], we derive an expression for the scattering cross section of the dipole channel (channel 1), normalized by its conventional limit,  $\sigma_{Max} = 3\lambda^2/2\pi$ :

$$\sigma_1/\sigma_{Max} = |f(\omega)|^2 \quad (6)$$

$$f(\omega) = \frac{id_1^2(\tilde{\omega}_a - \tilde{\omega}_0)}{(\tilde{\omega}_a - \tilde{\omega}_d)(\omega - \tilde{\omega}_a)} - \frac{id_2^2(\tilde{\omega}_d - \tilde{\omega}_0)}{(\tilde{\omega}_d - \tilde{\omega}_a)(\omega - \tilde{\omega}_d)} \quad (7)$$

For details, see the Supplementary Information S4. Each of the two terms in Eq. (7) accounts for the contribution of a hybrid QNM to the channel cross section. On the other hand,  $\tilde{\omega}_0 = \tilde{\omega}_b - \kappa d_2/d_1$  is a zero of the cross section. Near the resonance frequencies of the hybrid QNMs, only one of the terms in Eq. (7) is dominant. The mechanism through which the single-channel limit can be exceeded is illustrated in Fig. 3.

In the absence of coupling ( $\kappa = 0$ ),  $\tilde{\omega}_a = \tilde{\omega}_a$ ,  $\tilde{\omega}_d = \tilde{\omega}_b$  and  $\tilde{\omega}_0 = \tilde{\omega}_b$ , so that the contribution of QNM  $|d\rangle$  in Eq. (7) vanishes, as shown in Fig. 3a. We provide a scheme of this situation in Fig. 3b. The pole of  $f(\omega)$  associated with  $|d\rangle$  annihilates with the zero, cancelling its contribution to the cross section. In other words, QNM  $|d\rangle$  leaks only through the quadrupole channel and exhibits a high  $Q$ -factor (a quasi-BIC). Then, the maxima in the cross section for the dipole channel occurs only at  $\text{Re}(\tilde{\omega}_a) = \omega_a$  and is bounded to  $\sigma_{Max}$ , as in the usual case.

Introducing coupling ( $\kappa \neq 0$ ), results in several interesting effects, as shown in Fig. 3c, d. Firstly, in Fig. 3d, the pole associated with  $|d\rangle$  and the zero of  $f(\omega)$  are shifted away from one another. Thus, both the zero and the new pole contribute to the dipole channel (Fig. 3c). The dipole channel is now ‘open’ for QNM  $|d\rangle$ . Consequently, its radiative losses are increased (i.e., lower  $Q$ -factor), and the pole is pushed deeper into the complex plane (see Fig. 3d). Remarkably, we notice that at  $\text{Re}(\tilde{\omega}_d)$  or  $\text{Re}(\tilde{\omega}_d)$ , the maxima in the cross section of the channel is no longer bounded to  $\sigma_{Max}$  in Eq. (6). This is also true if one of the terms in Eq. (7) is dominant. Thus, by inducing coupling between two multipole resonances, we can create a hybrid mode that is able to enhance scattering by itself beyond the established limit.

Such peculiar behavior can be observed in Fig. 3e, where we plotted the normalized dipole cross section as a function of the tuning parameter  $\zeta$ . The functional form of the different elements in  $\mathcal{H}_0(\zeta)$  is given in the caption of Fig. 3. They are justified by first order QNM perturbation theory<sup>25,32,33</sup> (see Supplementary Information S2). In particular,  $\kappa(\zeta) = \alpha_3\zeta$ , where  $\alpha_3$  is a constant. Due to the nonzero coupling for any  $\zeta \neq 0$ , the hybrid QNMs ‘avoid’ the crossing due to strong interaction between the original modes (i.e., strong coupling). This is a particular example of the Friedrich-Wintgen mechanism<sup>33</sup>, which has been shown to lead to true BICs in extended structures<sup>34</sup>, or extremely high- $Q$  quasi-BICs in isolated cavities<sup>22,35,35</sup>. For the case under

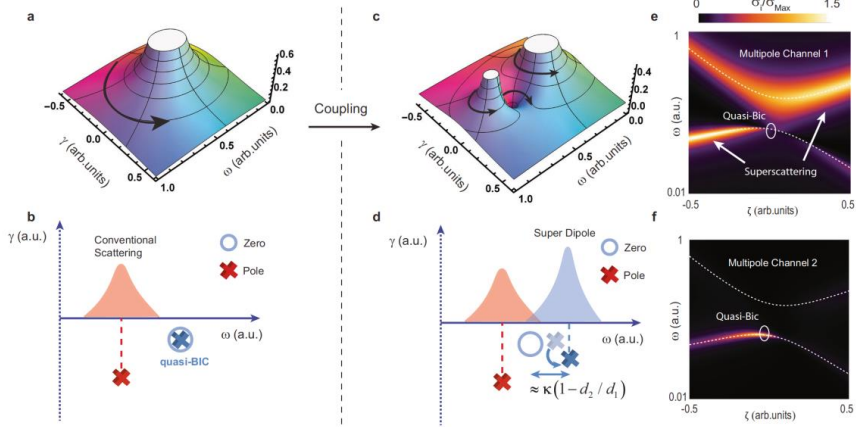


**Fig. 3 | Toy model describing the physics of the new superscattering regime.** **a** Complex plot of Eq. (7) for  $\kappa = 0$  (spherical symmetry, no coupling). Clockwise black arrows denote zeros of the function, while counterclockwise ones denote poles (resonances). In this first case, only QNM  $|a\rangle = |a\rangle$  contributes since the zero induced by QNM  $|d\rangle$  annihilates with the zero. **b** Schematic illustration of the zero-pole annihilation, corresponding to a quasi-BIC, and conventional multipole scattering. **c, d** Same as in **a, b**, but for the case with  $\kappa \neq 0$ . Now, the coupling separates in the complex plane the pole associated with  $|a\rangle$  and the zero. In exchange, the QNM gains additional losses, and is allowed to contribute to scattering, which is no longer bounded by the limit [blue-shaded area in **d**]. **e–f** Scattering cross section for

the dipole channel 1, and the quadrupole channel 2, respectively. All the values have been normalized by the limit of the dipole cross section  $\sigma_{\text{Max}} = 3\lambda^2/2\pi$ . For illustration purposes, we consider  $\omega_0(\zeta) = \omega_0^{(0)}/(1 + a_1\zeta)$ ,  $\omega_0(\zeta) = \omega_0^{(0)}/(1 + a_2\zeta)$ ,  $\kappa(\zeta) = a_3$ , with  $\omega_0^{(0)} = 0.6$ ,  $\omega_0^{(0)} = 0.4$ ,  $a_1 = 0.4$ ,  $a_2 = 0.38$ ,  $a_3 = 0.5$ . White dashed lines indicate the path followed by the hybrid eigenfrequencies  $\tilde{\omega}_{a,d}$ . At the quasi-BIC, scattering to the dipole channel by QNM  $|d\rangle$  is completely suppressed. Once coupling ‘opens’ the channel to  $|d\rangle$ , the scattering energy is transferred from the quadrupole channel to the dipole channel, exceeding its limit and reaching the ‘super dipole’ regime.

consideration, the quasi-BIC appears in the lower branch at  $\zeta = 0$ , since  $\kappa(0) = 0$  and the contribution of QNM  $|d\rangle$  to the dipole vanishes, while a resonance arises in the quadrupole channel (Fig. 3f). Only the lossy QNM  $|a\rangle$  is matched to the dipole. This corresponds to the usual scenario, where the dipole cross section cannot exceed the traditional limit.

For any  $\zeta \neq 0$ , there is coupling between the QNMs, and the lower branch can scatter as a dipole (Fig. 3e), which, from the mechanism discussed above, can largely exceed the limit in a sphere. We therefore refer to this unusual resonance as a ‘super dipole’. We bear in mind that, due to the mixed multipolar nature of the resonance, there is a small contribution to the quadrupole channel. We also remark that QNM  $|a\rangle$  can display similar features for positive  $\zeta$ , as shown in Fig. 3e.

Summarizing, we have derived a simple theory that allows us to describe the Friedrich-Wintgen mechanism leading to quasi-BICs in isolated cavities. We have demonstrated the occurrence of yet another surprising effect, namely, the possibility to create a resonance capable of enhancing scattering beyond the accepted limit in a subwavelength object, reaching the superscattering regime.

We stress again that our mechanism is in stark contrast with the conventional way to achieve superscattering. Typically, several orthogonal resonances (several QNMs matched to different multipole channels) must be overlapped at the same spectral position. Instead, here we exploit the Friedrich-Wintgen mechanism to ‘open’ the dipole channel to a quasi-BIC, forming a super dipole mode. So far, however, our predictions remain purely theoretical. In what follows, we employ multipolar theory and group-theoretical arguments to design two subwavelength scatterers displaying super dipole modes. We then

verify our results in the microwave range, confirming their existence for the first time.

### Subwavelength nanoresonators

We consider a Si nanosphere in air, illuminated with a normally incident, linearly polarized plane wave, with radius 100 nm. In the visible range, it supports two QNMs matched to the electric dipole (ED) and magnetic quadrupole (MQ) channels, respectively. Their electric field distributions are shown in the lower panel of Fig. 4c. We use the same notation as in the previous section, and label them as  $|a\rangle, |b\rangle$ . The far-field projections of the QNMs correspond to an  $x$ -polarized ED ( $p_x$ ) and the  $yz$  component of the MQ moment ( $M_{yz}$ ). The reason for our choice of QNMs will become clear in the following. Note that the chosen scatterer is deeply subwavelength, with the radius being at least five times smaller than the incident wavelength.

In order to couple both QNMs, it is necessary to break the spherical symmetry in some fashion. A simple way to do so is by reducing the rotational symmetry in the plane parallel to the direction of propagation, (refer to schematic insets in Fig. 4b). Formally, the point group of the resonator changes from  $O(3)$  (spherical symmetry) to  $D_h$  (cylindrical symmetry). Then, multipolar modes with the same parity (as in the case for the chosen QNMs), can couple<sup>36</sup>.

As depicted in Fig. 4b, we perform a controlled symmetry breaking by changing the ratio between the two orthogonal axes of the resonator  $r_1, r_2$ . In this case  $\zeta \equiv 1 - r_2/r_1$ . Cavity perturbation theory<sup>35</sup> (see Sec. S1 of the Supplementary Information), predicts the formation of hybrid QNMs, whose far fields are now a combination of  $p_x$  and  $M_{yz}$ . This results in an avoided crossing in the eigenfrequency spectrum (Fig. 4a).



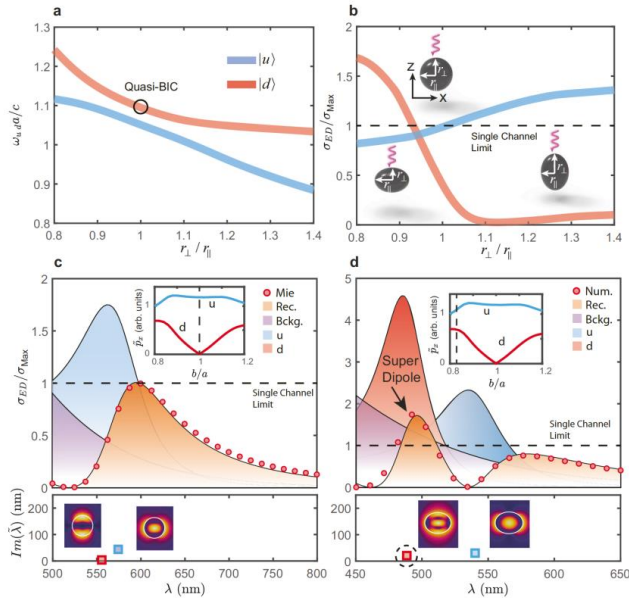


**Fig. 4 | Super-ED resonance in a dielectric nanoellipsoid. a** Evolution of the resonant frequencies of the ED and MQ modes of a silicon nanosphere (100 nm radius), when breaking the rotational symmetry along one of its axis, [generating an ellipsoid with semiaxis  $r_{\perp}, r_{\parallel}$  indicated in the insets of **b**]. An avoided crossing, the hallmark of strong coupling, can be clearly observed. **b** Scattering cross-section of the ED channel at the two resonance maxima as a function of ellipticity, under normally incident, linearly polarized plane wave illumination, with momentum oriented along the axis with broken rotational symmetry. For  $r_{\perp}/r_{\parallel}=1$  (a sphere), the cross-section is bounded to 1, and QNM  $|d\rangle$  features a quasi-BIC. For an oblate ellipsoid (left inset), QNM  $|d\rangle$  becomes a super-ED, and vice versa for QNM  $|u\rangle$  (right inset). **c, d** Contributions of the QNMs to the scattering cross-section of the ED channel in a sphere and a perturbed spheroid. **e** Sphere ( $r_{\perp}/r_{\parallel}=1$ ). Upper panel: ED scattering cross section obtained with conventional Mie theory and its reconstruction with QNMs (Rec.). The curves labeled *Bckg.*, *u,d* are evaluated as  $|\mathbf{p}_m|^2/I_0$

where  $m = \text{Bckg.}, u, d$  correspond to the non-resonant term<sup>52,53</sup>, the  $|u\rangle$  and  $|d\rangle$  QNMs, respectively. Inset: Normalized ED content of QNMs  $|u\rangle, |d\rangle$ , calculated as in ref. 54. They provide an estimation of the matching of a QNM to the ED channel. At the quasi-BIC there is no matching, thus  $\tilde{p}_z = 0$ . Lower panel: eigen wavelengths of  $|u\rangle, |d\rangle$ , in the complex plane, defined as  $\lambda_m = 2\pi c/\omega_m$ , and their field distributions in the  $x$ - $z$  plane ( $E_m$ , in arbitrary units). **d** Same as in **c**, but for an ellipsoid with  $r_{\perp}/r_{\parallel}=0.85$ . Note that QNM  $|d\rangle$  is now matched to the ED channel, since its ED content is nonzero (upper panel inset). Thus, it contributes to the cross section, and a super dipole appears in the spectra. The dashed circle in the lower panel indicates  $\tilde{\lambda}_y$ , which has been pulled deeper in the complex plane due to the additional radiation losses, in accordance with the mechanism described in the previous section. Due to coupling with  $|u\rangle$ , the field distribution of  $|d\rangle$  is drastically reshaped in comparison with the sphere. More details on the coupling mechanism can be found in Figure S1 of the Supplementary Information.

Now, an incoming ED or MQ wave will excite a QNM, but the latter will radiate as a combination of ED and MQ. Thus, the  $R$ -matrix is no longer diagonal, and energy can leak from one channel to another. At some critical values of  $r_{\perp}/r_{\parallel}$ , this results in the appearance of super dipoles. For instance, when the spheroid is oblate, the ED channel at  $\omega_d$  almost doubles its allowed bound (Fig. 4b), while we observe the same effect at  $\omega_u$  when the spheroid becomes prolate. Thus, depending on the sign of the deformation, we can enhance dipole scattering beyond the limit in one resonance or the other. This can also be confirmed in Figure S5 of the Supplementary Information, where the super-ED resonance is seen to exceed the single-channel limit, in contrast to the ED resonances of the perfect sphere.

We gain insight into the mechanism by evaluating the influence of each QNM to the ED scattering cross section (Fig. 4c, d). We consider three contributions: the resonant QNMs  $|u, d\rangle$  and a non-resonant background composed of modes outside the spectral range of interest. With the expressions of the multipoles given in the Supplementary

Information S4, the ED cross section is

$$\sigma_{ED} = \left| \sum_m \mathbf{p}_m \right|^2 / I_0 \quad (8)$$

$\mathbf{p}_m$  is the ED moment of the  $m$ -th QNM, and  $I_0$  is the intensity of the incident plane wave. The reconstruction is in excellent agreement with the exact analytical results of Mie theory for the sphere (Fig. 4c), and full-wave numerical simulations for the ellipsoid (Fig. 4d). It is important to note that the 'direct' cross section of each QNM, (i.e.,  $|\mathbf{p}_m|^2/I_0$ ) by itself, is not bounded by any limit. However, there is a bound in the total ED cross section, as given by Eq. (8), in the case of the sphere.

In the upper panel of Fig. 4c, the scattering cross section at the resonance of  $|u\rangle$  is clearly bounded to  $3\lambda^2/2\pi$ . However, once the sphere is deformed to an ellipsoid with  $r_{\perp}/r_{\parallel}=0.85$ ,  $|d\rangle$  inherits an ED

moment due to coupling, and manifests as a sharp peak in the ED scattering cross section (Fig. 4d, upper panel), which gives rise to a super dipole.

The lower panels in Fig. 4c, d show the eigen-wavelengths  $\tilde{\lambda}_m = 2\pi c/\tilde{\omega}_m$  of the two resonant QNMs in the complex plane, as well as their field distributions. For  $r_{\perp}/r_{\parallel} = 1$ ,  $\tilde{\lambda}_d$  is very close to the real axis. Once the spherical symmetry is broken, the additional radiative losses to the ED channel push  $\tilde{\lambda}_d$  deeper into the complex plane, as originally predicted in the previous section. In addition, the hybridization between the two QNMs leads to a drastic reshaping of the internal field distributions of QNM  $|d\rangle$  (compare the fields in the lower panels of Fig. 4c, d).

One important drawback of conventional superscattering is the fast degradation of the effect with intrinsic losses. Indeed, spectrally overlapping high order multipole resonances strongly maximizes scattering, but only when Ohmic losses are negligible. Unfortunately, even high-index dielectrics display small Ohmic losses in the visible, since their refractive index  $n_p$  features a small imaginary part  $\delta$ . In general, we will write it as  $n_p = n + i\delta$ . As we show in the Supplementary Information S5, large  $Q$ -factors imply a rapid drop of the cross section maxima, yielding a slope for small  $\delta$  of  $d\sigma/d\delta \sim -4Q/\omega_0$ , where  $\omega_0$  is the resonance frequency. Since high-order multipole resonances are associated with large  $Q$ -factors, their maximum scattering cross section decreases rapidly with increasing  $\delta$ . Herein the reason why almost a decade passed since the original proposal until the experimental demonstration of superscattering<sup>4</sup>.

As an example, consider the quasi-BIC resonance for the sphere case, displayed in Fig. 5a (indicated by the dashed line). In the lossless scenario, a strong scattering peak can be observed, reaching the maximum allowed for the MQ, i.e.,  $5\lambda^2/2\pi$ . Thus, if one is only interested in the overall scattering cross section, there is no apparent need to ‘transform it’ into a super-dipole resonance, since the quasi-BIC already provides a significant scattering enhancement beyond the dipole limit. Moreover, by adding a shell of a different material, one could spectrally overlap the quasi-BIC with, e.g., the electric dipole, to yield a large enhancement. However, there is a caveat: increasing  $\delta$  of the sphere by only 0.03 results in a drastic drop of the scattering cross section by more than 80%, even below that of a conventional dipole resonance. Therefore, in a practical scenario, high-order multipole resonances are not ideally suited to deliver the desired cross section.

Critically, super-multipole resonances, when formed through the FW mechanism, offer the ability to control the  $Q$ -factor. As discussed earlier, if the QNM is compatible with two scattering channels, the radiation losses increase, but contrarily to common belief, the total scattering cross section is not degraded, and can even increase at a super-multipole resonance. As a result, these novel states are more resilient to intrinsic losses, since the slope  $d\sigma/d\delta$  is smaller than the original uncoupled resonances. Figure 5b illustrates this with the example of the super-ED resonance. The sphere of Fig. 5a is deformed into an ellipsoid, and the quasi-BIC evolves into a super-ED with lower  $Q$ -factor (dashed line in Fig. 5b). In order to make a fair comparison, the volume of the nanocavity is kept constant. In stark contrast with the quasi-BIC, the drop in the cross section is appreciably smaller, and for  $\delta = 0.03$  it still remains above the single-channel limit.

A comparison between the maximal cross section attained by the quasi-BIC and the super-ED with increasing  $\delta$  is displayed in Fig. 5c. For small  $\delta$ , we confirm that the quasi-BIC maximum has a much steeper slope as a function of  $\delta$ , while from the start, the super-ED keeps a much higher cross section. Thus, due to their inherent robustness to losses, super-multipole resonances are better candidates to enhance the scattering cross section at the nanoscale.

### Scattering from a dielectric nanorod

The previous example illustrates nicely the formation of a super dipole from a symmetry-breaking perturbation. However, spheroids are in general not fabrication-friendly at the nanoscale. Instead, we can also reach this regime in a similar fashion in a silicon nanorod under normally incident illumination (refer to inset of Fig. 6a), since the latter also has cylindrical symmetry.

To do so, we perturb the height of the resonator by an amount of  $\Delta h$ , starting from a height of  $h_0 = 180\text{nm}$ , for which two modes radiating as ED and MQ are spectrally close. As in the spheroid, we obtain a system of two coupled resonant QNMs of relatively high  $Q$ -factor. We also remark the presence of two additional QNMs of very low  $Q$ , associated with the scattering background. The role of the background modes is disregarded in most analysis since their spectral signature is barely appreciable. However, the correct eigenfrequencies and the scattering response cannot be accurately reconstructed without taking them into account.

In Fig. 6a the  $Q$ -factors of the resonant QNMs display two peaks as a function of  $\Delta h/r$ . The most pronounced one corresponds to the

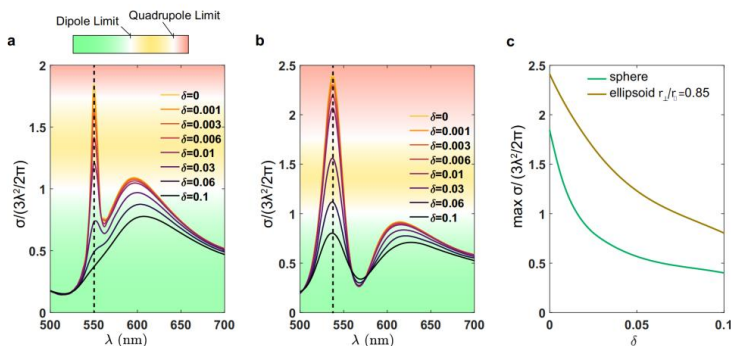


**Fig. 5** | Robustness of super-multipole resonances to Joule losses. **a** Evolution of the total scattering cross section with increasing imaginary refractive index  $\delta$  for a sphere and **b** an ellipsoid with  $r_{\perp}/r_{\parallel} = 0.85$ . The two scatterers have an equal

volume and real index  $n_p = 3.87$ . **c** Comparison of superscattering maxima [dashed lines in **a** and **b**] with increasing losses for the quasi-BIC (sphere) and the super-dipole resonance (spheroid).

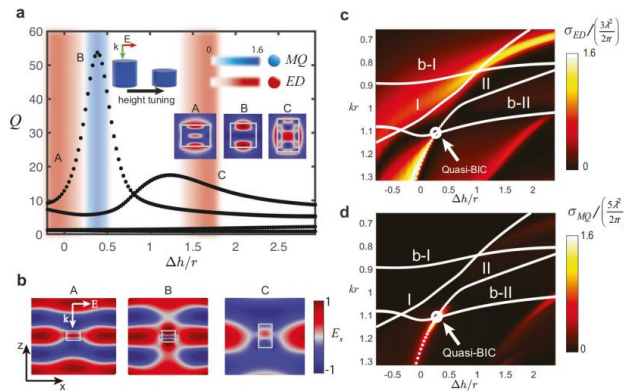


**Fig. 6 | Design of a super ED resonance in a Si nanorod.** **a** Quality factors and multipolar radiation of the QNMs as a function of a perturbation of the cylinder height  $\Delta h$ , normalized by the radius  $r = 130$  nm. The color-bars indicate the predominant multipole. The artistic inset depicts the illumination scheme and the deformation undergone by the resonator. Rightmost panels A, B, C: electric field norms in the  $x$ - $z$  plane of the QNMs at points A, B, and C. **b** Shows the  $E_x$  component of the total field at the superscattering points A-C indicated in **a**, under  $x$ -

polarized plane wave illumination (in arbitrary units). **c, d** 2D maps of the ED and MQ scattering cross-sections as a function of  $kr$  and  $\Delta h/r$ . White dotted lines indicate the paths followed by the eigenfrequencies, obtained with the perturbation theory derived in section S1 of the Supplementary Information. I, II correspond to the resonant QNMs, and b-I, b-II are the background ones. In agreement with theory, departing from the quasi-BIC condition results in hybridization and the possibility to enhance scattering of a single mode beyond the limit.

hybridization of the resonant QNMs, while the second is due to the hybridization of a resonant QNM with the low- $Q$  modal background. Superscattering in the ED channel (a super dipole) arises in the red-shaded regions. Interestingly, the super dipole appears for both resonant QNMs at relatively low  $Q$ -factors (points A and C). Near the quasi-BIC (point B), the dipole strength becomes quenched and the radiation leaks solely through the MQ channel, (blue-shaded region) with high- $Q$ . This peculiarity can also be clearly seen in the 2D maps of the ED and MQ cross-sections shown in Fig. 6c, d. In points A and C, the most appreciable signature of ED radiation is the appearance of a central electric field hotspot inside the nanorod, together with side lobes. As shown in the field insets of Fig. 6a, at the quasi-BIC, the hotspot disappears. This behavior is exactly analogous to what took place in the nanorod from Fig. 4. In all cases, the incident plane wave is significantly distorted by the scattered field (Fig. 6b).

In the super dipole regime, the ED is shown once again to almost double its established bound (Fig. 6c). Similarly, we observe a peak in the  $Q$ -factor (Fig. 6a) and an enhanced MQ scattering cross section (Fig. 6d) at the quasi-BIC. Thus, we have demonstrated the feasibility to obtain super dipoles in an experimentally accessible platform. This result reveals a new versatile strategy that can be used to engineer the  $Q$ -factor, scattering efficiency and radiation pattern of an isolated, subwavelength object in practical applications.

### Experimental demonstration

We perform a proof-of-concept experiment by measuring the extinction cross-section and scattering patterns of disk-shaped resonators in the microwave range. We reproduce the geometrical parameters of the rod in Fig. 6 using a set of ceramic resonators with fixed 4.0 mm radii, and permittivity  $\epsilon = 22$  with loss tangent 0.001. As shown in the inset of Fig. 7b, three samples are assembled from several disks to obtain the desired aspect ratios for the resonators. The measurement results of both the total extinction cross-section and electric near-field patterns are collected in Fig. 7 (for more details in the experiment, refer to section S8 of the Supplementary Information). The spectra are

normalized by the ED single-channel limit ( $\sigma_{Max} = 3\lambda^2/2\pi$ ). The experimental measurements are in a reasonable agreement with the numerical simulations, albeit the resonances appear suppressed due to material losses in the ceramic. Even with the latter, the ED cross section at the super ED is still significantly higher than the limit, as we show in Figure S3 of the Supplementary Information.

Since the resonances redshift with increasing size, the observations were performed in a broad frequency range. In the highlighted frequencies of Fig. 7a, c, we observe wide resonances with large extinction values, characteristic of the proposed super dipole modes. Indeed, the plane wave is seen to be strongly distorted in the near field (lower panels of Fig. 7). Furthermore, numerical calculations confirm that the ED exceeds its limit, even when considering losses, (refer to Fig. S3 of the Supplementary Information). The quasi-BIC appears at the expected value of  $\Delta h/r = 0.48$ , manifesting itself as a sharp peak in the spectra (Fig. 7b). The results provide experimental evidence of the control of both the  $Q$ -factor and scattered power between two resonances to achieve the superscattering regime with just a single mode.

### Boosting a super-multipole even further

In what follows, we discuss the possibility to enhance the cross-section of a single multipole beyond what has been achieved so far. For that purpose, we study a subwavelength rectangular prism with refractive index  $n = 3.3$  in the near-IR part of the spectra (inset of Fig. 8a). The prism has unequal sides in all  $x$ ,  $y$ , and  $z$  dimensions. Starting from an initial prism, we vary the  $y$  and  $z$  sides by the same amount  $\delta$ , keeping the  $x$  side constant. Tuning  $\delta$  towards negative or positive values results in the appearance of the quasi-BIC or the super MD resonance. In both cases, a drastic reshaping of the near fields takes place, particularly pronounced in the case of the lower (high- $Q$ ) branch (Fig. 8d).

As in the previous cases, we identify two coupled QNMs  $|u\rangle$  and  $|d\rangle$  (Fig. 8a). Now, however, the  $Q$ -factor at the quasi-BIC is two times larger. This is because the new quasi-BIC is associated not with a quadrupole, but with a pure magnetic octupole response, similar to the one investigated in<sup>5</sup>. On the other hand, QNM  $|d\rangle$  has a

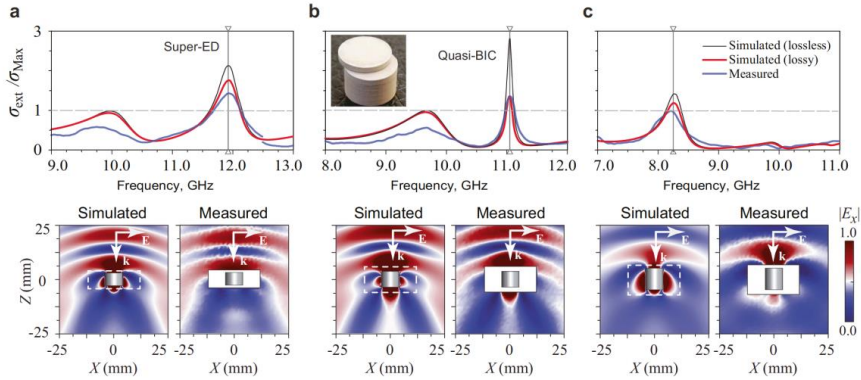


**Fig. 7 | Experimental confirmation of super-ED resonances.** Simulated and measured total extinction cross-sections and scattered electric near-field patterns. All the cross-sections are normalized by the single-channel limit for the ED,  $\sigma_{Max} = 3\lambda^2/2\pi$ . Insets show an example of the experimental resonator and the

electric field norms in the  $x$ - $z$  plane of the resonances indicated by vertical lines in the top plots. The white regions in the near-field patterns correspond to the physically inaccessible zones for the measurements. The aspect ratios of the disks are: **a**  $\Delta h/r = 0.25$ , **b**  $\Delta h/r = 0.475$ , and **c**  $\Delta h/r = 1.25$ .

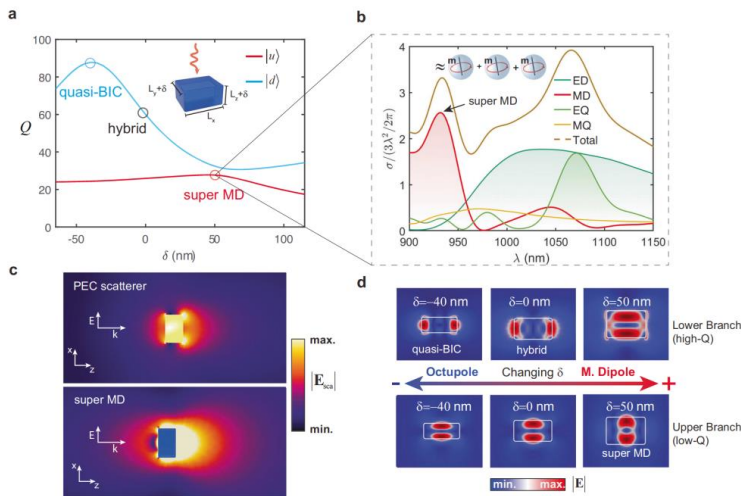


**Fig. 8 | Super-MD resonance produced by dipole-octupole hybridization.** **a** Inset: scheme depicting the geometry of the cavity and the incident illumination. The initial cavity is a rectangular prism with unequal sides  $L_x = 500\text{nm}$ ,  $L_y = 435\text{nm}$ ,  $L_z = 260\text{nm}$ , and refractive index  $n_p = 3.3$ .  $L_x$  is kept constant, while  $L_y$  and  $L_z$  are progressively tuned by an amount  $\delta$ .  $Q$ -factors of the two involved QNMs as a function of  $\delta$ . The quasi-BIC appears in the lower branch (blue circle), characterized by an overall high  $Q$ -factor, for  $\delta = -40\text{nm}$ , while the super MD appears at the upper branch (with overall low  $Q$ -factor) for a detuning of  $\delta = 50\text{nm}$  from the initial geometry (red circle). It coincides with a slight enhancement of the  $Q$ -factor of the upper branch and a decrease in the lower one. **b** Multipole decomposition of the scattering cross section for the cavity with  $\delta = 50\text{nm}$ , normalized by the dipole

limit. We observe a remarkable enhancement of the MD cross-section of  $>2.6$  times the conventional limit. The latter is almost equivalent to the cross section of three magnetic resonances of isolated spheres at the same wavelength (see inset). Incidentally, we also observe the accidental overlap of the high- $Q$  branch, radiating as a combination of electric quadrupole (EQ) and MD, with a super ED resonance similar to the nanorod in the previous section. **c** Comparison between the scattered fields produced by a perfect electric conductor (PEC) cavity (upper panel) and the designed superscatterer (lower panel), both with the same dimensions. The fields are recovered at the wavelength of  $935\text{nm}$ , corresponding to the large MD peak in **b**. **d** Near-field distribution of the involved QNMs for selected  $\delta$  (refer to discussion in text).

predominant magnetic dipole (MD) response. When changing  $\delta$ , we observe the emergence of a strong MD peak, with a cross section equivalent to almost three magnetic spheres (Fig. 8b). Interestingly, the super MD resonance appears in the  $|d'$  branch, which does not feature the quasi-BIC. This is not surprising since the branches are coupled and as discussed earlier, super-multipole resonances are not generally restricted to appear in either one of the two.

The reason for the stronger enhancement can be understood from noticing that, according to Eq. (1), the magnetic octupole with  $l=3$  is bounded to  $\sigma_{\text{Max}}=7\lambda^2/2\pi$ , while the magnetic quadrupole bound is  $5\lambda^2/2\pi$ . Thus, the higher the order of the multipole that couples to the dipole, the larger the enhancement of the dipolar cross section that can be achieved. In addition, numerical and experimental evidence has shown that quasi-BICs with high order multipole resonance have an increasingly larger  $Q$ -factor<sup>37</sup>. It is possible to utilize this fact as a handwaving design rule for super-multipole resonances: the larger the  $Q$ -factor at the quasi-BIC, the larger the potential enhancement of the low order multipole.

To visualize the strong scattering response of the super MD resonance, we compare it with a rectangular prism of the same size but composed of perfect electric conductor (PEC). Figure 8c shows the amplitude of the scattered electric field in both cases. It is worth noting that a significant enhancement can be appreciated for the dielectric prism, both in the forward and in the backward directions. This constitutes an important difference with respect to conventional

superscattering. In the vast majority of designs only forward scattering can be maximized<sup>4,18,23,26</sup>. Thus, super-multipole resonances offer an attractive strategy to enhance backscattering without the need to sacrifice the overall scattering efficiency, as is the case for the anti-Kerker effect<sup>38</sup>.

In principle, the strategy above allows to enhance scattering by a single multipole to arbitrarily large values. Another approach is to combine super-multipoles with Fan et al.'s original method<sup>16</sup>. Namely, we can spectrally overlap the super-multipole resonance with other conventional resonances. As a proof-of-concept, we designed a dielectric nanocylinder with  $n_p=3.3$  where a super-ED accidentally crosses with the MD resonance as a function of height. The combination of both resonances leads to very large cross-sections, in the order of 5 times the single-channel limit [Fig. 9b]. This result is more than three times what can be achieved when overlapping the conventional ED and MD resonances [Figure S4c in the Supplementary Information]. Moreover, we notice that 70% of the enhancement is entirely due to the super-ED.

Figure 9c shows simulations of the strong field distortion produced by such superscatterer. The latter leaves a large 'shadow' where field intensity is significantly lowered. In addition, Fig. 9d shows a comparison between the far fields of our superscatterer and a PEC cavity of the same dimensions. The superscatterer clearly exhibits superior performance, displaying enhanced forward and backward scattering.

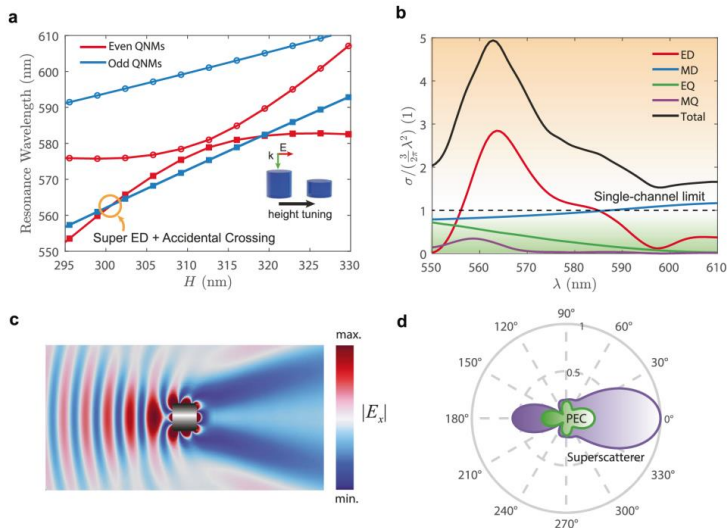


**Fig. 9 | Combining the old and the new mechanisms of superscattering.** Combining the old and the new mechanisms to achieve even more superscattering from passive, subwavelength nanostructures. **a** Calculated resonance wavelengths of the even and odd QNMs for a dielectric nanocylinder with  $n_p=3.3$  and radius 160 nm. The even QNMs are spectrally close and they couple, resulting in the formation of a quasi-BIC and a super-ED as a function of height ( $h$ ). Now, however, we designed the nanoparticle such that the super-ED spectrally overlaps with an odd QNM (accidental crossing), following the original strategy by Fan et al.<sup>16</sup>. Squares and dots denote the dispersions of different modes. **b** Scattering cross section for

$h=300$  nm. The super-ED boosts the ED cross-section by three times the single-channel limit. In combination with the MD and higher-order multipolar contributions, the total cross-section reaches five times the limit. **c**  $x$ -component of the electric field at  $\lambda=565$  nm. The field can be seen to be strongly distorted by the scatterer. **d** Comparison between the far fields produced by a perfect electric conductor (PEC) cavity (green pattern) and the designed superscatterer (purple pattern), both with the same dimensions. The fields have been normalized to the maximum of the superscatterer.

### Shielding nanoparticles from scattering forces

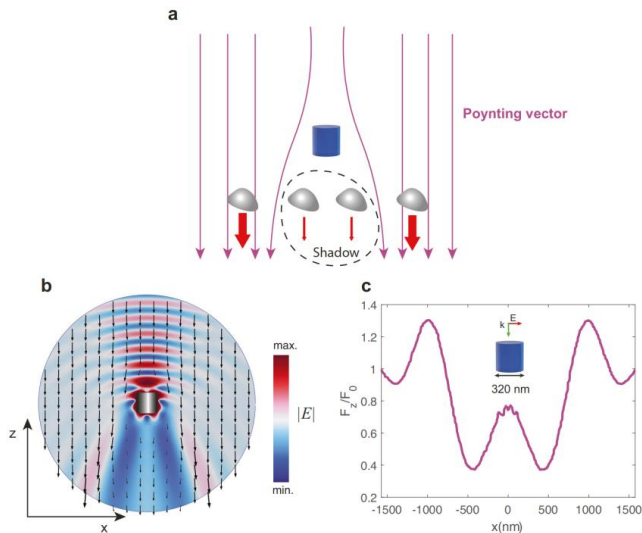
Finally, we provide a glimpse on the possibilities that can be unlocked in optics with the realization of the superscatterers introduced in this study. As an exemplary application, we propose a strategy to ‘protect’ an ensemble of nanoparticles (or one particle, but geometrically significantly larger than the superscatterer) from radiation. In particular, as a figure of merit we will consider parasitic scattering forces induced by an incident beam. Reducing the influence of scattering forces is essential for efficient optical traps for experiments in atom cooling or modern biology<sup>39,40</sup>.

Figure 10a illustrates the main idea. Due to the strong scattering, the Poynting vector lines (purple) near the superscatterer are strongly distorted, leading to a large ‘shadow’ area behind it. Several scatterers can be ‘hidden’ in the shadow, which significantly reduces the scattering force experienced by them (red).

In particular, we consider the scatterers can be modeled as point electric dipoles with an effective polarizability  $\alpha$ . In the case under consideration, the dominant scattering force experienced by dipolar particles is given by<sup>41</sup>  $F_z \propto \text{Im}(\alpha) S_z$ , where  $S_z$  is the z-component of the Poynting vector. The black arrows in Fig. 10b show the distribution of  $F_z$  as a function of position near the superscatterer presented in Fig. 9. Inside the shadow region, the latter can be seen to be strongly suppressed. Figure 10c shows the calculated ratio of optical force with and without the superscatterer at a fixed height. Remarkably, scattering forces can be decreased in a region much larger than the diameter of the superscatterer. Hence, several scatterers can be simultaneously hidden in the shadow.

### Discussion

We have demonstrated how strong coupling of two resonances can be harnessed to achieve novel superscattering regimes with sub-wavelength, nonspherical resonators. We have observed superscattering originating from an electric super dipole moment, being almost two times stronger than the currently established limit. In resonators without spherical symmetry, this effect arises when breaking the quasi-BIC condition by tuning some parameter. Then, power exchange between the scattering channels allows to engineer both  $Q$ -factors and multipolar contents of the resonances, while maintaining a high scattering cross-section. The new super-multipole resonances are more robust to Ohmic losses than their conventional counterparts. Furthermore, we have shown how the enhancement can be boosted even further when quasi-BICs associated with high order multipoles are involved. This enables the formation of super magnetic dipole moments with a cross-section equivalent to almost three magnetic spheres. Besides their fundamental interest, such exotic scattering can be employed in biosensing<sup>42,43</sup> or energy harvesting<sup>44–46</sup> devices. In the near future, strongly scattering dielectric nanoantennas, operating in a selective polarization regime, can replace their plasmonic counterparts as ultra-compact demultiplexers for on-chip circuitry<sup>47</sup>. Furthermore, the ability to selectively enhance the scattering pattern of a given multipole can unlock new degrees of freedom for optical manipulation<sup>48,49</sup>. In this direction, by taking advantage of the designed superscatterer, we have proposed a new strategy to shield an ensemble of particles from radiation, namely—parasitic scattering forces. Beyond optics, we expect super-multipoles to also



**Fig. 10 | Protecting other scatterers from radiation.** **a** Conceptual scheme. The superscatterer interacts with photons in a much larger area than itself. As a result, the Poynting vector field lines (purple arrows) are deflected, and the superscatterer leaves a large ‘shadow’, much larger than its diameter<sup>48</sup>. The scatterers placed within that shadow (gray shapes) are ‘protected’ from the radiation pressure (red arrows) induced by the incident beam. **b** Electric field norm in the vicinity of the superscatterer (same parameters as in Fig. 9), and calculated radiation pressure

experienced by dipolar particles (black arrows). The scattering force (and, consequently, visibility) is significantly decreased within the shadow. **c** Ratio between the scattering force with and without the superscatterer, experienced by dipolar particles positioned at a distance  $z = -1200$  nm from the superscatterer. The origin of coordinates is at the position of the superscatterer. Inset: artistic view of the superscatterer, scaled to match the grid dimensions of the  $x$  axis.

arise in acoustics and other areas of wave physics, paving a way to a venue of applications in strong forward or backward scattering, cloaking, energy harvesting, etc.

## Methods

### Temporal coupled-mode theory

General predictions on the interaction of the scattering channels with the QNMs can be made through a widely applicable phenomenological theory known as the TCMT. The formalism was originally used to introduce the concept of superscattering<sup>36</sup>. Here, we briefly introduce the theory, (whose details can be found in a number of seminal works, e.g.,<sup>30,31</sup>). The coupled mode equations can be written as

$$\frac{d}{dt} \begin{pmatrix} a \\ b \end{pmatrix} = -i\mathcal{H}_0 \zeta \begin{pmatrix} a \\ b \end{pmatrix} + i\sqrt{2D}^T \mathbf{s}^+ \quad (9)$$

and

$$\mathbf{s}^- = \mathbf{s}^+ + i\sqrt{2D} \begin{pmatrix} a \\ b \end{pmatrix} \quad (10)$$

For the derivation of the effective Hamiltonian  $\mathcal{H}_0$  as in Eq. (2), we refer the reader to the Supplementary Information S4. In addition, arguments based on time reversal symmetry and energy conservation constraints<sup>31</sup> lead to the relation

$$D^T D = \Gamma \quad (11)$$

where  $\Gamma = -Im\{\mathcal{H}_0\}$  is a diagonal matrix containing the radiative losses  $\gamma_{a,b}$  in its diagonal. Equation (11) implies that  $\gamma_{a,b} = d_{1,2}^2, d_i$  being the  $i$ -th element in the diagonal of  $D$ . It accounts for the coupling of the eigenmodes to the  $i$ -th multipole channel. The  $R$ -matrix, (Eq. (4) in the main text), can be derived by assuming time-harmonic dependence  $[d/dt \rightarrow -i\omega$  in Eq. (9)], and substituting Eq. (9) into Eq. (10) to eliminate  $(a \ b)^T$ . Further details on the connection between TCMT and rigorous QNM perturbation theory can be found in the Supplementary Information S2.

### Numerical simulations

Scattering and eigenmode simulations have been performed with the commercial finite element solver COMSOL Multiphysics ©.

### Experimental methods

A Taizhou Wangling TP-series microwave ceramic composite is used as a dielectric material for the fabrication of the cylindrical resonators. To measure the total extinction cross section, the samples are placed in an anechoic chamber and illuminated by normally incident, linearly polarized waves radiated and received by a pair of HengDa Microwave HD-10ISODRA10 horn antennas. A LINBOU near-field imaging system is used for the near-field mapping. More details on the fabricated samples and the experimental setup can be found in the Supplementary Information S8 and Figure S2.

### Data availability

All data needed to evaluate the conclusions in this study is presented in the manuscript and in the Supplementary Information.

## References

- El-Ganainy, R., Khajavikhan, M., Christodoulides, D. N. & Ozdemir, S. K. The dawn of non-Hermitian optics. *Commun. Phys.* **2**, 37 (2019).
- Hodaiei, H. et al. Enhanced sensitivity at higher-order exceptional points. *Nature* **548**, 187–191 (2017).
- Feng, L., Wong, Z. J., Ma, R.-M., Wang, Y. & Zhang, X. Single-mode laser by parity-time symmetry breaking. *Science* **346**, 972–975 (2014).
- Feng, L. et al. Experimental demonstration of a unidirectional reflectionless parity-time metamaterial at optical frequencies. *Nat. Mater.* **12**, 108–113 (2013).
- Koshelev, K. et al. Subwavelength dielectric resonators for nonlinear nanophotonics. *Science* **367**, 288–292 (2020).
- Chebykin, A.V., Orlov, A.A., Shalin, A.S., Poddubny, A.N. & Belov, P.A. Strong Purcell effect in anisotropic e-near-zero metamaterials. *Phys. Rev. B* **91**, 205126 (2015).
- Huang, Y., Shen, Y., Min, C., Fan, S. & Veronis, G. Unidirectional reflectionless light propagation at exceptional points. *Nanophotonics* **6**, 977–996 (2017).
- Park, J.-H. et al. Symmetry-breaking-induced plasmonic exceptional points and nanoscale sensing. *Nat. Phys.* **16**, 462–468 (2020).
- Canós Valero, A. et al. Theory, observation, and ultrafast response of the hybrid anapole regime in light scattering. *Laser Photon. Rev.* **15**, 2100114 (2021).
- Limonov, M. F., Rybin, M. V., Poddubny, A. N. & Kivshar, Y. S. Fano resonances in photonics. *Nat. Photonics* **11**, 543–554 (2017).
- Totero Gongora, J. S., Miroshnichenko, A. E., Kivshar, Y. S. & Fratalocchi, A. Anapole nanolasers for mode-locking and ultrafast pulse generation. *Nat. Commun.* **8**, 15535 (2017).
- Rybin, M. V. et al. High-Q supercavity modes in subwavelength dielectric resonators. *Phys. Rev. Lett.* **119**, 1–5 (2017).
- Friedrich, H. Interfering resonances and BIC. *Phys. Rev. A* **32**, 3231–3242 (1985).
- Qian, C. et al. Experimental observation of superscattering. *Phys. Rev. Lett.* **122**, 063901 (2019).
- Shcherbinin, V. I., Fesenko, V. I., Tkachova, T. I. & Tuz, V. R. Superscattering from subwavelength corrugated cylinders. *Phys. Rev. Appl.* **13**, 024081 (2020).
- Ruan, Z. & Fan, S. Superscattering of light from subwavelength nanostructures. *Phys. Rev. Lett.* **105**, 1–4 (2010).
- Cheng, L. et al. Superscattering, superabsorption, and non-reciprocity in nonlinear antennas. *ACS Photonics* **8**, 585–591 (2021).
- Ruan, Z. & Fan, S. Design of subwavelength superscattering nanospheres. *Appl. Phys. Lett.* **98**, 43101 (2011).
- Qian, C. et al. Multifrequency superscattering from subwavelength hyperbolic structures. *ACS Photonics* **5**, 1506–1511 (2018).
- Mirzaei, A., Miroshnichenko, A. E., Shadrivov, I. V. & Kivshar, Y. S. Superscattering of light optimized by a genetic algorithm. *Appl. Phys. Lett.* **105**, 113107 (2014).
- Lepeshov, S., Krasnok, A. & Alù, A. Nonscattering-to-superscattering switch with phase-change materials. *ACS Photonics* **6**, 2126–2132 (2019).
- Wan, W., Zheng, W., Chen, Y. & Liu, Z. From Fano-like interference to superscattering with a single metallic nanodisk. *Nanoscale* **6**, 9093–9102 (2014).
- Qian, C. et al. Breaking the fundamental scattering limit with gain metasurfaces. *Nat. Commun.* **13**, 4383 (2022).
- Lalanne, P., Yan, W., Vynck, K., Sauvan, C. & Hugonin, J. P. Light interaction with photonic and plasmonic resonances. *Laser Photon. Rev.* **12**, 1–38 (2018).
- Yan, W., Lalanne, P. & Qiu, M. Shape deformation of nanoresonator: a quasinormal-mode perturbation theory. *Phys. Rev. Lett.* **125**, 013901 (2020).
- Mirzaei, A., Shadrivov, I. V., Miroshnichenko, A. E. & Kivshar, Y. S. Cloaking and enhanced scattering of core-shell plasmonic nano-wires. *Opt. Express* **21**, 10454 (2013).
- Miller, O. D. et al. Fundamental limits to extinction by metallic nanoparticles. *Phys. Rev. Lett.* **112**, 1–5 (2013).
- Hsu, C. W., DeLacy, B. G., Johnson, S. G., Joannopoulos, J. D. & Soljačić, M. Theoretical criteria for scattering dark states in nanostructured particles. *Nano Lett.* **14**, 2783–2788 (2014).

29. Bogdanov, A. A. et al. Bound states in the continuum and Fano resonances in the strong mode coupling regime. *Adv. Photonics* **1**, 1 (2019).
30. Sweeney, W. R., Hsu, C. W. & Stone, A. D. Theory of reflectionless scattering modes. *Phys. Rev. A (Coll Park)* **102**, 063511 (2020).
31. Alpeggiani, F., Parappurath, N., Verhagen, E. & Kuipers, L. Quasinormal-mode expansion of the scattering matrix. *Phys. Rev. X* **7**, 1–13 (2017).
32. Muljarov, E. A. & Weiss, T. Resonant-state expansion for open optical systems: generalization to magnetic, chiral, and bi-anisotropic materials. *Opt. Lett.* **43**, 1978 (2018).
33. Doost, M. B., Langbein, W. & Muljarov, E. A. Resonant-state expansion applied to three-dimensional open optical systems. *Phys. Rev. A* **90**, 013834 (2014).
34. Hsu, C. W., Zhen, B., Stone, A. D., Joannopoulos, J. D. & Soljacic, M. Bound states in the continuum. *Nat. Rev. Mater.* **1**, 16048 (2016).
35. Odit, M. et al. Observation of supercavity modes in subwavelength dielectric resonators. *Adv. Mater.* **33**, 1–7 (2021).
36. Gladyshev, S., Frizyuk, K. & Bogdanov, A. Symmetry analysis and multipole classification of eigenmodes in electromagnetic resonators for engineering their optical properties. *Phys. Rev. B* **102**, 075103 (2020).
37. Huang, L., Xu, L., Rahmani, M., Neshev, D. & Miroshnichenko, A. E. Pushing the limit of high-Q mode of a single dielectric nanocavity. *Adv. Photonics* **3**, 1–9 (2021).
38. Olmos-Trigo, J., Abujetas, D. R., Sanz-Fernández, C., Sánchez-Gil, J. A. & Sáenz, J. J. Optimal backward light scattering by dipolar particles. *Phys. Rev. Res.* **2**, 013225 (2020).
39. Jones, P. H., Maragó, O. M. & Volpe, G. Optical tweezers: principles and applications. (Cambridge University Press, 2015).
40. Juan, M. L., Righini, M. & Quidant, R. Plasmon nano-optical tweezers. *Nat. Photonics* **5**, 349 (2011).
41. Canós Valero, A. et al. Nanovortex-driven all-dielectric optical diffraction boosting and sorting concept for lab-on-a-chip platforms. *Adv. Sci.* **7**, 1903049 (2020).
42. Kostina, N. et al. Optical binding via surface plasmon polariton interference. *Phys. Rev. B* **99**, 125416 (2017).
43. Barhom, H. et al. Biological Kerker effect boosts light collection efficiency in plants. *Nano Lett* **19**, 7062–7071 (2019).
44. Terekhov, P. D. et al. Broadband forward scattering from dielectric cubic nanoantenna in lossless media. *Opt. Express* **27**, 10924 (2019).
45. Terekhov, P. D. et al. Enhanced absorption in all-dielectric metasurfaces due to magnetic dipole excitation. *Sci. Rep.* **9**, 3438 (2019).
46. Kozlov, V., Filonov, D., Shalin, A. S., Steinberg, B. Z. & Ginzburg, P. Asymmetric backscattering from the hybrid magneto-electric meta particle. *Appl. Phys. Lett.* **109**, 203503 (2016).
47. Guo, R. et al. High-bit rate ultra-compact light routing with mode-selective on-chip nanoantennas. *Sci. Adv.* **3**, e1700007 (2017).
48. Wang, S. B. & Chan, C. T. Lateral optical force on chiral particles near a surface. *Nat. Commun.* **5**, 1–8 (2014).
49. Kislov, D. A. et al. Multipole engineering of attractive–repulsive and bending optical forces. *Adv. Photonics Res.* **2**, 2100082 (2021).
50. Ruan, Z. & Fan, S. Temporal coupled-mode theory for light scattering by an arbitrarily shaped object supporting a single resonance. *Phys. Rev. A* **85**, 1–8 (2012).
51. Suh, W., Wang, Z. & Fan, S. Temporal coupled-mode theory and the presence of non-orthogonal modes in lossless multimode cavities. *IEEE J. Quantum Electron.* **40**, 1511–1518 (2004).
52. Weiss, T. How to calculate the pole expansion of the optical scattering matrix from the resonant states. *Phys. Rev. B* **085433**, 1–12 (2018).
53. DeFrance, J. & Weiss, T. On the pole expansion of electromagnetic fields. *Opt. Express* **28**, 32363 (2020).
54. Wu, T., Baron, A., Lalanne, P. & Vynck, K. Intrinsic multipolar contents of nanoresonators for tailored scattering. *Phys. Rev. A* **101**, 011803 (2020).

## Acknowledgements

The research was supported by Priority 2030 Federal Academic Leadership Program. The authors gratefully acknowledge the financial support from the Ministry of Science and Higher Education of the Russian Federation (Agreement No. 075-15-2022-1150). The calculations of quasi-BICs and super-multipoles are partially supported by the Russian Science Foundation grant o. 23-72-00037. A.S.K. acknowledges financial support from the National Key R&D Program of China (project No. 2018YFE0119900). A.C.V. gratefully acknowledges funding from the Russian Science Foundation project No. 22-42-04420, for the calculation of QNMs of the nanorod. Y.K. acknowledges support from the Australian Research Council (grant DP210101292). V.B. acknowledges the support of the Latvian Council of Science, project: NEO-NATE, No. Izp-2022/1-0553.

## Author contributions

A.C.V. and H.K.S. conceived the idea. A.C.V. developed the theory and wrote the first draft of the manuscript. A.C.V. performed the initial numerical simulations. H.K.S. conducted numerical optimizations of the nanoscatterers. A.S.K. performed the experiment. A.S. and Y.K. extended the original idea, supervised the project, proofread the manuscript, and actively participated in the discussions. T.W. proofread the final version of the manuscript and provided valuable suggestions. A.A.P., V.B., and D.R. contributed to the writing of the manuscript and the discussions.

## Competing interests

The authors declare no competing interests.

## Additional information

**Supplementary information** The online version contains supplementary material available at <https://doi.org/10.1038/s41467-023-40382-y>.

**Correspondence** and requests for materials should be addressed to Adrià Canós Valero, Yuri Kivshar or Alexander S. Shalin.

**Peer review information** *Nature Communications* thanks the anonymous reviewers for their contribution to the peer review of this work. A peer review file is available.

**Reprints and permissions information** is available at <http://www.nature.com/reprints>

**Publisher's note** Springer Nature remains neutral with regard to jurisdictional claims in published maps and institutional affiliations.

**Open Access** This article is licensed under a Creative Commons Attribution 4.0 International License, which permits use, sharing, adaptation, distribution and reproduction in any medium or format, as long as you give appropriate credit to the original author(s) and the source, provide a link to the Creative Commons licence, and indicate if changes were made. The images or other third party material in this article are included in the article's Creative Commons licence, unless indicated otherwise in a credit line to the material. If material is not included in the article's Creative Commons licence and your intended use is not permitted by statutory regulation or exceeds the permitted use, you will need to obtain permission directly from the copyright holder. To view a copy of this licence, visit <http://creativecommons.org/licenses/by/4.0/>.

© The Author(s) 2023



## **11-PAPER:** Modelling and characterization of microspheres with silver molecular clusters for sensors applications

Mikharev, E.; Lunev, A.; Sidorov, A.; Redka, D. "Modeling and Characterization of Microspheres with Silver Molecular Clusters for Sensor Applications". (2023) Eng. Proc. 2023, 58,95. DOI: [10.3390/ecsa-10-16196](https://doi.org/10.3390/ecsa-10-16196)

Proceeding Paper

# Modeling and Characterization of Microspheres with Silver Molecular Clusters for Sensor Applications <sup>†</sup>

Egor Mikharev <sup>1,\*</sup>, Andrey Lunev <sup>1,\*</sup>, Alexander Sidorov <sup>2</sup> and Dmitry Redka <sup>1,3</sup>

<sup>1</sup> Department of Photonics, Faculty of Electronics, St. Petersburg Electrotechnical University “LETI”, St. Petersburg 197022, Russia; dnredka@etu.ru

<sup>2</sup> Research Center for Optical Material Engineering, ITMO University, St. Petersburg 197101, Russia; sidonov@oi.ifmo.ru

<sup>3</sup> Institute of Telecommunications, Riga Technical University, LV-1048 Riga, Latvia

\* Correspondence: eamikharev@stud.etu.ru (E.M.); ayulunoyov@stud.etu.ru (A.L.)

<sup>†</sup> Presented at the 10th International Electronic Conference on Sensors and Applications (ECSA-10), 15–30 November 2023; Available online: <https://ecsa-10.sciforum.net/>.

**Abstract:** This study explores silver-molecular-cluster-containing microspheres for advanced sensors. These microspheres are synthesized through an ion exchange process with silver nitrate and sodium nitrate, creating unique optical properties. A simulation shows an enhanced radiation interaction due to extended fundamental mode propagation. This study investigates luminescence in the visible range (400–600 nm) when excited by long-wavelength UV light (360–410 nm), offering the potential for sensing applications. These microspheres find use in environmental sensing (pollutant detection), biomedicine (drug delivery, bioimaging), and industrial process monitoring.

**Keywords:** microspheres; silver molecular clusters; advanced sensor applications; ion exchange; glass matrix; refractive index gradient; optical characteristics; luminescence; UV light excitation; sensor technologies

## 1. Introduction

In recent years, Whispering Gallery Mode (WGM) microcavities have garnered significant attention as potential optical sensors for the label-free detection of various biological and chemical molecules and particles. These sensors can identify a range of molecules with refractive indices differing from that of the surrounding environment, eliminating the need for labeling. They rely on the observation of frequency shifts in WGM resonance due to minute perturbations in the mode volume. The efficacy of these sensors has been demonstrated in the detection of a variety of objects, including individual proteins, DNA molecules, and viruses [1,2].

In our current research, we explore a novel material for use in these WGM sensors. We focus on silicate glass microspheres containing ions and neutral molecular clusters (MC) of silver. These glasses are exceptional materials that exhibit intense luminescence in the visible spectrum [3]. They are characterized by high quantum yields and resistance to degradation, making them more appealing than organic dyes. The primary limitation of such sensors lies in the requirement for physical coupling between the WGM resonator and external optics, such as a tapered fiber or bus waveguide, to provide phase-matched evanescent coupling [4]. An alternative approach is the concept of WGM sensors with optically active resonators [5], which enables pumping in the UV region via LEDs and remote measurements through free space optics.

The ion exchange (IE) method is currently widely utilized for synthesizing multifunctional glasses. This method is straightforward to execute and enables the attainment of a high concentration of silver ions near the glass surface. Although studies on glasses with



**Citation:** Mikharev, E.; Lunev, A.; Sidorov, A.; Redka, D. Modeling and Characterization of Microspheres with Silver Molecular Clusters for Sensor Applications. *Eng. Proc.* **2023**, *58*, 95. <https://doi.org/10.3390/ecsa-10-16196>

Academic Editor: Stefano Mariani

Published: 15 November 2023



**Copyright:** © 2023 by the authors. Licensee MDPI, Basel, Switzerland. This article is an open access article distributed under the terms and conditions of the Creative Commons Attribution (CC BY) license (<https://creativecommons.org/licenses/by/4.0/>).

Ag<sup>+</sup> ions and silver ions obtained through the IO method have been conducted for more than half a century, their potential remains far from being fully explored.

In soda-silicate glass, silver initially exists in its ionic form as Ag<sup>+</sup>. Structural defects in the glass may contain uncompensated negative charges. These defects can arise from various factors, including defects in the crystal lattice of the glass or the presence of additional ions that can form negatively charged sites. In the presence of electronic defects near glass structural defects, silver ions Ag<sup>+</sup> can readily be reduced to neutral silver atoms Ag<sup>0</sup>. This reduction occurs when the glass is heated, and electrons are released from electronic defects. Neutral silver atoms Ag<sup>0</sup> can aggregate into molecular clusters, potentially comprising multiple silver atoms, each with unique optical and electronic properties. The formation of these molecular clusters can be induced by the characteristics of glass structure defects and heating conditions.

## 2. Materials and Methods

To create the silicate glass microspheres, we employed glass with the composition detailed in Table 1. The production process involved several steps. Initially, we crafted a thin fiber, and subsequently, we formed the microspheres by melting the fiber's end using a propane flame. The microspheres were then subjected to the Low-Temperature Ion Exchange (LTIE) process.

**Table 1.** Composition of glass used for making samples.

Chemical Constituents	Glass (% Mass)
SiO <sub>2</sub>	72.2%
Na <sub>2</sub> O	14.3%
K <sub>2</sub> O	1.2%
CaO	6.4%
MgO	4.3%
Al <sub>2</sub> O <sub>3</sub>	1.2%
Fe <sub>2</sub> O <sub>3</sub>	0.03%
SO <sub>3</sub>	0.3%

The ion exchange process occurred in a molten salt mixture of silver nitrate (AgNO<sub>3</sub>) and sodium nitrate (NaNO<sub>3</sub>) at a temperature of 330 °C for a duration of 15 min. To monitor the progress of the process, we also included witness glasses with the same composition. These glasses, with a thickness of 0.17 mm, underwent the ion exchange process alongside the microspheres in a common crucible.

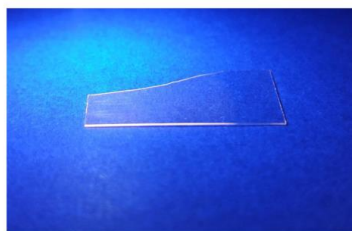
Following the LTIE process, we meticulously cleansed the samples. This cleansing process involved washing with distilled water and then with isopropyl alcohol to eliminate any residual salts remaining on the surface after the process.

Figure 1 display photographs of the samples we obtained. Notably, the smallest sample achievable through the described method had a diameter of 200 microns. Figure 2 shows one of the witness samples that was not completely immersed in the crucible; when the sample was illuminated with an LED with a wavelength of ≈390 nm, the luminescence of molecular clusters of silver was clearly visible, and the area where the glass passes was not immersed in the molten salts.

Cosmol Multiphysics was employed to determine the resonant frequencies and fundamental modes of the resonator. For an effective modeling of the WGM resonator, a two-dimensional axisymmetric approach was adopted. The grid was manually adjusted to facilitate a two-dimensional axisymmetric natural frequency analysis.



**Figure 1.** The obtained microsphere samples: (a) microsphere with a diameter of 380  $\mu\text{m}$ ; (b) microsphere with a diameter of 200  $\mu\text{m}$ .



**Figure 2.** Witness sample visible luminescence.

The investigation of the properties of silicate glass containing silver molecular clusters, synthesized through the LTIE method, encompassed both absorption measurements and luminescence spectra measurements. Absorbance measurements were conducted on the witness samples using a UV-VIS spectrophotometer (PB 2201). Luminescence spectral acquisition measurements were performed using a Fluorolog<sup>®</sup>-3 instrument with FluorEssence<sup>™</sup> (HORIBA Jobin Yvon SAS, Palaiseau, France). For all luminescence measurements, the integration time was 0.1 s.

### 3. Results and Discussion

#### 3.1. Investigation of the Properties of Silicate Glass Containing Silver Molecular Clusters

An experiment was conducted to measure the absorption of glass samples that underwent Low-Temperature Ion Exchange (LTIE), as well as transparent glass samples that were not subjected to LTIE treatment. The resulting spectrum is depicted in Figure 3. Notably, the absorption spectrum of the samples after the LTIE process lacks characteristic absorption peaks. This absence is attributed to the fact that, under the same process parameters used in the treatment, predominantly silver molecular clusters, such as  $\text{Ag}_{2...5}$ , are formed [6].

Figure 4 presents the results of measuring the luminescence intensity. When excited at wavelengths of 370 nm and 390 nm, the luminescence spectra of all synthesized glasses exhibit a broad luminescence band within the visible spectrum. This broadband luminescence spanning from 500 to 900 nm corresponds to the emission emanating from a small quantity of silver microcrystals formed directly during the LTIE process [7]. To generate molecular clusters (MC), it is imperative to reduce silver ions to their atomic state. This transformation leads to the creation of a certain quantity of silver microcrystals during the LTIE process, consequently giving rise to weak luminescence across the entire visible range.

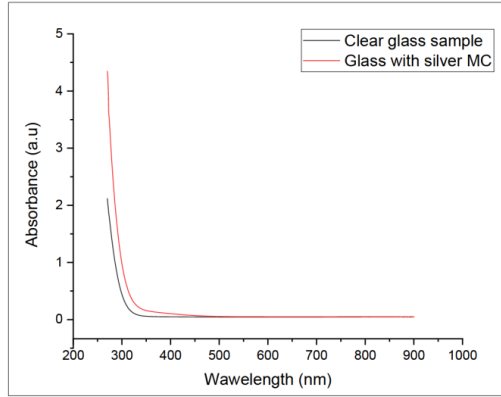


Figure 3. This is a figure. Schemes follow the same formatting.

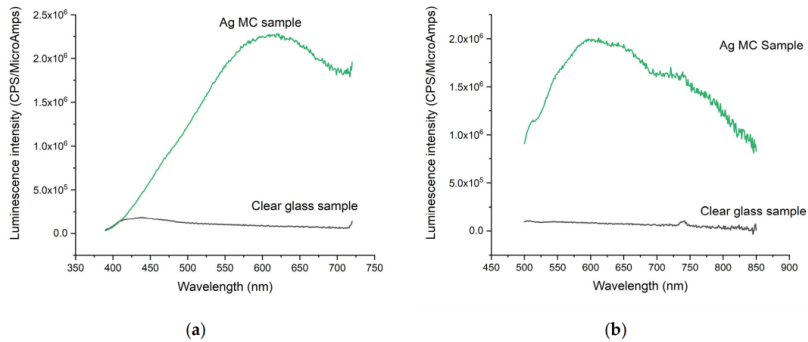


Figure 4. Luminescence intensity: (a) first sample,  $\lambda_{exc}$  370 nm; (b) second sample,  $\lambda_{exc}$  390 nm.

### 3.2. Modeling WGM Resonators

The simulated microspheres had a radius of 100  $\mu\text{m}$ . During the LTIE process with silver, glass changes its refractive index from 1.585 on the surface to 1.515. The simulated microsphere had a gradient refractive index from the edge of the microsphere to the center. To explore the potential of this material, simulations of microspheres in air and water were carried out. Figure 5 shows the distribution of the EM field in the cross-section of the microcavity in air (a) and water (b). The resonant wavelength for the fundamental mode of the microresonator near the luminescence peak was determined. For a microsphere in air, the resonant wavelength for the fundamental TE mode with azimuthal number 1608 was 600.988. For a microsphere in water, the resonant wavelength for the fundamental TE mode with azimuthal number 1608 was 601.294. The difference between the resonant wavelengths was 0.25 nm.

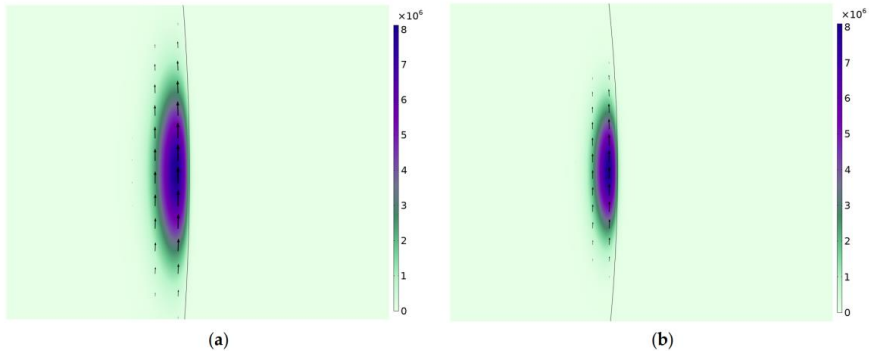


Figure 5. Fundamental mode localization: (a) microsphere in air; (b) microsphere in water.

#### 4. Conclusions

We have obtained a new material that is suitable for use in label-free sensors with active WGM resonators. This material is very simple to obtain and cost-effective. The experiment showed that glass samples subjected to Low-Temperature Ion Exchange (LTIE) showed distinct absorption characteristics, particularly the absence of characteristic absorption peaks, which was attributed to the formation of  $\text{Ag}_{2...5}$  molecular clusters of silver. Luminescence measurements demonstrated a broad emission band in the visible spectrum, especially in the 500–900 nm range, confirming the formation of silver microcrystals during the LTIE process.

According to the simulation results, the difference between the resonant wavelengths for media with different refractive indexes was 0.26 nm. This allows the material to be used for microsphere sensors without direct physical connection. The results obtained show the potential of soda silicate glass with molecular silver clusters as a material for WGM sensors.

**Author Contributions:** Conceptualization, E.M. and A.S.; methodology, A.S.; software, A.L.; validation, E.M. and A.L.; formal analysis, A.S.; investigation, A.L. and E.M.; resources, D.R.; data curation, A.S.; writing—original draft preparation, E.M.; writing—review and editing, E.M. and A.L.; visualization, A.L.; supervision, A.L.; project administration, D.R. All authors have read and agreed to the published version of the manuscript.

**Funding:** This research received no external funding.

**Institutional Review Board Statement:** Not applicable.

**Informed Consent Statement:** Not applicable.

**Data Availability Statement:** Data are contained within the article.

**Conflicts of Interest:** The authors declare no conflict of interest.

#### References

1. Foreman, M.R.; Swaim, J.D.; Vollmer, F. Whispering gallery mode sensors. *Adv. Opt. Photon.* **2015**, *7*, 168–240. [[CrossRef](#)] [[PubMed](#)]
2. Vollmer, F.; Arnold, S. Whispering-gallery-mode biosensing: Label-free detection down to single molecules. *Nat. Methods* **2008**, *5*, 591–596. [[CrossRef](#)] [[PubMed](#)]
3. Demichev, I.A.; Ignat'ev, A.I.; Nikonorov, N.V.; Sgibnev, E.M.; Sidorov, A.I.; Khrushcheva, T.A.; Shakhverdov, T.A. Specific features of the luminescence of silicate glasses with silver introduced by ion exchange. *Opt. Spectrosc.* **2014**, *116*, 587–592. [[CrossRef](#)]

4. Wienhold, T.; Kraemmer, S.; Wondimu, S.F.; Siegle, T.; Bog, U.; Weinzierl, U.; Schmidt, S.; Becker, H.; Kalt, H.; Mappes, T.; et al. All-polymer photonic sensing platform based on whispering-gallery mode microgoblet lasers. *Lab Chip* **2015**, *15*, 3800–3806. [[CrossRef](#)] [[PubMed](#)]
5. Hanumegowda, N.M.; White, I.M.; Oveys, H.; Fan, X. Label-free protease sensors based on optical microsphere resonators. *Sens. Lett.* **2005**, *3*, 315–319. [[CrossRef](#)]
6. Sheng, J.; Li, J.; Yu, J. The development of silver nanoclusters in ion-exchanged soda-lime silicate glasses. *Int. J. Hydrog. Energy* **2007**, *32*, 2598–2601. [[CrossRef](#)]
7. Simo, A.; Polte, J.; Pfander, N.; Vainio, U.; Emmerling, F.; Rademann, K. Formation Mechanism of Silver Nanoparticles Stabilized in Glassy Matrices. *J. Am. Chem. Soc.* **2012**, *134*, 18824–18833. [[CrossRef](#)] [[PubMed](#)]

**Disclaimer/Publisher's Note:** The statements, opinions and data contained in all publications are solely those of the individual author(s) and contributor(s) and not of MDPI and/or the editor(s). MDPI and/or the editor(s) disclaim responsibility for any injury to people or property resulting from any ideas, methods, instructions or products referred to in the content.



**Dmitrii Redka** was born in 1989 in Germany. He received a Master's degree in Quantum and Optical Electronics (2010) from Saint Petersburg State Electrotechnical University (Russia). He is currently a researcher at the Institute of Photonics, Electronics and Telecommunications of RTU Faculty of Computer Science, Information Technology and Energy.